Quadrupole Mass Filters Operated in Higher Stability Regions

by

WEI CHEN

B.Sc., (Chemistry) Wuhan University, 1990

M.Sc., (Chemistry) Wuhan University, 1993

A THESIS SUBMITTED IN PARTIAL FULFILMENT OF THE

REQUIREMENT FOR THE DEGREE OF DOCTOR OF PHILOSOPHY

in

THE FACULTY OF GRADUATE STUDIES

(Department of Chemistry)

We accept this thesis as confirming

to the required standard

THE UNIVERSITY OF BRITISH COLUMBIA

June 2002

In presenting this thesis in partial fulfilment of the requirements for an advanced degree at the University of British Columbia, I agree that the Library shall make it freely available for reference and study. I further agree that permission for extensive copying of this thesis for scholarly purposes may be granted by the head of my department or by his or her representatives. It is understood that copying or publication of this thesis for financial gain shall not be allowed without my written permission.

Department of Chemistry

The University of British Columbia
Vancouver, Canada

Date Dec 2. 2002

DE-6 (2/88)

Abstract

This thesis describes experimental and theoretical studies of the properties of a quadrupole mass filter operated in the fourth stability region (Mathieu parameters $a \approx 0$ and $q \approx 21.3$) and the sixth stability region (Mathieu parameters $a \approx 8$, $q \approx 6$). The experimental work is done with a thermal ionization quadrupole mass spectrometer. The objective is to improve the resolution of inductively coupled plasma mass spectrometers for elemental analysis.

With a quadrupole operated in the fourth region, a resolution measured as full peak width at half height ($R_{1/2}$) of up to 13,900 with 40 eV $^{39}K^+$ ions is obtained and a resolution of several thousand at *m/z* 39 with ions of several keV energy is achieved. The transmission is somewhat lower than that of the second stability region for a given resolution between 1500 and 5000, but much higher than that expected from acceptance calculations.

Operation in the sixth stability region gives a maximum resolution of $R_{1/2}$=2000 for $^{39}K^+$ ions with an axial ion energy of 20 eV, and resolution of several hundred with high energy ions (>1000 eV). Operation at the upper (M) tip usually gives relatively higher resolution and transmission than operation at the lower (S) tip for the same ion energy. Thus for ions of intermediate energy, a quadrupole operated in the sixth stability region can also be used as an independent mass filter. This region could also be used as an additional mass filter to eliminate alias ions when a quadrupole is operated in regions II or IV.

This thesis also describes a theoretical calculation of the ion optical properties of a quadrupole operated near the fourth and the sixth regions. For these regions, ions experience fewer RF cycles inside the quadrupole field because relatively higher energies are required to penetrate the fringing field at the entrance of the quadrupole rods. Ions outside the stability regions can thus pass through the quadrupole. Thus the stability boundaries are considered diffuse. For the fourth stability region, a narrower peak could not be obtained with $a>0$ for ion energies larger than 500 eV, and split peaks were observed with a scan line operated above the tip of the region. For the sixth stability region, broader peaks are obtained with higher energy ions, and the y-stability band dominates the ion transmission. Peaks were observed when using a quadrupole operated beyond the two tips of this region.

Table of Contents

List of Tables

List of Figures

List of Symbols

Symbols	Description
$\vec{F}$	Force
$\vec{a}$	Ion acceleration
$\vec{E}$	Electric field
$\hat{i}, \hat{j}$ and $\hat{k}$	Unit vectors in the x, y and z directions, respectively
ω	Angular frequency
∇	Gradient operator, given by $\nabla = \hat{i}\frac{\partial}{\partial x} + \hat{j}\frac{\partial}{\partial y} + \hat{k}\frac{\partial}{\partial z}$
ξ	Time in radians
μ	Constant (parameter of the increment of exponential growth of the ion oscillation amplitude during one period)
β	Stability number
ε	The acceptance ellipse area divided by π.
Γ	Parameter of the acceptance ellipse
λ	U/2V
Φ (x, y)	Electrical potential
$\Delta\xi$	Integration step size
Φ_0	Electric potential applied to electrodes
ξ_0	Initial phase

Δm	Measured peak width
$\Delta m_{1/2}$	Measured peak width at half height
Ω_n	Frequency of ion motion
Δq	Width of a scan line within a stability region
β_x or β_y	Values of β for in the x or y directions
$\dot{u}_0$	Initial transverse velocity
a	Parameter in the Mathieu equation of ion motion that depends on U
A	Parameter of the acceptance ellipse
A and B	Constants
a_G, q_G,	Values of a, q at the tip of the fourth stability region
α' and α''	Integration constants
B	Parameter of the acceptance ellipse
C_{2n}	Constant
E_z	Axial ion energy
e	Electronic charge
f	Focusing parameter equal to $\dot{u}/u$
$\hat{F}$	Transformation matrix
h	Constant
k	Constant
m	Ion mass
m_1, m_2 and m_3	Ion mass
M	Transfer matrix

m_{11}, m_{12}, m_{21}, and m_{22}	Elements of the transfer matrix
n	Integer =0, ±1, ±2, ±3…
n	The residence time, in terms of the number of RF cycles, that ions spend in the quadrupole field
n_f	The number of RF cycles that an ion spends in the fringing field
N_{in}	Total number of ions that were injected into the quadrupole field
N_{out}	Number of ions transmitted through the mass filter
N_p	Number of initial points on the input aperture
P	Number of initial phases
q	Parameter in the Mathieu equation of ion motion that depends on V
r_0	Field radius (the distance between the center and an electrode)
$R_{1/2}$	Resolution at half peak height ($m/\Delta m_{1/2}$)
r_a,	Radius of the circular input aperture of the quadrupole field
T	Ion transmission
t	Time in seconds
U	DC voltage applied between each quadrupole rod and ground
u	Generally spatial coordinate, represents x or y transverse displacement
u_0	Initial transverse position
V	Amplitude (zero-to-peak) of the radio frequency (RF) voltage applied between each rod and ground
x	Transverse coordinate (conventionally indicates the direction toward

	the positively biased electrodes)
x_0, y_0	Initial positions in x and y directions, expressed in units of r_0
y	Transverse coordinate (conventionally indicates the direction toward the negatively biased electrodes)
z	Axial coordinate
z	The number of electronic charge
Z_f	Effective fringing field length

List of Abbreviations

Abbreviations	Descriptions
TOF	Time-of- flight
MALDI	Matrix-assisted laser desorption /ionization
RF	Radio frequency
DC	Direct current
DRC	Dynamic reaction cell
ICP-MS	Inductively coupled plasma mass spectrometer
ICP	Inductively coupled plasma
QMF	Quadrupole mass filter
ETV	Electro-thermal vaporizer
RK-N-DP	Runge-Kutta Nystorm and Dormand - Prince
DAC	Digital - to - Analog Converter
CEM	Channel electron multiplier
TTL	Transistor-transistor logic
T-R	Transmission versus resolution
FT-ICR	Fourier transform ion cyclotron resonance
GC	Gas chromatography

Acknowledgements

I am sincerely grateful to Dr. Don Douglas, my supervisor, for his patience, guidance, kindness, multiple and careful readings of this thesis, and valuable comments on this thesis. I learned a lot during the years in Don's lab. My heartfelt thanks also go to Bruce Collings, who helped me at every level with my experiments and gave me many helpful suggestions. I really appreciate his time and patience. I would also like to thank Dr. Michael Blades for the review of this thesis. In addition, I would like to thank all other former and present members, especially Nikolai Konenkov and Michael Sudakov (visiting scholars from Russia) for giving me their programs, Aaron and Kevin for proofreading Chapter 1, Chuanfan, Dunmin, Yu-luan and Annie for helpful suggestions. I also appreciate my friends Aihua and Xinxiang for the their kind assistance.

Assistance from the electronic (Dave Tonkin) and mechanical shops (Brian Snapkauskas, Oskar Greiner and Des Lovrity) was highly appreciated.

Funding for my project provided by Don's NESEC SCIEX Industrial Chair was greatly appreciated.

Finally, I would like to thank my parents, sister, and my husband Xuejun for their love and support. Also my little son, Aaron, who brings me a lot of fun and challenge. This thesis is dedicated to them.

Chapter 1

Introduction

1.1 Review of Recent Developments in Quadrupole Mass Spectrometry

Over the past 30 years, quadrupole mass filters have been the most widely used mass analyzers because of their small size, ease of use, and low cost. [1, 2] Since Paul *et al.* published their first paper describing the basic principles of quadrupole mass filters,[3] quadrupoles have received continuous attention. Highlighting the significance of quadrupole mass analyzers, two books were published: "Quadrupole Mass Spectrometry and Its Applications"[4] and "Quadrupole Storage Mass Spectrometry".[5]

The recent instrumental innovations and creative applications of quadrupoles can be classified in two areas. One area is the use of quadrupoles as transmission elements, reaction regions, or storage devices when combined with a mass spectrometer. For this type of development, quadrupoles are usually operated with an applied radio frequency (RF) only. In a triple-quadrupole tandem mass spectrometer, for example, the central RF-only quadrupole is used as a "collision cooling" and reaction or fragmentation chamber.[6-9] With a relatively high pressure of target gas in the collision cell (e.g., 4-6 mTorr in a 15 cm long cell), the MS/MS efficiency and resolution measured in the third quadrupole are improved. In an orthogonal time-of-flight (TOF) mass spectrometer

coupled with an electrospray or matrix-assisted laser desorption/ionization (MALDI) ion source, an RF-only quadrupole can also reduce the axial energy spread of the ions and can be used to confine fragment ions. [10, 11] RF-only quadrupoles are also used to study ion/molecule reactions, such as hydrogen/deuterium exchange.[12]

Tanner *et al.* [13-15] used a radio frequency/direct current (RF/DC) quadrupole as a dynamic reaction cell (DRC) to suppress plasma-based molecular and isobaric interfaces for trace elemental analysis with an inductively coupled plasma mass spectrometer (ICP-MS). For these experiments, the DRC was placed between the atmosphere/vacuum interface of the ICP and the mass analyzer.

In a second area, novel ways of using quadrupoles as mass analyzers are being investigated. The goal is to improve the mass resolving power of the mass filter. Amad and Houk[16, 17] recently described a "multipass" approach. A resolution (defined in terms of full width at half maximum height) of 11,000 for the separation of CO^+ and N_2^+ was obtained by applying a square wave voltage to the entrance and exit lenses of a quadrupole to reflect the ions for multiple passes. A higher resolution of 22,000 was obtained with pulsed ion injection.

Miseki,[18] de Maack,[19] and Beaugrand[20] separately demonstrated another method to increase the resolution of a quadrupole mass filter by applying an additional sine wave the rods. This sine wave could generate unstable bands inside the stability region in order to narrow the peak profile and thus enhance the resolution. This method gave a resolution of up to 10,000 at mass to charge (*m/z*) 1466.[19] Recently, Konenkov *et al.* reinvestigated this auxiliary RF mode of operation in the first stability region theoretically and experimentally. They demonstrated that this method substantially

increased abundance sensitivity and greatly improved peak shapes, but did not significantly increase the limiting resolution.[21]

An alternative way to improve the mass resolution of a quadrupole mass filter is to operate it in a higher stability region (A brief review of the higher stability regions is given later in this chapter.). Douglas et al. recently extensively explored the operation of quadrupole mass filters in higher stability regions.[22-28] The primary objective, which is also the goal of this thesis, was to improve the resolution for one of the main applications of quadrupole analyzers: elemental ion analysis *via* inductively coupled plasma (ICP) ionization.

1.2 Objective and Outline of the Thesis

ICP-MS with a quadrupole mass filter (QMF) has become a very powerful and widely accepted tool for elemental analysis. [29-35] At present, several thousand ICP-mass spectrometers are used worldwide. The quadrupole-based ICP-MS owes its popularity mainly to (i) sub-pg ml^{-1} detection limits, (ii) multi-element analysis capabilities, (iii) a wide linear dynamic range, and (iv) relatively simple spectra.[36]

However, ICP-MS with a quadrupole mass filter also has limitations. One important problem is the spectral interferences[37] that may hamper accurate determination of trace elements, especially at *m/z* less than 80 and for complex sample matrices. This is mainly due to the limited mass resolution available with a quadrupole mass filter operated in the first stability region. For example, peaks of $^{28}Si^+$, $^{40}Ca^+$ and $^{56}Fe^+$ are seriously overlapped by background species $^{14}N_2^+$, $^{40}Ar^+$ and $^{40}Ar^{16}O^+$,

respectively. In some cases ICP double-focusing mass spectrometers are used because they offer higher resolution (10,000 or more defined in terms of full peakwidth at half height) at low mass. [38, 39] Table 1.1 lists some examples of the nominal resolution that is required to separate commonly encountered interferences. Recently, it was reported that a Fourier transform ion cyclotron resonance (FT-ICR) mass spectrometer, with a resolution of about 10,000 (defined on the 10% valley basis) already obtained in practice, was used for elemental analysis.[40] However, both double focusing and ICR systems are relatively expensive, complex, and large.

Table 1.1 Examples of the nominal resolution required to separate spectral interferences

Interfered isotope (*m/z*)	Interferences	Resolution required ($m/\Delta m$)
$^{56}Fe^{+}$	$^{40}Ar^{16}O^{+}$	2,639
$^{75}As^{+}$	$^{40}Ar^{35}Cl^{+}$	8,051
$^{103}Rh^{+}$	$^{87}Sr^{16}O^{+}$	60,532
	$^{206}Pb^{2+}$	1,260
	$^{63}Cu^{40}Ar^{+}$	7,623
$^{104}Pd^{+}$	$^{88}Sr^{16}O^{+}$	29,434
	$^{208}Pb^{2+}$	2,021
	$^{64}Zn^{40}Ar^{+}$	7,623
$^{58}Fe^{+}$	$^{58}Ni^{+}$	28,032
$^{64}Zn^{+}$	$^{64}Ni^{+}$	54,379

Besides providing high resolution, the double-focusing ICP-MS can mass analyze ion beams that have keV ion energies.[38] The use of high energy (keV) ion beams have the potential to reduce space charge repulsion effects downstream of the skimmer, which have been cited as a cause of non-spectroscopic interelement interferences.[41-44] Therefore the ability to mass analyze these beams without deceleration is attractive. As noted by Yu and Dawson[45, 46] and Konenkov *et al.*,[47] it is possible to mass analyze high energy ions with a quadrupole operated in higher stability regions. It is well known that space charge strongly defocuses the ion beam downstream of the skimmer with a quadrupole conventionally operated in the first stability region,[42, 43] because the ions with high energies must be slowed at the entrance of the quadrupole. Hence if the quadrupole of the ICP-MS is operated in a higher stability region, the space charge defocusing can be eliminated and the current density can be increased.

Another advantage of operation of a quadrupole in the higher stability regions is that the quadrupole can be scanned faster with higher energy ion beams. This is compatible with the multielemental analysis of a transient sample such as that from an electro-thermal vaporizer (ETV) or chromatographic sources.

Douglas *et al.* also noted that high resolving power can be achieved with a quadrupole operated in the higher stability regions, at the expense of sensitivity.[25, 28] To overcome this tradeoff, they reinvestigated the gas dynamics of the interface between the ICP source and the ion optics.[48] A modification of the interface produced a high energy (2,000 eV) ion beam with a current density (~200 μA) at least 100 times greater than that of a commercial ICP-MS system.[49] This new ion extraction method combined with

operation of a quadrupole in a higher stability region could, in principle, produce an inexpensive, high resolution ICP-MS with a quadrupole mass analyzer.

This thesis discusses the theory and experimental investigations of the ion optical properties of a quadrupole mass filter operated in the fourth and sixth stability regions. The primary objective is to improve the resolution of a quadrupole analyzer for ICP-MS. This thesis is organized as follows: in the remainder of this chapter, a brief review of the principles of the quadrupole mass filter operation, and a review of the literature for quadrupole mass filters operated in the second and third stability regions, are given. The experimental apparatus and theoretical simulation methods are described in detail in Chapter 2. Chapters 3 and 4 focus on the investigation of the fourth and sixth stability regions, respectively. In both chapters, the peak shapes and the relationship between ion energy and resolution are discussed first. Then a comparison of resolution and transmission between the second, fourth and sixth regions is presented. Most of Chapter 3 has been published.[28] Chapter 5 provides a theoretical interpretation of the unexpected observations with a quadrupole operated in the fourth and sixth regions. This theory may be applied to the other unexplored higher stability regions in the future. Finally, Chapter 6 provides a summary of the thesis and discusses future work with quadrupole mass filters operated in the unexplored higher stability regions.

1.3 A Review of Quadrupole Mass Filter Operation

The principles of quadrupole mass filter operation have been described by Dawson[4], and March and Hughes[5]. The following is a brief review.

1.3.1 The mass filter geometry, field and applied potential

The quadrupole mass filter device consists of four parallel electrodes; it is ideally constructed from rods with hyperbolic cross section as shown in Figure 1.1. In practice, cylindrical rods are typically used for simplicity in manufacturing and mounting. An electric potential is applied to opposite pairs of rods to generate the quadrupole field as shown in Figure 1.2. For a positive ion, the x direction and y direction correspond to Φ_0 and $-\Phi_0$ (see Figure 1.1). The potential within the quadrupole is given by

$$\Phi(x,y) = \frac{(x^2 - y^2)}{r_0^2}\Phi_0 \qquad (1.1)$$

where, x and y are the displacements from the center to any point, r_0 is the field radius (the distance between the center and an electrode) and Φ_0 is the potential applied to a rod. This potential distribution satisfies the Laplace equation ($\nabla^2\Phi = 0$). The potential is invariant along the rods and increases quadratically from zero at the center-line.

The applied potential Φ_0, is given by

$$\Phi_0 = (U - V\cos\omega t) \qquad (1.2)$$

where U is the DC voltage applied between each quadrupole rod and ground, V is the amplitude (zero-to-peak) of the radio frequency (RF) voltage applied between each rod and ground, ω is the angular frequency and t is the time in seconds.

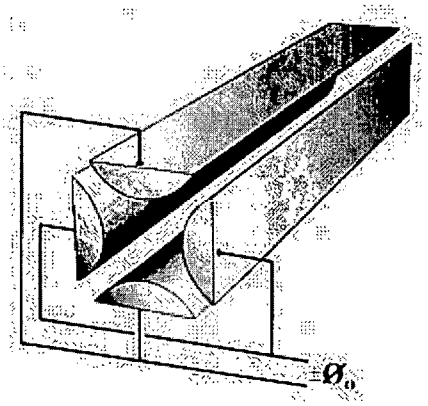

Figure 1.1 A quadrupole with hyperbolic rods, where Φ_0 is the potential applied to opposite pairs of rods. (Adapted from http://ms.mc.vanderbilt.edu/tutorials/ms/fig8.htm)

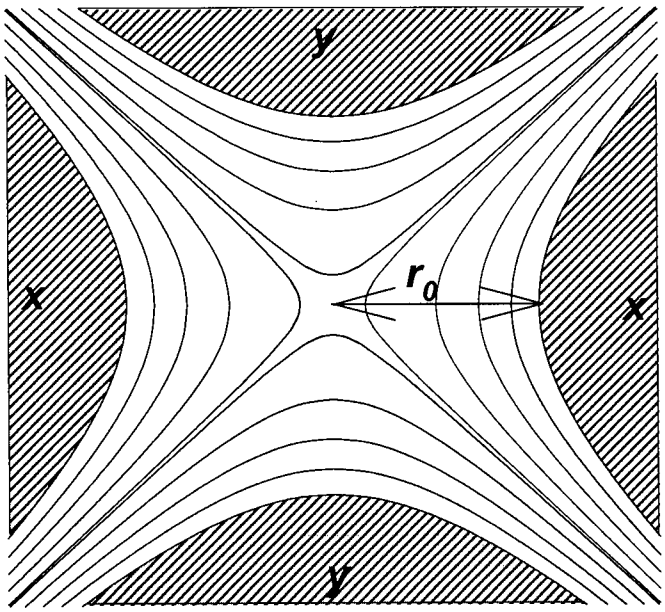

Figure 1.2 The quadrupole electrical potential field. The shaded areas are the cross sections of hyperbolic rods. Curved lines are the equipotential contours in the xy plane.

1.3.2 The equation of ion motion

The motion of an ion of mass m is determined by Newton's law of motion ($\vec{F} = m\vec{a}$), where $\vec{a}$ is the ion acceleration. The force $\vec{F}$ is given by $\vec{F} = ze\vec{E}$, where $\vec{E}$ is the electric field, e is the electronic charge, and z is the number of electronic charges. The electric potential is related to the potential by

$$\vec{E} = -\nabla\Phi(x, y, z) \tag{1.3}$$

where ∇ is the gradient operator, given by $\nabla = \hat{i}\frac{\partial}{\partial x} + \hat{j}\frac{\partial}{\partial y} + \hat{k}\frac{\partial}{\partial z}$, and $\hat{i}, \hat{j}$ and $\hat{k}$ represent unit vectors in the x, y and z directions, respectively. Hence, three independent equations are obtained.

$$\frac{d^2x}{dt^2} + (\frac{ze}{mr_0^2})\Phi_0 x = 0 \tag{1.4}$$

$$\frac{d^2y}{dt^2} - (\frac{ze}{mr_0^2})\Phi_0 y = 0 \tag{1.5}$$

$$\frac{d^2z}{dt^2} = 0 \tag{1.6}$$

Equation 1.6 is straightforward. There is no acceleration along the rods, and so the axial velocity is constant. Equations 1.4 and 1.5 show one important feature of the quadrupole potential. The ion motions in the x and y directions are independent and can be considered separately for an ideal hyperbolic field without fringing fields.

Equation 1.2 can be substituted in Equations 1.4 and 1.5. Both equations can then be written in the standard form of the Mathieu Equation.[4, 5]

$$\frac{d^2u}{d\xi^2} + [a_u - 2q_u\cos(2\xi)]u = 0 \tag{1.7}$$

where u represents either the x or y transverse displacement and the two parameters(a,q) of the quadrupole field are given by

$$a_u = a_x = -a_y = \frac{8zeU}{m\omega^2 r_0^2} \tag{1.8}$$

$$q_u = q_x = -q_y = \frac{4zeV}{m\omega^2 r_0^2} \tag{1.9}$$

The variable ξ is the time in radians defined via the applied RF, and is given by

$$\xi = \frac{\omega t}{2} \tag{1.10}$$

The analytical solutions to the Mathieu Equation 1.7 can be written [4].

$$u(\xi) = \alpha' e^{\mu\xi} \sum_{n=-\infty}^{\infty} C_{2n} e^{2in\xi} + \alpha'' e^{-\mu\xi} \sum_{n=-\infty}^{\infty} C_{2n} e^{-2in\xi} \tag{1.11}$$

where α' and α'' are integration constants which depend on the ion's initial conditions, i.e. the initial transverse position, u_0, the initial transverse velocity, $\dot{u}_0$ and the initial phase, ξ_0, which represents the phase of the RF field when the ion first experiences it. The constants C_{2n} and μ depend only on the values of a and q. Thus all ions, with the same (a, q) values and different initial conditions, have the same period of motion. Based on the nature of μ, the solutions can be divided into two groups. In one, motion is mathematically stable and periodic. For these solutions, u remains finite as $\xi \to \infty$,with $\mu=i\beta$, where β, the stability number, is not an integer. Such stable solutions can be written in another form:

$$u = \mathrm{A} \sum_{n=-\infty}^{\infty} C_{2n} \sin[(2n+\beta)\xi] + \mathrm{B} \sum_{n=-\infty}^{\infty} C_{2n} \cos[(2n+\beta)\xi] \tag{1.12}$$

where the constants A and B are similar to α' and α'', n=0, ±1, ±2, ±3, ... and the constants C_{2n} depend on the (a, q) value. From this form, it is seen that the parameter β, which depends on the (a, q) value, determines the frequency of ion motion Ω_n, through

$$\Omega_n = (2n + \beta)\frac{\omega}{2} \qquad (1.13)$$

The value of β can be calculated with a transfer matrix M, which is used to compute ion position and ion velocity for one complete cycle. [4, 50] If M is represented by $\begin{bmatrix} m_{11} & m_{21} \\ m_{12} & m_{22} \end{bmatrix}$, then

$$2\cos(\pi\beta) = m_{11} + m_{22} \qquad (1.14)$$

where m_{11} and m_{22} are the two elements of the transfer matrix M and $|m_{11} + m_{22}| < 2$.

The second type of solution gives unstable motion; u is unlimited as $\xi \to \infty$ ($\mu \neq i\beta$). The parameter μ, the increment of exponential growth of the ion oscillation amplitude during one period, is given by

$$2\cosh(\mu) = |m_{11} + m_{12}| \qquad (1.15)$$

where $|m_{11} + m_{12}| > 2$

1.3.3 The stability diagrams, mass analysis and ion trajectories

By solving the equations for ion motion, the conditions for stable ion motion in both the x and y directions can be expressed mathematically in terms of a and q on a stability diagram as shown in Figure 1.3. The values of a, q for the x and y directions differ by a factor of –1 (see Equations 1.8 and 1.9). There is an infinite number of stability regions. The first six regions are labeled in Figure 1.3 with the notation taken

from Dawson.[45] Other authors may use different notations. The first, second, and fourth stability regions are symmetric about the q axis, therefore the ion optical properties are the same for the upper and lower halves of the region. By convention, only the upper halves of the regions are shown in the following thesis. Almost all the commercial quadrupole mass filters are operated in the first stability region, which is shown in more detail in Figure 1.4.

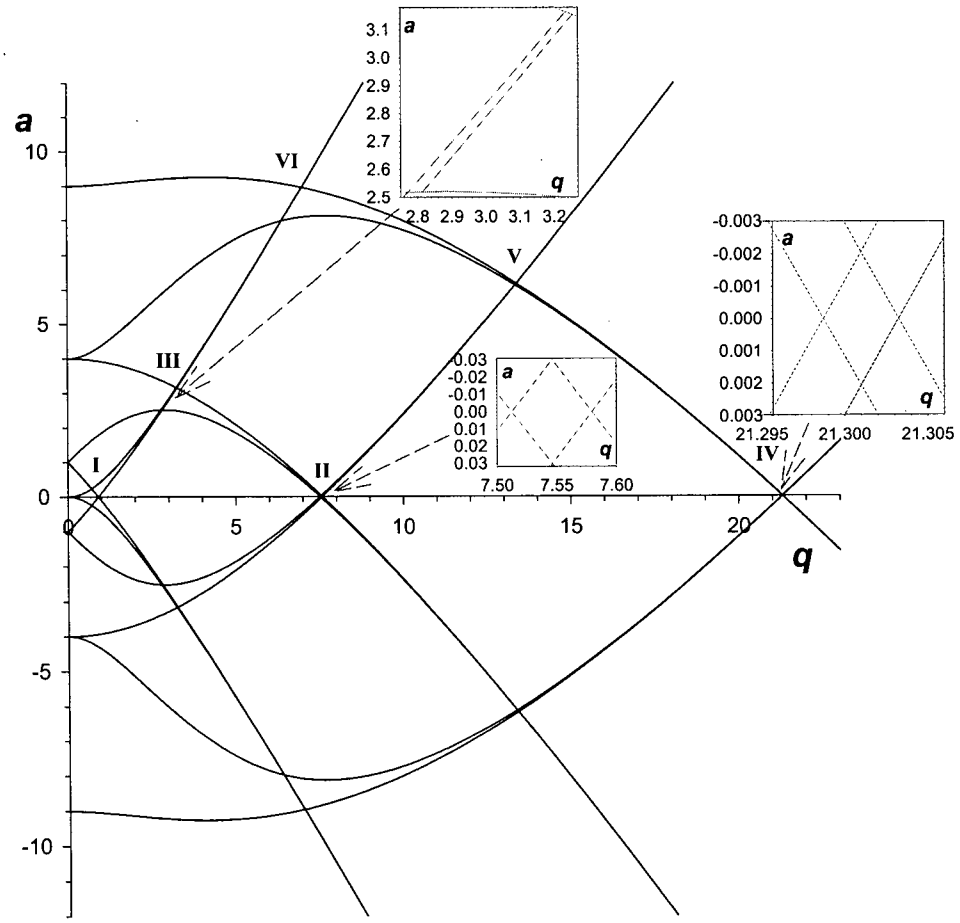

Figure 1.3 The stability diagram for the x and y directions. The first six regions, where ion motion is simultaneously stable in the x and y directions, are labeled I, II, III, IV, V and VI.

The boundary lines of the stability diagram have integer values of β. Inside the stability region, the values of β for the x or y directions (β_x or β_y) are between the values on the boundaries of the stability band for motion in the corresponding direction. For example, in the first stability region, the boundary values of the x stability band are $\beta_x = 0$ and $\beta_x = 1$. So within this region, $0 < \beta_x < 1$. Similarly, $0 < \beta_y < 1$. The dashed lines in Figure 1.4 are some of the iso-β lines. In general, the values of β for x and y motion are different at a given position in the stability region.

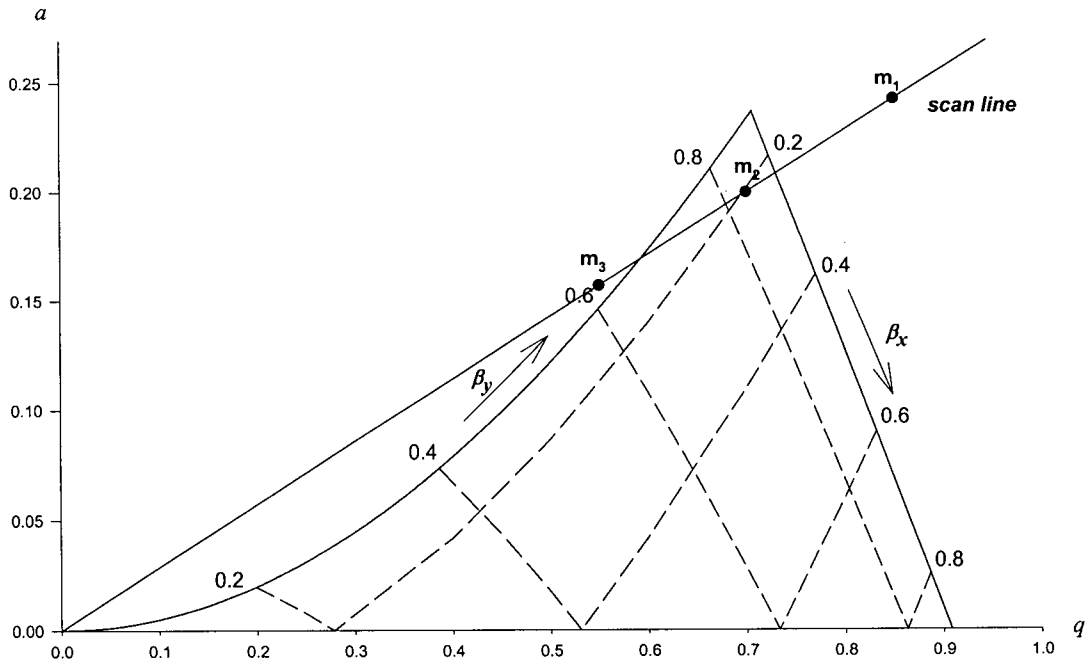

Figure 1.4 The first stability region.

From Equations 1.8 and 1.9, it can be seen that all ions with the same *m/z* have the same operating point (*a*, *q*) in the stability diagram for fixed values of *U*, *V*, r_0 and ω. Because

a/q is equal to $2U/V$, to provide mass analysis, the DC (U) and RF (V) voltages are adjusted so that the ion of interest, for example m_2 in the Figure 1.4, is inside the stability diagram near the tip. The ions with lighter mass m_1 and heavier mass m_3 are outside the stability region. Thus ions of mass m_2 are transmitted and ions of mass m_1 and m_3 are not. This principle applies to all stability regions.

Ion trajectories are more a vivid way to show the quadrupole operation. Ion trajectories are generally calculated by numerical integration of the Mathieu equation. Typical results are plotted in Figure 1.5. Ions of mass m_2 (Figure 1.4) have stable trajectories in both the x and y directions which are similar to those in Figure 1.5b, and are transmitted. Lighter ions of mass m_1 have unstable trajectories in the x direction but stable trajectories in the y direction, similar to those shown in Figure 1.5a. Ions of mass m_3 are unstable in the y direction but stable in the x direction, and are similar to those in Figure 1.5c. Thus ions of both mass m_1 and m_3 are rejected by the filter.

1.3.4 Resolution

Resolution is usually defined as $m/\Delta m$ where m is the center of the mass peak, Δm is the measured peak width (actually $m/z \big/ \Delta m/z$). Here, we use resolution defined as full width measured at half peak height, $R_{1/2}=m/\Delta m_{1/2}$. It is obvious that the resolution increases as a scan line moves toward the tip of the stability region. In theory, the resolution is calculated from the calculated width of the stability region for each of the scan lines. Therefore, the resolution can be unlimited if an ion is placed just at the tip of the stability region. However, the theoretical stability diagram is for a quadrupole with

an infinite length and a perfect field. In practice, for a quadrupole with finite length and round-rods, the resolution[51-54] is generally expressed as

$$R = \frac{n^2}{h} \qquad (1.16)$$

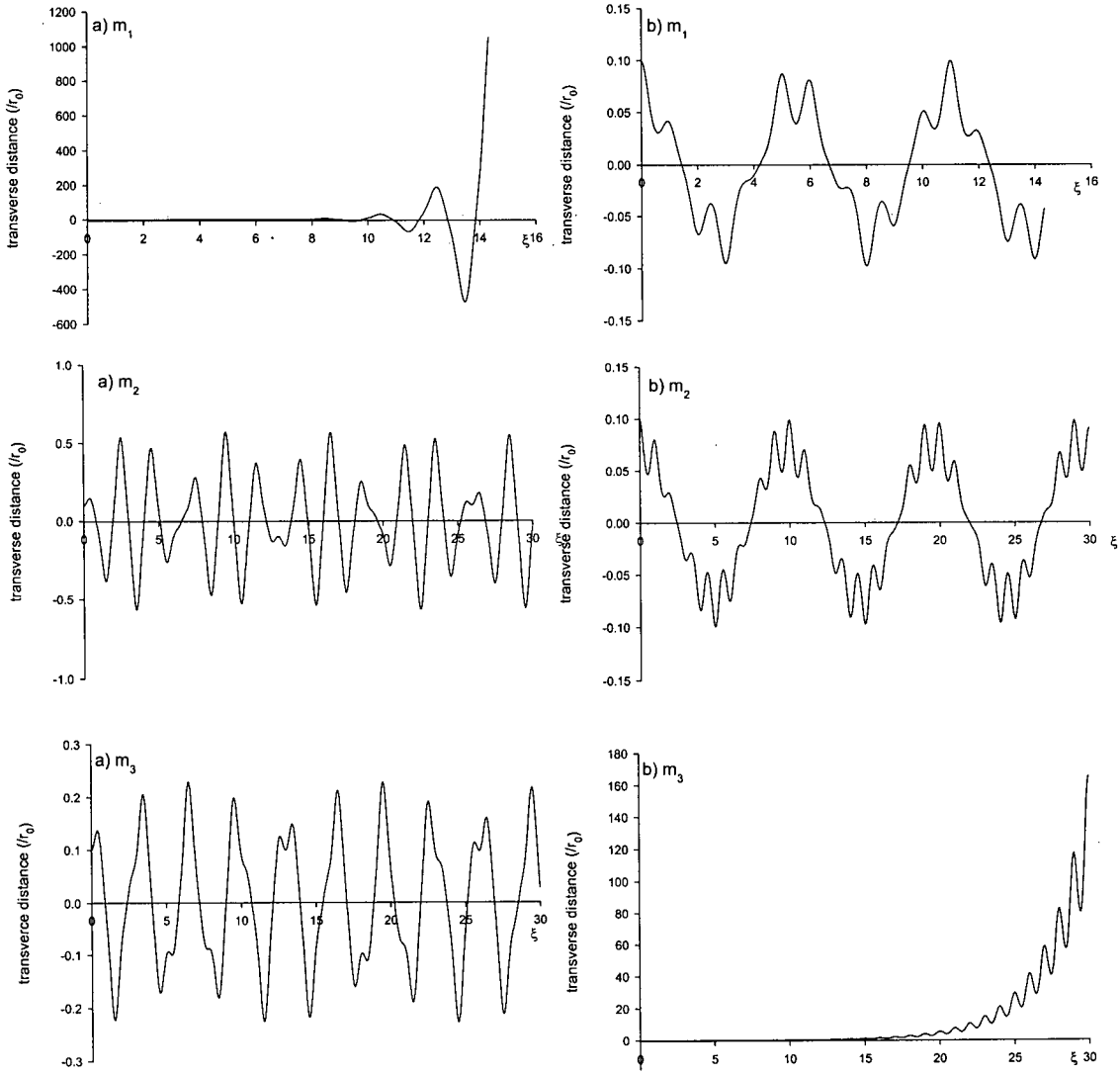

Figure 1.5 Typical ion trajectories for ions of mass m_1, m_2, m_3 at the points shown in figure 1.4. (a) trajectories in the *xz* plane; (b) trajectories in the *yz* plane.

where, h is a constant and n is the residence time, in terms of the number of RF cycles that ions spend in the quadrupole field. The value of constant h varies dramatically for different stability regions (see Table 1.2). For a given stability region, h depends

Table 1.2 Values of h for the different stability regions.

Stability region	I[53, 55]	II[45-47, 53, 55, 56]	III[22, 47, 53, 55]	IV[28]	VI[chapter 4.3.2]
Value of h	10-20	0.038-0.077	0.70-1.4	0.00093	0.018-0.026

somewhat on the quality of rods and how an ion source is matched to a quadrupole. Titov[53, 54] calculated the resolution possible with a quadrupole operated in the first three regions. He pointed out that Equation 1.16 is only valid for small n. For the larger n the resolution follows

$$R = kn^{\frac{4}{3}} \qquad (1.17)$$

where k is a constant. Its value should be similar to h^{-1} in Equation 1.16. This means the resolution increases less with large values of n than indicated by equation 1.16.

1.3.5 The relationship between the transmission and resolution (T-R curve) and peak shape

Two major performance characteristics of a quadrupole performance are (i) the relative transmission versus resolution (T-R) for ions of different energies and (ii) the peak shape. In order to better understand these two characteristics, several possible factors that influence the QMS performance are reviewed.

a) Acceptance

Even though some ions have mathematically stable trajectories, they may not be transmitted by the quadrupole. This is because their maximum amplitude of oscillation is too large and therefore a definition of the acceptance of the mass analyzer is required [50, 57]. The acceptance is defined as a function of the initial ion position μ_0 (i.e., distance from the quadrupole axis in the x or y direction) and of the initial transverse velocity, $\dot{u}_0$, which results in ion transmission at a given operating point for each initial phase ξ_0. Since the ion motions in the x and y directions are independent, the acceptance can also be described separately for the x and y directions. It can be represented by an ellipse in phase space called the acceptance ellipse, given by:

$$Bu^2 + 2Au\dot{u} + \Gamma \dot{u}^2 = \varepsilon \qquad (1.18)$$

where $\dot{u}$ =du/dξ. *A, B* and Γ are the parameters of the ellipse and are functions of the quadrupole parameters. The parameter ε is equal to the ellipse area divided by π.

For a static and uniform ion source, Dawson introduced the "average" acceptance[58] which is the overlap area of acceptance ellipses for the all initial phases for the x or y directions, with a given fraction of transmission. In Chapter 4, examples of the acceptance ellipses, with and without effects of fringing fields, for the transverse x and y directions are shown in Figure 4.2 and Figure 4.8. In the calculation, the initial positions are usually expressed in units of r_0 and the initial transverse velocity in units of r_0 per radian of the applied field (r_0/ξ). The acceptance of a quadrupole field was examined experimentally by Hennequin and Inglebert. [57, 59]

b) Emittance

An ideal ion source with a uniform distribution of ions can be represented by an emittance ellipse in the phase plane. A real source might be represented by a series of intensity contours in the phase plane.[60] The area of the emittance ellipse in the phase plane does not change as the ions pass through the quadrupole field, unless there is a constricting aperture placed between the ion source and quadrupole analyzer. In order to best match an analyzer acceptance, the shape and orientation of an emittance ellipse can be altered by adjusting ion lenses and drift spaces between the ion source and quadrupole.[50]

Dawson[61] was the first to quantitatively study the effects of particular changes in the source emittance on changes of the T-R relationship in a quadrupole mass filter. These changes included: sources of different size and different orientation, the "hollow" source, and misaligned source. Douglas and Konenkov [23] reported that the ion source emittance could strongly affect the T-R behavior of a quadrupole operated in the second stability region.

c) Fringing field

The fringing field is a region where the quadrupole field increases from zero (outside of the rods) to its full value (inside the rods). Brubaker [62]first considered the fringing field in detail and found that the ion motion in the y direction becomes unstable as ions spend a long period in the fringing field. He also gave a linear model[62] which has been further examined by Dawson.[63, 64] Hunter and McIntosh [65] proposed a quadratic model, which was used to study the fringing field with quadrupole operation in the second [47] and third [66] stability regions.

Real fringing fields have coupled ion motions in the x, y, and z directions. These motions are very complex, and only one brief study of a three-dimensional field has been published.[67]

The fringing field can modify the acceptance ellipse in shape and orientation, but not in area. However, based on the stability regions that have been studied, any fringing field usually decreases the overlap of the ellipses of different RF initial phases, except at certain fringing field lengths, for the first and third stability regions. With operation in the first stability region, there is an optimum fringing field length of about two RF cycles which was verified theoretically and experimentally. [68, 69] With operation in the third region the optimum length is 1.2 RF cycles.[66] Hence, the fringing field generally decreases the ion transmission [50, 70] except at the optimum fringing field lengths for the first and third regions.

In general, there are two ways to minimize the fringing field effect. One is the "delayed DC ramp" developed by Brubaker [62]. The other is to reduce the ion residence time in the fringing field by putting an aperture lens with a high accelerating potential at the entrance of the quadrupole, and then to decelerate the ions at the entrance of the quadrupole [23, 53, 54]

d) Field faults (Field imperfections)

Field faults may result from one or more factors such as the use of round rods, incorrect positioning of one or more rods, or contamination of the rod surfaces. As a result, the field faults add higher order potentials (i.e., hexapole, octopole ....) to the ideal quadrupole field. These higher order multipoles can couple the motion in the x and y directions at certain values of β_x and β_y, and produce a nonlinear resonance. Ions with

(a, q) values at these points have larger oscillation amplitudes than usual, and fewer ions are transmitted. This leads to peak splitting and distortion of a peak. Dawson and Whetten [71] studied the influence of nonlinear resonances on the peak shapes with a quadrupole operated in the first stability region. Recently, Wang *et al.* gave the β_x, β_y and β_z values for generating non-linear resonances in an ion trap. [72]

e) Ion collection effects

At the ion exit, the emerging ion beam is at times highly focused or defocused. If the ions are defocused at the exit, they may be less efficiently captured by the ion detector. This can lead to structure on a peak. These defocusing effects depend on the fundamental frequency of the ion oscillation and the number of RF cycles that ions experience in the quadrupole field. The positions of structures on the peak vary with ion mass and energy. The irregular positions can be plotted on the stability diagram.[58, 73] Dawson studied these effects with a quadrupole operated in the first region.[58, 73] Du *et al.* showed this effect with quadrupole operation in the second[24] and third regions[27].

In summary, the ion transmission is determined by the overlap between the quadrupole acceptance and the ion source emittance. The fringing field can change the acceptance strongly, and field imperfections can also affect transmission to some extent. Generally, it is clear that, with operation in the first stability region, at low resolution, ion acceptance will be high and the transmission may be "source limited" and vary little with increase in resolution. With increasing resolution, the acceptance becomes smaller than the source emittance and the transmission will be "analyzer limited".[74] Peak shape distortions are usually attributed to ion collection effects and non-linear resonances.

1.4 Review of the 2nd and 3rd region stability regions

Operation of a quadrupole in higher stability regions can usually give higher resolution than conventional operation in the first region. However, operation in higher stability regions also has some disadvantages: (i) for analysis of ions of the same *m/z*, higher DC and RF voltages are required and therefore stronger fringing fields are present. (ii) for some higher stability regions (*e.g.* the second and fourth regions), it is necessary to use a pre-filter or a post-filter to eliminate "alias ions", which are ions of lighter *m/z* that are simultaneously transmitted by a quadrupole when they are stable in the lower regions crossed by a scan line of the analyzing region .[47]

Prior to the work described in this thesis, almost all work concerning higher stability regions was done with a quadrupole operated in the second or the third regions. Du *et al.* [25] recently published a comprehensive review of the properties of these two regions. The following is a brief discussion of the ion optical properties of these two regions, for comparison with the ion optical properties of the fourth and sixth regions described in this thesis.

1.4.1 The second stability region

The second stability region is shown in Figure 1.6. The tip position is (a = 0.0295, q = 7.547). These values mean that an RF voltage of 5,000 V (pole to ground; zero to peak) requires only 10 V of DC (pole to ground). A nominal resolution of 114 can be obtained with a quadrupole operated with RF only (a = 0). In this region there can be simultaneous transmission of ions with $q < 0.908$ as well as those with $7.514 < q < 7.580$. Thus a pre-filter is required.

Use of this region was first suggested by Post[75], then was theoretically examined by Uchida[76]. Dawson and Yu were the first to study this region theoretically and experimentally.[45, 46] They calculated acceptance ellipses and a theoretical limiting resolution of $R_{1/2} = 180n^2$ ($h = 0.00556$). However, their experiment showed

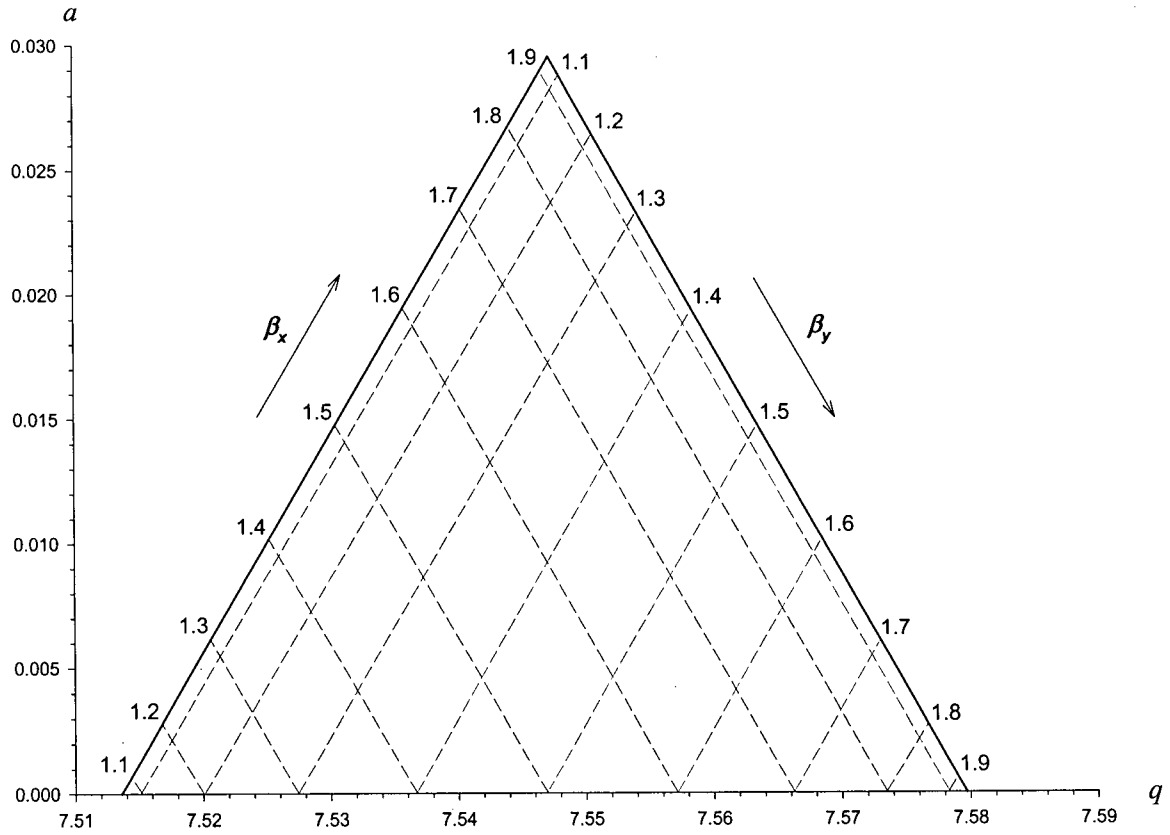

Figure 1.6 The second stability region.

that $R_{1/2} = 19n^2$ ($h = 0.0526$). Similarly, Douglas *et al.* found $R_{1/2} = 13n^2$ ($h = 0.0769$) with an ICP source[56] and $R_{1/2} = 26n^2$ ($h = 0.0385$) with a thermal ionization source.[25] Titov[55] and Konenkov and Kratenko[47, 77] found the same value for $R_{1/2} = 24n^2$ ($h = 0.0417$). The experimental values for h are much larger than the theoretical estimated

value(h= 0.00556). Comparison with the first region where $R_{1/2}=n^2/20$, fewer RF cycles are required to achieve the same resolution. In other words, ions with energies of several hundred eV can be mass analyzed at unit resolution. Du *et al.* [25] demonstrated unit resolution on 1000 keV K^+ ions with a thermal ionization source. Hiroki [78]showed unit resolution on 2.0 keV ions of N_2^+ and O_2^+. Based on this advantage, Grimm and co-workers [79] increased the quadrupole scan speed to 1000 scans per second for ion energies up to 1000 eV in order to match very narrow gas chromatography (GC) peaks for organic analysis.

Dawson and Yu [46]also demonstrated a resolution of several thousand for Kr^+ ions with ion energies between 5 eV and 300 eV, and a resolution of about 1500 for separating $^{131}Xe^+$ (130.905 u) from $C_3F_5^+$ (130.992 u) with 300 eV ions. Ying and Douglas[56] demonstrated $R_{1/2}$ = 5000 at m/z = 56 with ions of 24 eV with an ICP source. This was sufficient to separate $^{56}Fe^+$ from $^{40}Ar^{16}O^+$, the notorious molecular ion interference in ICP-MS. Wei[80] used this region to separate H_2O^+ from $^{36}Ar^{2+}$, and HF^+ from $^{40}Ar^{2+}$.

The fringing fields of this region are strongly defocusing. Calculation of the acceptance shows that the transmission remains high if ions pass through the fringing field in less than 0.6 RF cycles.[23, 45, 55]

1.4.2 The third stability region

The third stability region has an approximately rectangular shape. The upper and the lower tips, shown in Figure 1.7, can be used for mass analysis, and there is no "aliasing" problem associated with this region.

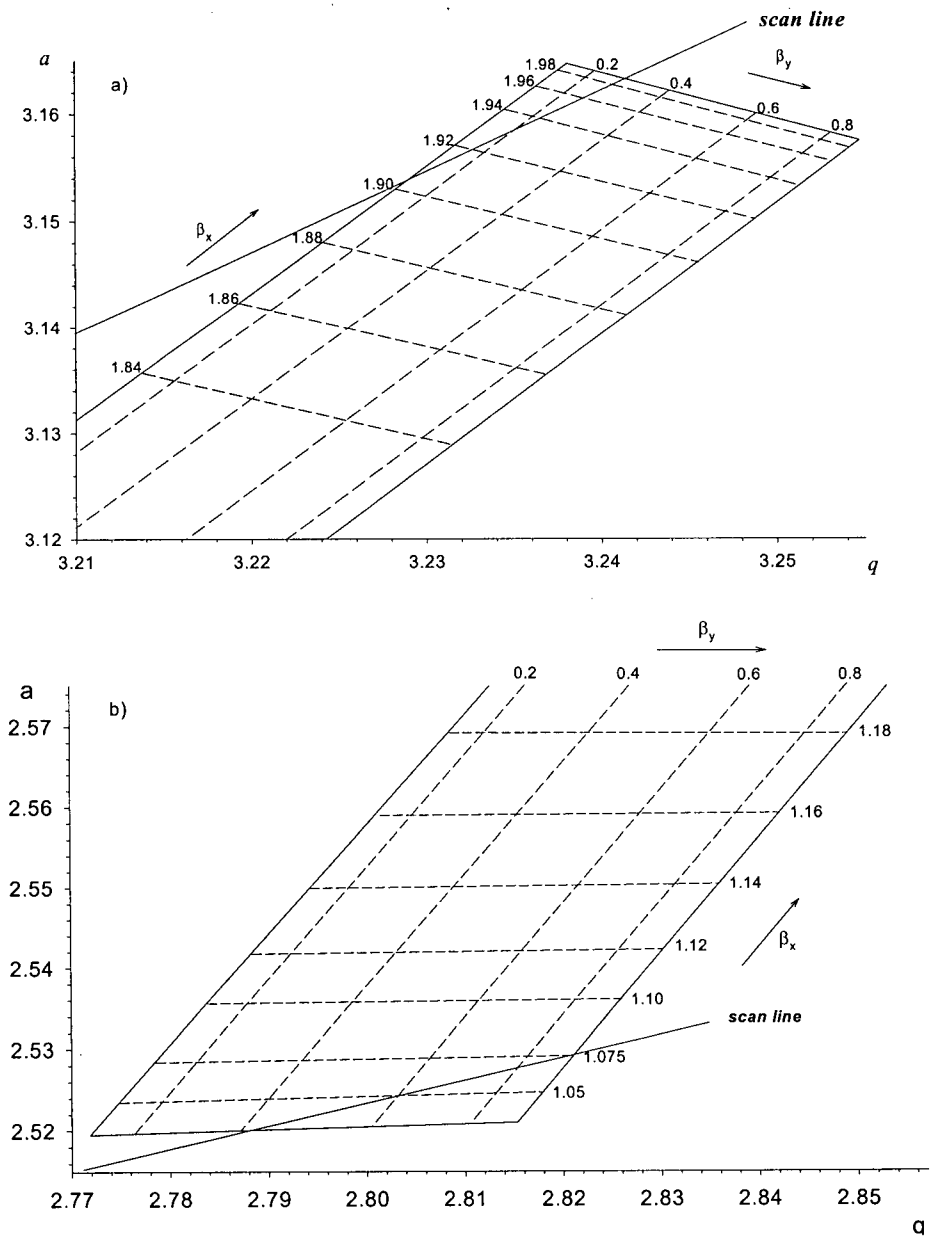

Figure 1.7 The upper tip (a) and the lower tip (b) of the third stability region.

With a quadrupole operated in this region, Konenkov *et al.* ,[47, 81, 82] Hiroki and co-workers [78, 83-89] and Pedder and Schaeffer[90, 91] demonstrated separation of Ar^{2+} from Ne^+ (m/Δm = 1778), [82] $^{20}Ne^+$ from D_2O^+ (m/Δm = 656),[82] He^+ from D_2^+ (m/Δm =

157,[81] 320,[83]750,[84] 3700($R_{1/2}$)[90]), $^3He^+$ from HD^+ (m/Δm = 518),[86, 87] CO^+ from N_2^+ (m/Δm = 2500),[91] and the separation of N_2O^+ from CO_2^+ (m/Δm = 3926),[91] respectively. Du *et al.*[22] investigated the application of this region to ICP-MS and obtained a resolution at half height of about $R_{1/2}$ = 4000. This is close to the resolution that is required to separate $^{56}Fe^+$ from $^{40}Ar^{16}O^+$. However, at this resolution the sensitivity was only about a few hundred counts per second per μg ml^{-1} of Fe in solution. Nevertheless, it was found that a very high abundance sensitivity (>10^7) was possible with operation at moderate resolution ($R_{1/2}$ = 500 to 1000). In comparison with operation at the middle of the first region, the ion intensity is only about one order of magnitude lower for a given resolution. Konenkov and his colleges also pointed out that energy spread from the ion source limited resolution.[25, 92] The relationship between $R_{1/2}$ and the square of the number of the RF cycles in the quadrupole field was also measured. Du *et al.*[22] found $R_{1/2} = 1.0n^2$ (h=1). Similarly, $R_{1/2} = 0.7n^2$ (h=1.4) and $R_{1/2} = 1.4n^2$ (h = 0.7) were measured by Konenkov et al[47] and Titov,[55] respectively. The values of h mean that a relatively high resolution can be obtained with an ion injection energy of tens of eV. For example, a resolution at half height of about $R_{1/2}$ = 590 was obtained for 28 eV Co^+ ions, $R_{1/2} \approx 180$ for 110 eV Co^+ ions at the upper tip and $R_{1/2} \approx 150$ for 120 eV Co^+ ions at the lower tip.[26] However, in the latter two cases, the peak shapes were structured.

The variation of transmission with resolution was investigated extensively for this region. Dawson,[93] Konenkov *et al.*[66, 94] and Titov[53, 55] reported the calculated acceptance for this region. The calculations include either fringing fields[66, 93, 94] or both fringing fields and field imperfections,[55] and show that the acceptance in the x direction

is significantly larger than that in the y direction. The acceptances at the lower tip are slightly larger than that at the upper tip, but both acceptances decrease in a similar fashion as the resolution is increased. Konenkov *et al.*[25] also showed that the T-R curves with operation at the upper and lower tips, measured without a photon stop(in the ion lens between the source and quadrupole) are very similar to the calculated T-R curves for the acceptance. A "hollow beam " produced by the stop dramatically changed the overlap of the emittance with the quadrupole acceptance for the operation at the lower tip, hence the T-R behavior is different.

The fringing fields of the third region are more strongly defocusing than those of the first region, but less strongly defocusing than those of the second region. High transmission can be maintained as long as the ion residence time in the fringing field is less than 1.2 RF cycles.[66] In addition, in this region, the 3^{rd} and 4^{th} order non-linear resonance lines do not pass through either tip. However, ion collection effects can result in structured peaks.[27]

Chapter 2

Experimental

2.1 Instrumentation

The thermal ionization quadrupole mass spectrometer system (TI-QMS) is shown schematically in Figure 2.1, and a simple electric circuit designed to heat the filament and produce the high energy ions is illustrated in Figure 2.2. Details of the commercial components are listed in Table 2.1.

A simple home-made thermal ionization source was used to produce high energy K^+ ions. The filament was a 0.127 mm diameter 10 mm long tungsten wire (H.CROSS Company, Weehawken NJ, USA) spot welded to two parallel stainless steel rods, so that the replacement of a filament was straightforward. The two rods were fixed on a MACOR plate by four washers and nuts. The rods' surface was threaded, so the length inside the ionization source chamber, and therefore the distance between the filament and the lens L1, could be adjusted. A distance of 1 mm was found to be optimum.

The circuit (Figure 2.2) was designed to heat the filament in order to generate K^+ ions and to float the filament to a high positive voltage. The variable transformer T1 (Warner Electric, Bristol, CT, Type 3PN117C-60Hz) was connected to the mains supply (110 V) and used to adjust the current to the filament. Transformer T5 had a turns ratio

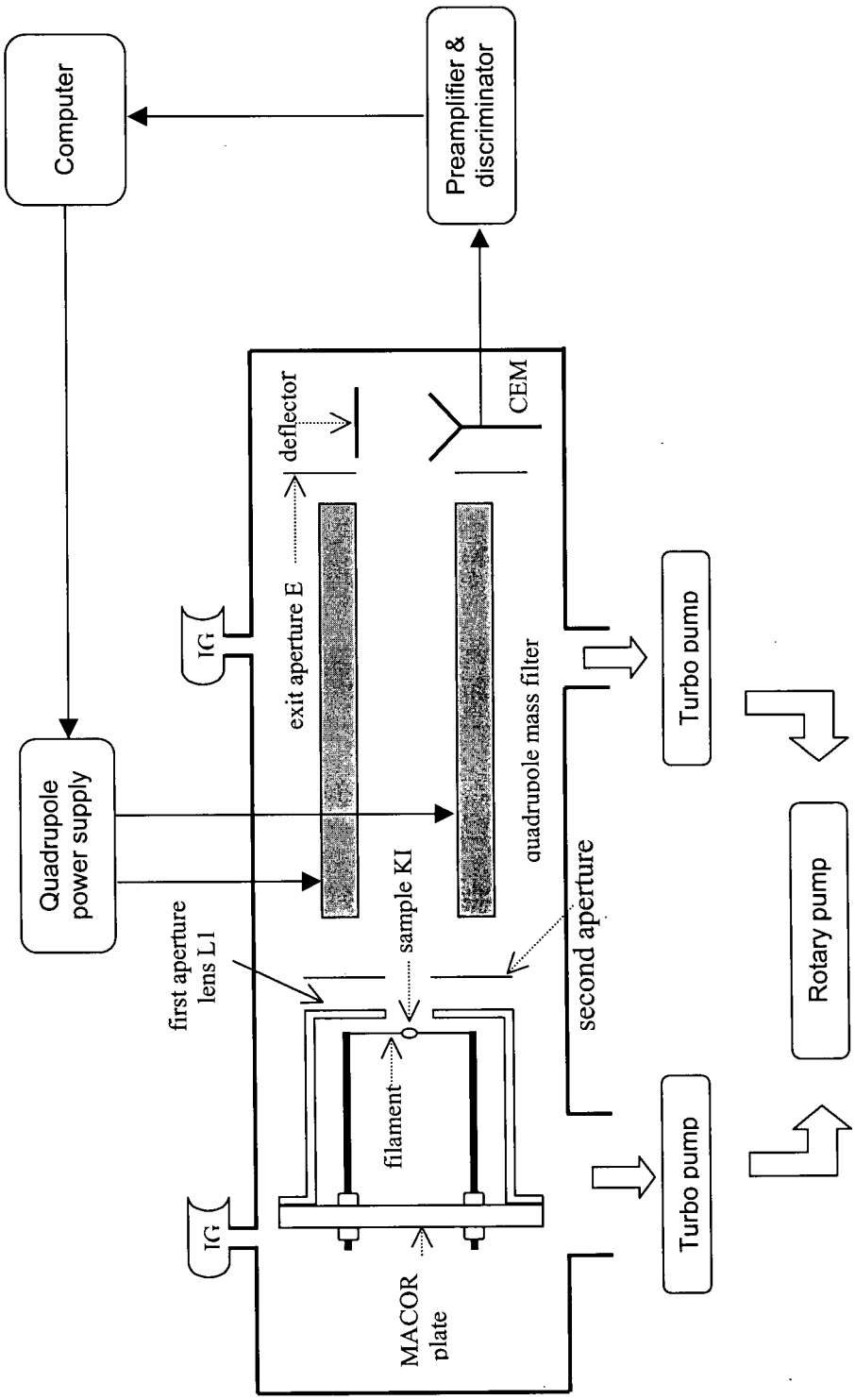

Figure 2.1 Schematic of the thermal ionization quadrupole mass spectrometer. IG, ionization gauge; solid arrows, electric connections; hollow arrows, gas flow; dotted arrows, the names of corresponding components. CEM, channel electron multiplier.

Table 2.1 Instrumentation

High voltage power supply for filament	Stanford Research System Inc. (Sunnyvale, CA), Model PS350/5000V-25W
AC ammeter	Wilbac Panel Meters, Model 21/2"(Range 0-5A)
Power transformers for ion source	T1, Warner Electric (Bristol, CT), Type 3PN117C-60Hz T2, 3, 4, Hammond Manufacturing (Canada) Model 167G100 T5, Hammond Manufacturing (Canada) Model 167P10
High voltage resistors	K and M Electronics. Inc (Springfield, MA), Type KO2540
Pumping system	Rotary pump, Leybold (Germany) Trivac D 16A Turbomolecular pump 1, (Germany) Leybold Turbovac 361 Turbomolecular pump 1 controller, Leybold (Germany) Turbotronik NT 150/360 Turbomolecular pump 2, Leybold (Germany) Turbovac 50 Turbomolecular pump 2 controller, Leybold (Germany) Turbotronik NT 10
Quadrupole rod set	PE SCIEX (Concord, ON) API III
Quadrupole power Supply	Modified PE SCIEX (Concord, ON) API III quadrupole power supply

(continued)

Ion gauges	Varian (Lexington, MA) Model 0571-k2471-306
Hot cathode controller	HPS Division, MKS Instruments Inc. (Boulder, Co) Model 919
Detector	Galileo channeltron electron multiplier (Sturbridge, MA) Model 4879
High voltage power supply for detector	Quantar Technology, INC.(Santa Cruz, CA), High Voltage supply, Model 3160, (0 to +/-6kV, 0 to 1mA)
Lens power supplies	Bertan Associate Inc. (Hicksville, NY), Model 305 (0-5000V, 0-1/2mA) Bertan Associate Inc. (Hicksville, NY), Model 342A
Preamplifier & discriminator	Quantar Technology, INC.(Santa Cruz, CA), Amplifier/Discriminator, Model 7011
Computer	Macintosh IIci, Apple Computer, Inc. (Cupertino, CA), System software 2.0

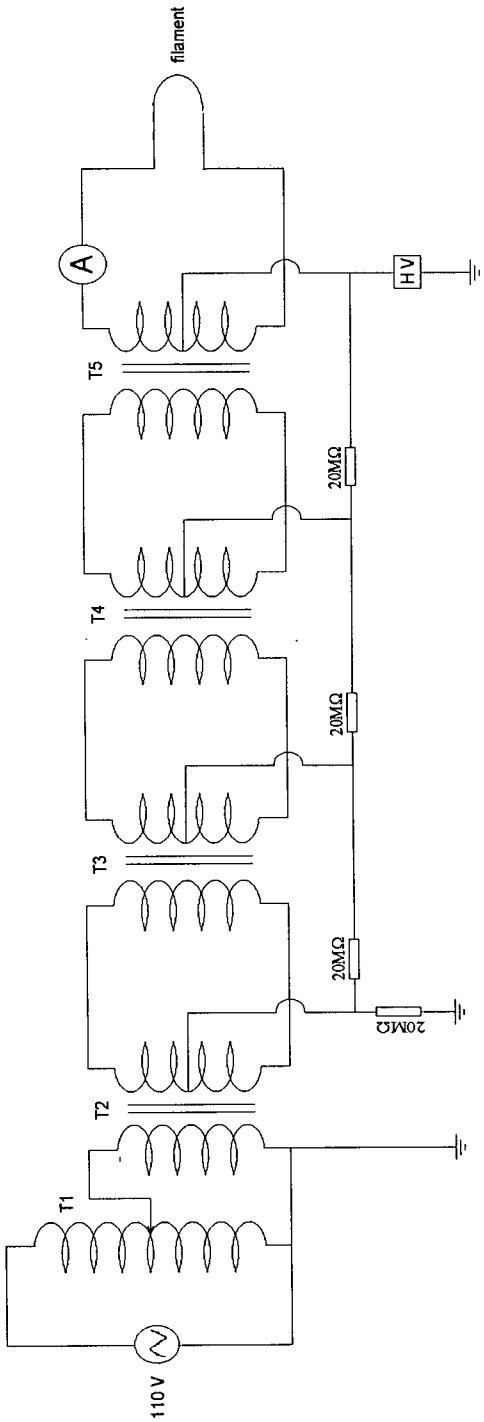

Figure 2.2 The electric circuit of the ion source. T1 is a variable transformer, T2, T3 and T4 all have a fixed turns ratio of 115:100, and T5 has a fixed ratio of 115:10. A is an AC ammeter.

of 115:10 and was used to decrease the voltage applied to the filament. The ac current meter was used to monitor the current through the filament. The three transformers, T2, T3, T4 have the same fixed turns ratio of 115:100. Between these four transformers and ground, there are four 20 MΩ high voltage resistors. Both T2, T3, T4 and the four 20 MΩ resistors were used to distribute the high voltage on the transformers 1 to 5. Therefore the voltage drop on each resistor was one-fourth of the total float voltage of the filament. The float potential of the filament could be varied up to +5000V (the voltage limit of the electrical feedthroughs used).

A 10 μl drop of 5 mg ml^{-1} KI solution was applied to the center of the filament by a pipet (MANDEL Scientific Company Ltd., Gilson pipetman® Model: P20) and dried under a lamp. The filament was then placed in the ion source chamber. The source was mounted just in front of the quadrupole rods. The sample was usually baked in vacuum with 0.5 V of 60 Hz ac (current ca. 0.5 A) for about 2 hours and then heated with typically 1-2 V of 60 Hz ac (current ca. 1.2 A) to generate K^+ ions. Ions leaving the filament pass through a 2.0 mm diameter aperture in the plate L1 at a potential typically 1-2 V below the filament float potential, through a second aperture L_2 (I.D. 2.0 mm) and into the quadrupole mass analyzer. The spacing between the two aperture lenses was 2.35 mm and the second aperture plate L_2 was 2.0 mm from the end of the quadrupole rods. The quadrupole rod set was from PE SCIEX (Concord, Ontario), had a field radius r_0 = 6.8 mm, and was 200 mm long. The quadrupole had an exit aperture (E) of 10 mm diameter in a plate spaced 2.0 mm from the end of the rod set. The exit aperture potential was 0 V. All the lenses were made by the mechanical shop of the Chemistry Department at UBC.

The vacuum chamber was from PE SCIEX (Concord, Ontario). It was evacuated by two turbomolecular pumps (Leybold TMP 361 and Leybold TMP 50, Leybold Canada, Mississauga, Ontario, Canada) to an operating pressure of $1\text{-}2\text{x}10^{-6}$ torr. The two turbomolecular pumps were backed by one common rotary pump (Leybold Trivac D16A).

The quadrupole power supply was a modified API III supply (SCIEX, Concord, Ontario) which could be operated in the first, second, third (upper tip M and lower tip S), fourth and sixth regions. A simplified block diagram of the quadrupole power supply is shown in Figure 2.3. Designed originally to operate in the first stability region, this power supply has a maximum RF output voltage, V, of 5,000 V (the zero to peak voltage between pole and ground) and DC output voltage, U, of 840 V (the voltage between pole and ground). The RF frequency was either 1.0 MHz or 0.768 MHz depending on the experiment. The frequency of 1.0 MHz was generated by the original crystal oscillator inside the power supply. To generate a frequency of 0.768MHz, an external crystal oscillator replaced the internal oscillator. A new matched load coil for the RF power amplifier was used. This RF transformer has two primary coils at the center and two secondary coils at each end. When the supply was operated in the second and fourth stability regions, the standard +/- 840V DC circuit boards were removed and an external power supply was used to produce a much lower DC voltage between the quadrupole rods. With this power supply the maximum DC voltage between rods was 20 V (i.e., U= +/-10 V). This is because the very small a value in these two regions requires a very low ratio U/V. The third region requires a ratio of DC voltage to RF voltage of U/V = 0.4892 at the upper tip (M) and U/V = 0.4478 at the lower tip (S). To do this, it is necessary to

lower the RF output of the quadrupole supply while leaving the DC output unchanged. Thus the RF mass command voltage was reduced from its original maximum of 10 V for the first region, to 3.474 V for the upper tip and 3.796 V for the lower tip. The electrical circuit for this is illustrated in Fig 2.4 (constructed by Mr. David Tonkin, electronic shop of the Chemistry Department, UBC). Resistive voltage dividers were added to the RF mass command circuit. For the operation at the upper tip, a 9.09 KΩ resistor, a 500 Ω potentiometer and a 4.75 kΩ resistor were connected in series to common. By adjusting the 500 Ω potentiometer, 3.474 V (maximum) was set on the 4.75 kΩ resistor and part of the potentiometer. For the operation at the lower tip, a similar resistive voltage divider in which the 9.09 kΩ resistor was replaced by a 7.8 kΩ resistor gave a voltage setting at 3.796 V (maximum). With these modifications, the resolution control provides about a 10% variation in the U/V ratio in both cases. For the sixth region, the U/V ratio is 0.6408 at the upper tip and 0.6248 at the lower tip. The range of U/V ratios between tips in this region is so small that only one voltage divider, similar to that used for operation in the third region, is needed. Thus a 13.5 kΩ resistor, a 500 Ω potentiometer and a 4.75 kΩ resistor were connected in series to ground. A maximum voltage of 2.658 V, which gives U/V= 0.6320, was set by the adjustment of the 500 Ω potentiometer. With this modification, a scan line can be set to cover the sixth region from the upper tip to the lower tip with the resolution control.

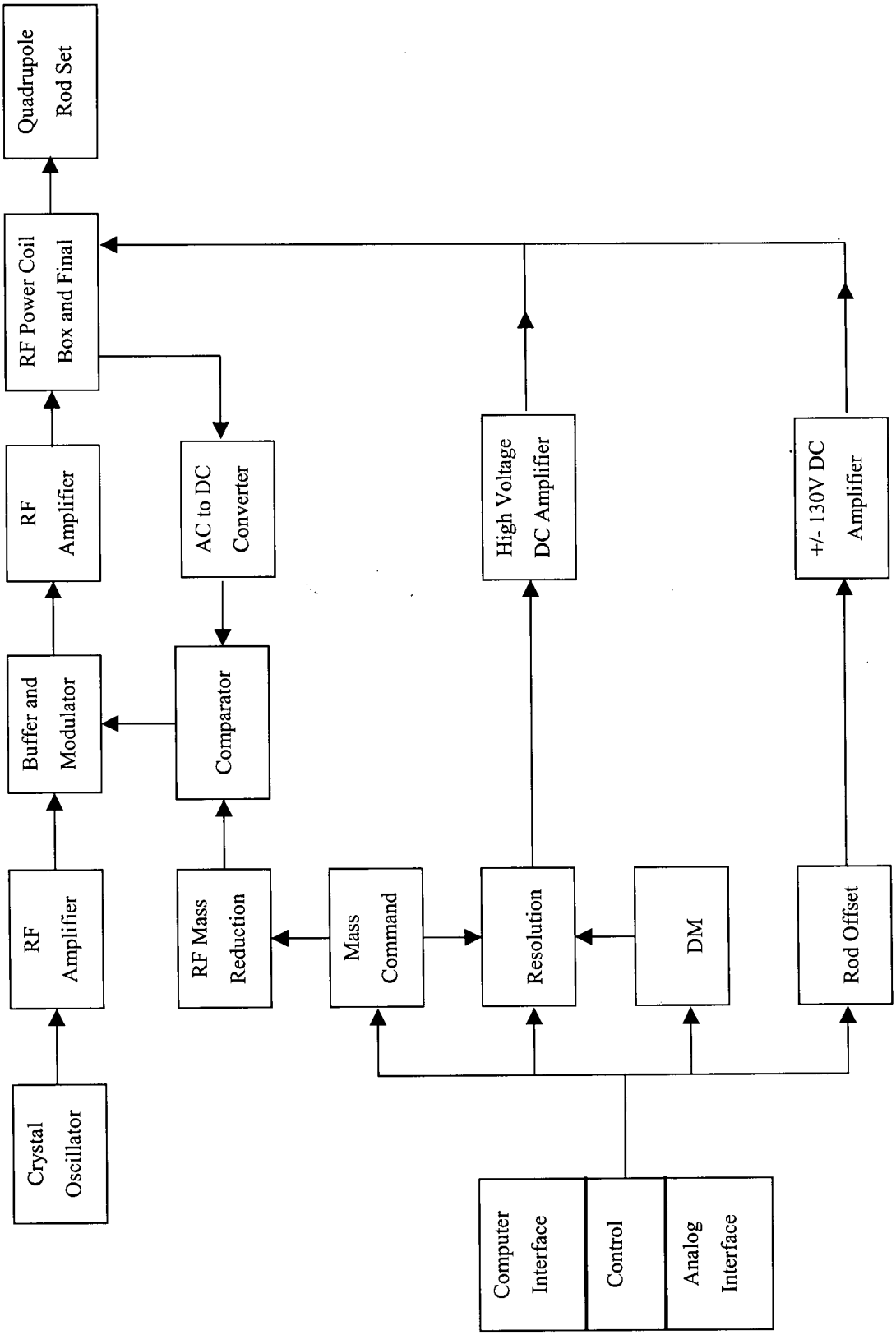

Figure 2.3 Simplified block diagram of the quadrupole power supply.

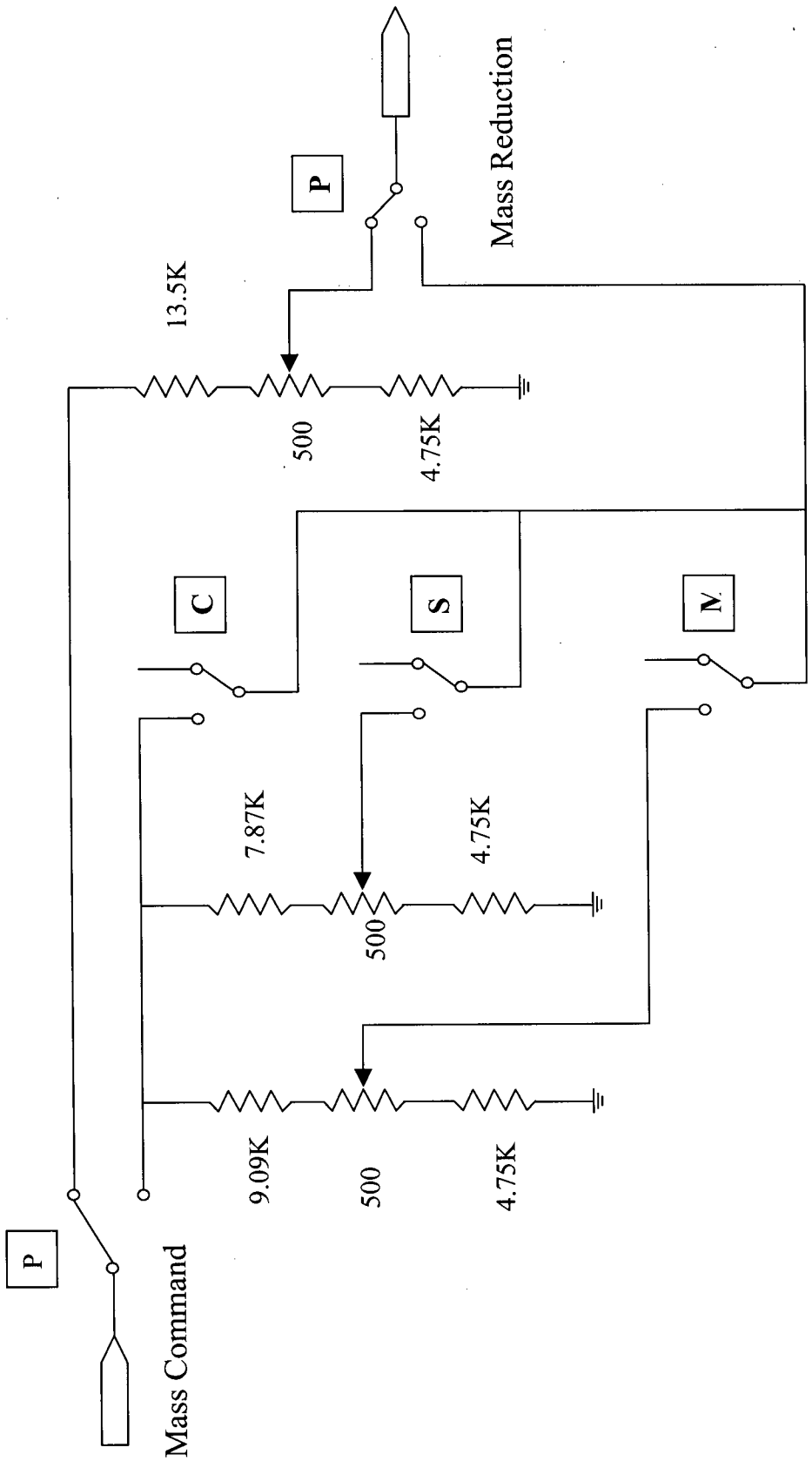

Figure 2.4 The RF mass command voltage reduction circuit. With the switch C closed, the power supply is operated in the first region, the switch S is for operation at the lower tip of the third region, the switch M is for the upper tip of the third region. The switch P is for operation at the sixth region.

The quadrupole was scanned under computer control (program Tune 2.0.21, SCIEX, Concord, Ontario). For different regions, the API III supply had a different RF maximum output. This, together with the different frequencies available, gave different mass ranges. Because a 16 bit Digital-to-Analog converter (DAC) board was used to set the mass, the smallest step size possible was equal to the mass range/ 2^{16}.

The detector was a channel electron multiplier (CEM) which had an overall gain in the range of $10^{7} - 10^{8}$ electrons out per incident ion. Ion counting was used for detection and multiple scans could be added to improve the signal to noise ratio. Each incident ion generates a pulse with an amplitude of 20-35 mV and a width of about 50 ns at the CEM output into a preamplifier. The pulse was then amplified about ten times by a preamplifier and triggered a discriminator to produce a transistor-transistor logic (TTL) square wave pulse with a width of 100 ns. The output TTL pulses were counted by a board (National Instruments Corporate, Austin, TX, Model *NB-DIO-32F*) in the computer.

2.2 Sample Preparation

A solution of 5 mg/mL KI was prepared by dissolving solid potassium iodide (Reagent A.C.S, Fisher Scientific, Nepean, Ontario, Canada) in water distilled and deionized with a NANO pure II ultra water system (Barnstead/Themolyne, Dubuque, IA, USA).

2.3 Computer Simulations

All the programs were originally written by Nikolai Konenkov, Department of General Physics, Ryazan State Pedagogical University, Ryazan, Russia and modified by Wei Chen for easy calculation. The modifications include: adding loops, setting calculation range, and changing input and output style.

2.3.1 Numerical integration

Two programs with the Runge-Kutta Nystorm and Dormand - Prince (RK-N-DP) numerical method[95, 96] were used to simulate ion trajectories, peak shapes and transmission curves for a finite length quadrupole. The RK-N-DP numerical method was developed for numerical simulations of dynamics in astronomy. It is a direct method that does not require starting the method in the first step of integration; in other words, it is suitable for calculating a large number of ion trajectories with different initial conditions. The RK-N-DP numerical method gave a global error about 10^{-4} on the interval of ξ 0-100π with an integration step size as large as $\Delta\xi = \pi/4$ Rad. These programs were written in turbo- PASCAL 7.0 and could be run under DOS on any PC with a VGA monitor. The PASCAL codes are listed in Appendices I and II.

The ion trajectory simulation program (Appendix I) was based on the integration of the equation of ion motion (Equation 1.7). The integration step size $\Delta\xi$ was typically set at $\pi/40$ Rad. In this way the position of an ion at any time can be determined. If the ion strikes a rod over the defined number of RF cycles, it is said to be unstable within

this number of cycles. Conversely a stable ion can be described as an ion which does not make contact with either of the pairs of rods.

The program for simulation of peak shapes or ion transmission curves (Appendix II) could calculate peak shapes with different scan lines and different ion energies. The peak shape was usually represented by 20-40 points across the peak in the calculation. At each point, the transmission T was determined as the fraction of input ions which passed through the mass analyzer:

$$T = N_{out} / N_{in} \qquad (2.1)$$

where N_{in} is the total number of ions that were injected into the circular input aperture of the quadrupole field with a radius r_a, and N_{out} is the number of ions transmitted through the mass filter. The transmission T depends on the ion distribution at the input aperture plate. In the program, a random uniform ion distribution was selected to represent ion initial transverse positions at the input aperture. The number of initial points at the input aperture was chosen to be N_p=100. The transverse velocity was equal to fx_0 or fy_0, where, f is the focusing parameter and equal to $\dot{u}/u$, which represents the degree of ion focusing into the mass analyzer; x_0 and y_0 are initial positions in the x and y directions expressed in units of r_0. If f is negative, the ion beam is converging. The integration step size $\Delta\xi$ was also set at $\pi/40$ Rad. The step size of the initial RF phase is set at $\pi/50$ Rad, which means the number of initial RF phases used in the calculation of one period was equal to P =50. This is necessary for the higher stability regions where the very narrow acceptance ellipses rotate with an angular frequency ω. Therefore, the number of ions falling onto the aperture per RF period is equal to $N_{in} = P*N_p = 100*50 = 5000$. This means that every point on the transmission curve is the result of calculations

for 5000 ions. For 40 points across the mass peak, 40*5000 trajectories were calculated.[97] The fringing fields at the entrance of the quadrupole were included in the calculation and were based on the model of McIntosh and Hunter[65].

2.3.2 Matrix methods

A program for calculating the acceptance for an infinitely long quadrupole field was used. This program can calculate the acceptance at any point (a,q) in the stability diagram taking into account the input fringing fields (using the model of McIntosh and Hunter) The following assumptions are made: the ion velocity in the z dimension is constant in the fringing field; the quadrupole field is ideal and has an infinite length; the fringing fields at the quadrupole exit are neglected, that is, all ions exiting the mass filter are collected.

The acceptance was represented in units of $\pi r_0^2 f$ for different transmission levels expressed as a percent, and was calculated for different lengths of the fringing fields expressed in terms of the number of RF cycles. The fringing field effects were incorporated by calculating a matrix $\hat{F}$ that transforms the initial positions u_f and velocities $\dot{u}_f$ on the entrance plate ($\hat{F}$=0) into position u and velocities $\dot{u}$ in the quadrupole mass filter field when $\hat{F}$=1.[4]

The matrix elements can be found by calculating trajectories in the x and y directions with the initial conditions u_f = 1, $\dot{u}_f$ = 0 and u_f = 0, $\dot{u}_f$ = 1. To obtain the matrix $\hat{F}$ a combination of methods was used in the program. First, the third order Runge-Kutta method[98] was employed to find the initial values for the Numerov

method[99] which is particularly suitable for solving the equations of ion motion in the fringing field. Then the Numerov method was used for calculating ion trajectories. Finally, with the values thus determined the Meisner matrix method[4] was used to calculate transverse ion velocities. This combined numerical method can solve these equations with sufficiently high accuracy. The tolerance is $1x10^{-3}$. The transformation matrix $\hat{F}$ was then used to calculate modified parameters of the acceptance ellipse from the parameters of an ideal quadrupole mass filter. This program has been used previously to study the ion optics properties of quadrupole mass filters operated in the second [23] and third stability regions [66, 94]. The program was written in BASIC and run under DOS on a PC, and is listed in Appendix III.

Chapter 3

A quadrupole mass filter operated in the fourth stability region

3.1 Introduction

The fourth stability region [45, 100] has a triangular shape and is shown in detail in Figure 3.1. Along the q axis, the stability region extends from 21.298631 to 21.303174. At the tip G, a_G = 2.06x10^{-3}, q_G=21.30095. The frequencies of ion motion in a quadrupole, Ω_n, are given by

$$\Omega_n = (2n + \beta)\frac{\omega}{2} \qquad n = 0,\pm1,\pm2,... \qquad (3.1)$$

where n is an integer and β is determined by the a,q parameters. [4, 45] For this stability region, β_x and β_y, for motion in the x and y directions respectively, vary from 2 to 3. Because of the small value of a and the large value of q, a quadrupole power supply with V = 5,000 volts (pole to ground) requires a maximum dc voltage, U, of only 0.24 volts (pole to ground) to reach the tip of the stability region. The theoretical resolution defined in terms of the width at the base of a peak with an infinitely long quadrupole mass filter can be expressed by:

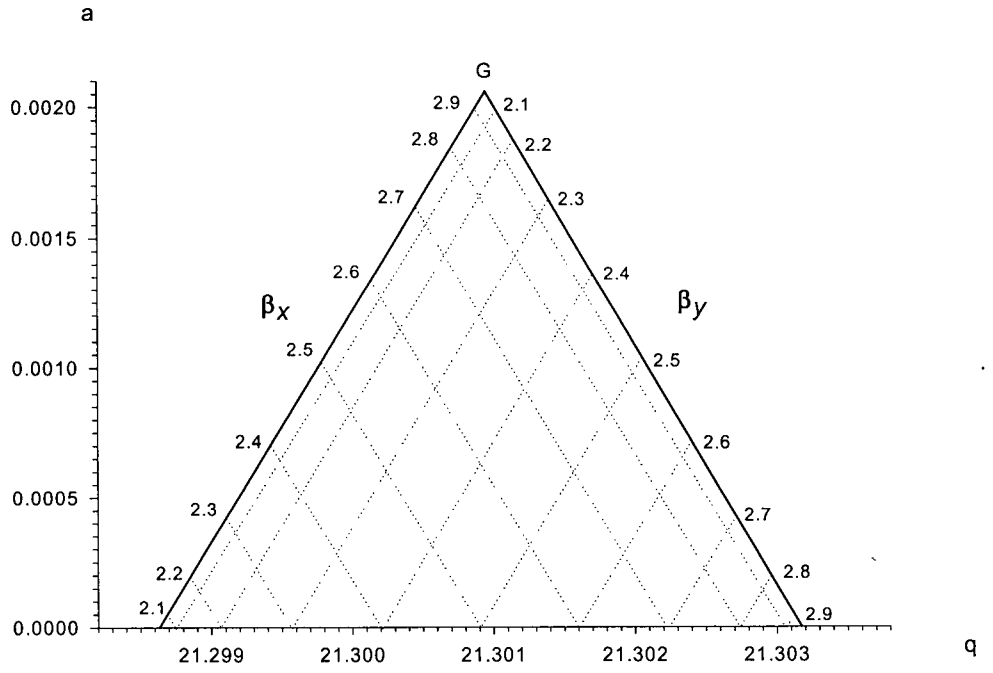

Figure 3.1 The fourth stability region

$$R_{IV} = \frac{m}{\Delta m} = \frac{q_G}{\Delta q} \approx \frac{4700}{1-\lambda/\lambda_G} \qquad (3.2)$$

where Δm is the peak width at the base, i.e. the peak width at the base, q_G is the q value at tip G of the region, $\lambda = U/V = a/2q$, $\lambda_G = a_G/2q_G$, and a_G is the a value at the tip of the peak. The width of the stability region at $a = 0$ (i.e. with no DC applied between the quadrupole rods) gives a resolution at the base of a peak of $\frac{q_G}{\Delta q} = 4700$, which, if a triangular peak is formed, gives $R_{1/2} = 9400$. This resolution is sufficient to separate atomic ions from many of the common molecular ion interferences in ICP-MS. Higher resolution is expected with values of $a > 0$. When ions with mass to charge ratio m/z are

transmitted in this region with q = 21.3, ions with $m'/z = 2.82m/z$ and $m''/z \geq 23.46m/z$ are simultaneously transmitted in the second and first regions respectively. Thus use of the fourth region requires some sort additional mass filter or other means to eliminate this aliasing.

3.2 Experimental

The experimental apparatus is shown in Figure 2.1. The quadrupole power supply (model API III, SCIEX, Concord, Ontario) was operated in the second and fourth regions at 1.0 MHz. The maximum output of the power supply is V = 5,000 volts, which gave an upper *m/z* limit of 48.8 with operation in the fourth region. This range was sufficient to test the properties of this stability region with $^{39}K^+$ ions. Because a 16 bit digital to analog converter was used to set the mass, the smallest step size possible was $48.8/2^{16} = 7.4 \times 10^{-4}$ *m/z*. Most experiments were done with $a = 0$, *i.e.* no DC between the rods. This was easily done by setting the quadrupole to "RF only" mode. The rod offset of the quadrupole was 0 V so that the ion energy through the quadrupole was determined by the filament float potential.

To record the relative transmission of the quadrupole in the second and fourth regions, the quadrupole was scanned from ca. *m/z* = 13 to 15 and from *m/z* 39 to 40, respectively. With the quadrupole mass calibrated for the fourth region, $^{39}K^+$ ions were transmitted in the second region when the mass setting was *m/z* = 13.8 (*i.e.* (1/2.82) x 39). The ratio of the transmission in the fourth region to the transmission of the second region was simply given as the ratio of the peak intensity at *m/z* = 39 to that of the peak at *m/z* = 13.8.

3.3 Results and discussion

3.3.1 Resolution and Ion Energies with RF only Operation

The experimental peak shape obtained with $^{39}K^+$ ions with 40 eV energy is shown in Figure 3.2. Here $a = 0$. The peak width at half height is 2.8×10^{-3} *m/z* and the measured resolution at half height is 13,900. The width of the base of the peak is 8.2×10^{-3} *m/z* which corresponds to a resolution at the base of 4750, in good agreement with that expected from the width of the stability diagram (4700).

The resolution at half height was measured for ion energies up to 4800 eV. Under conditions where the resolution is controlled by the ion residence time in the quadrupole, the resolution is expected to increase linearly with the square of the number of RF cycles (n) that the ion spends in the quadrupole. [4] Figure 3.3a shows the measured $R_{1/2}$ vs. n^2. The highest resolution of 13,900, with $n^2 = 202$, corresponds to 40 eV ions and the lowest resolution of 1000 with $n^2 = 1.7$ represents 4800 eV ions. Figure 3.3b shows the first four points with n^2 values from 1.7 to 4 (ion energies from 4800 to 2040 eV respectively). The solid line is a linear fit passing through the origin and gives $R_{1/2} = 829n^2$. For comparison, $R_{1/2} = 26n^2$ with operation in the second region, $R_{1/2} = 1.0n^2$ with operation in the third region and $R_{1/2} = 0.05n^2$ with operation in the first region. [25] The points in Figure 3.3b show a systematic deviation from the simple $R_{1/2} \sim n^2$ relation. A better linear fit to the data is $R_{1/2} = -730 + 1078n^2$, shown by the dashed line in Figure 3.3b.

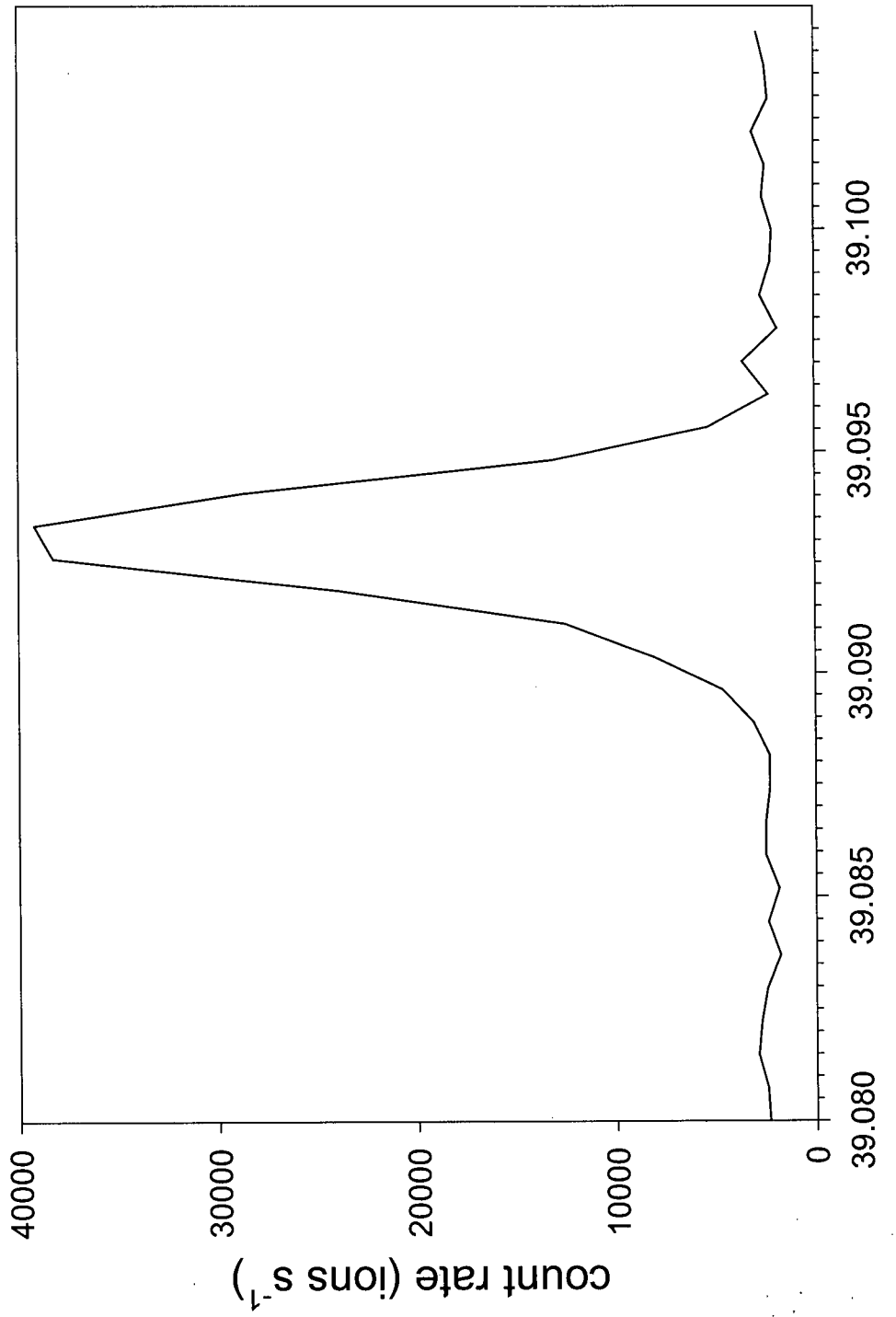

Figure 3.2 Peak shape with $R_{1/2}$ = 13,900 obtained with 40 eV $^{39}K^{+}$ ions.

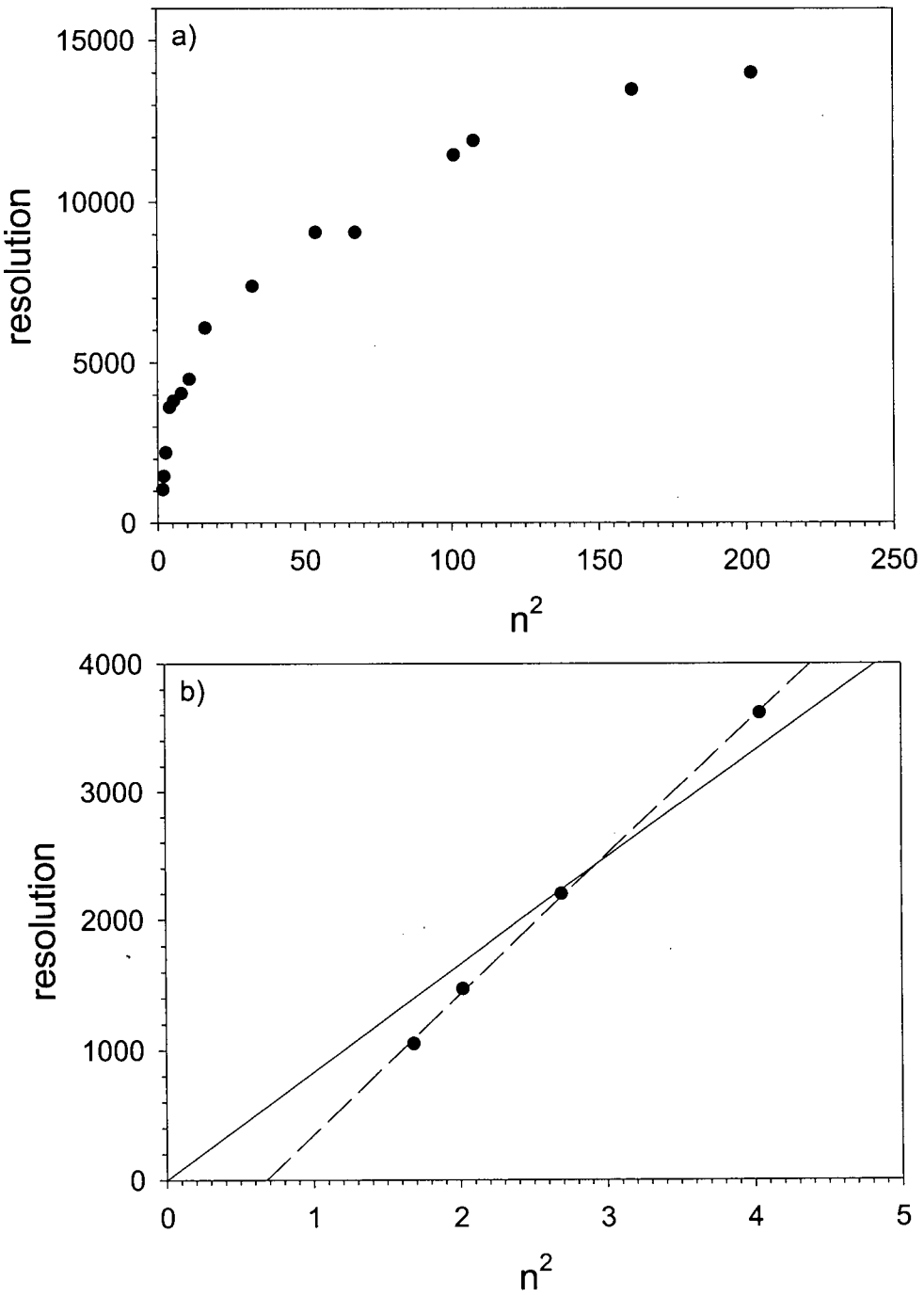

Figure 3.3 (a) resolution (defined at half height of peak) *versus* the square of the number of cycles the ions spend in the quadrupole field for $^{39}K^{+}$ and $a = 0$ (b) expansion of the region between $n = 0$ and $n = 5$. The solid line is a fit to $R_{1/2} = 829n^2$ and the dashed line a fit to $R_{1/2} = -730 + 1078n^2$.

These relationships can be used to calculate the highest ion energy for which unit resolution can be obtained for $^{39}K^+$ ions ($R_{1/2}$ = 78). From $R_{1/2} = 829n^2$ it is calculated that n needs to be only 0.307, which, for the quadrupole used, gives a calculated ion energy of 86,000 eV. This calculation probably overestimates the ion energy for which unit resolution can be obtained. From the better fit $R_{1/2} = -730 + 1078n^2$, it is calculated that $R_{1/2}$ = 78 requires n = 0.866 which corresponds to an ion energy of 10,800 eV. While these extrapolations to higher ion energy are approximate, they do illustrate that unit resolution can be obtained with ions with energy of several keV.

Another interesting feature of this region is that relatively high resolution can be obtained with ions of comparatively high energy. Figure 3.4a shows the peak shape obtained when $R_{1/2}$ = 5000 and the ion energy is 750 eV. A resolution of 5000 can be obtained with operation in the second stability region provided that a > 0. However, with the second region, to obtain this resolution the ion energy is limited to *ca.* 20 eV or less.[56] Figure 3.4b shows the peak shape and resolution obtained with 4000 eV ions and a = 0. The peak width at half height is 0.028 *m/z* which gives $R_{1/2} \approx 1400$. While the peak is relatively narrow at half height it shows considerable symmetric broadening at the base. The peak width at 10% of the peak maximum is 0.1 *m/z* which gives $R_{1/10}$ = 390.

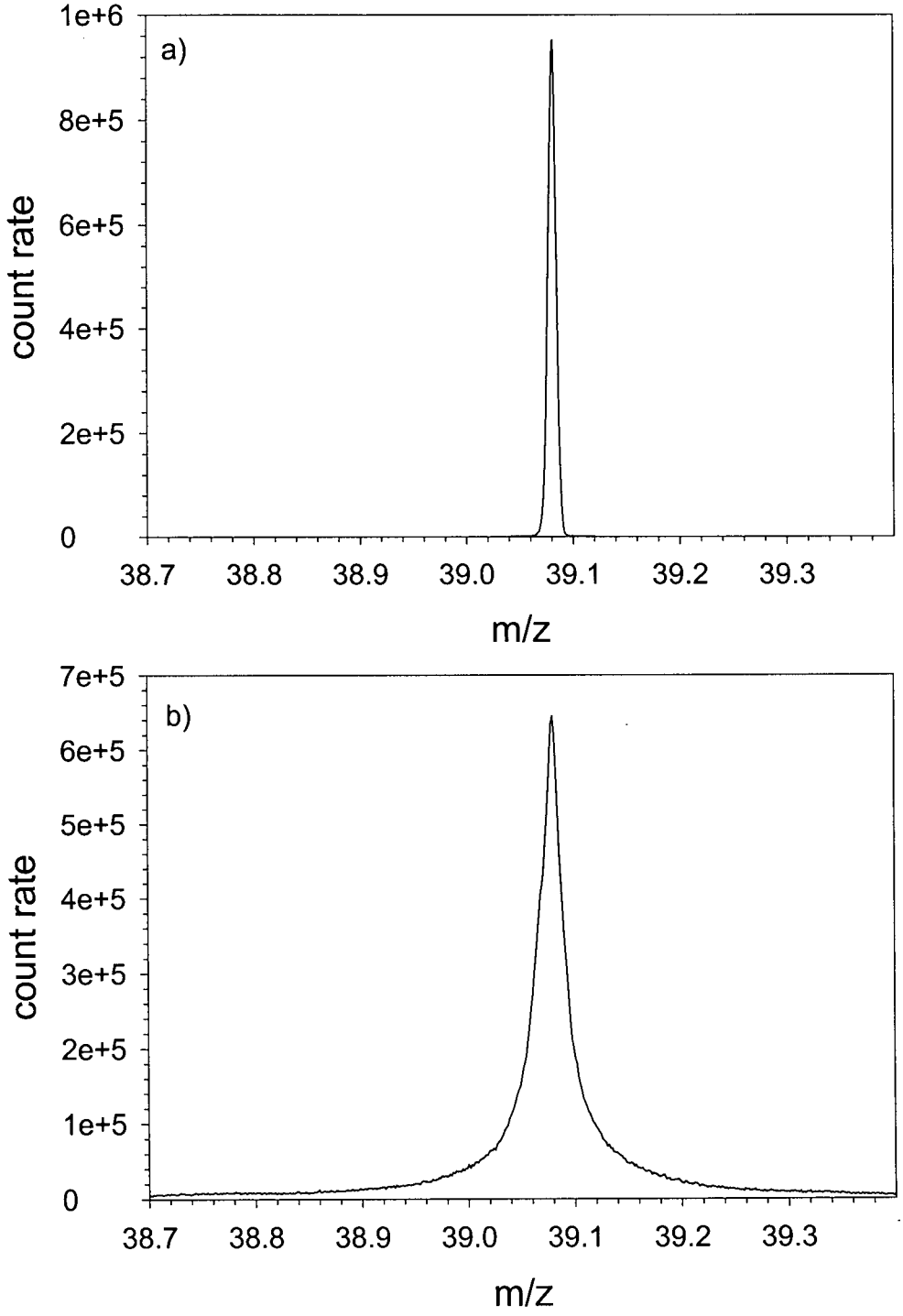

Figure 3.4 (a) peak shape with 750 eV ions, $R_{1/2}$ = 4500 (b) peak shape with 4000 eV ions, $R_{1/2}$ = 1400.

3.3.2 Fourth region with a > 0

Attempts were made to increase the resolution in the fourth region by adding DC between the rods ($a > 0$). The resolution at half height with different ion energies was measured for scan lines moving from the bottom of the stability region ($a = 0$ or U = 0) to the tip ($a = 2.06 \times 10^{-3}$ or U = 240 mV). Figure 3.5 shows the measured $R_{1/2}$ *versus* n^2 when the DC voltage was 0 mV, 80 mV and 160 mV, respectively. The ion energies range from 500 eV to 4000 eV. Figures 3.6(a,b) show two groups of peak shapes for ions with different values of U, at a low kinetic energy of 500 eV (a) and a higher kinetic energy of 2000 eV (b). At high ion energies the resolution is dominated by the number of RF cycles in the field; no increases in resolution were seen (Figure 3.6(b)), while the transmission decreased slowly with increasing U. At low ion energies, a distorted peak with a dip was formed (Figure 3.6(a)), which may be related to field imperfections or ion collection effects. [25] The resolution close to the tip of the stability region is slightly greater than that at the base. However, the values of the resolution at half-height obtained from these experiments are about 3 to 15 times lower than the theoretical resolution at half-height for an ideal quadrupole mass filter. Figure 3.7 shows the difference between the experimental and the theoretical resolution. The theoretical resolution at the half-height of the peak is equal to $2 * \frac{q_G}{\Delta q}$. Possible reasons for this discrepancy are discussed in Chapter 6.

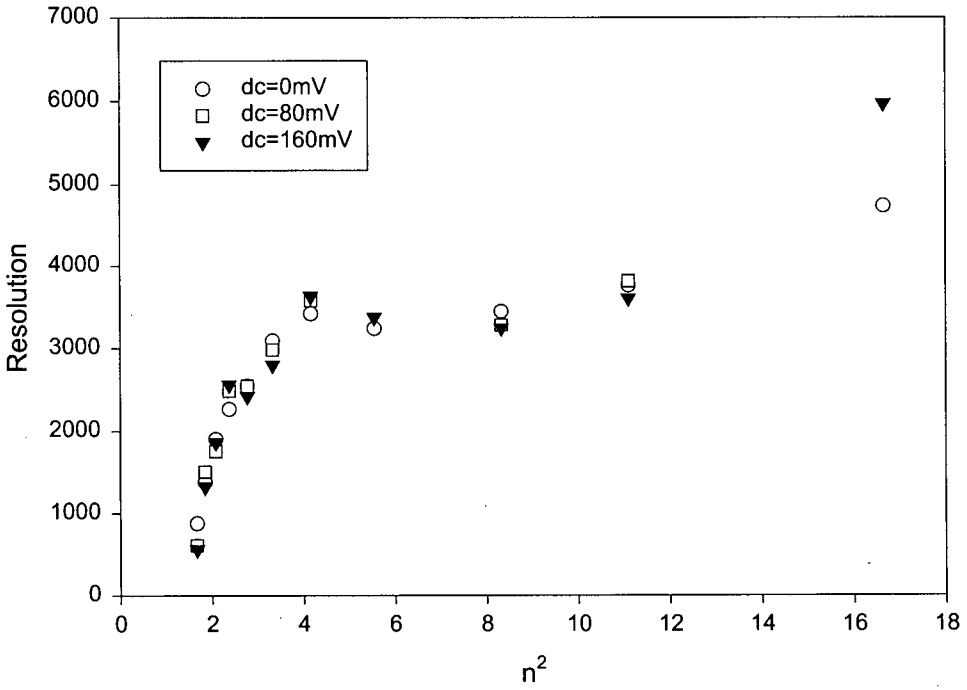

Figure 3.5 Resolution at half height *versus* the square of the number of RF cycles that $^{39}K^{+}$ ions spend in the quadrupole field, for different DC voltages U between the rods. The symbols "○", "□",and "▼" refer to DC voltages of 0 mV, 80 mV, and 160 mV , respectively.

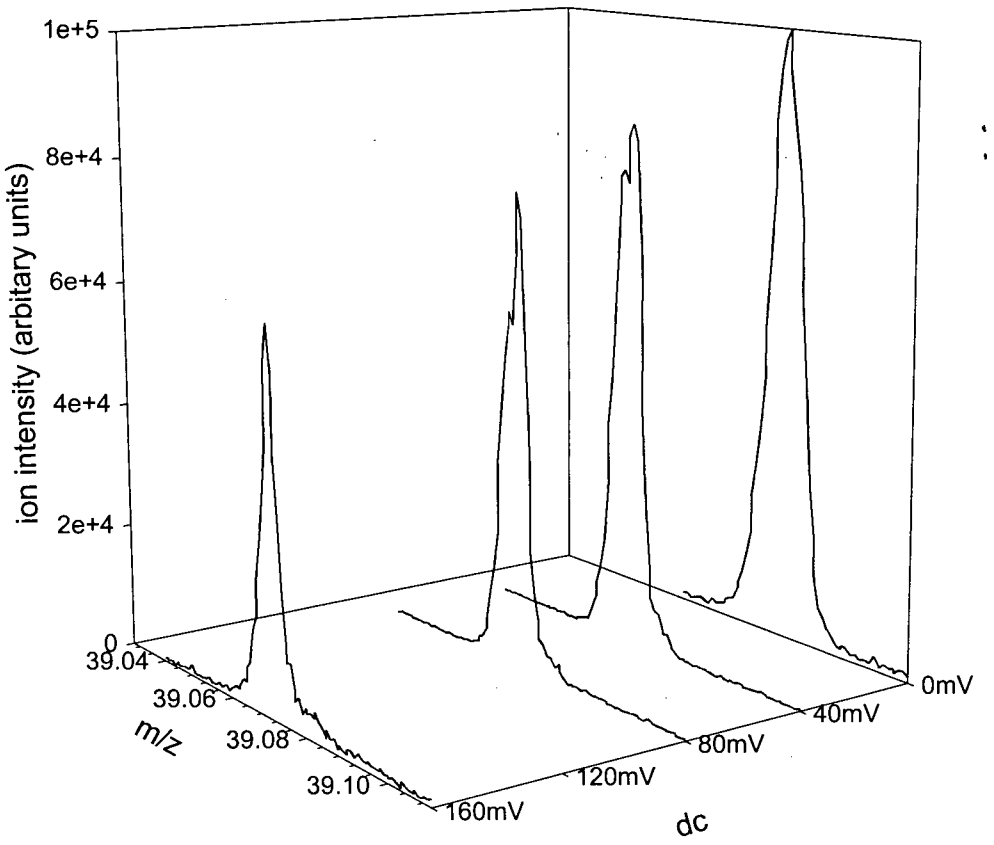

Figure 3.6a Peak shape with different DC voltages U between the rods obtained with 500 eV $^{39}K^{+}$ ions.

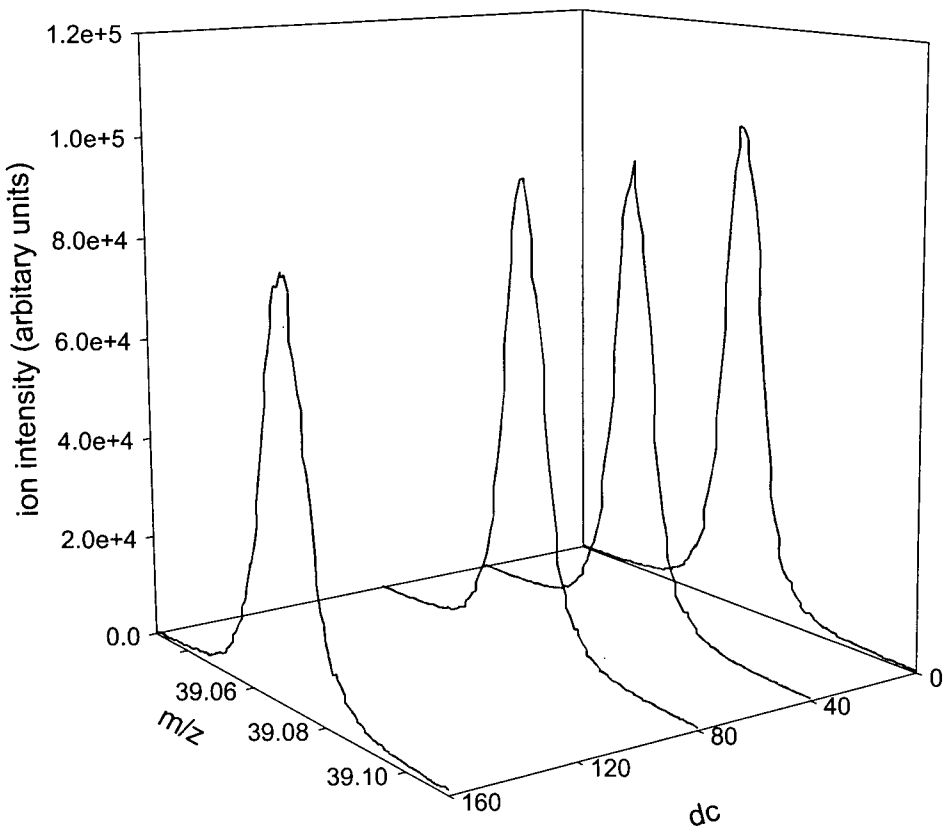

Figure 3.6b Peak shapes with different DC voltages U between the rods obtained with 2000 eV $^{39}K^{+}$ ions.

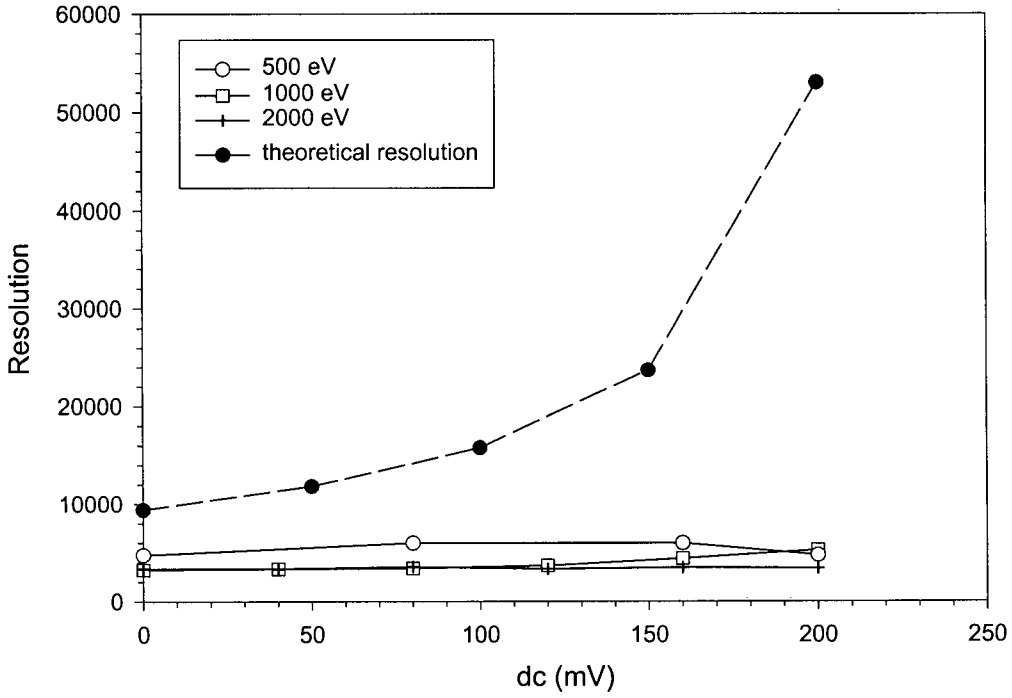

Figure 3.7 Comparison of the theoretical resolution to the experimental resolution. The dashed line is the theoretical resolution for an ideal quadrupole field, while the solid lines combined with the symbols "○", "□" and "+" refer to experimental resolutions obtained with ion energies of 500 eV, 1000 eV and 2000 eV, respectively.

3.3.3 Acceptance and Fringing Fields (Comparison with the Second Stability Region)

As described in Chapter 1, the acceptance is a useful concept for evaluating the transmission of a quadrupole mass filter under various operating conditions. The fringing field at the entrance to a quadrupole can be defocusing, and this acts to decrease the acceptance of the quadrupole. The magnitude of the decrease depends on the residence time of the ion in the fringing field. This is usually expressed in terms of the

number of RF cycles, n_f, that an ion spends in the fringing field. If n_f is small, the field does not have time to defocus the ions, and the acceptance is not significantly decreased. Figure 3.8 shows the effect of n_f on the calculated acceptance of a quadrupole operated in the fourth stability region with $a = 0$ and $q = 21.30093$ (i.e. at the center of the stability diagram). The fringing field was based on the model of McIntosh and Hunter [65] and had a length of $1.5r_o$. The acceptance, in units of $\pi r_0^2 f$, was calculated for transmission levels of the quadrupole of 25%, 50% and 75% as described in detail in ref. 8 . Figure 3.8 shows that there is a strong decrease in the acceptance at the 50% and 75% levels for $n_f > 0.3$. For the quadrupole used here, $n_f < 0.3$ requires $^{39}K^+$ ion energies of 230 eV or more to avoid losses in transmission. These results can be compared to the same calculations for the second stability region with $a = 0$, shown in Figure 3.9. For the second region the transmission remains nearly constant for n_f up to 0.7. Therefore ion transmission can be maintained for $^{39}K^+$ ion energies down to about 43 eV in the second region.

The acceptance in x at $n_f = 0$ is ca. $2x10^{-4}$ (T = 25%, Figure 3.8). For the case where $a = 0$ the acceptance in y will equal the acceptance in x and the combined acceptance will be $4x10^{-8}$. For comparison, with operation in the second region and $a = 0$, the acceptance in x is $1.5x10^{-2}$ (T = 25%) and the combined acceptance is $2.25x10^{-4}$.[8] Thus in the absence of any other effects, the transmission in the fourth region might be expected to be about $2x10^{-4}$ times that in the second region. Similarly, comparison of the acceptances at other transmission levels (50%, 75%) also shows that the combined acceptance in the fourth region is many orders of magnitude lower than that in the second region. However, operation with $a = 0$ in the second region gives a nominal

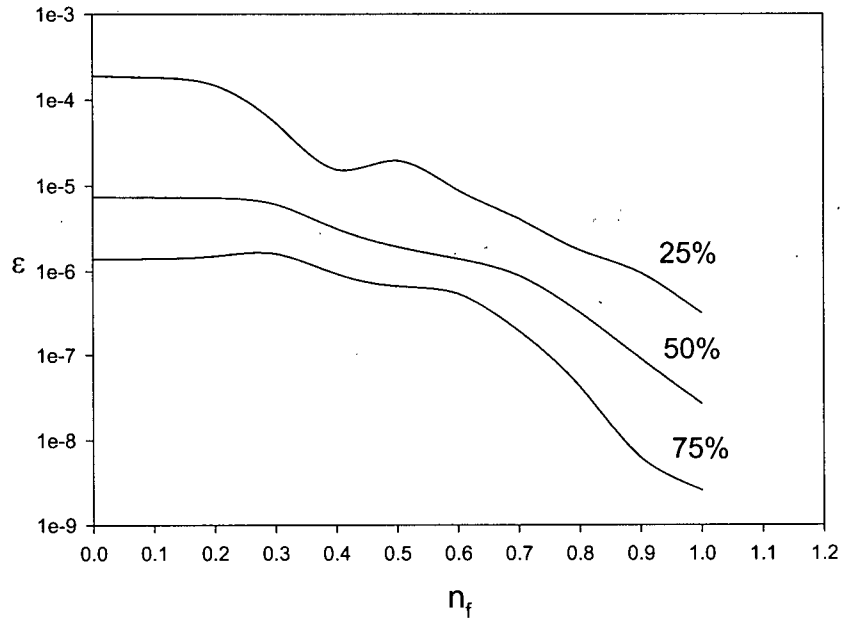

Figure 3.8 The acceptance ϵ of the quadrupole in the x or y direction with operation in the fourth region with a = 0, q=21.30095, for different numbers of RF cycles in the fringing field, n_f. The acceptance is in units of $\pi r_0^2 f$.

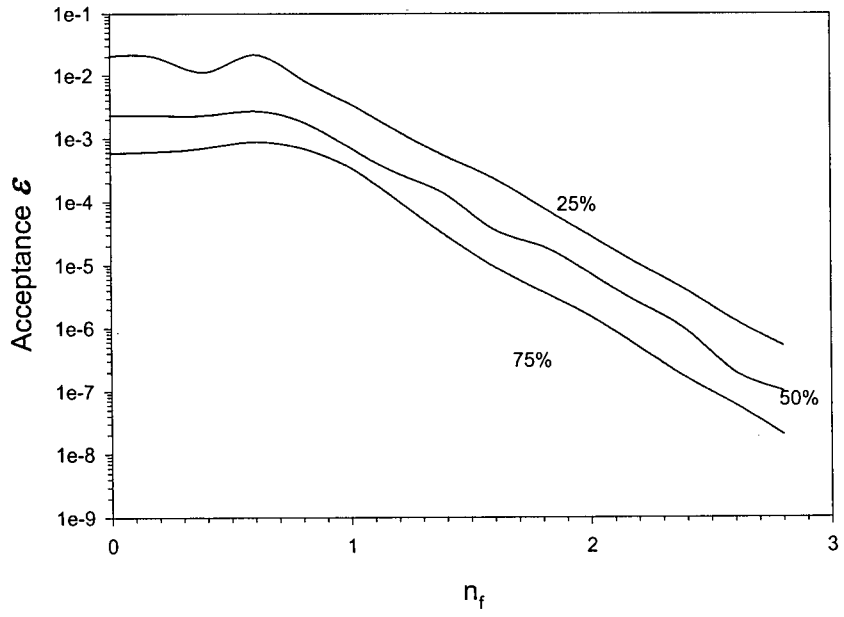

Figure 3.9 Acceptance of a quadrupole in the x or y direction with operation in the second region for different numbers of RF cycles in the fringing field, n_f, for a = 0, q = 7.547.

resolution, $q/\Delta q$, of 114, whereas the fourth region gives a nominal resolution of 4700. It is more informative to compare acceptances at the same resolution. The acceptances in x and y in the second region at higher resolution (i.e. with DC applied between the rods so $a > 0$) have been calculated[23] and at $q/\Delta q = 4700$ are 1.9×10^{-3} and 7×10^{-4} respectively, for a combined acceptance of 1.33×10^{-6}. Here $n_f = 0.5$ and the transmission level was taken to be 25%. Thus when compared at a resolution of $q/\Delta q = 4700$, the acceptance in the fourth region is still 3×10^{-2} of the acceptance in the second region.

These acceptance calculations serve as a rough estimate of the relative transmission that might be expected for the two regions. However the acceptance calculation is for an infinitely long quadrupole, that is, for the case where the ion spends an unlimited number of RF cycles in the quadrupole. Most of the experiments here were done with ion energies sufficiently high that the simple acceptance arguments do not apply. At higher ion energies the acceptance increases because ions do not spend a sufficient number of RF cycles in the quadrupole to be rejected. An ion outside the calculated acceptance ellipse can still be transmitted. This increases the acceptance and decreases the resolution. The relative transmissions are best determined experimentally.

Figure 3.10 shows the ratio of the ion transmission in the fourth region to the transmission in the second region, recorded as described in the experimental section. Here $a = 0$ in every case. It is seen that under all conditions, the transmission in the fourth region is substantially less than that of the second region. At ion energies greater than ca. 2000 eV the transmission in the fourth region is about 4×10^{-3} of that in the second region. At lower ion energies there is a decrease in the relative transmission in the fourth region. At the lowest energy of 75 eV the transmission in the fourth region is

$2x10^{-5}$ of the transmission in the second region. This is about a factor of 10 lower than the relative transmission expected from the calculated acceptances ($2x10^{-4}$) with $n_f = 0$. The additional loss can be attributed to the defocusing fringing field at the quadrupole entrance. With 75 eV ions in the fourth region, $n_f = 0.53$ and Figure 3.8 shows that the acceptance in x decreases by a factor of 2-10 (depending on the transmission level considered) and the combined acceptance by a factor of 4-100. In contrast to this, with $n_f = 0.53$, the acceptance in the second region remains close to that calculated for $n_f = 0$. At low resolution the transmission in the second region is about a factor of ten lower than in the first region. Thus for low energy ions, the transmission in the fourth region is calculated to be $2x10^{-6}$ or less than that of the first region.

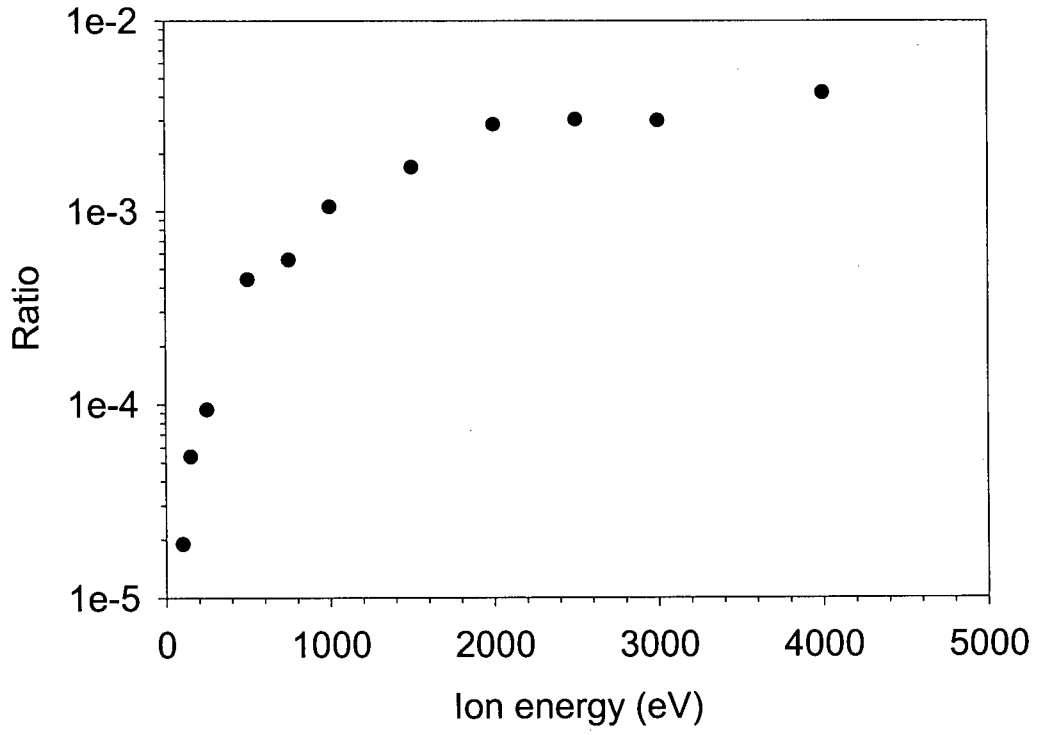

Figure. 3.10 The ratio of ion transmission in the fourth region to the transmission in the second region for ion energies between 75 and 4000 eV.

These considerations then suggest that the acceptance and transmission in the fourth region are so low that it may be of no practical use. However, the data of Figure 3.7 do not contain any information about resolution. For example at low ion energies, $R_{1/2}$ = 78 in the first region (if operated at unit resolution), $R_{1/2} = 167$ in the second region[8] and $R_{1/2} \approx 13{,}900$ in the fourth region. High resolution cannot be obtained with operation in the first region, and high resolution in the second region requires low ion energies where the fringing fields can decrease the transmission. Again it is more informative to compare transmission at the same resolution. To do this, the ion energy was lowered and DC added between the poles with operation in the second region to produce higher resolution. This measurement is approximate because the ion optics were not adjusted for the highest transmission in each region. Table 3.1 shows the ratio, *r*, of transmission in the fourth region to that in the second region for different resolutions. For resolutions of several thousand, the transmission in the fourth region remains comparable to that of the second region, but decreases at $R_{1/2}$ = 5000. However it should be noted that $R_{1/2} > 9000$ could not be obtained with the second region so in these cases the fourth region has higher (but low) transmission.

Table 3.1 Comparison of ion energies and ratio, *r*, of transmission in the fourth region to transmission in the second region

$R_{1/2}$	ion energy second region (eV)	ion energy fourth region (eV)	*r*
1500	100	4000	0.58
2500	60	3000	0.43
3700	20	2000	0.30
5000	15	600	0.12

3.4 Summary

A resolution at half height of up to 13,900 at *m/z* 39 can be obtained with a quadrupole operated in the fourth stability region and a resolution of several thousand can be obtained with ions of several keV energy. The transmission is somewhat lower than that of the second stability region for a given resolution, but not as low as acceptance calculations suggest. Attempts to obtain resolution higher than 13,900 by adding DC between the quadrupole rod pairs were unsuccessful.

This work was partly motivated by the possible use of the fourth region for ICP-MS. For resolutions of several thousand, the transmission is 2-10 times lower than that using the second region, but this resolution can be obtained with ion energies of 750 eV or more. Thus one potential use of this region is to obtain high resolution on high energy ion beams, with an attendant reduction of space charge problems. The low acceptance

will require brighter ion beams from the ICP source. Extracting such beams is an ongoing research project in this laboratory, and current densities at least 100 times greater than that of commercial ICP-MS systems have been obtained. [49] Thus new ion extraction methods might be combined with operation of a quadrupole in the fourth region to give a high resolution quadrupole ICP-MS system which also has reduced problems from space charge effects.

Chapter 4

A quadrupole mass filter operated in the sixth stability region

4.1 Introduction

The sixth stability region is located approximately between (a = 8, q = 6) and (a = 9, q = 7) and is shown on the general Mathieu stability diagram (Figure 1.3). It is a nonlinear narrow quadrangle as shown in Figure 4.1. The a, q values of the four tips are: M (6.9939, 8.9637), P (6.9952, 8.9634), R (6.3807, 7.9761), and S (6.3835, 7.9767). Mass resolution is expected to be obtained with operation at the upper tip (M tip) and at the lower tip (S tip). These two tips are shown in detail in Figure 4.2a and Figure 4.2b, respectively. At the upper tip, the resolution is increased by increasing the DC to RF voltage ratio, while at the lower tip, the resolution is increased by decreasing this ratio.

At the upper tip the fundamental angular frequency of ion motion Ω, is given by:[47]

$$\Omega_x = (3- \beta_x) \omega/2 \qquad (4.1)$$

$$\Omega_y = \beta_y \omega /2 \qquad (4.2)$$

and at the lower tip it is given by

$$\Omega_x = (\beta_x - 2)\omega/2 \qquad (4.3)$$

$$\Omega_y = (1 - \beta_y)\omega/2 \qquad (4.4)$$

where ω is the angular frequency of the quadrupole RF. The iso-β lines, determined by the *a, q* parameters, are shown in Figure 4.2a and 4.2b. For this stability region, β varies from 2 to 3 for x motion and from 0 to 1 for y motion. The value of β varies from 0 to 1 for x and y motion in the first stability region and from 2 to 3 for x and y motion in the fourth stability region. Therefore from an ion optical point of view, the sixth stability region is a mix of the first and fourth stability regions. For this region, there is no "aliasing" problem as described for the second[45, 46] and fourth stability[28] regions because the operating lines do not pass through other lower stability regions.

The peak shapes with a scan line which crosses the R tip of the stability region have been reported previously.[101] In this chapter, we have theoretically and experimentally explored the whole stability region by calculating the acceptance, the effect of the fringing field, and investigating resolution, transmission, required separation times and peak shapes.

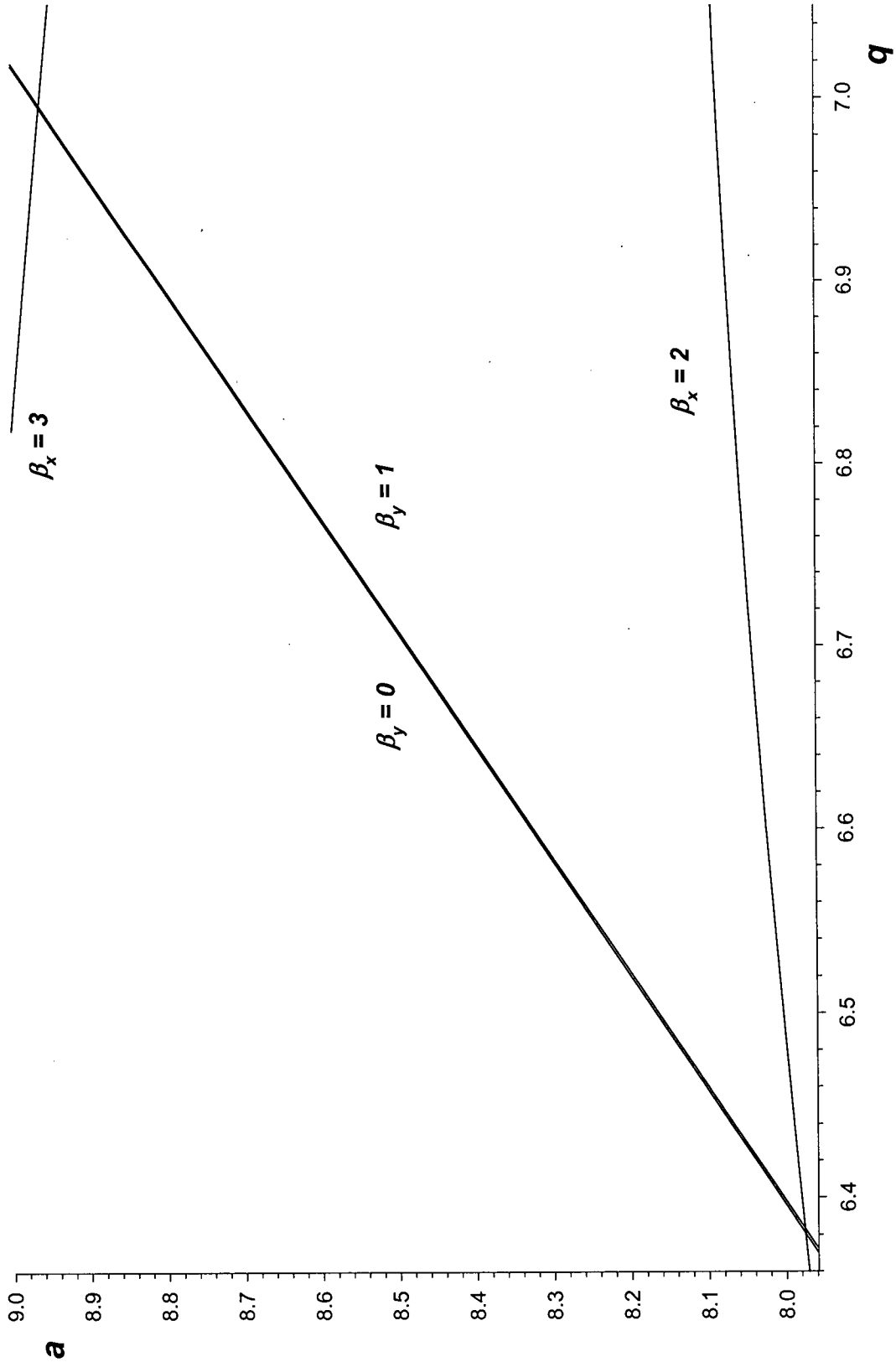

Figure 4.1 The stability diagram of region VI.

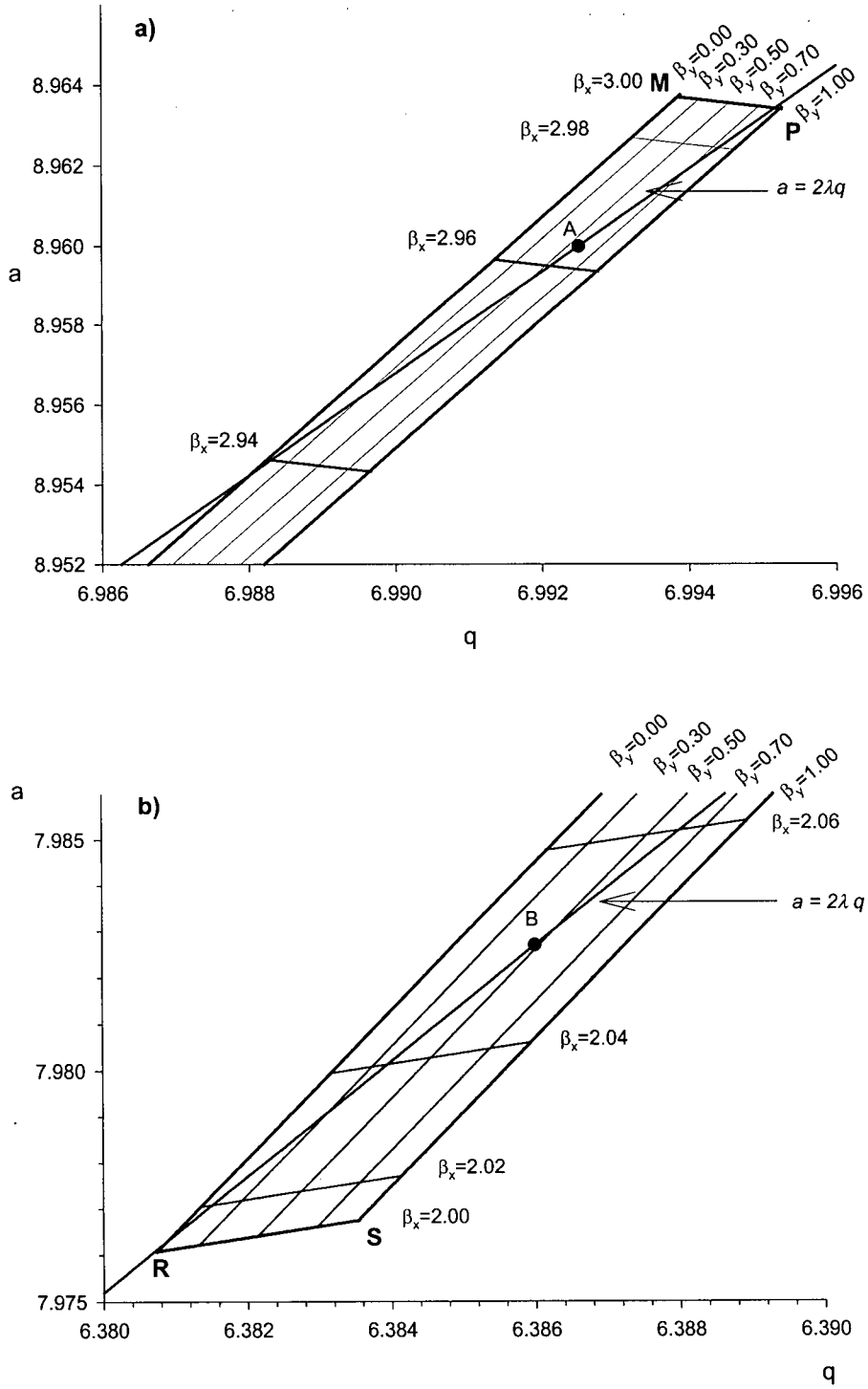

Figure 4.2 a) The upper tip, M, of stability region VI used in mass filter operation showing iso-β lines for the x and y directions and a typical operating line $a = 2\lambda q$, where $\lambda = U/V = 0.6407$. b) The lower tip, S, of region VI. $\lambda = 0.6250$.

4.2 Experimental Methods

The experimental arrangement is shown in Figure 2.1. The quadrupole power supply (model API III, SCIEX. Concord, Ontario) was run in the sixth region at a frequency of 0.768 MHz. The RF voltage of the power supply, 10,000 V (peak-peak, pole-ground), gave a maximum *m/z* of 255 at the upper tip and 279 at the lower tip. However, the maximum mass was limited by the DC voltage of the power supply to *m/z* = 63.6 at the upper tip and *m/z* = 71.5 at the lower tip. Thus the sixteen bit digital-to-analog converter (DAC) could give minimum step sizes of 0.00097 and 0.00109 *m/z* at the upper and lower tips, respectively. When a scan line moves across the stability region, the peak position, which corresponds to the q value of the intersection between the region boundaries, will shift along the *m/z* axis. For the work in this chapter, the mass calibration was set so that *m/z* 68 corresponds to a scan line across the middle of the sixth region.

The effects of the fringing field at the entrance of the quadrupole were investigated by varying either the ion energy or the distance between the rods and the entrance aperture plate. Figure 4.3 is a schematic of the apparatus used to change the distance between the rods and the entrance aperture plate. A heavy duty, micrometer driven, linear motion feedthrough (MDC Vacuum Products Corporation, Hayward, CA, USA, Model No: K100-BLM-2) was mounted at the front of the vacuum chamber. This feedthrough allows linear displacement of the ion source. The ion source was supported by a cylindrical Pyrex tube with the same inner diameter as the outer diameter of the quadrupole case. Since the second aperture lens L2 was mounted on the ion source, the

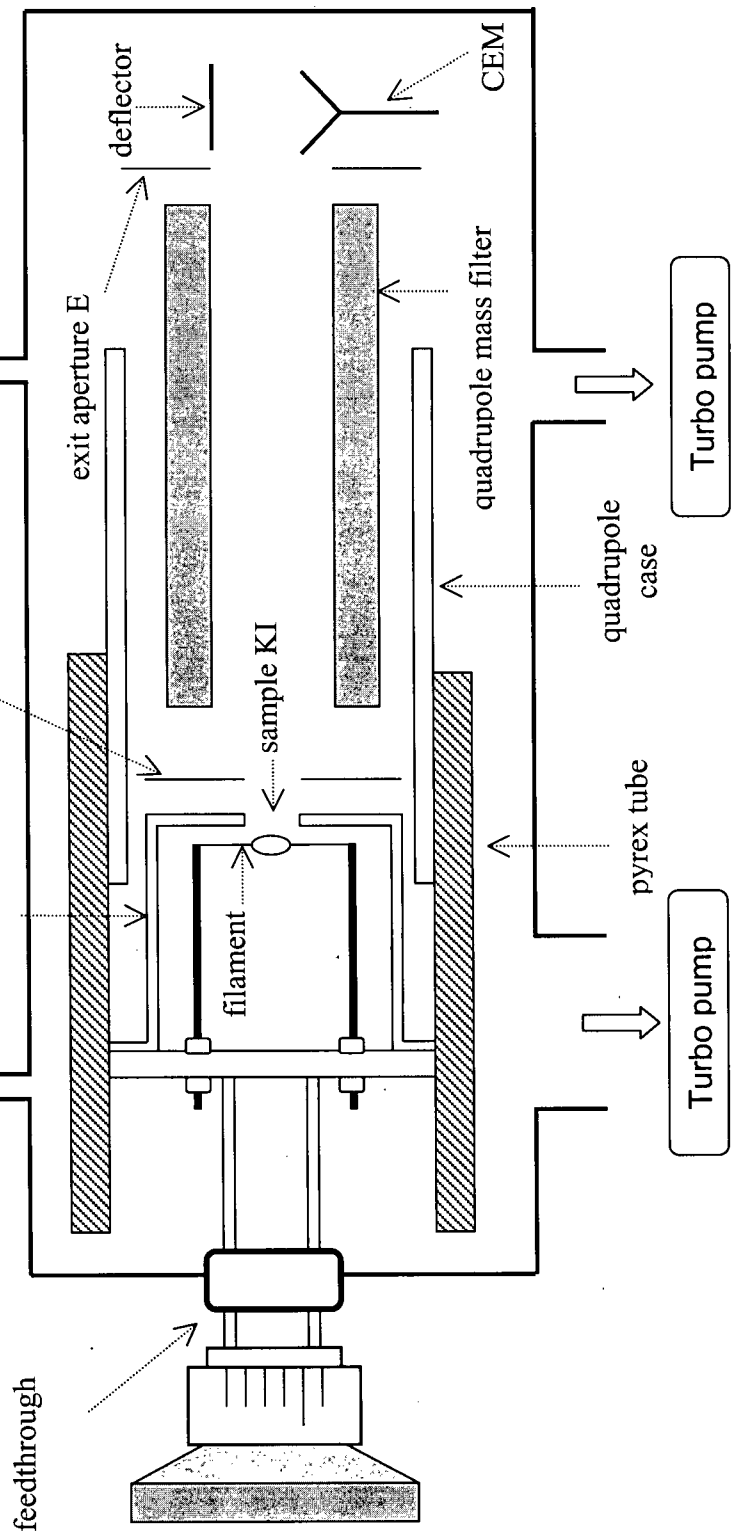

Figure 4.3 Schematic of the thermal ionization quadrupole mass spectrometer as used for fringing field measurements. IG represents the ionization gauge; dotted arrows represent the names of corresponding parts; hollow arrows, gas flow.

distance between L2 and the quadrupole rod set could be varied.

To record the relative transmission of the quadrupole in the second and sixth regions, the quadrupole was scanned by the software (Tune 2.02, SCIEX, Concord, Ontario) with different resolution settings. For the sixth region, the resolution parameter was set to a resolution corresponding to a scan line across the middle of the region. For the second region, the resolution parameter in the software was set to 0. This gives an "RF – only" mode, and the scan line passes through the base of the second region on the $a = 0$ axis. Since the q values of the second region and the sixth region are very close, the mass calibration was not changed.

4.3 Results and Discussion

4.3.1 Acceptance and Fringing Field Calculations

As described in Chapter 3, the acceptance determines a quadrupole's transmission and the fringing fields are important in determining the quadrupole acceptance. With the exception of the first stability region, fringing fields generally decrease the acceptance. (In the first stability region, there is an optimum fringing field residence time of about two RF cycles) [28, 50, 57, 102]. Here the phase space dynamics method (Experimental Section) was used to calculate the acceptance and the effect of fringing fields on the acceptance at the upper tip and lower tip of region VI. In this method we assume the quadrupole field is infinitely long and ideal. The fringing field model of McIntosh and Hunter[65] was used.

For region VI, only short fringing field residence times are expected since ions can be relatively energetic and have to spend few cycles in the main field. As shown later in this chapter, under our experimental conditions, 20 eV is approximately the minimum ion energy required for ion transmission through the quadrupole operated in the sixth region. For a distance between the rods and aperture plate of 2 mm, a $^{39}K^{+}$ ion of 20 eV energy will spend about 0.7 RF cycles in the fringing field before it enters the main quadrupole field. Therefore the following calculations only include the effects of the fringing field within one RF cycle. Figure 4.4(a, b, c) and Figure 4.5(a, b, c) illustrate the calculated changes to the quadrupole acceptance caused by the input fringing fields for the x and y motion, respectively. The operating point for these calculations is a = 8.960, q = 6.9925, at the upper tip of the sixth region. The acceptance contours for a transmission level of 25% for the x direction for different numbers of cycles that the ions spend in the fringing field, n_f, are shown in Figure 4.4(a). Similar data for 50% and 75% transmission levels are given in Figure 4.4(b, c). The acceptances for y motion with transmission levels of 25%, 50% and 75% are given in Figure 4.5(a, b, c).

From Figure 4.4 and Figure 4.5 it is seen that, for short fringing fields, the acceptance ellipses are approximately parallel to the u axis. A parallel ion beam is required to match this. For the longer fringing fields, the ellipses for both the x and y directions are off the u axis to some extent. To match this, a slightly focused beam is required. The acceptance contours for x and y motion for the operating point a = 7.9827, q = 6.386 at the lower tip of the region are shown in Figures 4.6 and 4.7, respectively. The characteristics are similar to those at the upper tip. The only difference is that for the longer fringing field, the acceptance ellipses for both x and y motion are further off the u

axis compared to those at the upper tip. Operating a quadrupole mass filter at the lower tip requires a more strongly focused ion beam to match the acceptance.

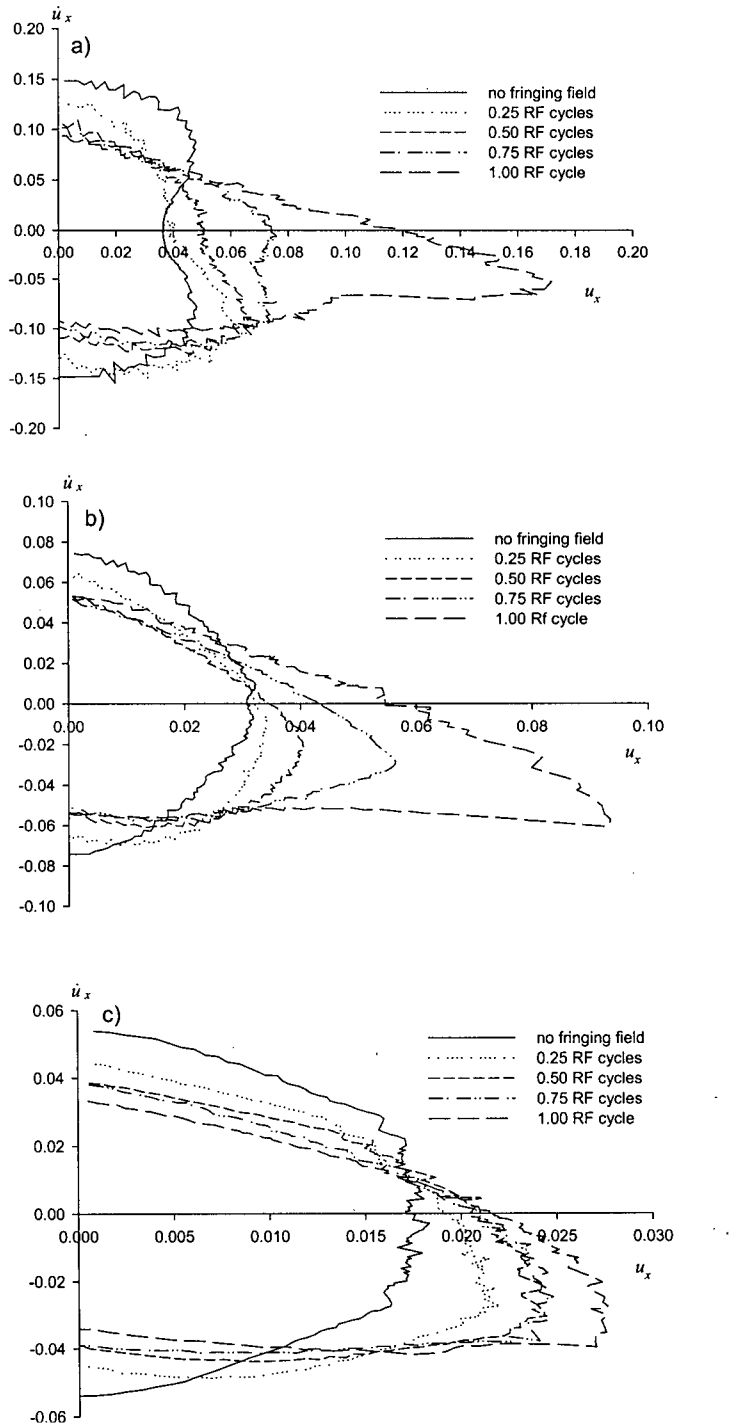

Figure 4.4 Acceptance contours for x motion at the operation point a = 8.9600, q = 6.9925: a) 25%, b) 50% and c) 75% transmission level, for values of n_f = 0.00, 0.25, 0.50, 0.75 and 1.00.

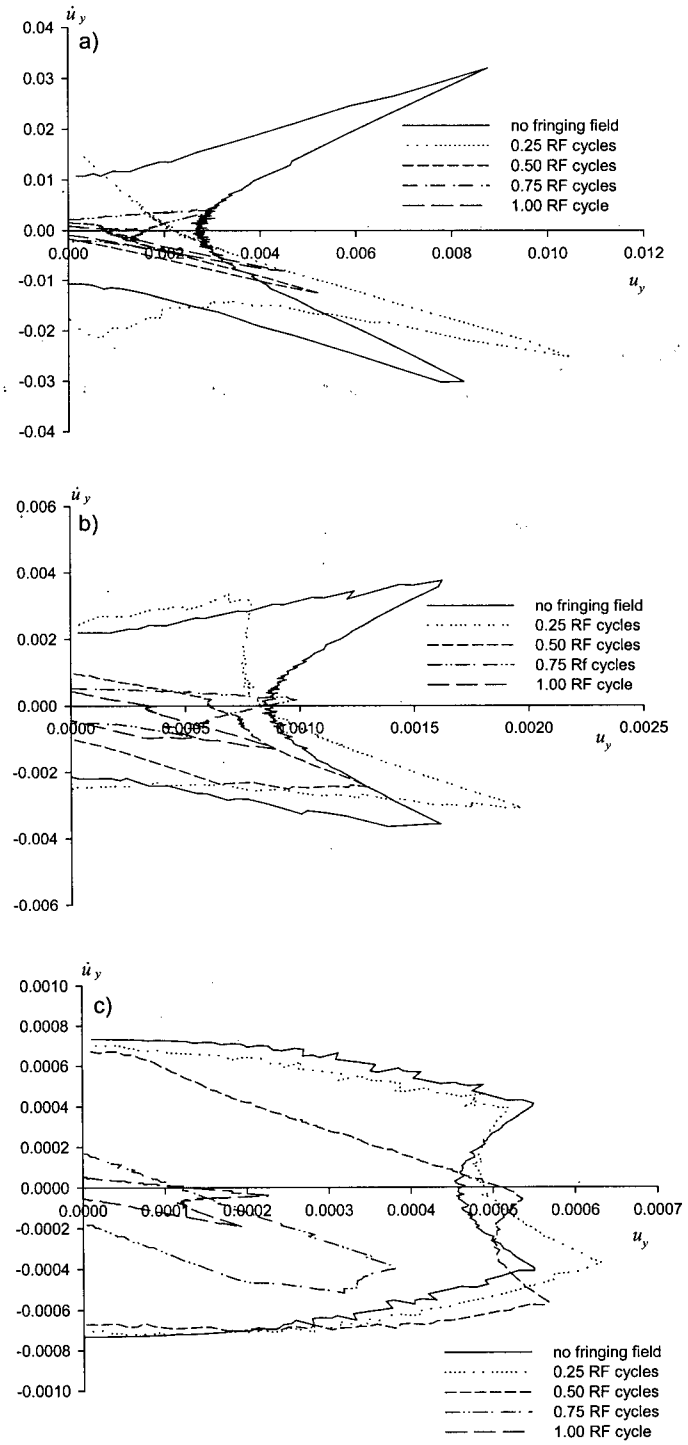

Figure 4.5 Acceptance contours for y motion at the operation point a = 8.9600, q = 6.9925: a) 25%, b) 50% and c) 75% transmission level, for values of n_f = 0.00, 0.25, 0.50, 0.75 and 1.00.

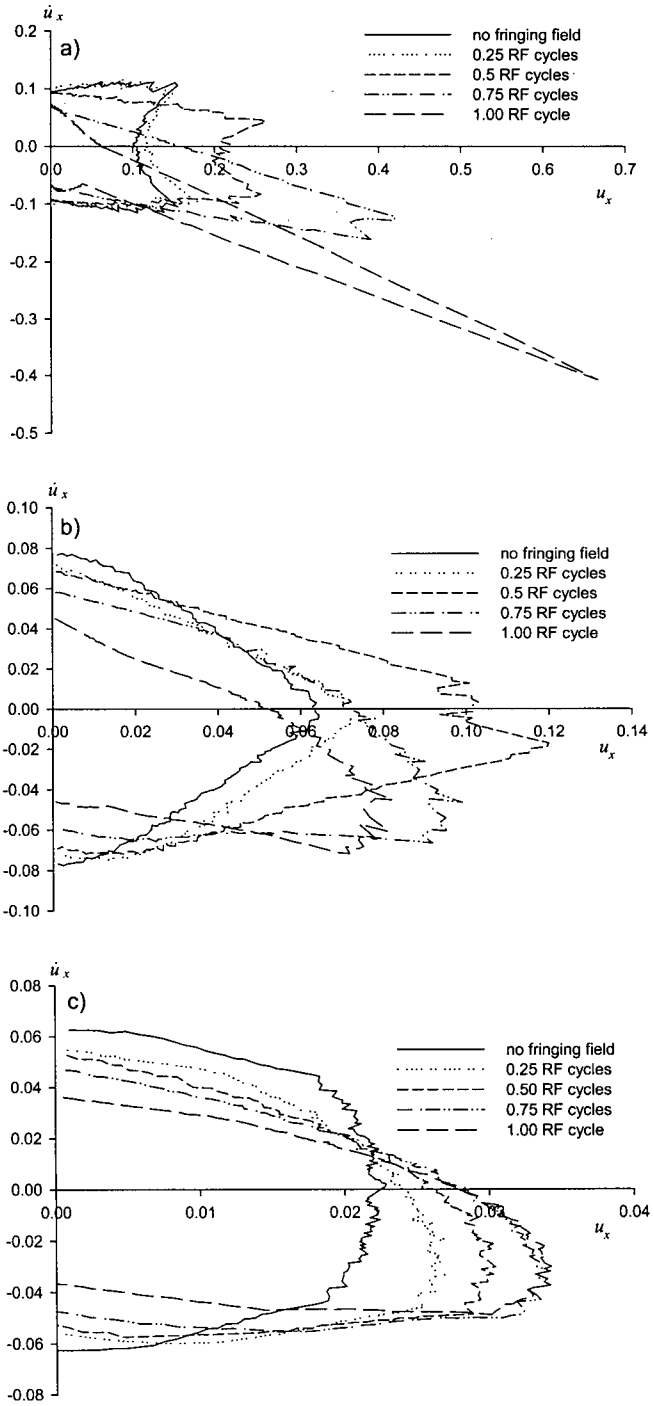

Figure 4.6 Acceptance contours for x motion at the operation point a = 7.9827, q = 3.3860: a) 25%, b) 50% and c) 75% transmission level, for values of n_f = 0.00, 0.25, 0.50, 0.75 and 1.00.

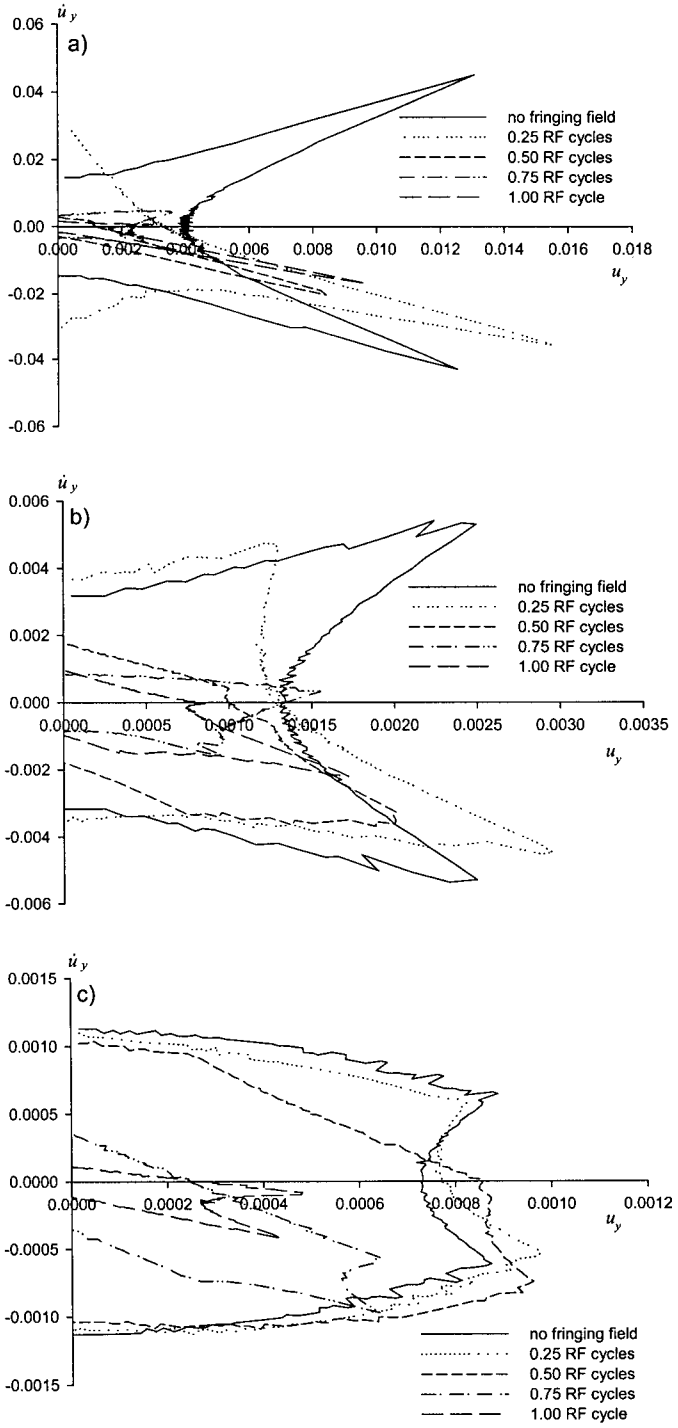

Figure 4.7 Acceptance contours for y motion at the operation point a = 7.9827, q = 3.3860: a) 25%, b)50% and c)75% transmission level, for values of n_f = 0.00, 0.25, 0.50, 0.75 and 1.00.

Figure 4.8(a,b,c) shows the dependence of the area of the acceptance ellipses at the upper tip (Figure 4.4) on the number of cycles, n_f, that the ions spend in the fringing field for different transmission levels. Figures 4.8a and b are the acceptance, in units of $\pi r_0^2 f$, for the x and y directions, respectively. Figure 4.8c is the combined acceptance for these two directions, in units of $\pi^2 r_0^4 f^2$. For the 25% and 50% transmission levels, the acceptance for the x direction has no change in the first half cycle and increases about 20% from 0.50 to 1.00 RF cycles. The acceptance in the x direction for the 75% transmission level has almost no change. The acceptance for the y direction has almost no change up to about n_f =0.4, then starts to decrease. For transmission levels of 25% and 50%, there is a small increase between n_f = 0.6 and n_f = 0.8. In comparison with the acceptance in the x direction, the acceptance in the y direction is about two orders of magnitude less and decreases more rapidly with n_f than that for the x direction. Therefore, the combined acceptance for both directions begins to decrease at n_f =0.4. For the quadrupole used here, n_f < 0.4 requires a $^{39}K^+$ ion energy of 80 eV or more. For comparison, the acceptances begin to decrease at n_f = 0.7 (26 eV $^{39}K^+$ ion energy) with operation in the second region and at n_f = 0.3 (144 eV $^{39}K^+$ ion energy) with operation in the fourth region. Figure 4.9 (a, b, c) gives the variation of the area of acceptance with n_f for operation at the lower tip of region VI. The combined acceptance at the lower tip is about 2 or 3 times larger than that at the upper tip.

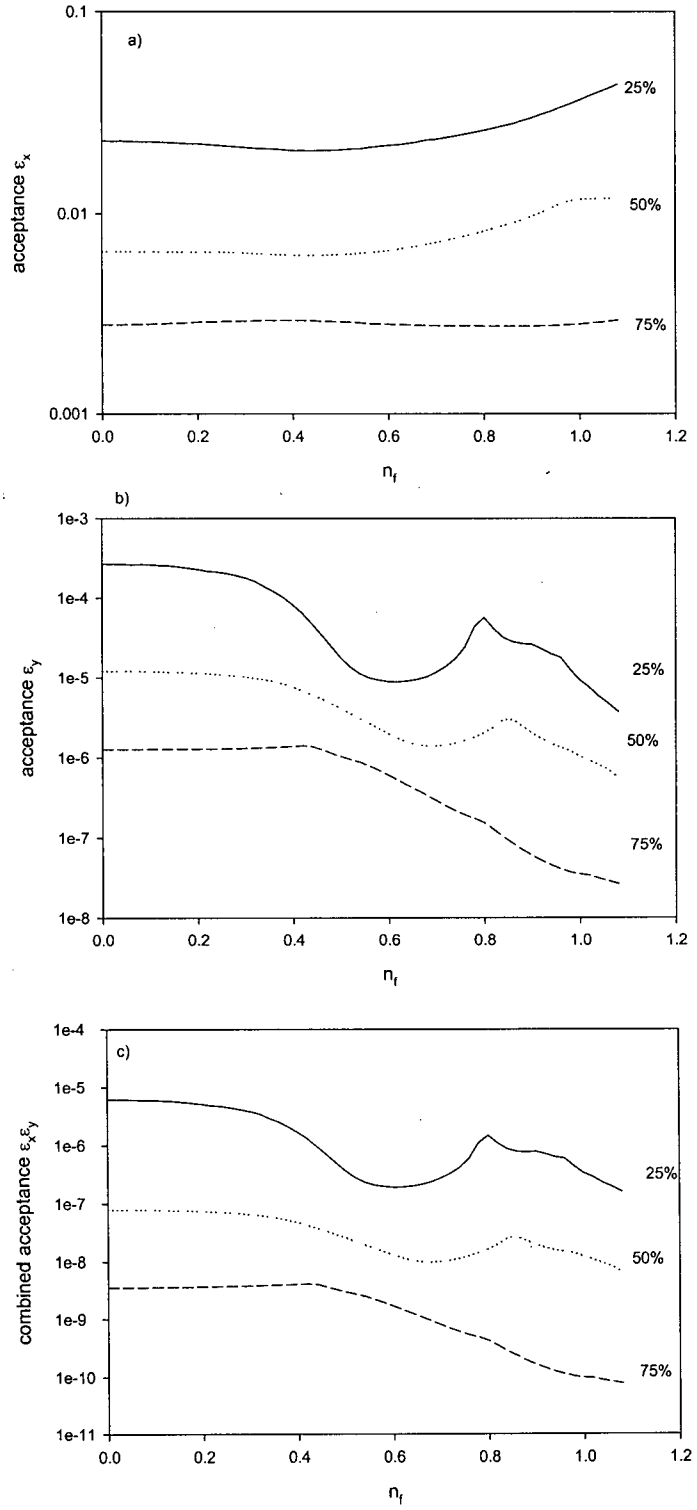

Figure 4.8 Acceptance of a quadrupole mass filter with different number of RF cycles in the fringing field, n_f, for a = 8.960, q = 6.9925 at the upper tip of region VI. a) the acceptance for x motion, b) the acceptance for y motion and c) the combined acceptance.

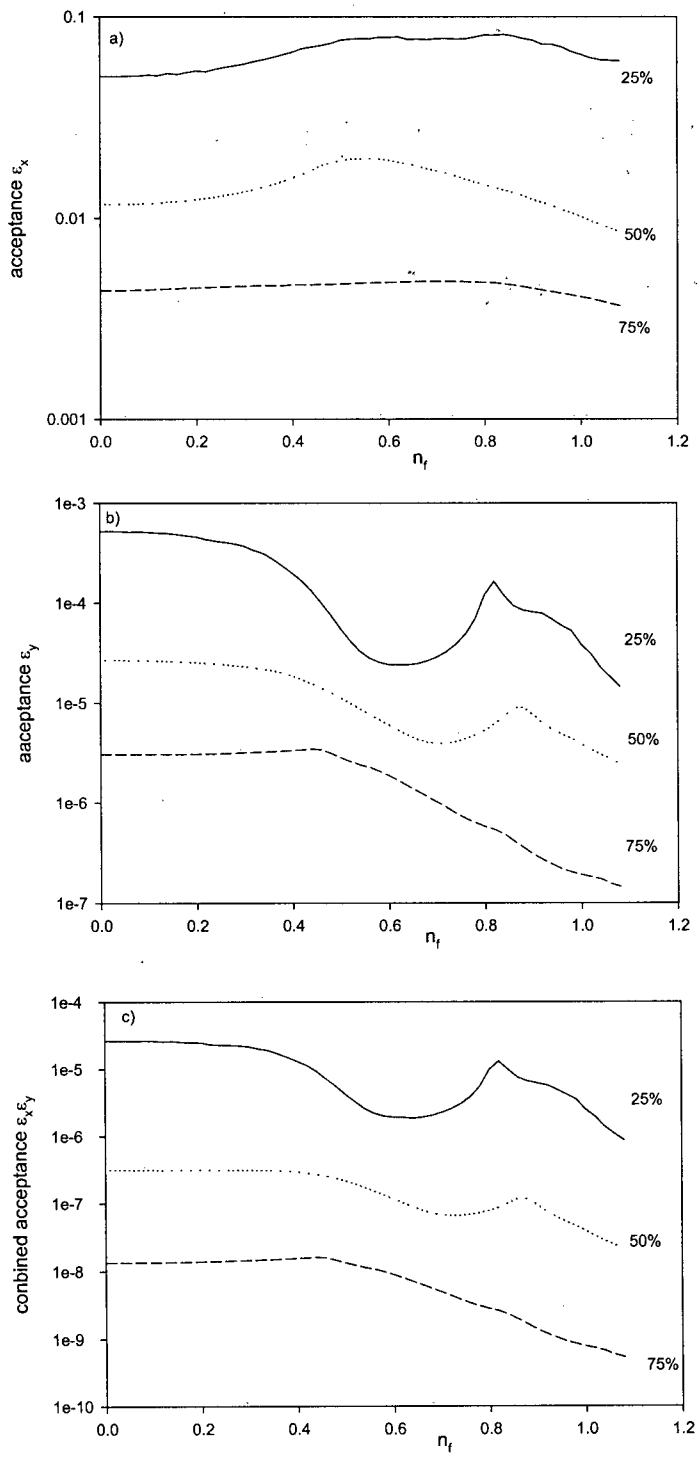

Figure 4.9 Acceptance of a quadrupole mass filter with different number of RF cycles in the fringing field, n_f, for a = 7.9827, q = 6.3860 at the lower tip of region VI. a) the acceptance for x motion, b) the acceptance for y motion and c) the combined acceptance.

4.3.2 Resolution and Ion energies

The peak shape with a scan line across the middle of the region is shown in Figure 4.10. A resolution at half-height of 1,510 is obtained with 20 eV $^{39}K^+$. The width of the peak base is 0.060 *m/z* units, which corresponds to a resolution at the base of 675. This is close to the theoretical resolution, 710, for a scan line which goes through the middle of the region.

With operation at the upper tip, the highest resolution at half-height that was obtained was about 2,000 with 20 eV $^{39}K^+$ ions. The peak shape is shown in Figure 4.11. With the operation at the lower tip, the highest resolution was about 1,110 with 20 eV $^{39}K^+$ ions. The peak shape is shown in Figure 4.12.

Compared with peak shapes obtained with operation in the first and third stability regions, the peak shapes in the sixth region are more symmetric. The peak shape for high energy ions is quite smooth (Figure 4.13), i.e. there are few ion collection effects on the peak shape. Collection effects could be observed easily with high energy ions with operation in the second and third stability regions.[24, 27]

The resolution at half-height was measured for ion energies up to 3000 eV with different scan lines. The resolution ($R_{1/2}$) plotted against the square of the number of cycles the ions spend in the quadrupole field (n^2), for $^{39}K^+$ with scan lines at the upper tip, the middle and the lower tip of the region, are shown in Figures 4.14 a, b and c, respectively. The solid lines are linear fits between $n = 0$ and $n = 10$ passing through the origin and give $R_{1/2} = 55\ n^2$, $R_{1/2} = 39\ n^2$, and $R_{1/2} = 43\ n^2$ for the upper, middle and lower parts of the region, respectively. Extrapolation of the resolution to high energies (low n_f)

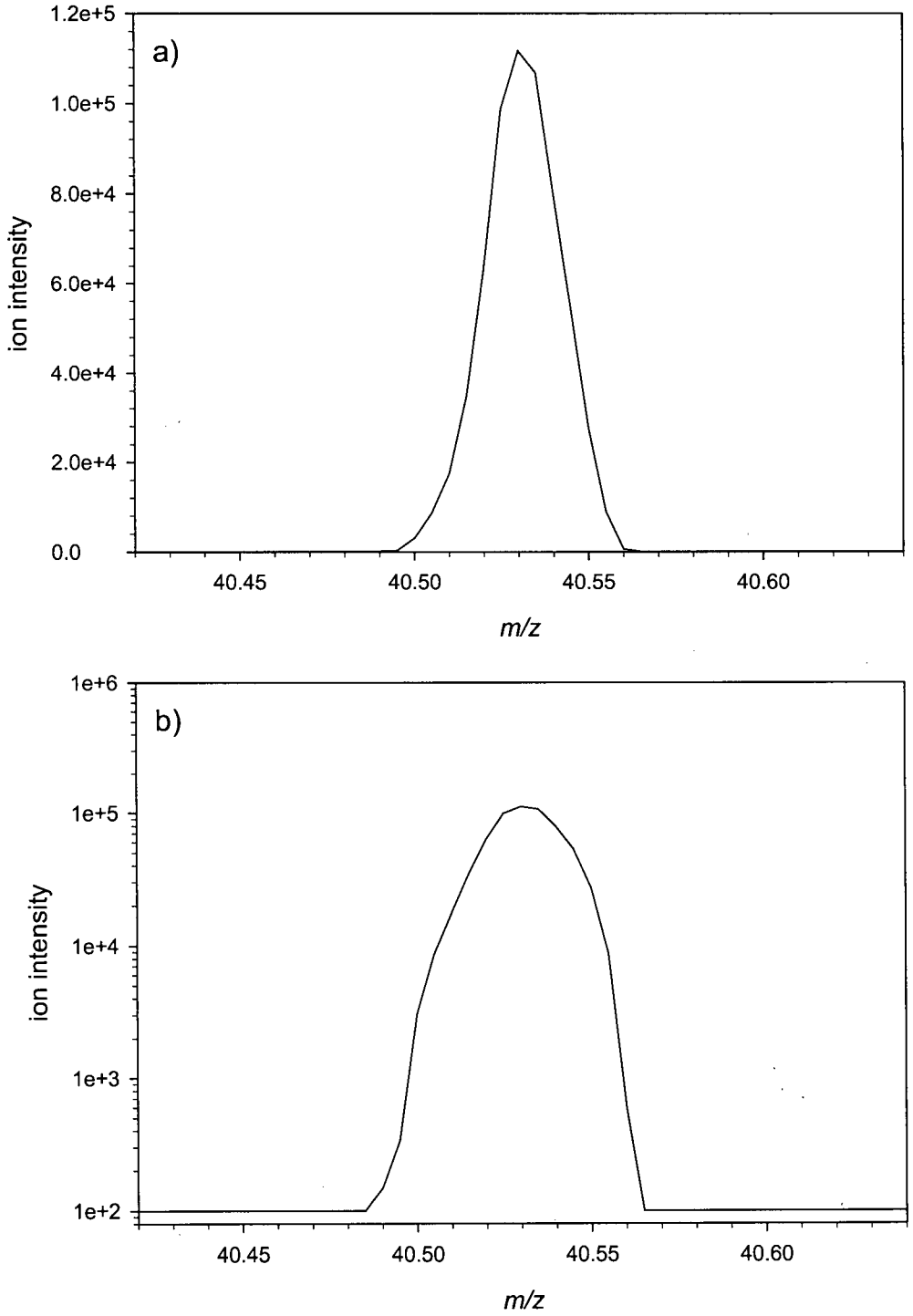

Figure 4.10 Peak shape of 20 eV $^{39}K^{+}$ ions with a scan line across the middle of region VI. a) on a linear scale and b) on a logarithmic scale.

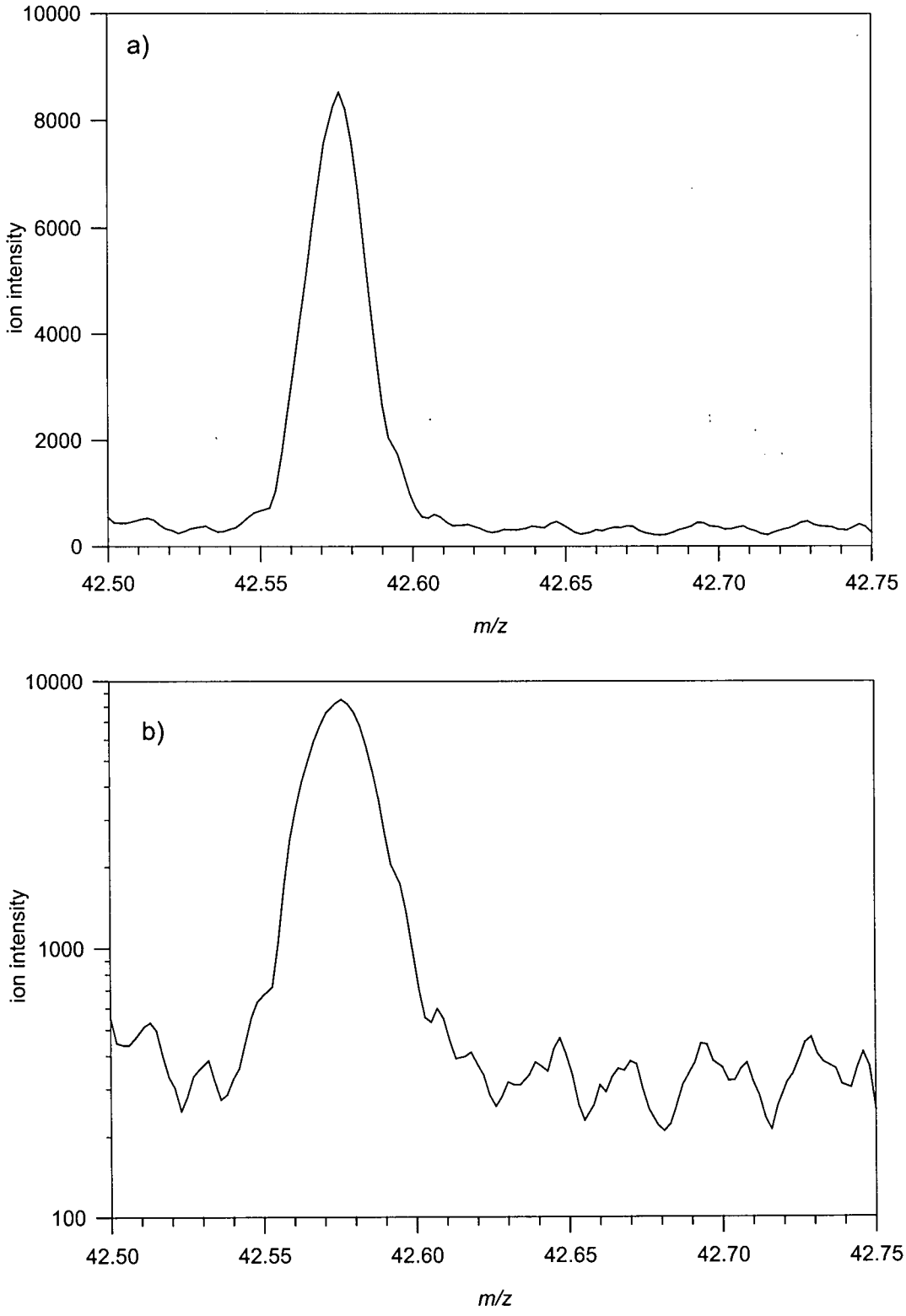

Figure 4.11 Peak shape at upper tip of region VI with 20 eV $^{39}K^{+}$ ions. a) on a linear scale and b) on a logarithmic scale.

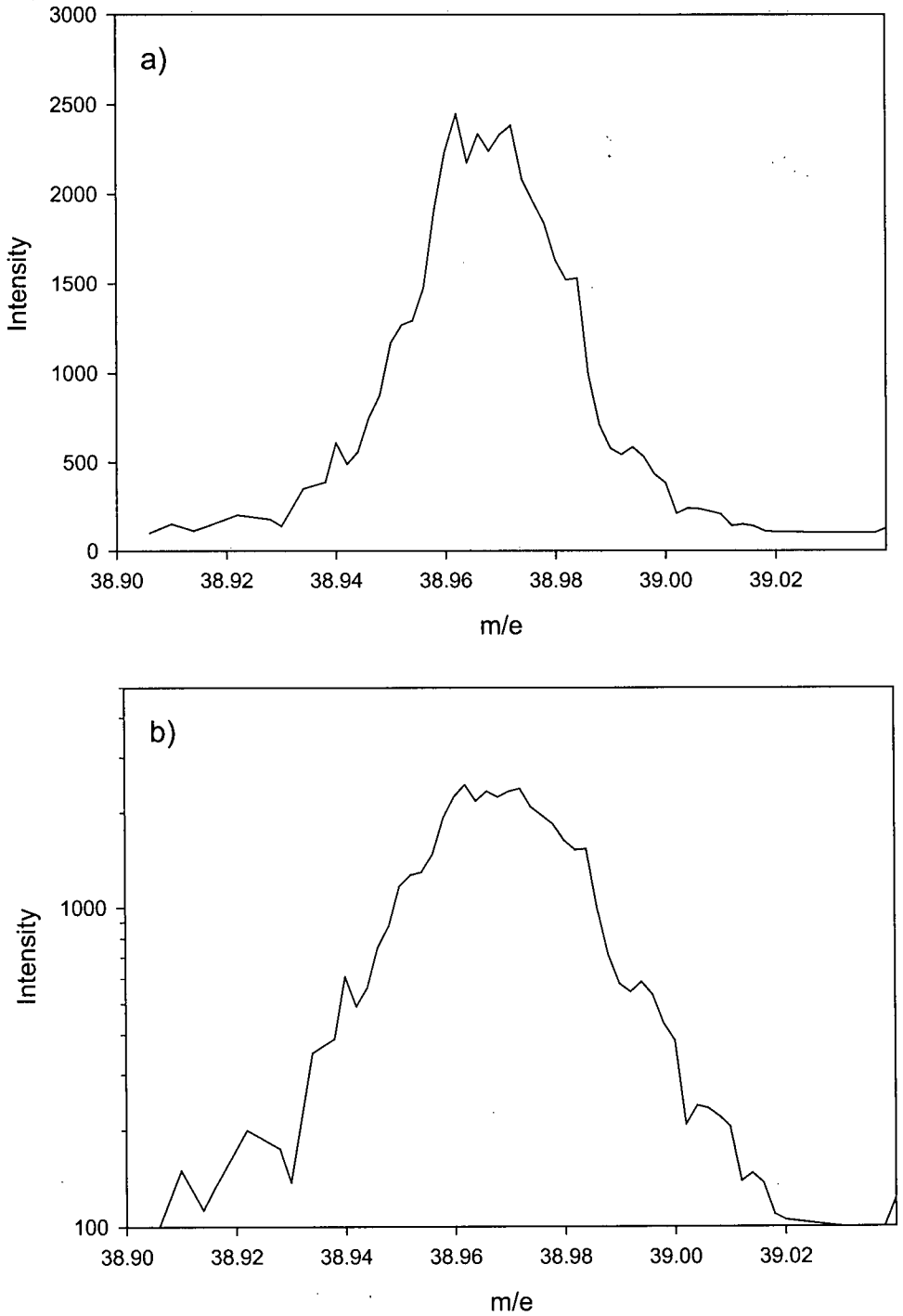

Figure 4.12 The peak shape at lower tip of the sixth stability region with 20 eV $^{39}K^{+}$. a) on a linear scale and b) on a logarithmic scale.

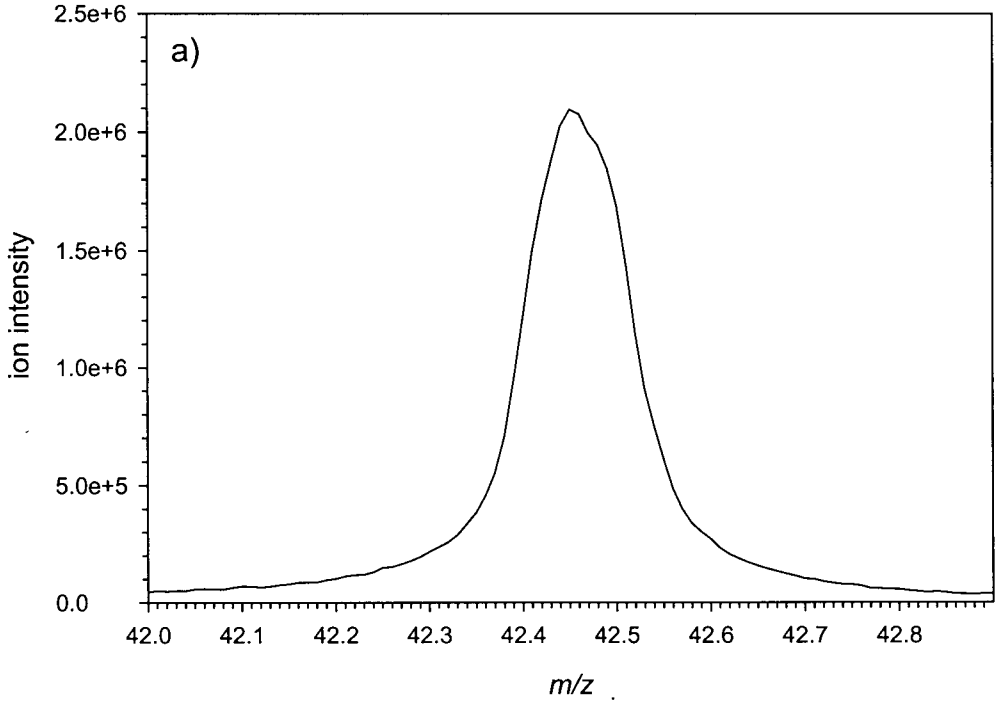
a)
2.5e+6
2.0e+6
1.5e+6
1.0e+6
5.0e+5
0.0
ion intensity
42.0
42.1
42.2
42.3
42.4
42.5
42.6
42.7
42.8
m/z

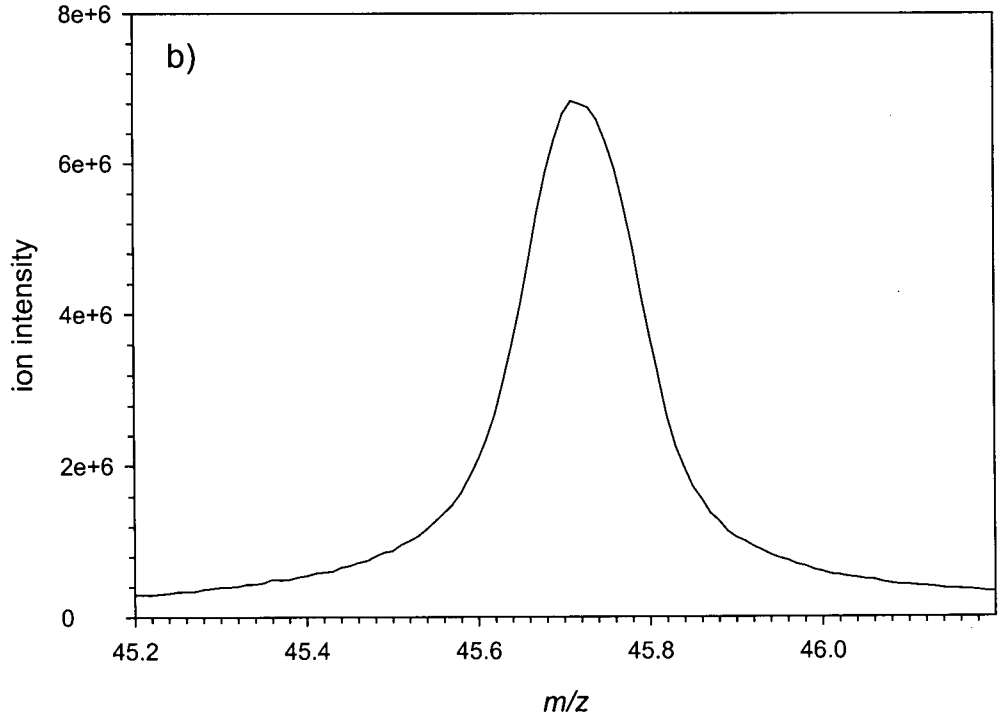
b)
8e+6
6e+6
4e+6
2e+6
0
ion intensity
45.2
45.4
45.6
45.8
46.0
m/z

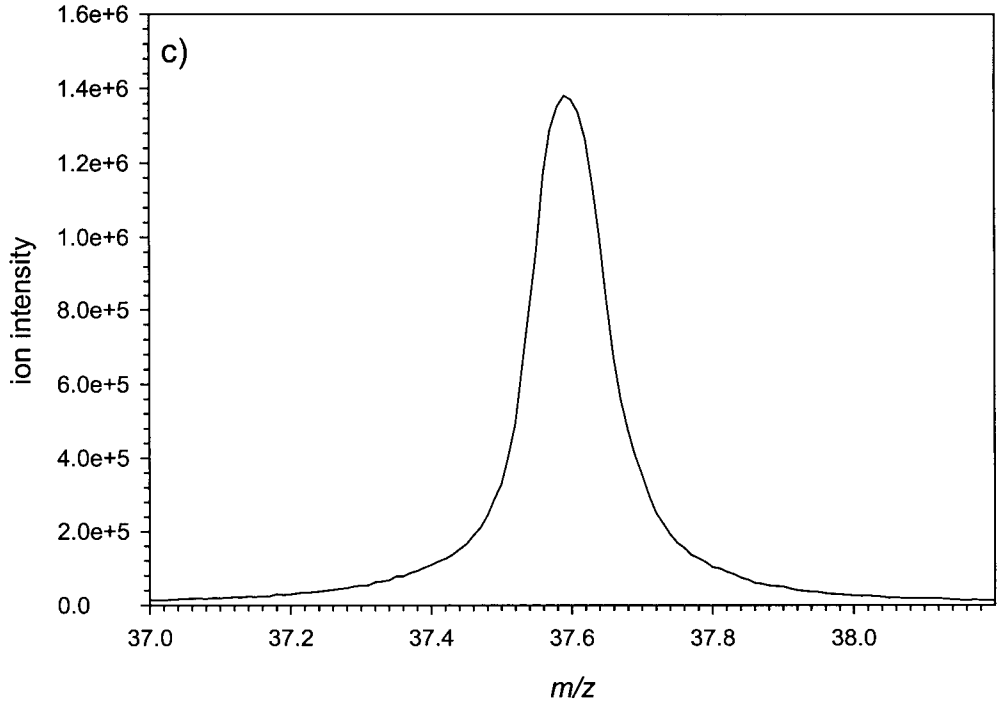

Figure 4.13 Peak shape of 1000 eV $^{39}K^{+}$ ions at a) the upper tip, b) the middle region and c) the lower tip of the sixth stability region.

shows that unit resolution should be possible with $^{39}K^{+}$ ion energies of 3,400 eV, 2,400 eV and 2,600 eV with operation at the upper tip, the middle and the lower tip of the sixth stability region, respectively.

Another interesting observation is that when a quadrupole is operated in this region and the ion injection energy is sufficiently high, peaks can be obtained with operation below the lower tip or above the upper tip of the region. This is discussed in Chapter 5.

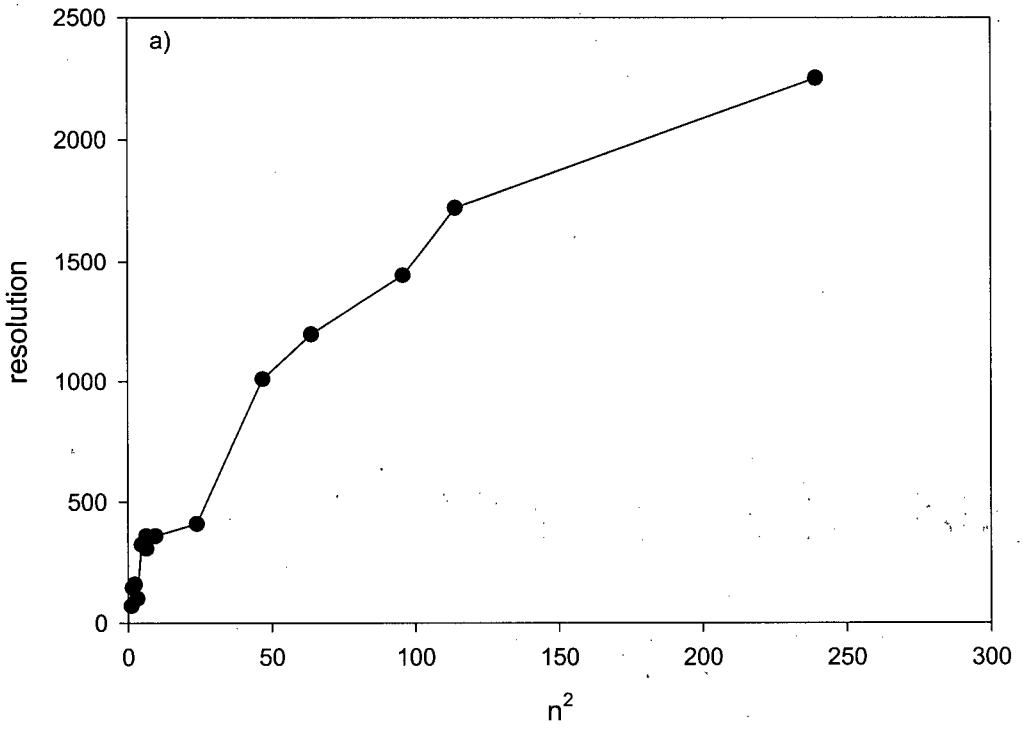
a)
resolution
2500
2000
1500
1000
500
0
0
50
100
150
200
250
300
n2

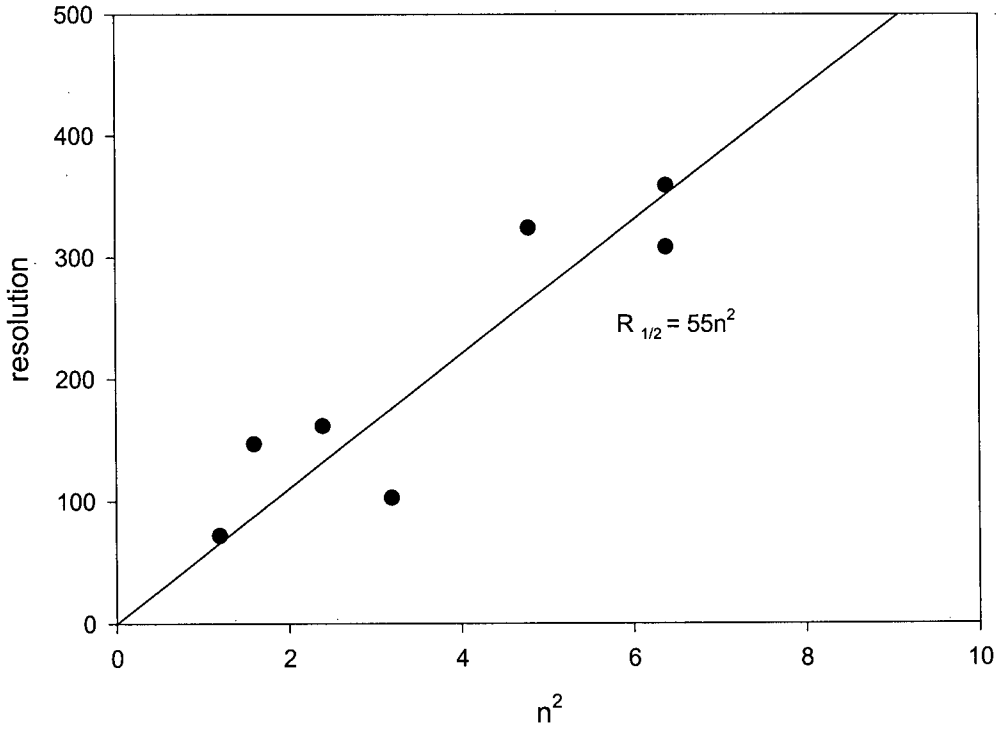
resolution
500
400
300
200
100
0
0
2
4
6
8
10
n2
R 1/2 = 55n2

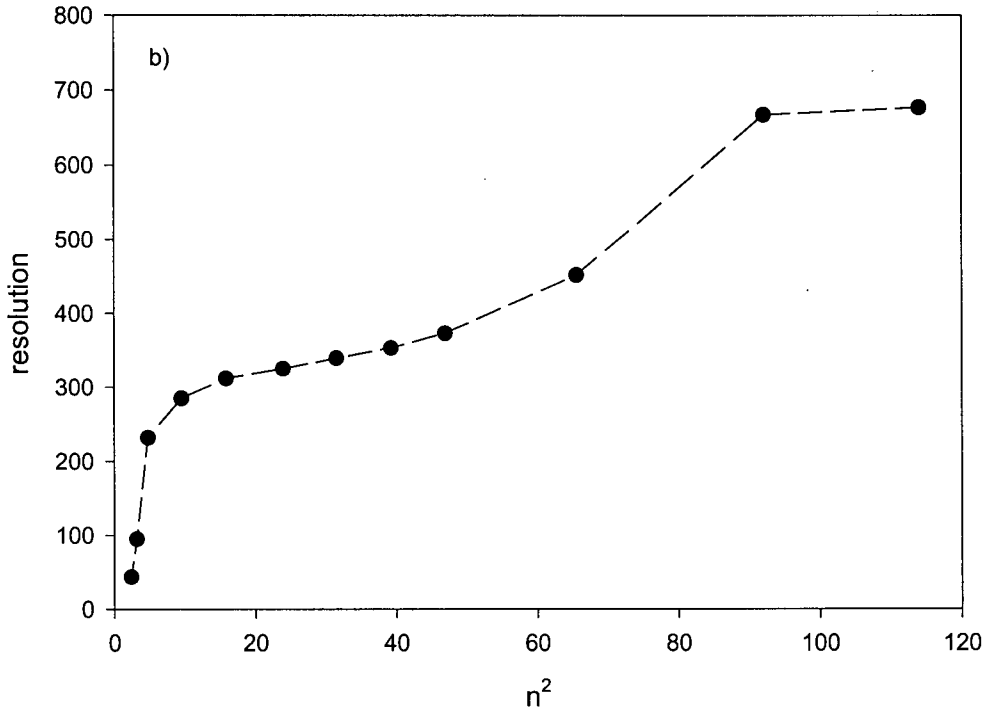
b)
resolution
n2
0
100
200
300
400
500
600
700
800
0
20
40
60
80
100
120

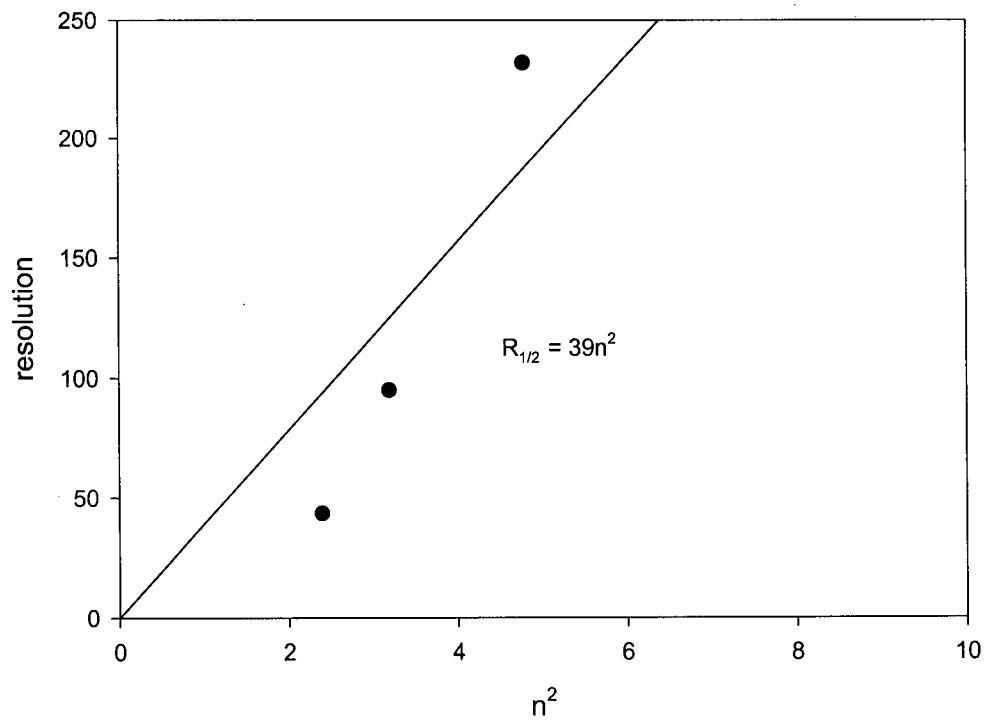
resolution
n2
R1/2 = 39n2
0
50
100
150
200
250
0
2
4
6
8
10

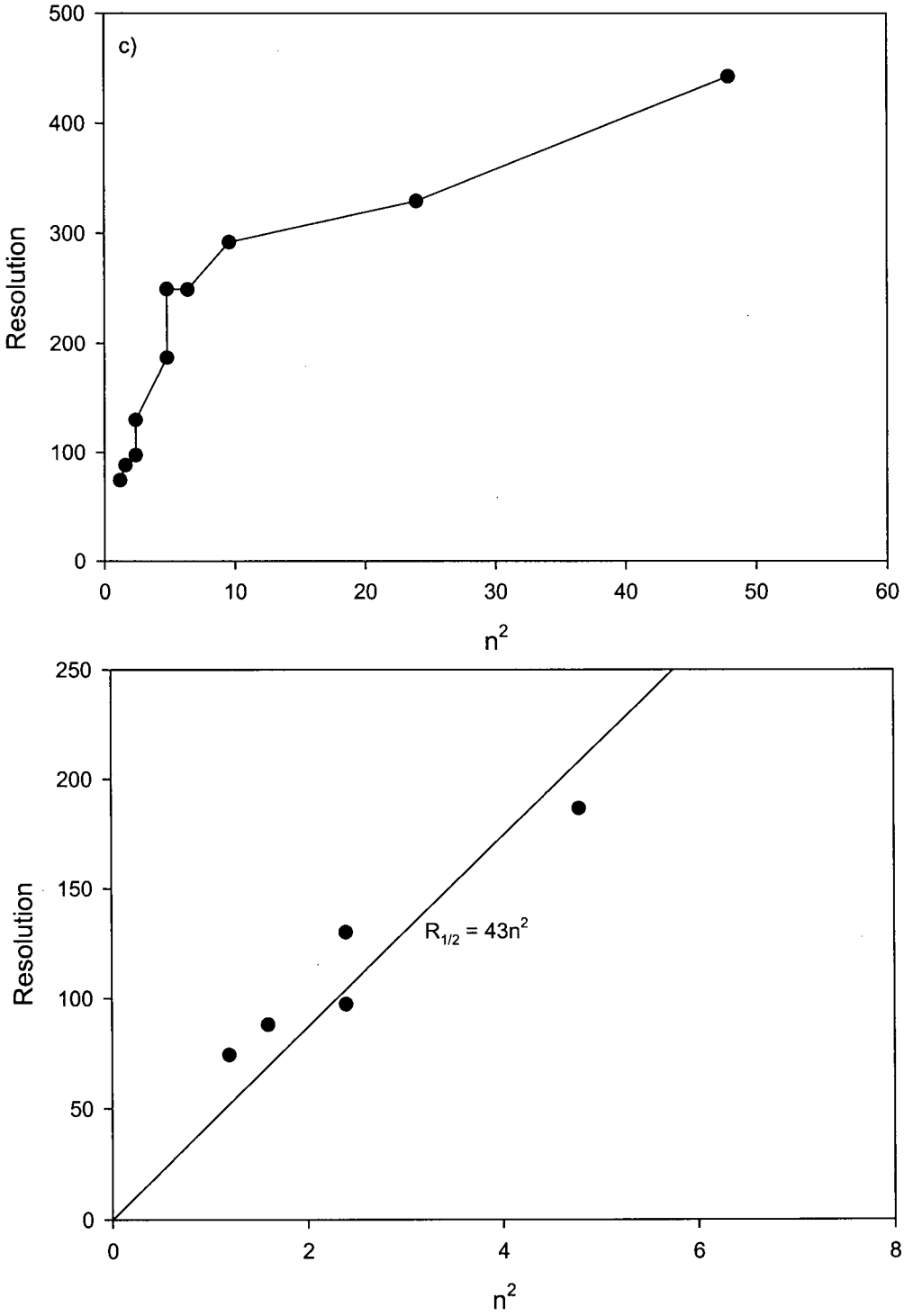

Figure 4.14 The measured resolution at half height $R_{1/2}$ for $^{39}K^+$ versus the square of the number of RF cycles the ions spend in the quadrupole field (n^2) for operation at a) the upper tip (M), b) the middle area and c) the lower tip (S) of the sixth region. The solid lines are linear fits to the same data for $n^2 < 10$.

4.3.3 Transmission and Resolution

The variation of sensitivity of the system with resolution for $^{39}K^{+}$ ions with energies between 20 eV and 3000 eV has been studied and is shown in Figure 4.15. The solid lines indicate the measurements that were done with a scan line that crosses the stability region, and the dashed lines correspond to the measurements with a scan line outside the stability region. At the upper tip, increasing the DC/RF ratio causes the resolution to increase and the sensitivity to decrease. T-R (transmission versus resolution) curves with ion energies from 20 eV to 3000 eV are shown in Figure 4.15a. The resolution can be up to 2000 for 20 eV ions and up to 200 for 3000 eV ions. For high-energy ions (>1000 eV), the transmission decreases very slowly, covering less than one order of magnitude, as the resolution increases, probably because when ion energies are large enough, the ions can pass through the quadrupole even though they are outside the calculated acceptance. For the low energy ions, the quadrupole acceptance becomes limiting and the transmission decreases. A limiting resolution is reached which partly depends on the ion energies. For the ions of intermediate energy, at low resolution, the behavior is similar to high energy ions. At higher resolution, the behavior is similar to low energy ions. These observations may indicate that the upper tip of this region could be used as an independent mass analyzer for low-energy ions, or as a pre- (or post-) mass filter to eliminate alias ions when a quadrupole is operated in region II or region IV.

The transmission versus resolution curves for operation at the lower tip of region VI are shown in Figure 4.15b. At the lower tip of region VI, decreasing the DC/RF ratio causes the sensitivity to drop sharply with little increase of resolution for low energy ions. For higher energy ions, moving the scan line towards the lower tip

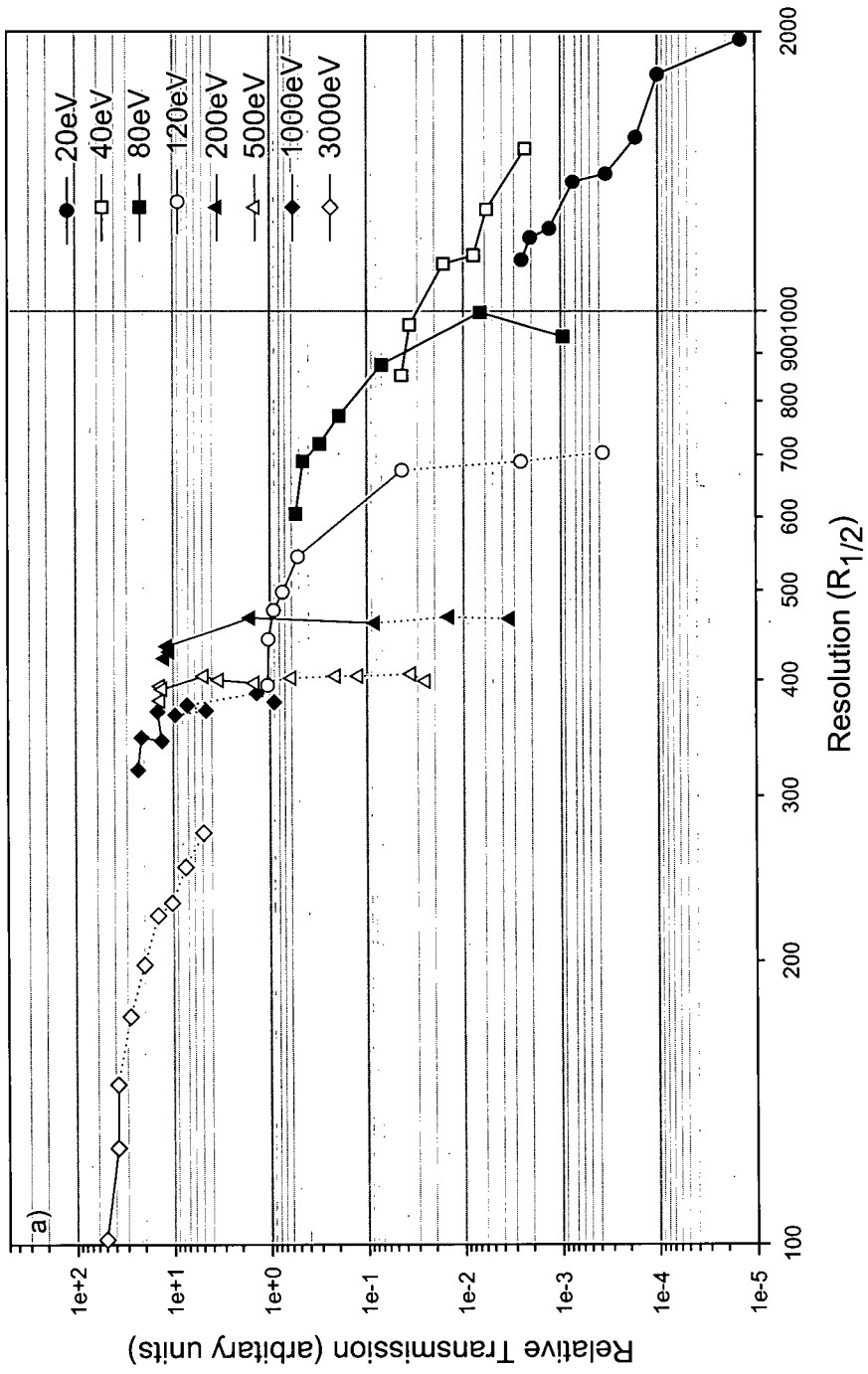
a)
20eV
40eV
80eV
120eV
200eV
500eV
1000eV
3000eV
Relative Transmission (arbitary units)
1e+2
1e+1
1e+0
1e-1
1e-2
1e-3
1e-4
1e-5
100
200
300
400
500
600
700
800
900
1000
2000
Resolution ($R_{1/2}$)

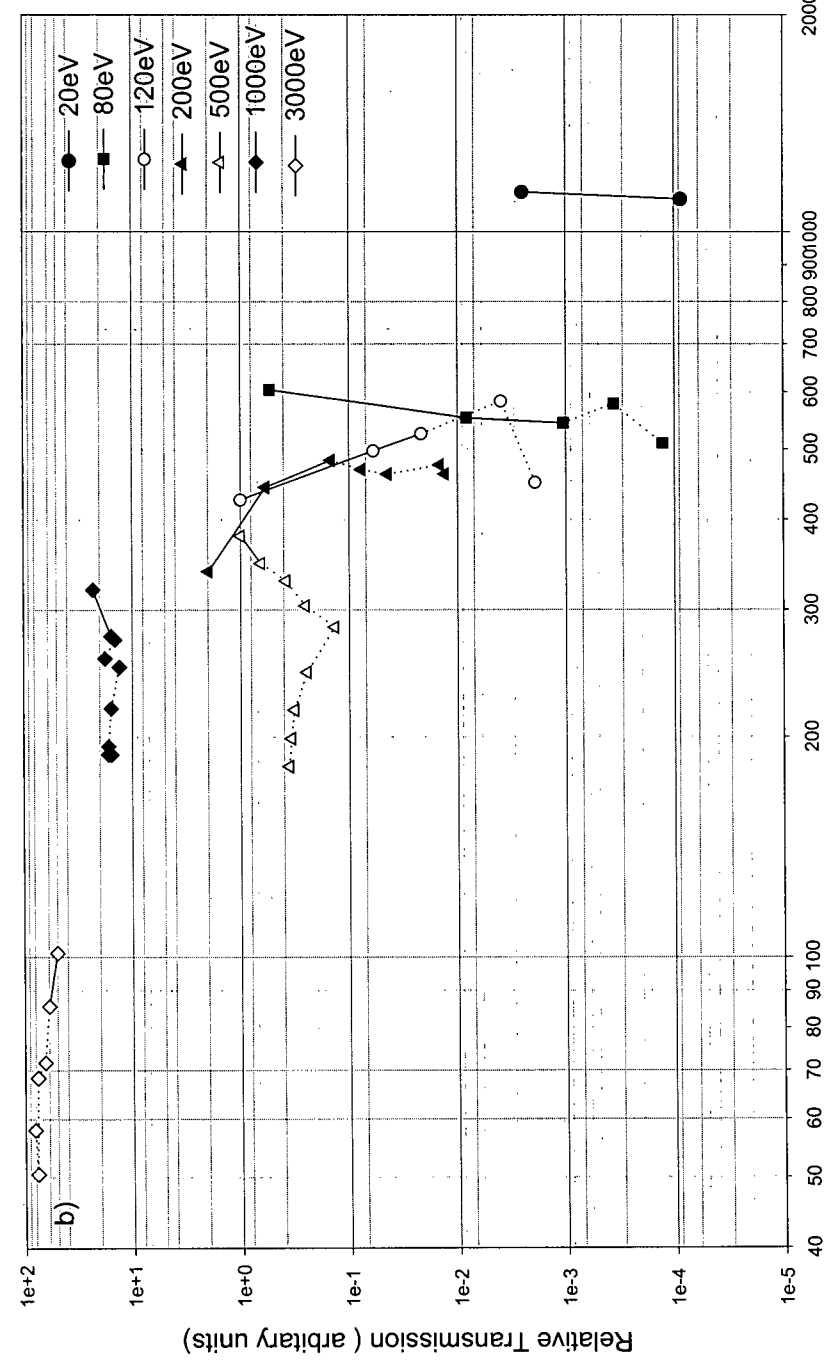

Figure 4.15 Relative transmission versus resolution ($R_{1/2}$) for $^{39}K^+$ ions of various axial energies as indicated by each legend for operation at a) the upper tip and b) the lower tip of region VI. The dashed lines represent measurements with operation outside the sixth region.

produces almost no change in the peak width and ion intensity, but moves the peak towards lower mass settings. The resolution decreases slowly as the DC/RF ratio decreases. This is probably because the resolution is dominated by the ion separation time in the y direction only. (This is discussed in Chapter 5.)

4.3.4 Influence of fringing fields on ion transmission

Since the calculated fringing field effect is for an idealized model, it can only serve as a rough estimate of the effects on ion transmission. The influence of the fringing fields on ion transmission was investigated experimentally as described in the section 4.2. The variation of effective fringing field length, Z_f, with the rod to entrance plate separation, was previously investigated by McIntosh and Hunter.[65] The measured distance between the quadrupole rods and the entrance aperture plate was converted to the corresponding fringing field length, Z_f , in the model of McIntosh and Hunter. The number of RF cycles in the fringing field, n_f, is then expressed in terms of the quadrupole mass filter parameters as

$$n_f = Z_f f (m/2E_z)^{1/2} \qquad (4.5)$$

Where f is the frequency of the applied RF, m is the ion mass, and E_z is the axial ion energy.

Figures 4.16(a, b, c) show the variation of relative transmission versus the fringing field length measured in RF cycles with operation at the upper tip, the middle and the lower tip of region VI, respectively. For the whole region, there is little change in transmission up to about $n_f = 0.25$, i.e. when ions pass through the fringing field in 0.25 RF cycles or less, the ion transmission is constant. This is a lower value of n_f than that

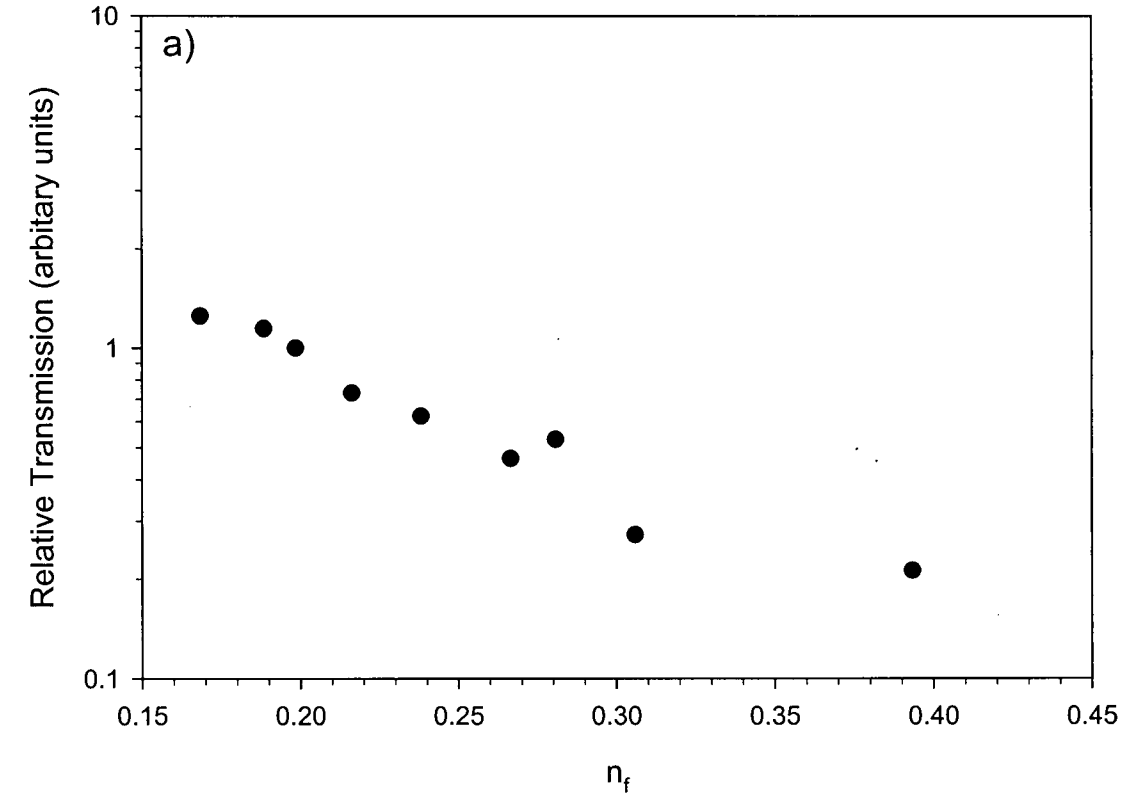
a)
Relative Transmission (arbitary units)
10
1
0.1
0.15
0.20
0.25
0.30
0.35
0.40
0.45
n_f

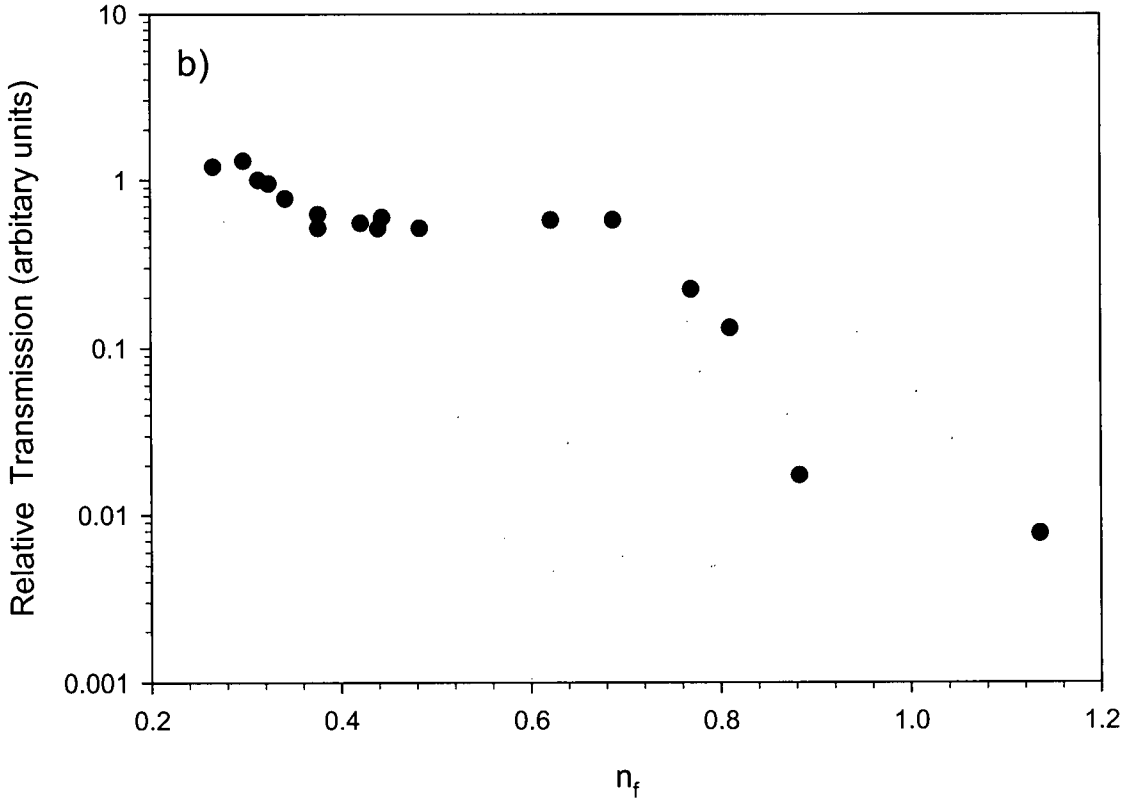
b)
Relative Transmission (arbitary units)
10
1
0.1
0.01
0.001
0.2
0.4
0.6
0.8
1.0
1.2
n_f

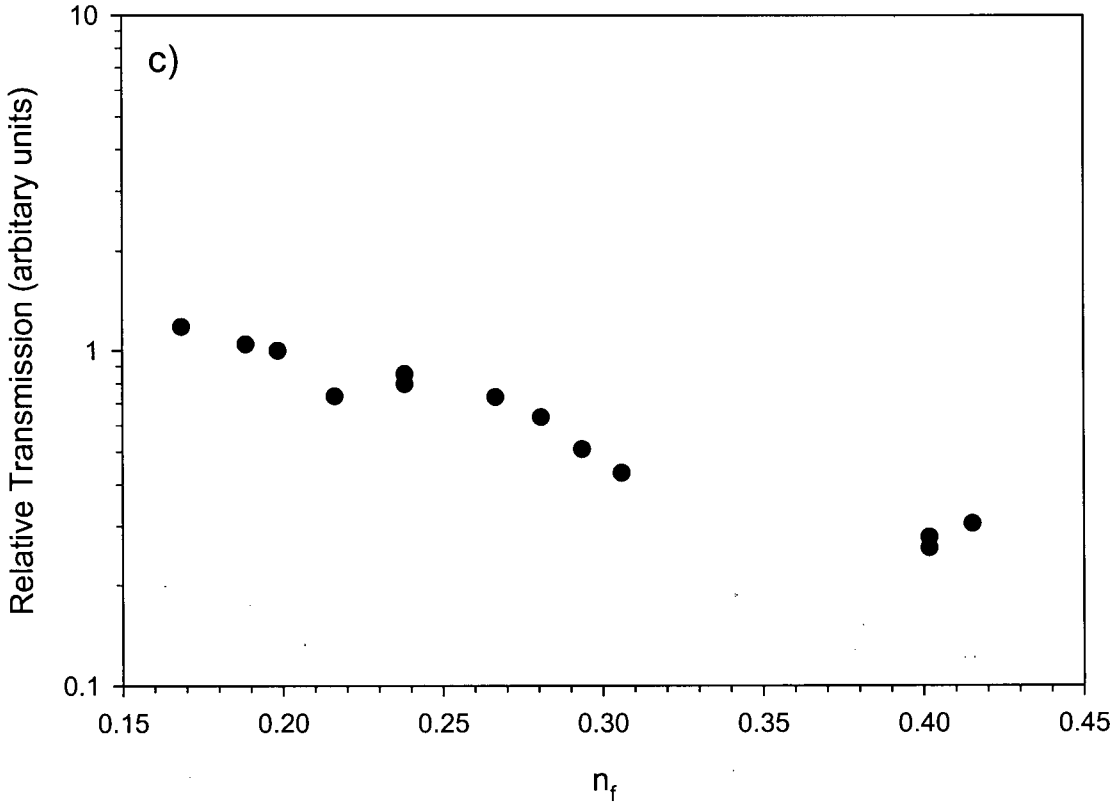

Figure 4.16 The relative transmission versus the number of RF cycles that ions spend in the fringing field. Figure a) is for the upper tip, b) for the middle area of the region, and c) for the lower tip.

found in the calculations. This is probably because the real fringing field couples the ion motions in the x, y and z directions. Thus transverse amplitudes of the ion trajectories could be larger than those predicted by the model calculation when ions pass through the fringing field. For a given n_f, the required axial ion energy, E_z, can be calculated as:

$$E_z \geq (m/2)\,(1.5\, r_0 f/n_f)^2 = 1.17*10^{-2}*\, M\,(r_0 f/n_f)^2 \qquad (4.6)$$

where M is the ion mass (Da), r_0 is the field radius (mm), and f is the RF frequency (MHz). For our instrument with $n_f = 0.25$, the ion energy should be larger than 210 eV to achieve high transmission.

4.3.5 Comparison of ion transmission to that of the second region and the fourth regions

Figure 4.17 shows the ratio of the ion transmission with the operation in the middle of the sixth region to the transmission with operation in the second region with a = 0, recorded as described in the experimental section. It is seen that the transmission in the sixth region is less than that of the second region. However, in general, the ratio of ion transmission in the sixth region to the transmission in the second region is about two orders of magnitude higher than the ratio to the transmission in the fourth region to the transmission in the second region. At ion energies greater than ~ 500 eV, the transmission in the sixth region is about 0.3 of that in the second region. At lower ion energies, there is a decrease in the relative transmission in the sixth region. At the lowest energy of 20 eV, the transmission in the sixth region is about 5×10^{-3} of the transmission in the second region.

As discussed in Chapter 3, it is more reasonable to compare transmission at the same resolution. The resolution at half height in the middle of the sixth region is about 1,200 for 20 eV ions. The resolution at half height in the second region with a quadrupole in RF-only mode is about 200 with several eV ions. To achieve $R_{½}$ =1,200, with operation in the second region the transmission decreases by a factor of 8 or 9.[25] Therefore, with the same resolution, the ratio of ion transmission in the sixth region to that in the second region should be about one order of magnitude higher than that shown in Figure 4.17. If this factor is extended to higher energy ions, the ion transmission in the sixth region, with ion energies larger than about 100 eV and with the same resolution, should be larger than that in the second region. Since the sixth region does not have an

"aliasing" problem, it could be used to mass analyze ions of intermediate energy without an additional mass filter.

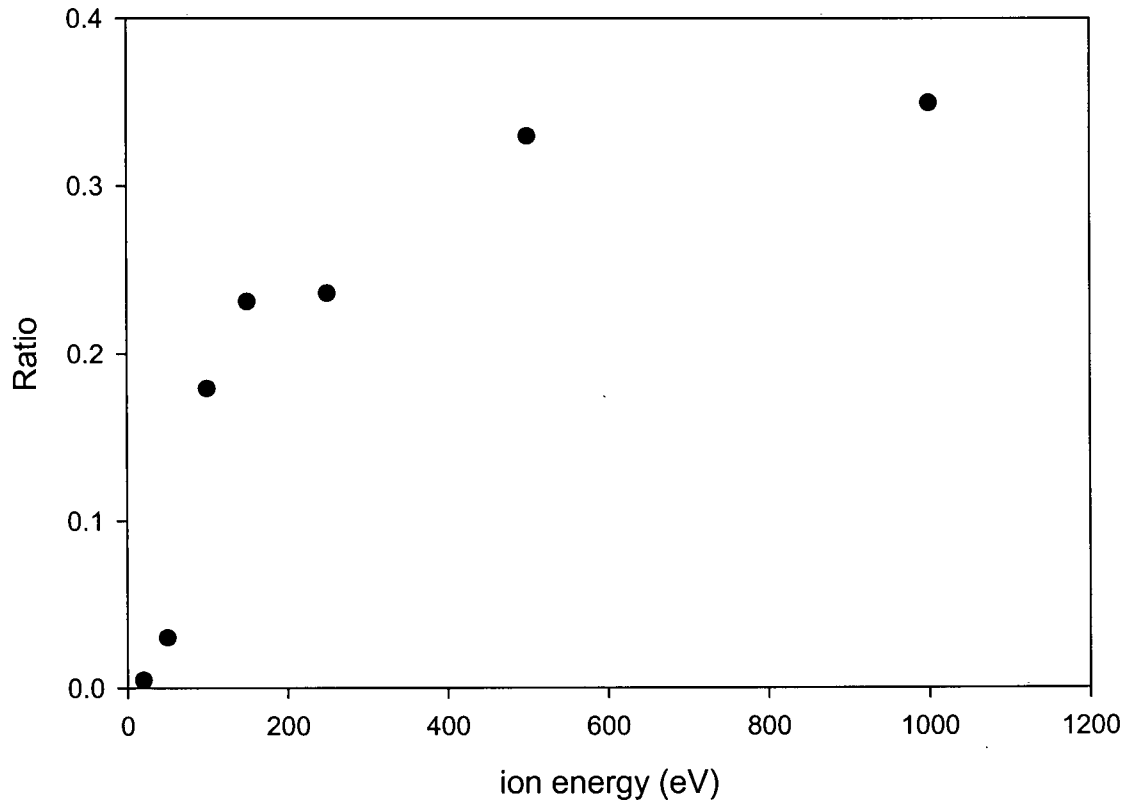

Figure 4.17 Ratio of ion transmission with operation in the middle of the sixth region to the transmission in the second region for ion energies between 20 eV and 1000 eV.

4.4 Summary

In this chapter, the properties of a quadrupole mass filter operated in the sixth region with Mathieu parameters (a, q)≈(8,6) have been investigated experimentally and theoretically.

For the sixth region, a resolution of several hundred was obtained with high energy ions (>1000 eV). This region could be used as an additional mass filter to

eliminate alias ions when a quadrupole is operated in regions II or IV. For ions of intermediate energy, the sixth stability region can be used as an independent mass filter. The maximum resolution achieved was $R_{1/2} = 2000$ with $^{39}K^+$ ions with an axial ion energy of 20 eV.

At the lower tip it was not possible to change the resolution for high energy ions by moving the scan line towards the tip. This is probably because the ion separation is dominated by the narrow stability band in the y direction only (Chapter 5).

Chapter 5
Ion transmission with quadrupoles operated outside the stability regions

5.1 Introduction

The transmission of the mass filter is an important parameter for the sensitivity of a quadrupole mass spectrometer system. Here we use the ion transmission to study the characteristics of a quadrupole mass filter operated outside of the stability regions. As described in Chapter 1, ion motions in the x and y directions in a quadrupole mass filter are independent, and the equations of ion motion can be expressed as the Mathieu equation. This equation leads to a stability diagram (Figure 1.3) plotted in the plane of the a and q parameters. The stability regions indicate where ion motion is simultaneously stable in the x and y directions, while the unstable regions have ion motion that is unstable either in the x direction or in the y direction, or unstable in both directions. The theoretically calculated stability diagram is based on the assumption of a mass filter of unlimited length. However, a real quadrupole mass filter has a finite length. Most commercial quadrupoles are about 20 cm long with field radii between

about 4 mm and 7 mm. When a quadrupole is operated in the first stability region, the ion injection energy is a few eV and ions with mass larger than 10 Daltons usually stay in the quadrupole field for tens of RF cycles. Under these conditions the output peak shapes are determined by the stability boundaries. However, when a quadrupole is operated in the higher stability regions, ions need higher energy to penetrate the entrance fringing field. When the ion injection energy is set so that an ion is just able to pass through the fringing field, the peak shape is still determined by the stability boundaries. (This is because ions operated in the higher stability zones usually need less separation time, i.e. fewer RF cycles.) When ions with high energy experience only a few RF cycles in the quadrupole field, some ions within *a, q* parameters in an unstable region may pass through the quadrupole. In this case, the theoretical boundaries of stability regions are considered diffuse.

This chapter describes investigations of the ion transmission and resolution with a quadrupole operated outside of the fourth and sixth stability regions. Experiments, calculated ion trajectories, and ion transmission and peak shapes are shown.

5.2 Experimental Methods

The experimental apparatus is shown in Figure 2.1. The quadrupole field radius, r_0, was 6.96 mm. The quadrupole power supply (Model API III, SCIEX, Concord, Ontario) was operated in the second and fourth regions at a frequency of 0.768 MHz. For the second region, the maximum DC voltage required between poles is 20 V (i.e., U = ±10 V). To scan at the apex of the fourth stability region, a DC voltage, U, of 0.20 V is sufficient for $^{39}K^+$. Thus once the DC voltage, U, is set higher than 0.20 V for $^{39}K^+$, the

scan line is above the tip of the fourth region. For the measurements with operation in or near the sixth stability region, the quadrupole power supply was also operated with a frequency of 0.768 MHz. For this, the U/V ratio was set to 0.6320. Using the resolution control (Figure 2.3), the U/V ratio could be varied up to ± 10%, which corresponds to a range between 0.6952 and 0.5698. In the sixth stability region, the U/V ratio is 0.64085 at the upper tip or 0.62479 at the lower tip. Thus when the U/V ratio is either higher than 0.64085 or lower than 0.62479, the quadrupole is operated above the upper tip of the sixth region and below the lower tip of the sixth region, respectively.

Two computer programs were used for ion trajectory simulations and for simulation of ion transmission curves. For the ion trajectory simulation programs, trajectories in the xz plane and yz plane were calculated separately for one operating point on the stability diagram. When the transverse positions of ions in either the x or the y direction were larger than the field radius, r_0, the calculation stopped. Forty trajectories for forty different initial phases (i.e., $\xi_0 = 0, \pi/40, 2\pi/40, \ldots, 39\pi/40$) were calculated for each operating point. The integration step size for ξ was $\pi/40$. The length of the quadrupole mass filter was set to 10 RF cycles for calculations involving the fourth region, and 20 RF cycles for the sixth region. Based on the calculated acceptances for the fourth and sixth regions, the initial positions of the ions for the calculations of operation in or near the fourth stability region were set to $x_0 = 0.00010r_0$, $y_0 = 0.00010r_0$; the focusing parameter, as defined in Chapter 2, $f = \dot{u}/u$, was chosen to be -1.0. For the calculations involving the sixth region the initial positions of the ions were $x_0 = 0.010r_0$, $y_0 = 0.00010r_0$, and the focusing parameter was -2.0.

For the ion transmission curves, each peak with operation inside or near the fourth stability region was calculated from 100 points across the peak. The input aperture radius, r_a, was $0.00075r_0$. The focusing parameter was –1.0 and the integration step size was $\pi/40$ radians. The peak shape for operation inside or near the sixth stability region was calculated from 40 points across the peak. The input aperture radius, r_a, was $0.010r_0$, the focusing parameter was -2.0 and the integration step size was $\pi/40$.

5.3 Results and Discussion

5.3.1 Transmission outside the fourth stability region

a) Peak shape with operation outside the fourth stability region

In Chapter 3, the first mass spectra and the first measurements of the ion optical properties of a quadrupole operated in the fourth stability region were described. Unexpected results were obtained when DC was added between the rods to increase the resolution ($0<a<0.002$). No increase in resolution was observed, but the transmission decreased as the scan line moved up to the tip. To explore the reasons for this, the scan line was moved above the tip of the fourth stability region. Figure 5.1 shows the fourth stability region and the surrounding regions of instability.

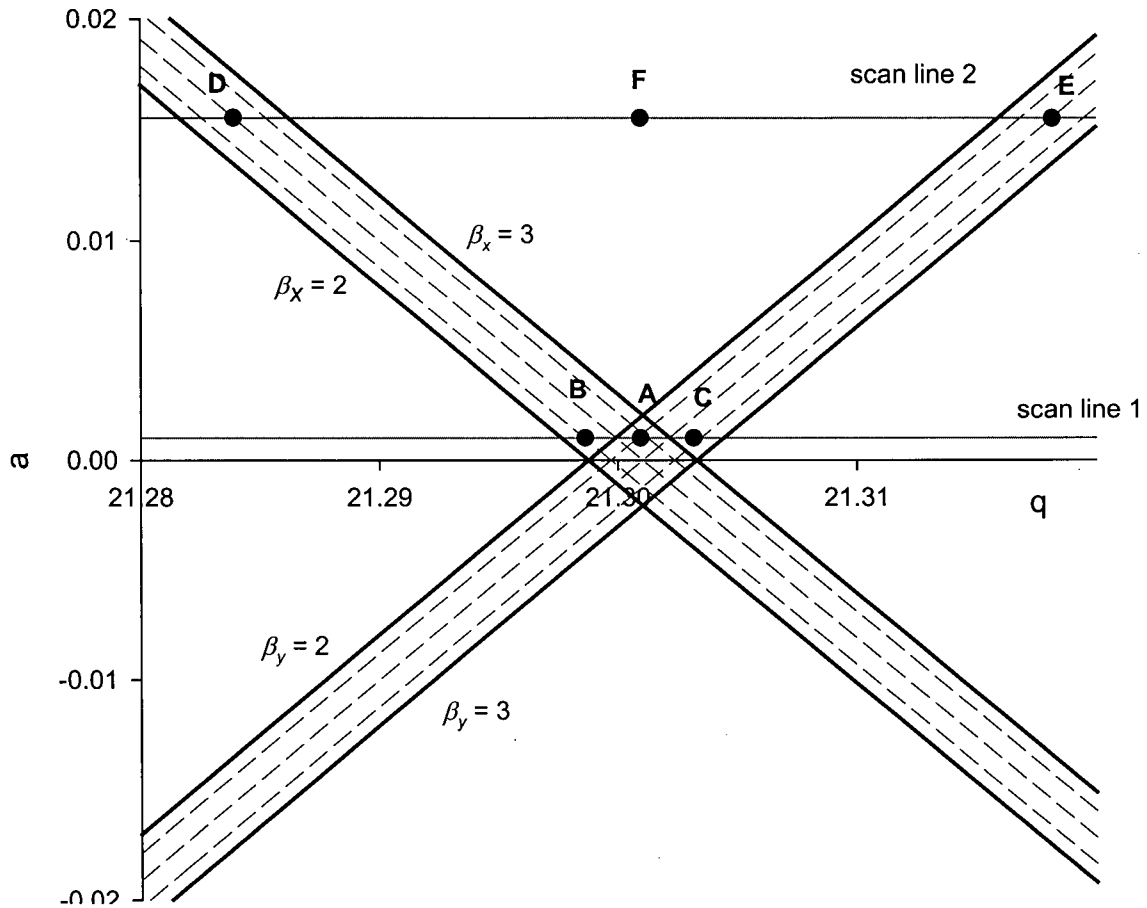

Figure 5.1 The fourth stability region and the regions of instability near it.

Five peak shapes obtained with DC = 0.0000, 0.2800V, 0.8000V, 3.200 V and 6.400 V (i.e., a = 0.000, 1.439 x 10^{-3}, 4.111 x 10^{-3}, 1.644 x 10^{-2} and 3.288 x 10^{-2}) for $^{39}K^{+}$ ions with 2000 eV energy are shown in Figure 5.2 (a-e). Figure 5.2a is a peak obtained with operation inside the stability region for comparison. Figure 5.2b shows that when the scan line was moved just above the tip of the fourth stability region, the peak remains almost the same. When the scan line was moved up further, a broader peak was obtained with lower transmission and a small dip in the middle (Figure 5.2c). (Ion transmission

loss in Figures 5.3(a-e) can not be compared, because the current of the ion beam was increased as the DC voltage was increased, in order to observe peak profiles with reasonable sensitivity. Otherwise, no peak could be seen as the DC voltage was increased.) At a higher DC voltage, two peaks are obtained (Figure 5.2d). The gap between the two peaks becomes larger as the DC voltage is increased (Figure 5.2e). To understand the observed peaks, the peak positions (m/z) were converted to the corresponding RF voltages, and the RF and DC voltages were used to calculate the corresponding a, q values on the stability diagram. It was found that the operating points for the peak positions are inside the stability band for a single direction (either x or y). This means it is possible to obtain peaks with operation outside of the combined stability region.

The variation of peak shape with the ion injection energy was also investigated when the quadrupole was operated outside the fourth stability region. It was found that as the ion energies increased, the split peaks became broader. The two peaks started to overlap each other, but the peak positions did not change. To understand these observations, ion trajectory simulations and peak shape simulations were used.

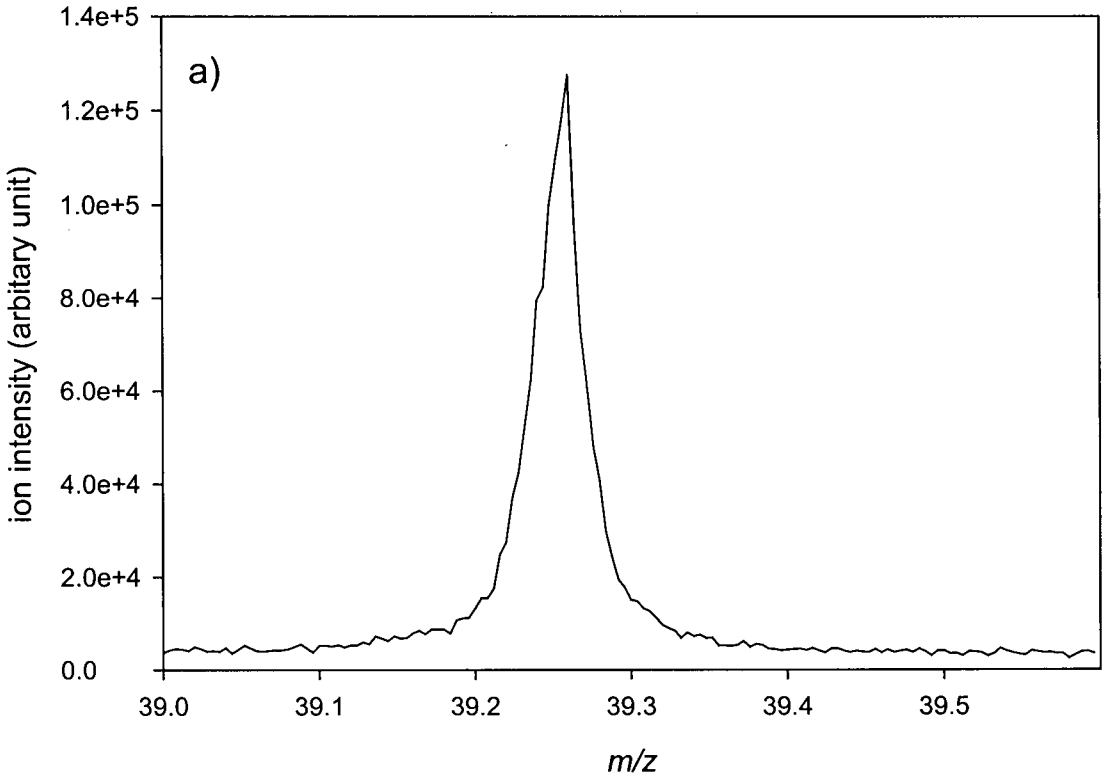
a)
1.4e+5
1.2e+5
1.0e+5
8.0e+4
6.0e+4
4.0e+4
2.0e+4
0.0
ion intensity (arbitary unit)
39.0
39.1
39.2
39.3
39.4
39.5
m/z

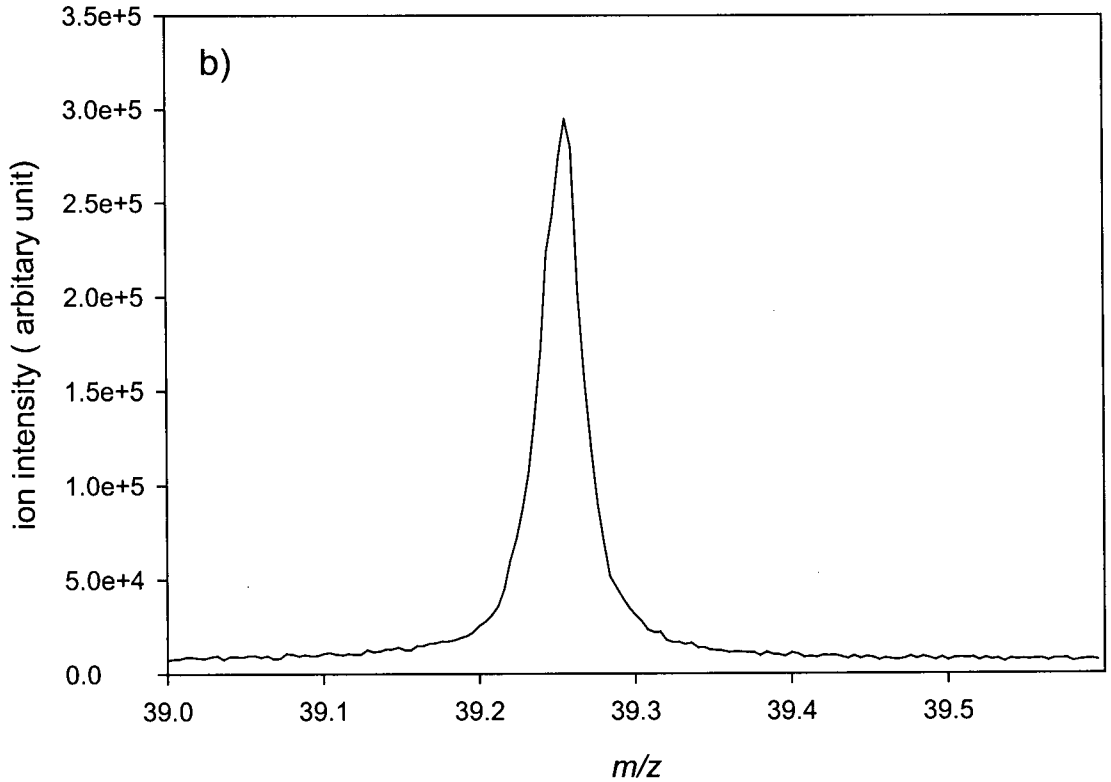
b)
3.5e+5
3.0e+5
2.5e+5
2.0e+5
1.5e+5
1.0e+5
5.0e+4
0.0
ion intensity (arbitary unit)
39.0
39.1
39.2
39.3
39.4
39.5
m/z

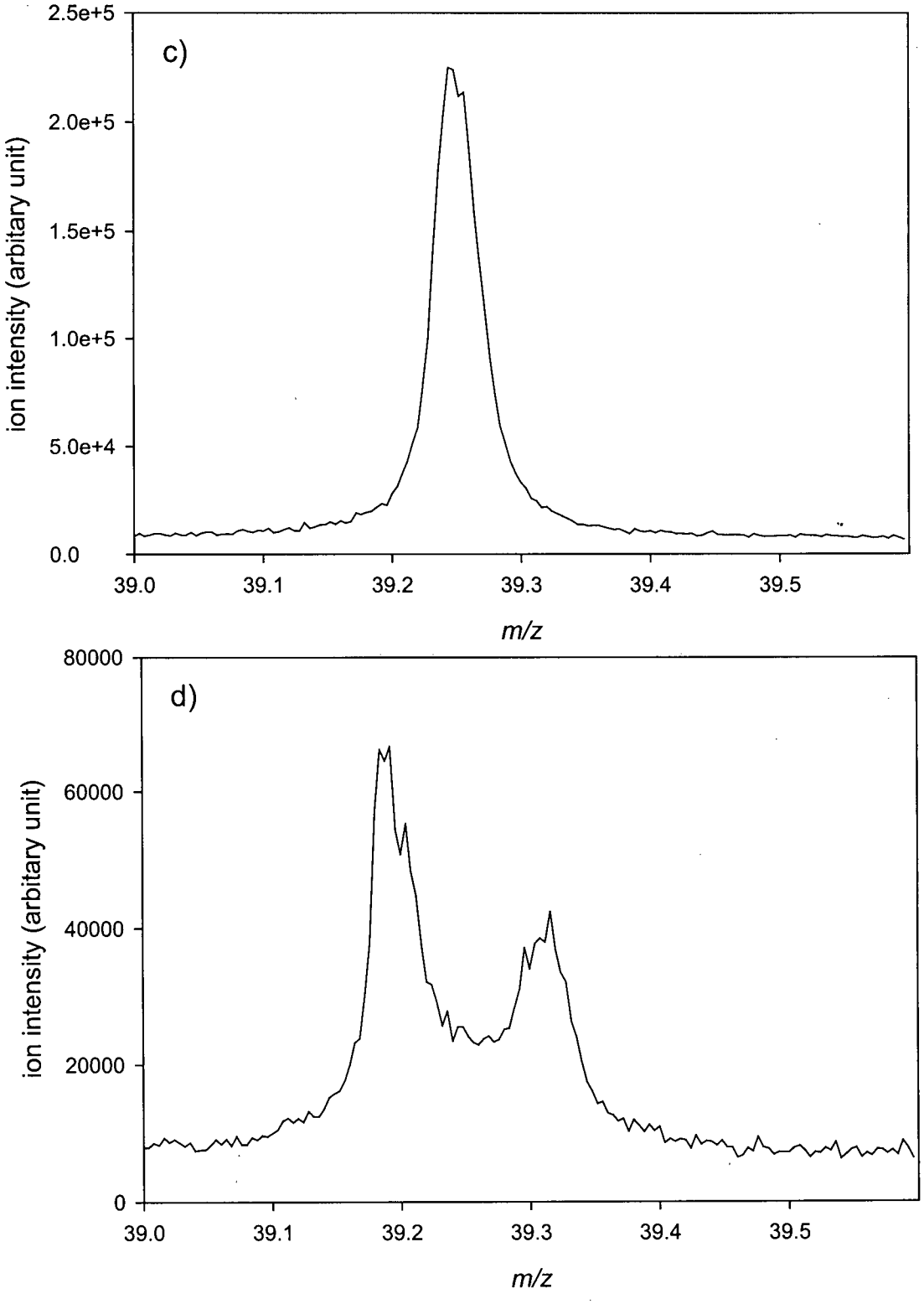
c)
2.5e+5
2.0e+5
1.5e+5
1.0e+5
5.0e+4
0.0
ion intensity (arbitary unit)
39.0
39.1
39.2
39.3
39.4
39.5
m/z
d)
80000
60000
40000
20000
0
ion intensity (arbitary unit)
39.0
39.1
39.2
39.3
39.4
39.5
m/z

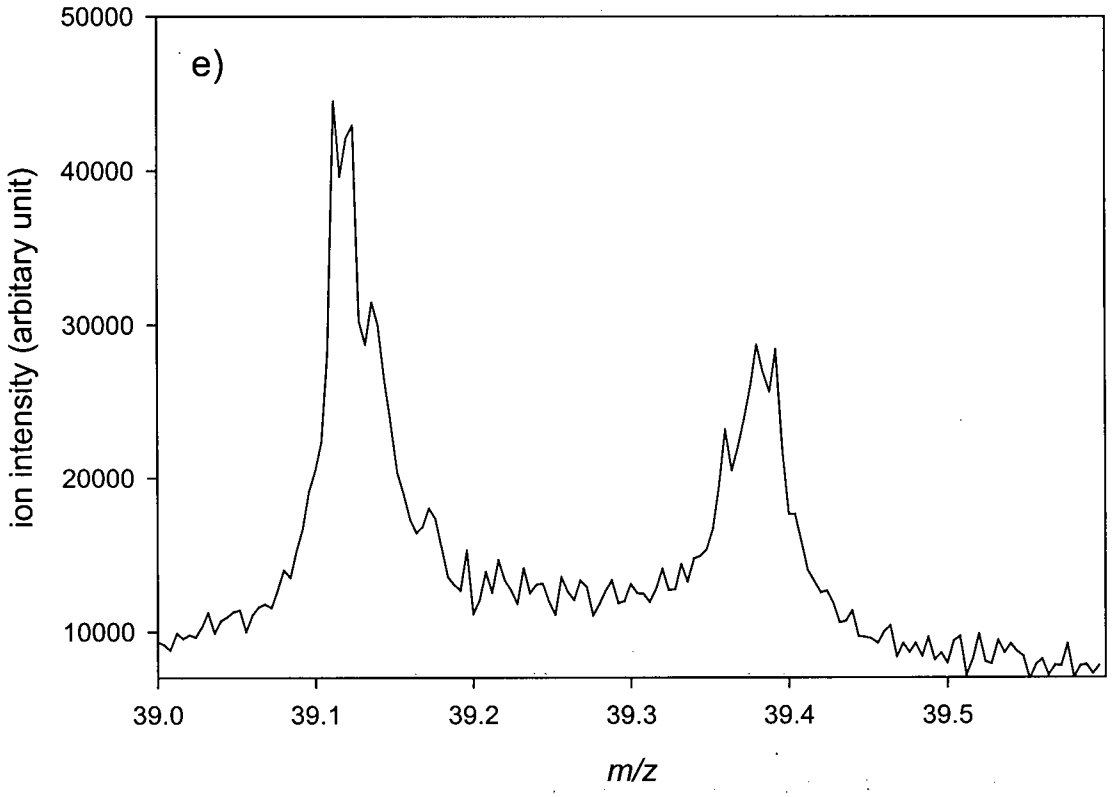

Figure 5.2 The peak shapes with a scan line moving from inside the fourth stability region to outside of the region. The DC voltages added to the rods are a) 0.0000 V, b) 0.2800 V, c) 0.8000 V, d) 3.200 V and e) 6.400 V.

b) Ion trajectory simulations

Six operating points on the two scan lines shown in Figure 5.1 were selected for ion trajectory simulations. Scan line 1 crosses the middle of the fourth stability region. Point A is inside the region, points B and C are outside of the region, but are inside the single direction stability bands, for x and y respectively. The (a, q) values of these operating points are: A (1.03000×10^{-3}, 21.30095), B (1.03000×10^{-3}, 21.29863) and C (1.03000×10^{-3}, 21.30317). Their corresponding β values are A (β_x = 2.65162, β_y = 2.31803), B (β_x = 2.31002, μ_y = 0.32329) and C (μ_x = 0.28802, β_y = 2.64450), where μ is the increment of exponential growth of the ion oscillation amplitude within one period and can be calculated from Equation 1.15. Scan line 2 corresponds to 1.500 V of DC voltage added between the opposite rods (i.e., $\lambda = 7.300 \times 10^{-4}$). Operating points D and E are in the x only and the y only-stability bands, respectively. Operating point F is outside the stability region. Their (a, q) positions on the stability diagram are: D, (1.55497×10^{-2}, 21.28390); E, (1.55497×10^{-2}, 21.31818); F, (1.55497×10^{-2}, 21.30095) and their β values are D,(β_x = 2.50000, μ_y = 1.08430); E, (μ_x = 1.08408, β_y = 2.50000); F, (μ_x = 2.75333, μ_y = 2.20769).

The ion trajectory simulations for the xz and yz planes, for 10 RF cycles, for these six operating points are shown in Figure 5.3 to Figure 5.8. For the point A, the ion trajectories in the x direction are shown in Figure 5.3a and the trajectories in the y direction in Figure 5.3b. The trajectories in both the x and the y directions are stable and transverse amplitudes of all the trajectories are less than the field radius r_0. This means that at operating point A, all the ions with these initial conditions, can pass through the quadrupole field with a length of 10 RF cycles (48 eV for $^{39}K^+$ ions). Figure 5.4 shows

that at operating point B, the ion trajectories in the x direction are stable, but some of the trajectories in the y direction start to become unstable after 1.5 RF cycles. This indicates that $^{39}K^+$ ions with energies larger than 2120 eV can still pass through the quadrupole. Four out of forty trajectories are stable within 6 RF cycles, which means the ion intensity at operating point B could be about one tenth of the maximum intensity at point A with 132 eV $^{39}K^+$ ions. Hence, with an intermediate ion energy (for example, larger than 300 eV), more than 10% of the ions can pass through the quadrupole at operating point B and a relatively broader peak than theoretically expected may be obtained. Figure 5.5 shows trajectories for the operating point C, which is outside of the fourth stability region, opposite to the point B. There are unstable ion trajectories in the x direction and stable ion trajectories in the y direction. Also, the ion motion in the x direction is relatively more stable than the ion motion in the y direction at point B (compare μ_x = 0.28802 at point C, μ_y = 0.32329 at B). Most ions stay in the quadrupole field for 5 RF cycles (190 eV), and about 30% of the ions can be stable for 10 RF cycles (48 eV). This indicates that operating at point C, on the high mass side of the peak, the ion transmission may be higher than that at point B. No increases in resolution are observed with a>0 with operation inside the fourth region because the length of the quadrupole field is limited and nominally unstable ions can be transmitted by the quadrupole.

Ion trajectories calculated for points D and E, shown in Figure 5.6 and Figure 5.7, respectively, are similar to those at point B and point C, respectively. The trajectories in the x direction at point D and in the y direction at point D are stable. The trajectories in the y direction at point D are stable for longer times in the quadrupole than those in the x direction at point D. Three out of forty $^{39}K^+$ ions are transmitted by the

quadrupole at point D for 10 RF cycles, while no ions can be transmitted at point E. For 6 RF cycles, nine trajectories stay in the rods at point B and seven at point C. For 4 RF cycles, all the ions can be transmitted by the quadrupole at both points for the given initial position and velocity. The combined trajectories at point D usually require more RF cycles than those at point B to become unstable. Most of the $^{39}K^{+}$ ions can pass through the quadrupole filter if they have an ion energy larger than 300 eV (i.e., 4 RF cycles). Some ions with lower energy can still pass through the quadrupole (for this initial position and velocity). In comparison to ions at the point D, $^{39}K^{+}$ ions for the point E with higher energy (i.e. 300 eV) have almost the same transmission, but for the lower energy ions, there is a sharp decrease in transmission. Ion trajectories for point F are shown in Figure 5.8. Ion motion in the both x and y directions are unstable. There is no ion transmission unless the ion energy of $^{39}K^{+}$ is larger than 1,200 eV. The ion trajectories at these three operating points show that two peaks with similar ion intensity can be obtained above the tip of the fourth stability region with a higher energy ion source.

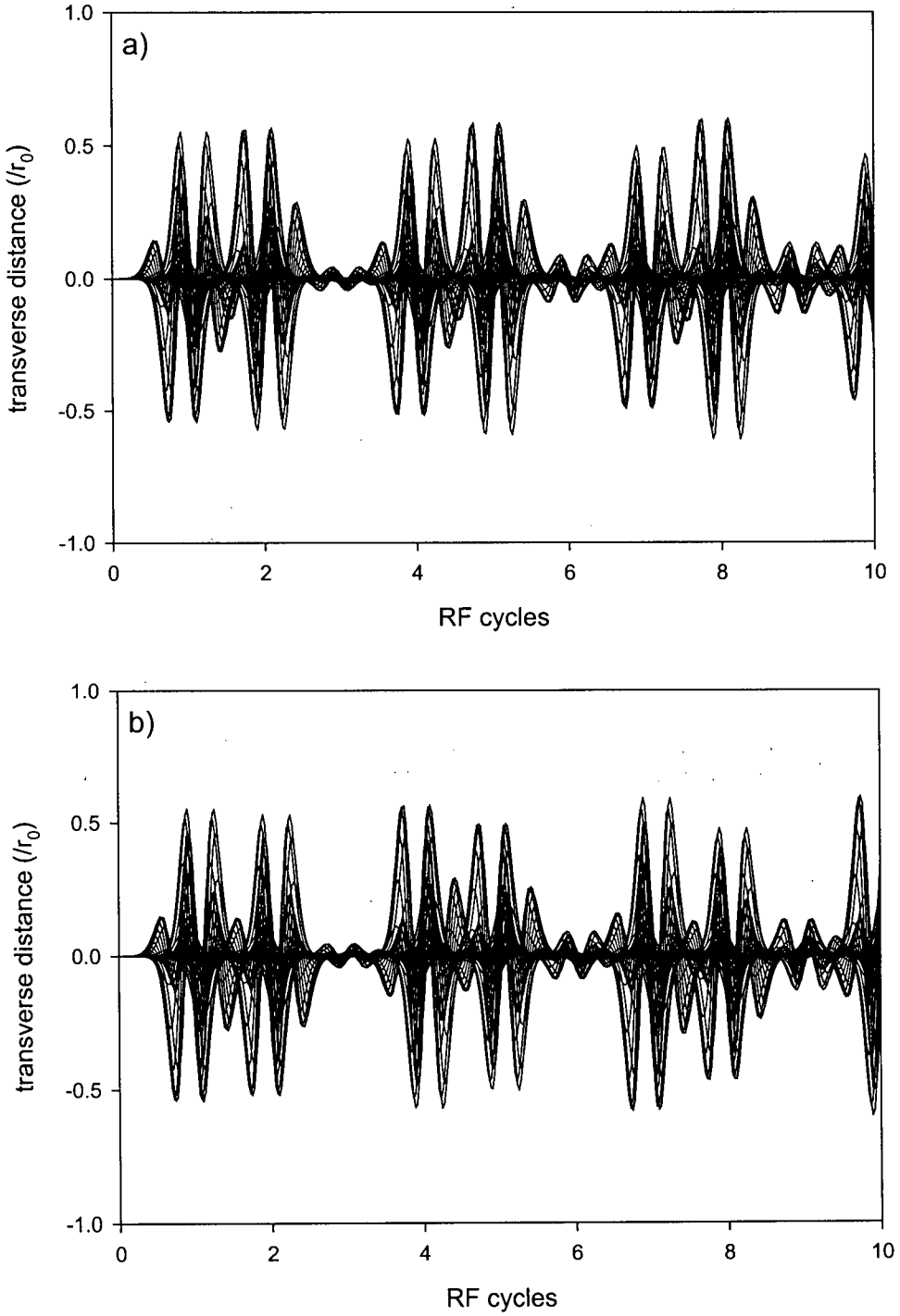

Figure 5.3 Ion trajectories for forty initial phases for the operating point A (a = 1.03000x10^{-3}, q = 21.30095) inside the fourth stability region on a scan line across the middle of the region. (a) The trajectories in the xz plane; (b) The trajectories in the yz plane.

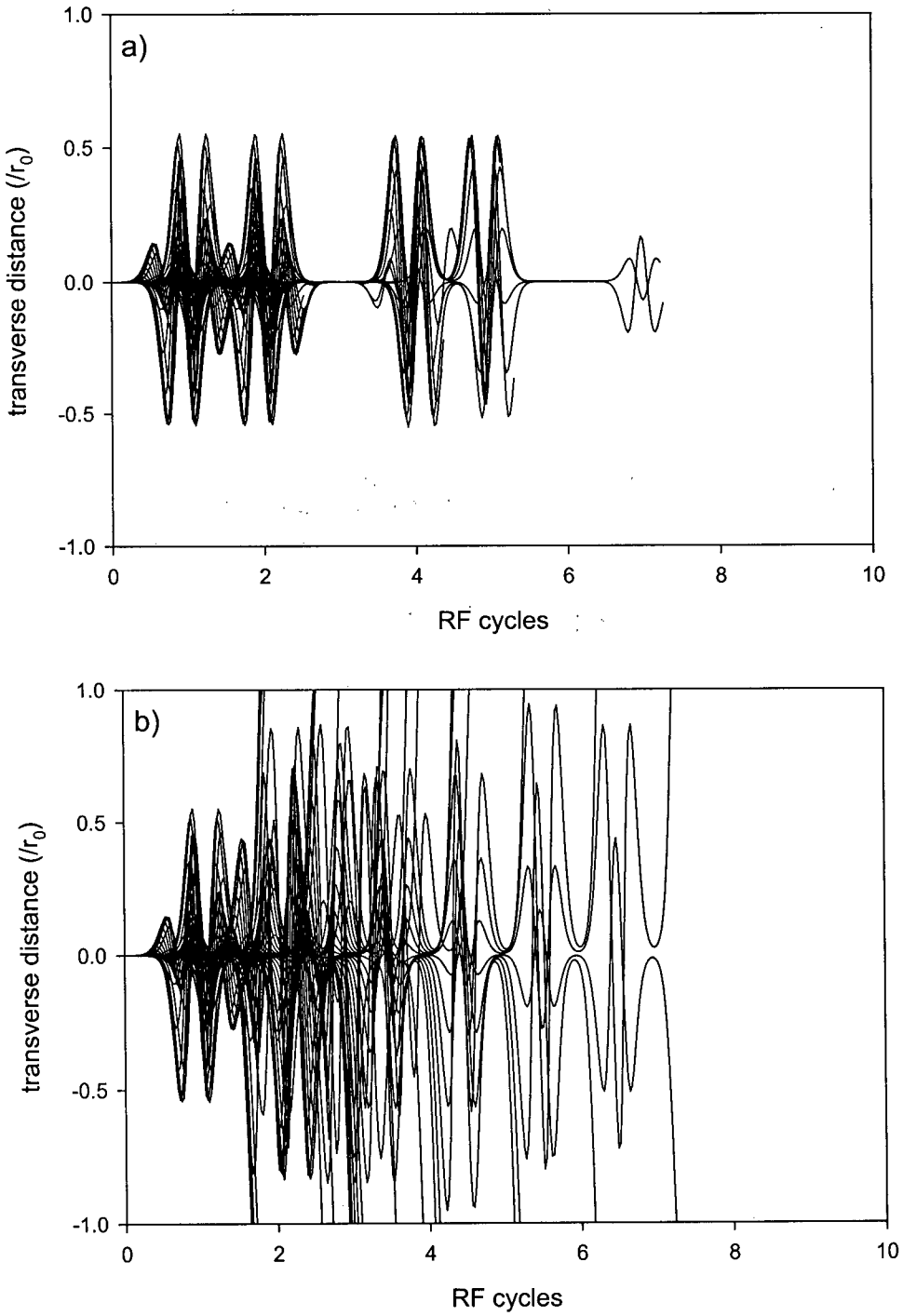

Figure 5.4 Ion trajectories for forty initial phases for the operating point B (a = 1.03000x10^{-3}, q = 21.29863) outside the fourth stability region on a scan line across the middle of the region. (a) The trajectories in the xz plane; (b) The trajectories in the yz plane.

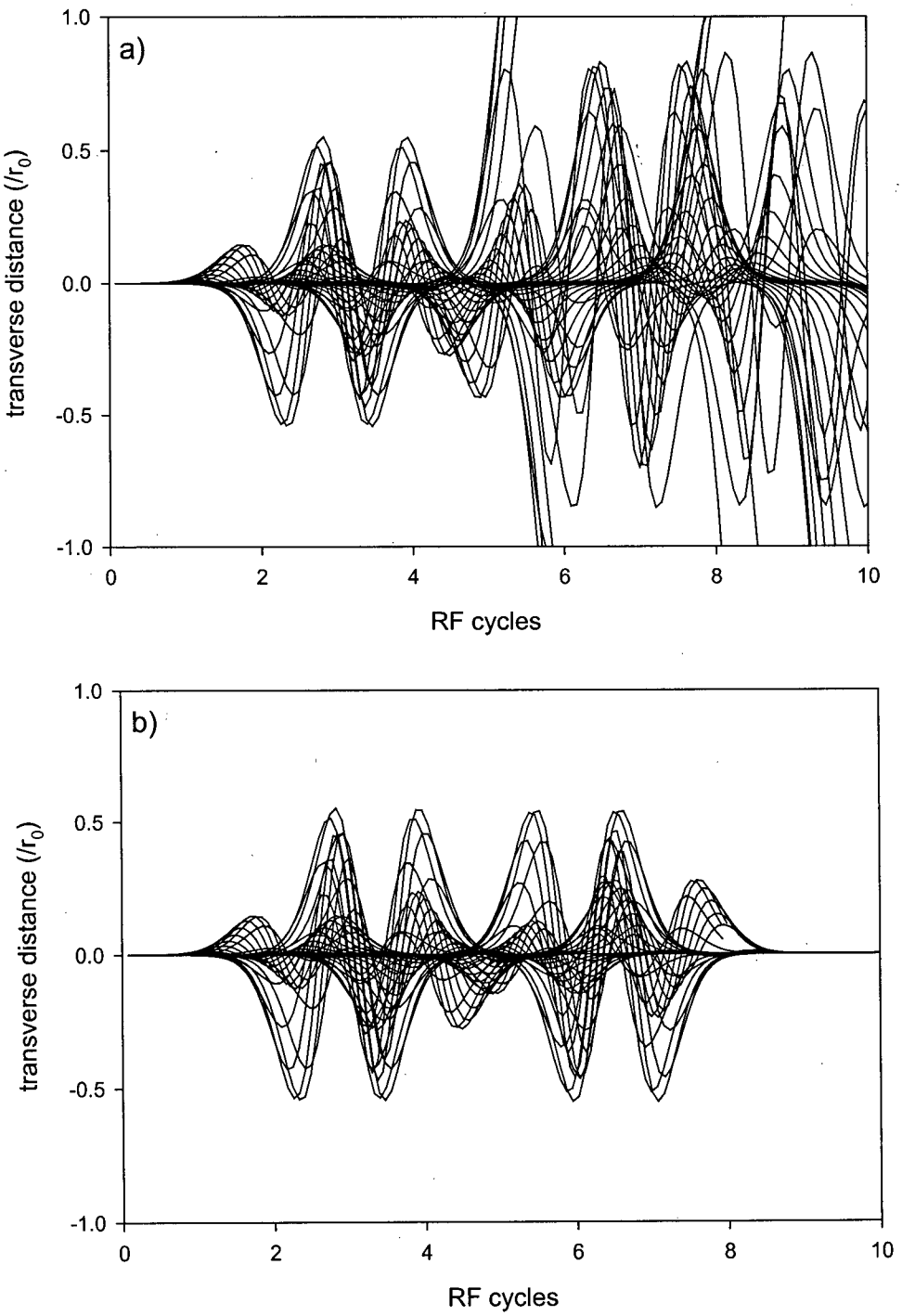

Figure 5.5 Ion trajectories for forty initial phases for the operating point C (a =1.03000x10^{-3}, q = 21.30317) inside the fourth stability region on a scan line across the middle of the region. (a) The trajectories in the xz plane; (b) The trajectories in the yz plane.

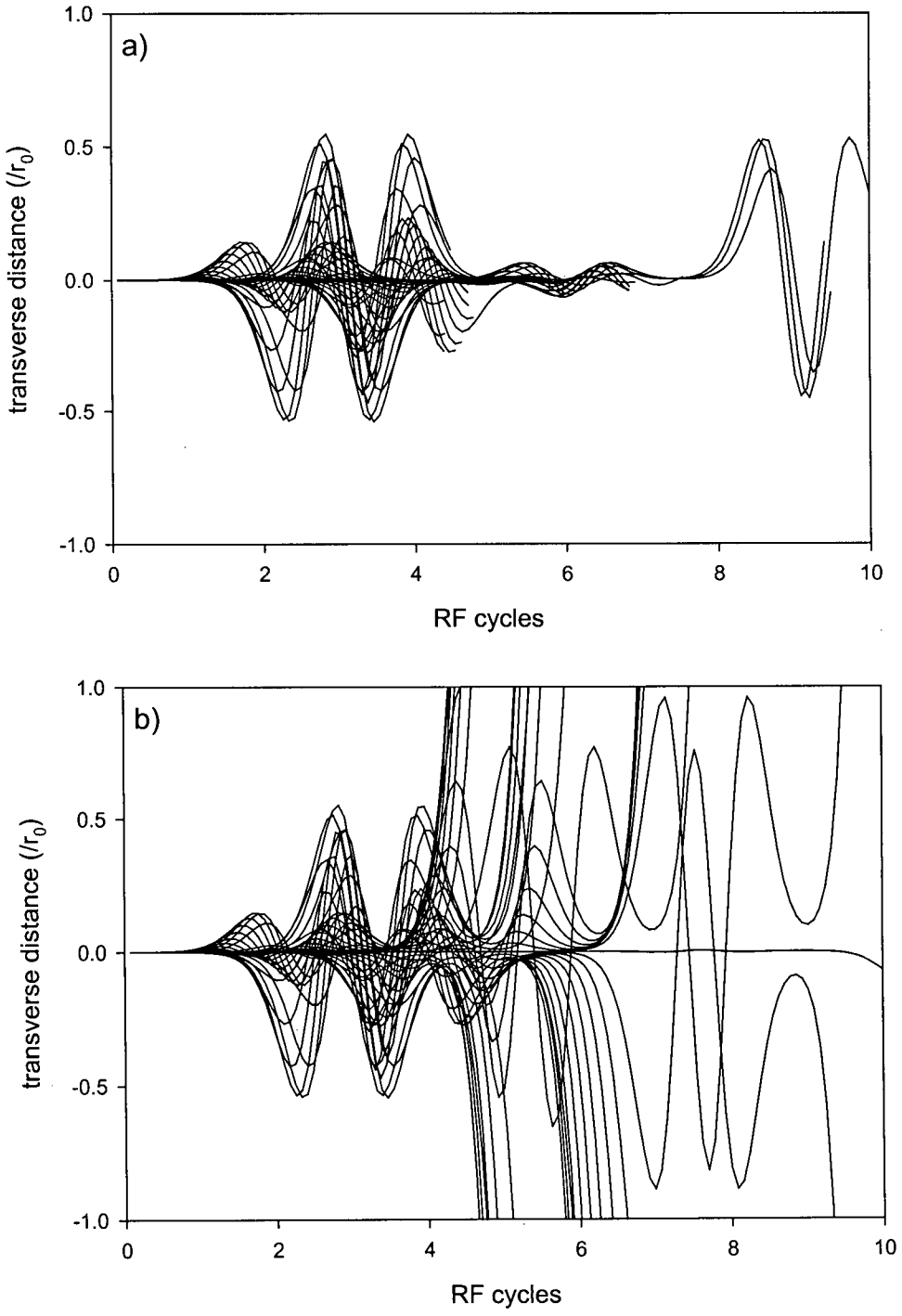

Figure 5.6 Ion trajectories for forty initial phases for the operating point D (a =1.55497x10^{-2}, q = 21.28390) above the fourth stability region on a scan line with λ = 0.00073. (a) The trajectories in the xz plane; (b) The trajectories in the yz plane.

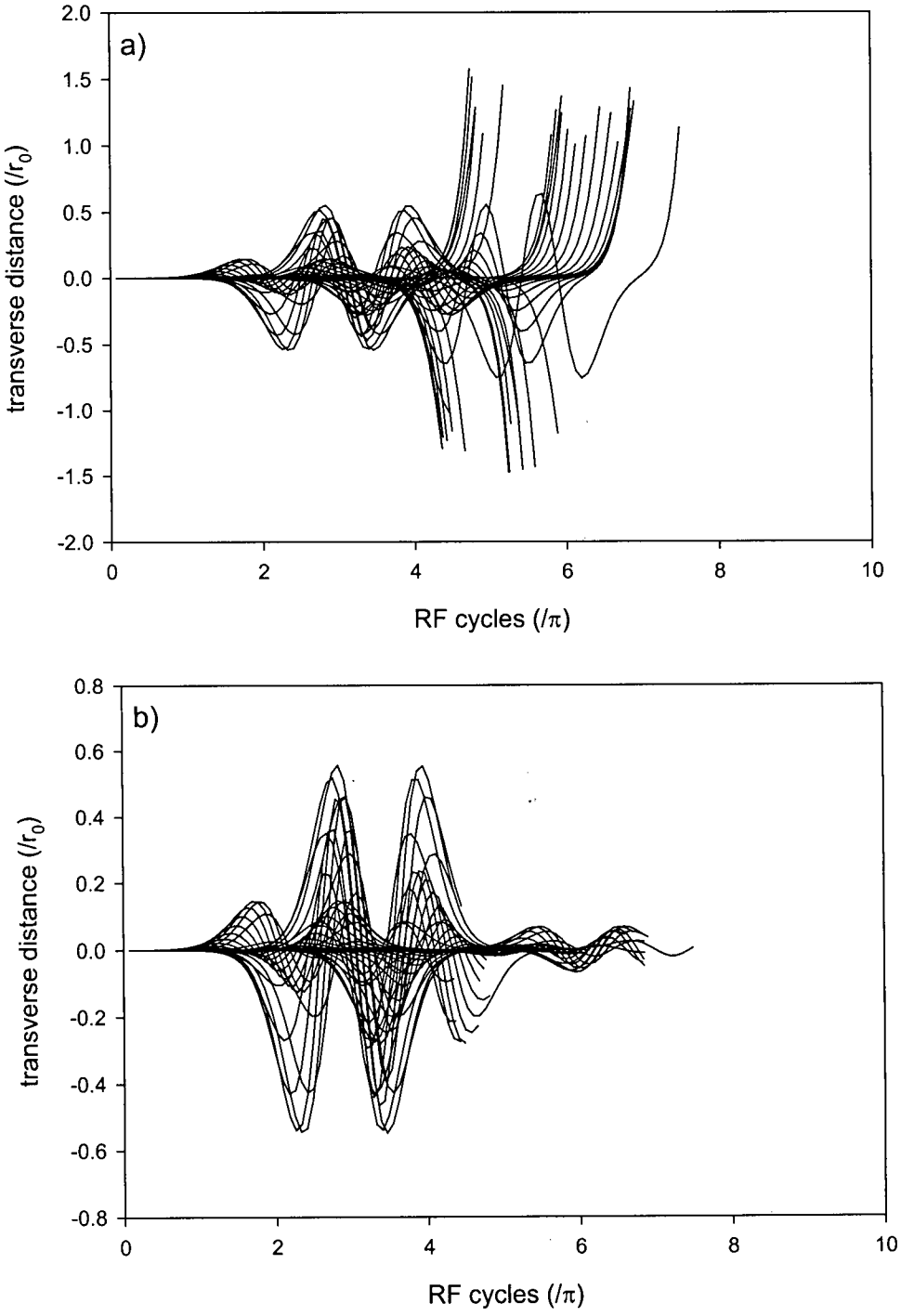

Figure 5.7 Ion trajectories for forty initial phases for the operating point E (a =1.55497x10^{-2}, q = 21.31818) above the fourth stability region on a scan line with λ = 0.00073. (a) The trajectories in the xz plane; (b) The trajectories in the yz plane.

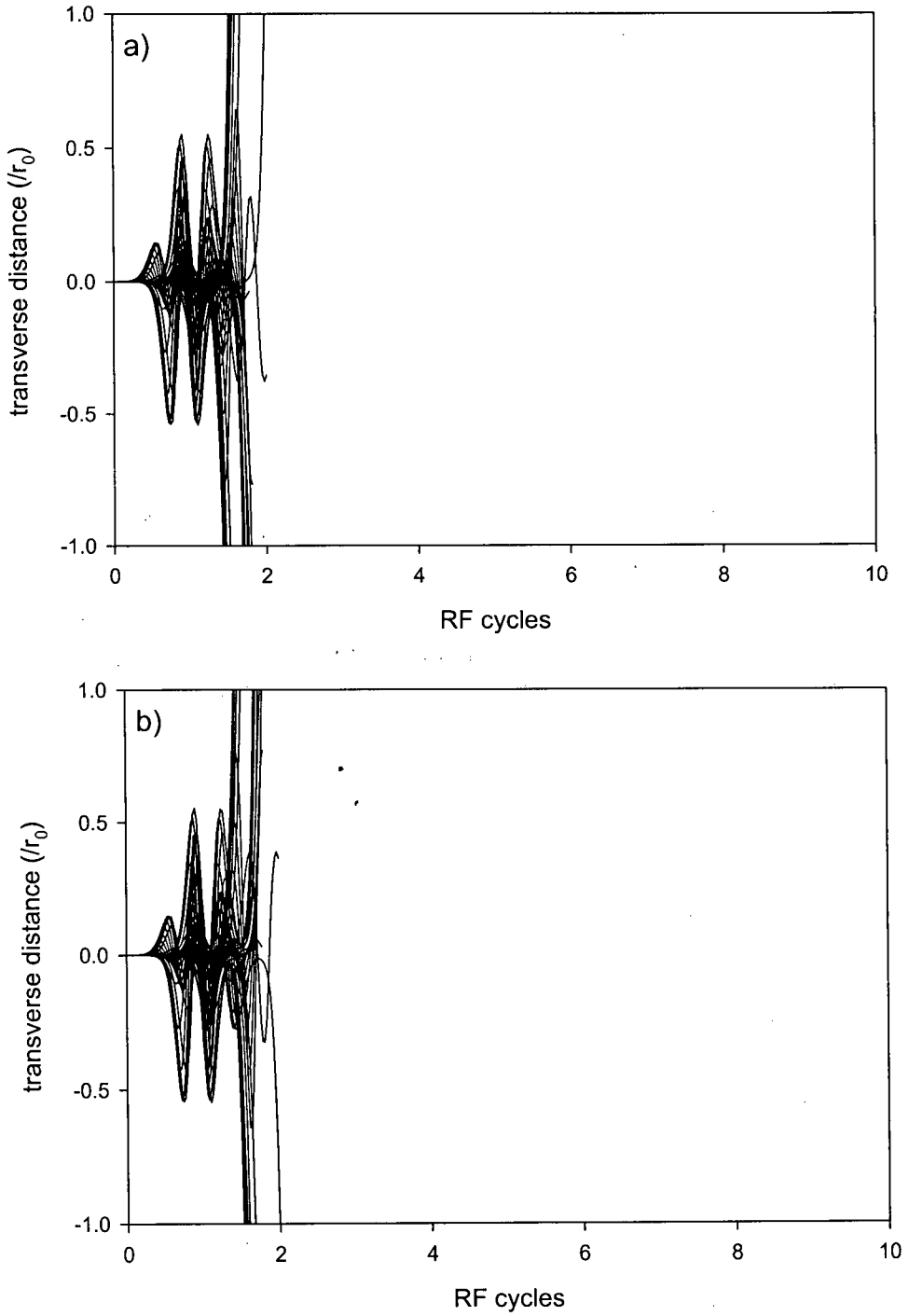

Figure 5.8 Ion trajectories for forty initial phases for the operating point F (a =1.55497x10^{-2}, q = 21.30095) above the fourth stability region on a scan line with λ = 0.00073. (a) The trajectories in the xz plane; (b) The trajectories in the yz plane.

c) Transmission Curve simulations

Simulation of transmission curves (Appendix II) provides a more direct method to investigate ion transmission. Figure 5.9 shows the calculated peak shapes with operation in the fourth region when different DC voltages are added between the quadrupole rods. For operation within the region, i.e. $0 \leq U < 0.20V$, as the DC voltage increases, the ion intensity decreases and there is no increase in resolution. As a higher DC voltage is added and the scan line moves outside of the stability region, split peaks appear and the gap between the two parts of the split peak increases. In Figure 5.10, a group of peaks are calculated with 3.000 V of DC between the rods and different ion injection energies. As the ion injection energy increases, the ion intensity increases and the peaks become broader and overlap each other. The positions of the two peaks remain the same. The experimental gap between the two peaks is compared with the theoretical gap between the two stability bands for motion in the x and y direction, respectively, in Figure 5.11. The above calculations agree with the experimental observations.

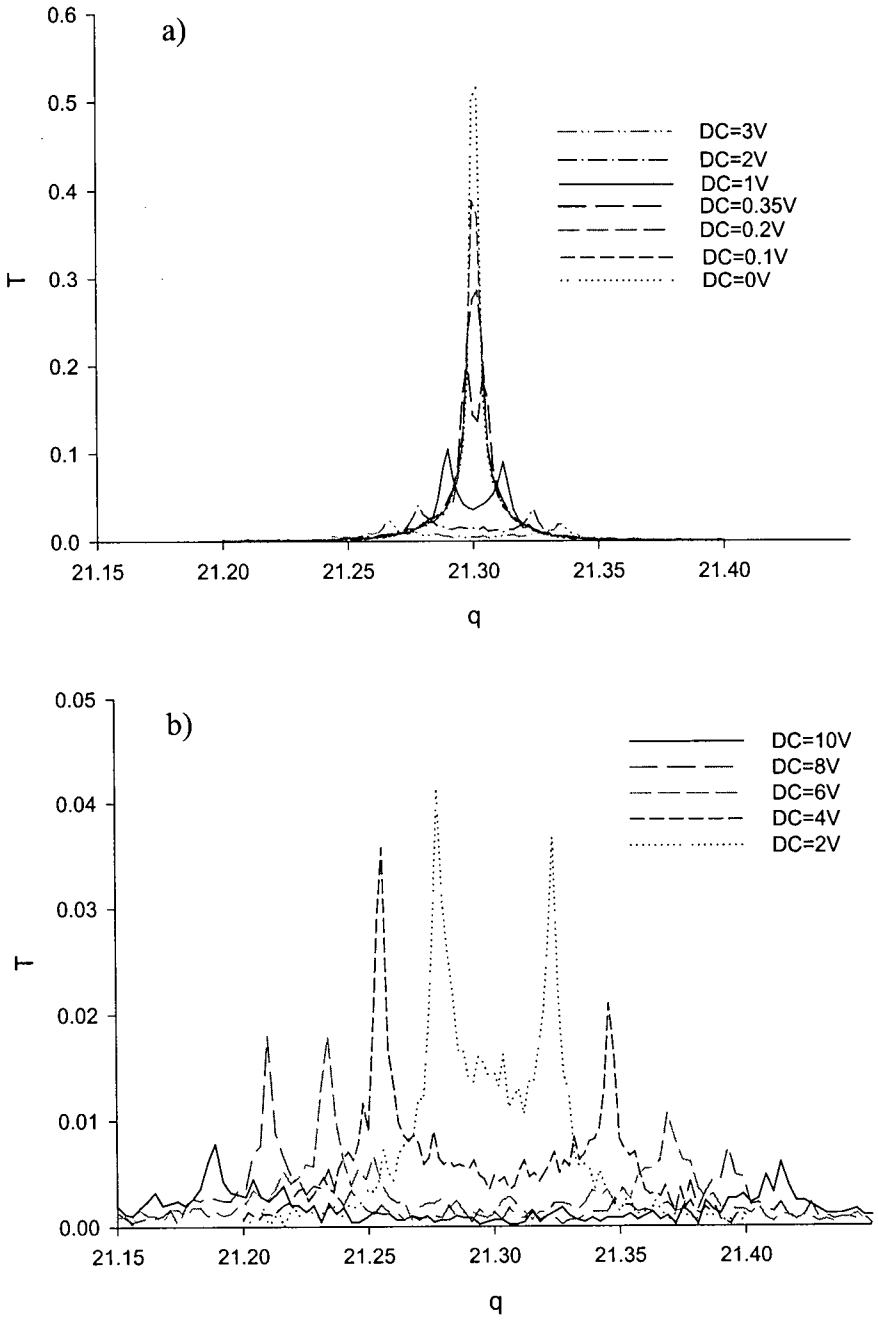

Figure 5.9 The calculated peak shapes of region IV for 2000 eV $^{39}K^{+}$ ions with different DC voltages added between the rods. a) The values of DC voltage are between 0.00 V and 3.00 V. b) The values of DC voltage are between 2.00 V and 10.00 V.

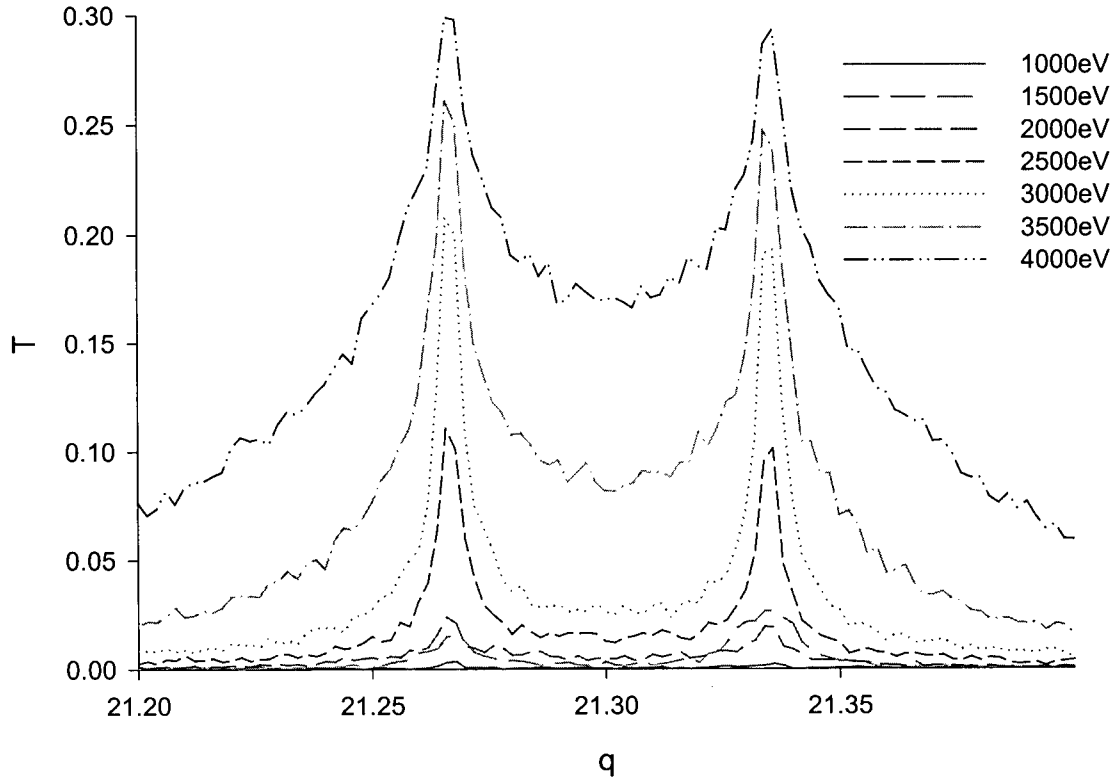

Figure 5.10 The calculated peak shapes above the fourth stability region for different injection ion energies with 3.000 V DC voltage added to the rods.

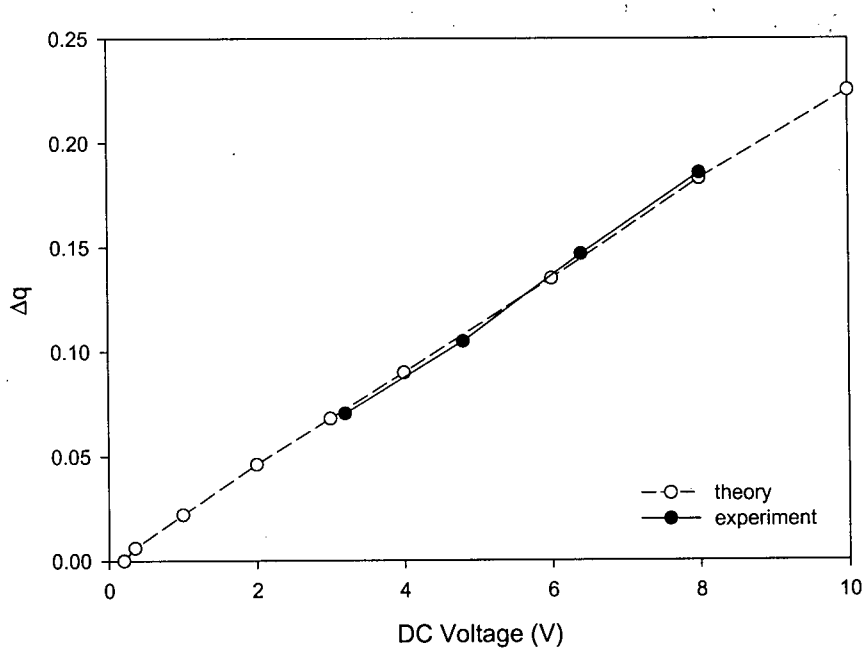

Figure 5.11 Comparison of the calculated gap between the split peaks to the experimental values.

5.3.2 Ion transmission outside of the sixth stability region

In Chapter 4, we found an unexpected T-R curve with operation at the lower tip of the sixth stability region. When a scan line was moved toward the lower tip, the transmission decreased without an increase in resolution for low energy ions and with a slow decrease in resolution for high energy ions. It was also found that peaks could be observed with operation above the upper tip and below the lower tip of the sixth stability region. Ion trajectory and peak shape simulations have been used to understand these results.

a) Ion trajectory simulations

A total of four scan lines were chosen for the upper and the lower tips of the sixth region. These are shown in Figure 5.12. Three operating points on each scan line were selected for ion trajectory calculations. At the upper tip of the sixth stability region, scan line 1 crosses the tip with $\lambda = 0.6408$. Point A is set midway between the intersections of the scan line with the stability region boundaries, point B is midway between the intersections of the scan line with the two y-stability boundaries and point C is set so that the line segment CA is half of the segment AB. The (a, q) values for these points are: A (8.96287, 6.99350), B (8.96671, 6.99650) and C (8.96108, 6.99210). Their corresponding β values are: A ($\beta_x = 2.99212$, $\beta_y = 0.21043$), B ($\mu_x = 3.52765 \times 10^{-2}$, $\beta_y = 0.50294$) and C ($\beta_x = 2.96758$, $\mu_y = 0.17786$). The scan line 2 has $a = 1.28170q$, and is above the upper tip with the operating points similar to these for the scan line 1. The a, q values for these points are: D ($a = 8.96453$, $q = 6.99425$), E ($a = 8.96991$, $q = 6.99845$) and F ($a = 8.96338$, $q = 6.99335$). Their β values are: D ($\mu_x = 1.77522 \times 10^{-2}$, $\mu_y = 0.165800$), E ($\mu_x = 5.00046 \times 10^{-2}$, $\beta_y = 0.493293$) and F ($\beta_x = 2.98759$, $\mu_y = 0.268710$).

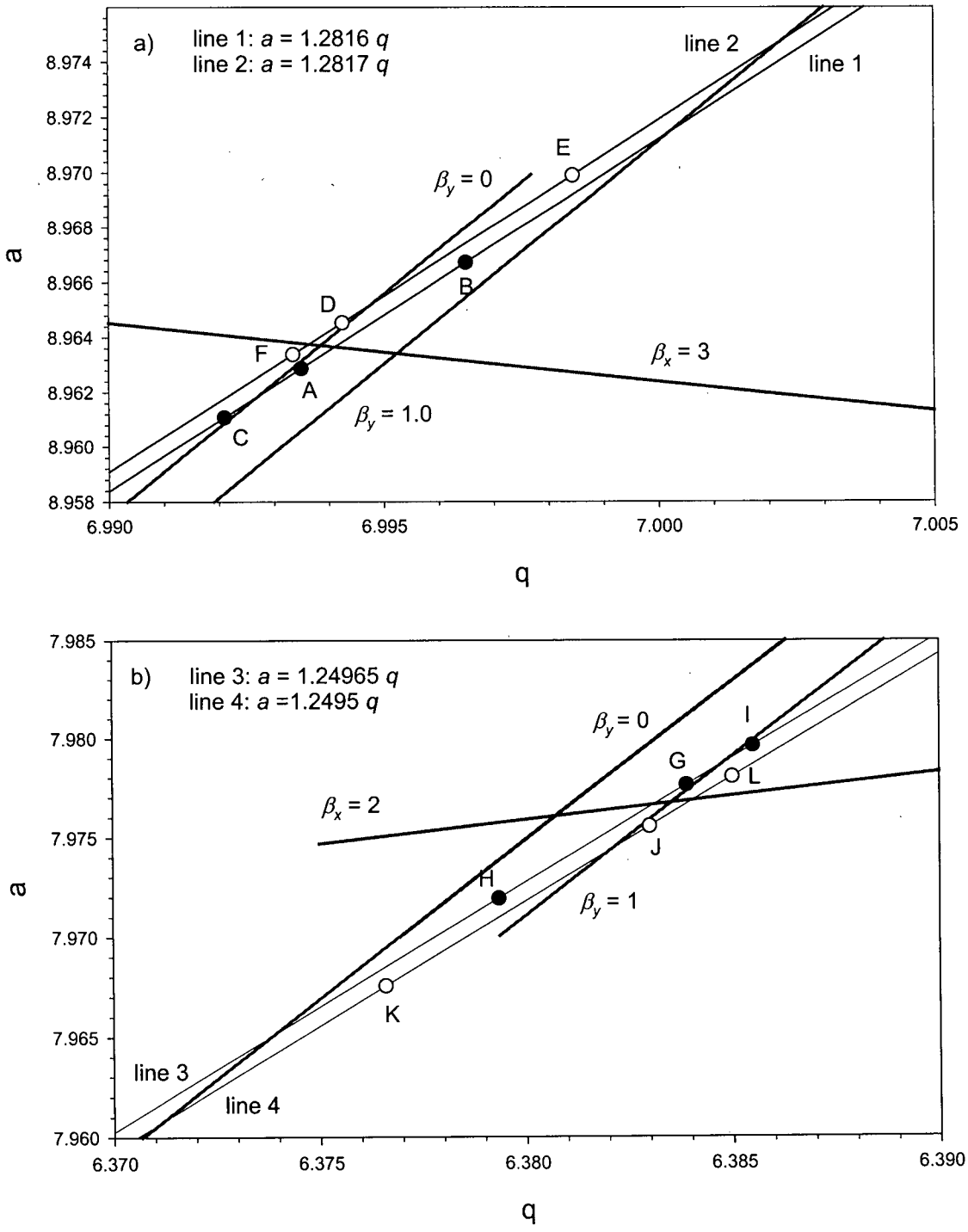

Figure 5.12 a) The upper tip of the sixth region and the unstable region near it. b) The lower tip of the sixth region and the unstable region near it.

Scan line 3 crosses the lower tip and has $a = 1.24965q$. Scan line 4 is just below the lower tip and has $a = 1.24950q$. The (a, q) positions for the selected operating points are: G (7.97764, 6.38390), H (7.97195, 6.37935), I (7.97964, 6.38550), J (7.97556, 6.38300), K (7.96756, 6.37660), and L (7.97806, 6.38500). The corresponding β values are: H ($\mu_x = 4.28771 \times 10^{-2}$, $\beta_y = 0.498947$), I ($\beta_x = 2.03434$, $\mu_y = 0.165144$), J ($\mu_x = 2.26687 \times 10^{-2}$, $\mu_y = 0.185600$), K ($\mu_x = 6.03428 \times 10^{-2}$, $\beta_y = 0.496083$) and L ($\beta_x = 2.02163$, $\mu_y = 0.319603$).

Calculated ion trajectories for the x and y directions for the twelve operating points at the upper and the lower tips of the sixth stability region are shown in Figure 5.13 to Figure 5.24. At the upper tip of the region, on scan line 1, operating point A is inside the sixth region, while operating point B is only inside the y-stability band. It is interesting to see that for a separation time of 20 RF cycles, there are more ion trajectories at point B (Figure 5.14), which can stay within the rods than those at point A (Figure 5.13) for the same given initial condition ($x_0 = 0.010r_0$, $y_0 = 0.00010r_0$, $f = -2.0$). This is because the value of β_x at point A is large. All of the ion trajectories in the x and y directions at point A are mathematically stable, but some of them have larger amplitudes of oscillation in the x direction than the field radius (outside acceptance). In contrast, the ion trajectories in the x direction at operating point B are theoretically unstable, but their transverse distances in the x direction over 20 RF cycles are smaller than the assumed field radius. Therefore all of the ions can pass through the quadrupole field in 20 RF cycles. At the operating point C (trajectories in Figure 5.15), the ion transmission is determined by the ion motion in the y direction. If the ions experience 5 RF cycles or less in the quadrupole field, which corresponds to an ion energy of about

200 eV or more, all the ions are transmitted. For a residence time of 10 RF cycles (45 eV ions), 30 out of 40 trajectories remain stable. This indicates that when a scan line crosses the upper tip of the sixth stability region, we can expect to observe a much broader peak than expected from the stability boundaries. On scan line 2, the ion trajectories in the y direction determine the ion transmission at the operating points D (Figure 5.16) and F (Figure 5.17). Compared with point D, point F is further away from the y-stability band, so the ion transmission at point F is less than that at point D. Since the operating point E (Figure 5.18) is inside the y-stability band, all the ions pass through the quadrupole mass filter for the given initial condition. This means that it is possible to obtain a peak with operation above the upper tip of the sixth stability region. The peak shape is determined by the y-stability band.

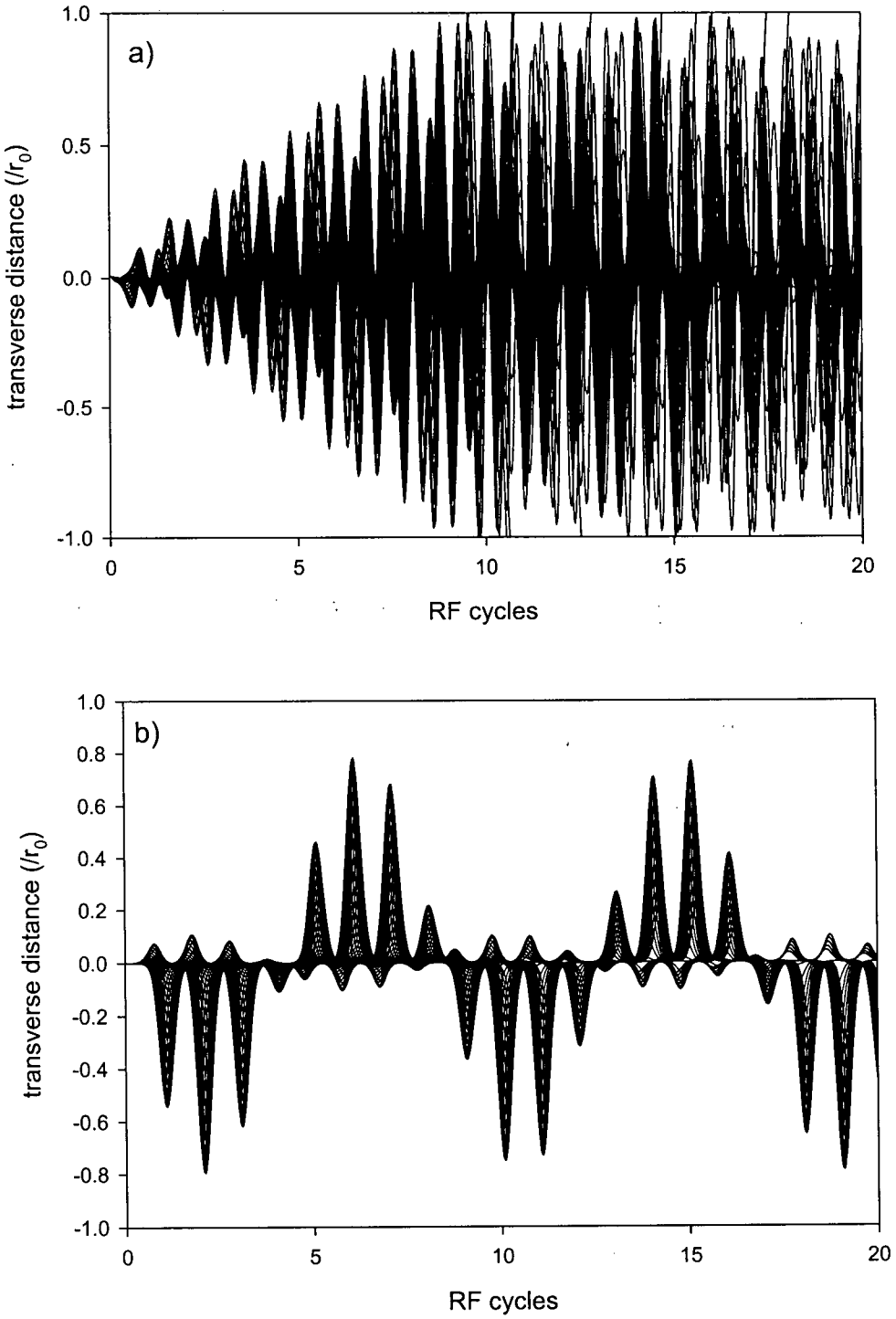

Figure 5.13 Ion trajectories for forty initial phases for the operating point A (a = 8.96287, q = 6.99350) inside the sixth stability region on a scan line across the upper tip of the region. (a) The trajectories in the xz plane; (b) The trajectories in the yz plane.

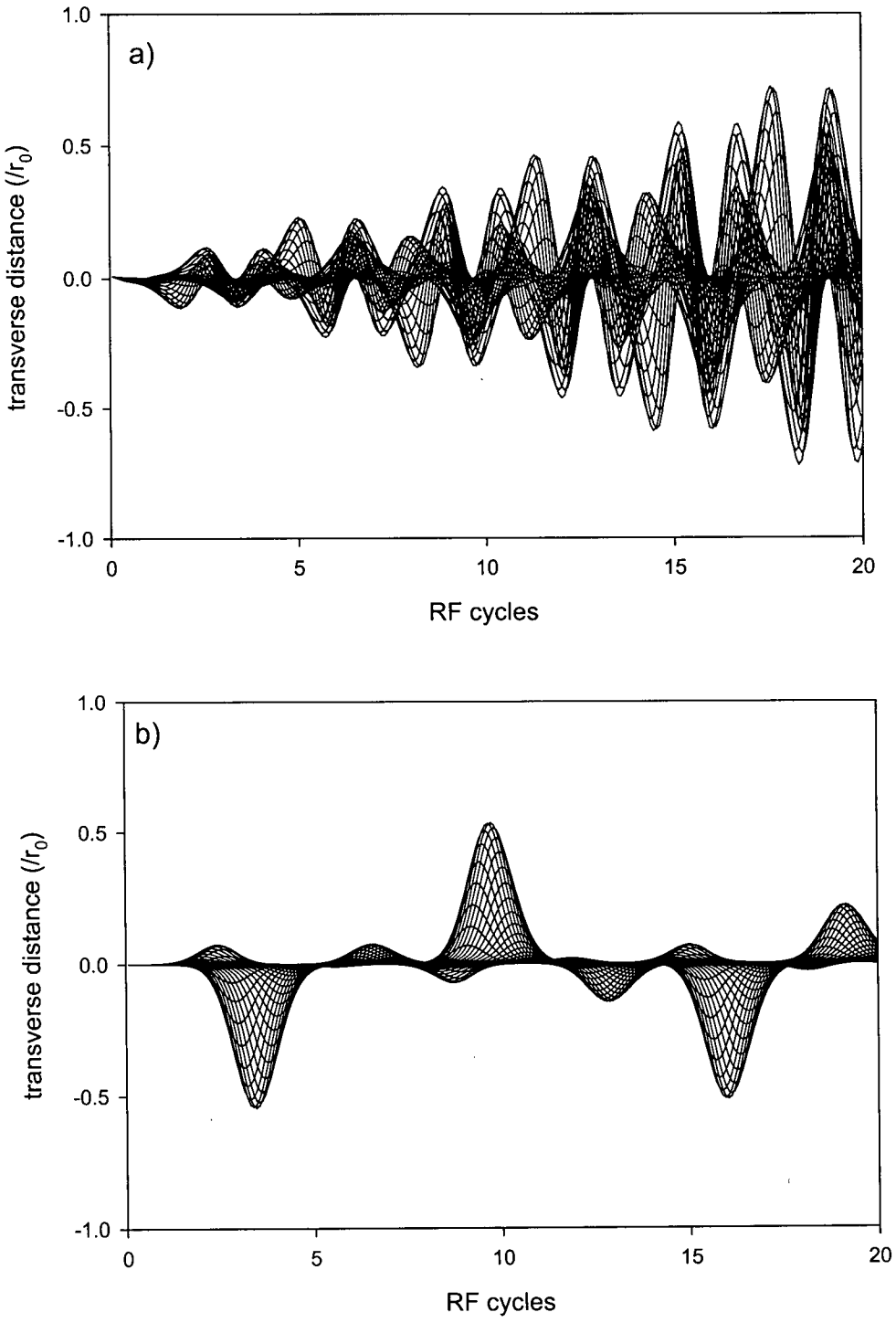

Figure 5.14 Ion trajectories for forty initial phases for the operating point B (a = 8.96671, q = 6.99650) outside the sixth stability region on a scan line across the upper tip of the region. (a) The trajectories in the xz plane; (b) The trajectories in the yz plane.

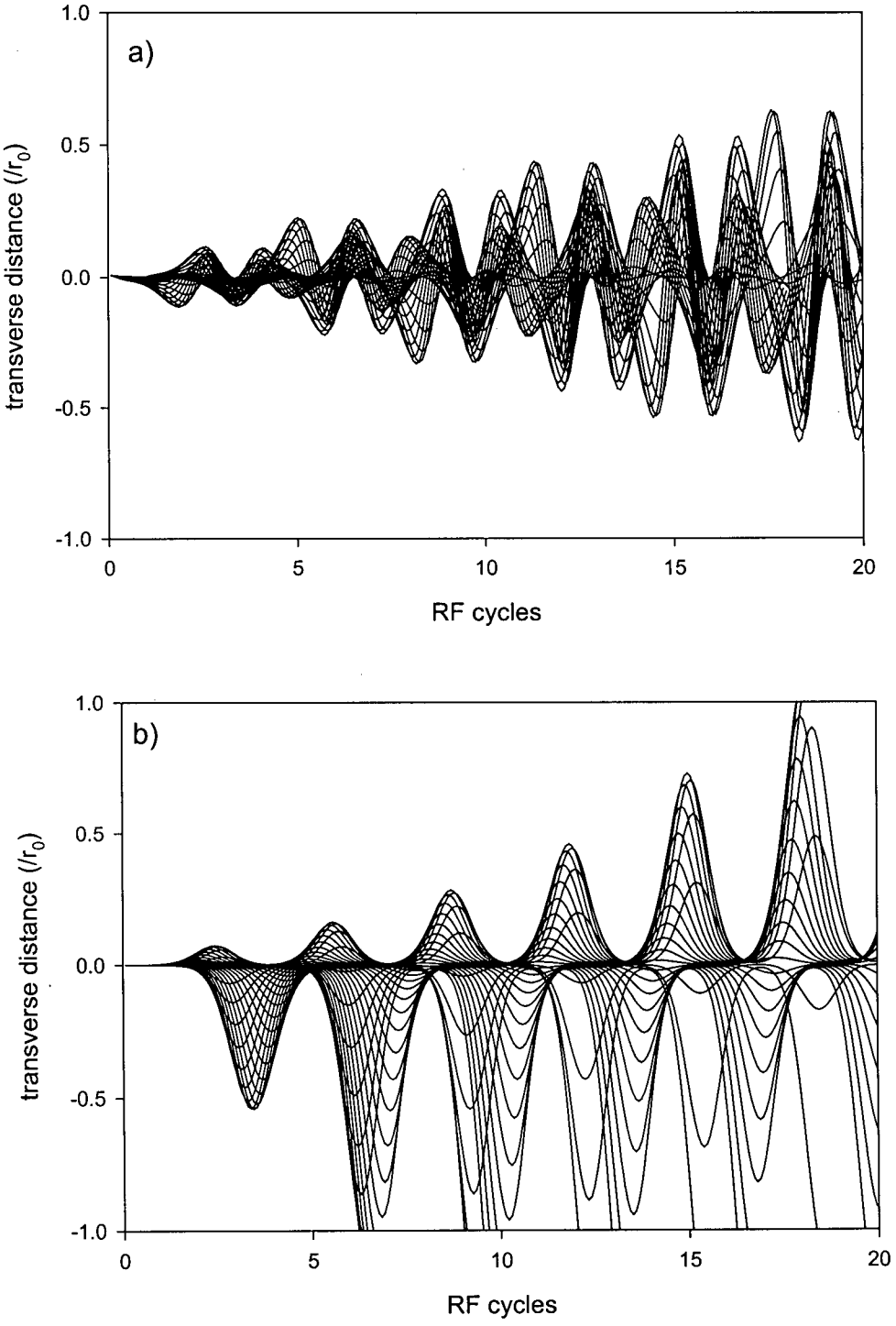

Figure 5.15 Ion trajectories for forty initial phases for the operating point C (a = 8.96108, q = 6.9921) outside the sixth stability region on a scan line across the upper tip of the region. (a) The trajectories in the xz plane; (b) The trajectories in the yz plane.

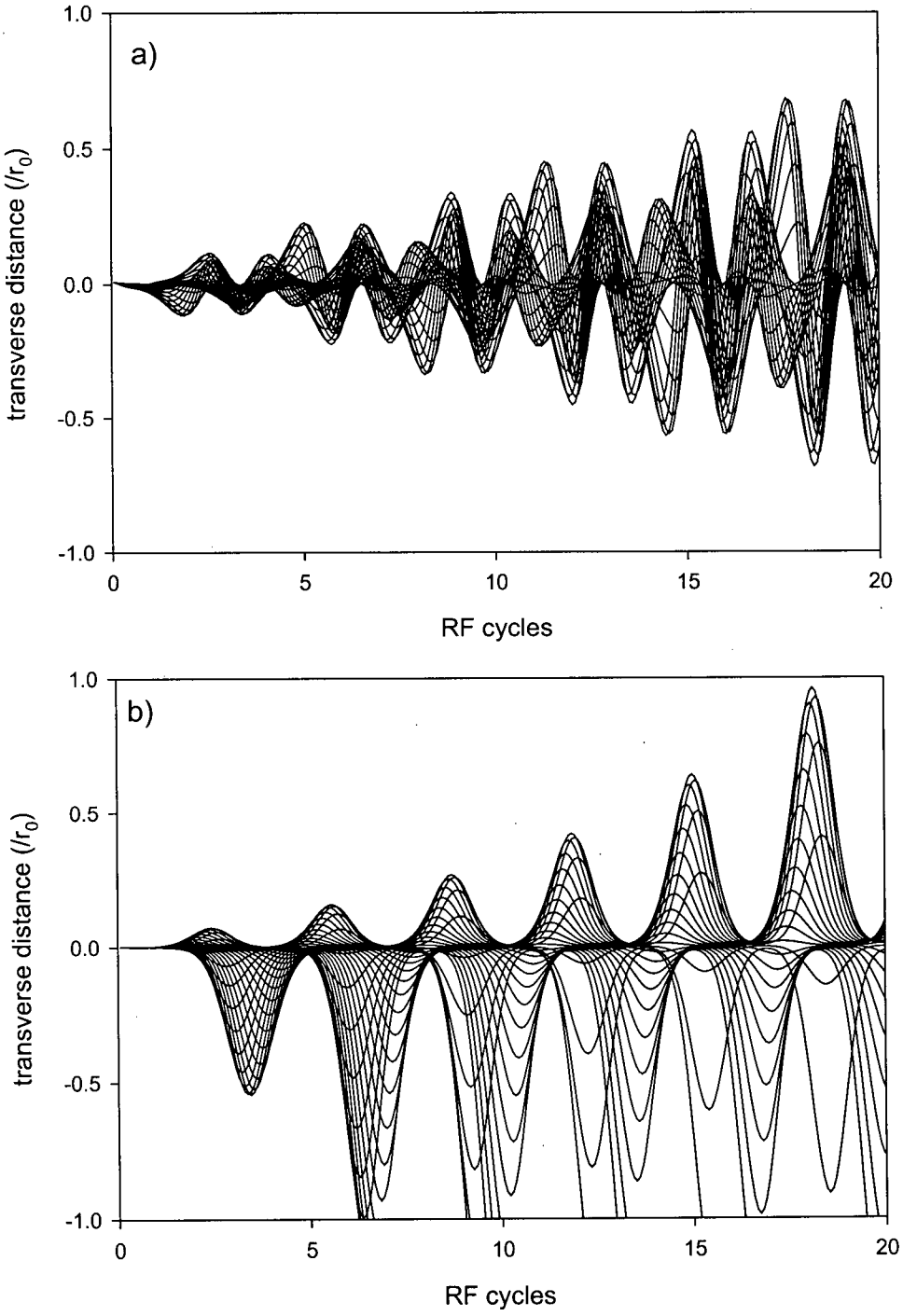

Figure 5.16 Ion trajectories for forty initial phases for the operating point D (a = 8.96453, q = 6.99425) outside the sixth stability region on a scan line that is above the upper tip of the region. (a) The trajectories in the xz plane; (b) The trajectories in the yz plane.

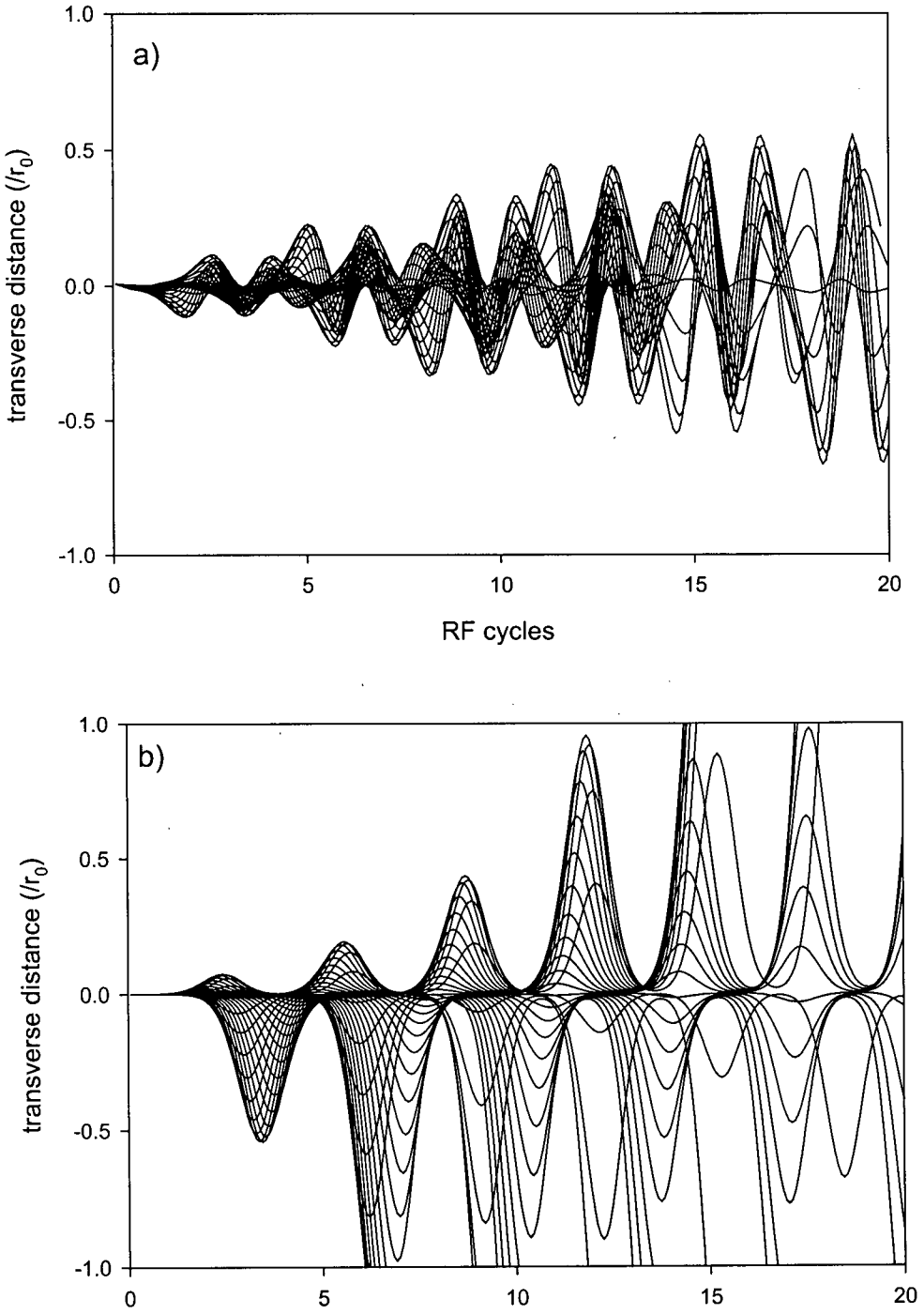

Figure 5.17 Ion trajectories for forty initial phases for the operating point F (a = 8.96338, q = 6.99335) outside the sixth stability region on a scan line that is above the upper tip of the region. (a) The trajectories in the xz plane; (b) The trajectories in the yz plane.

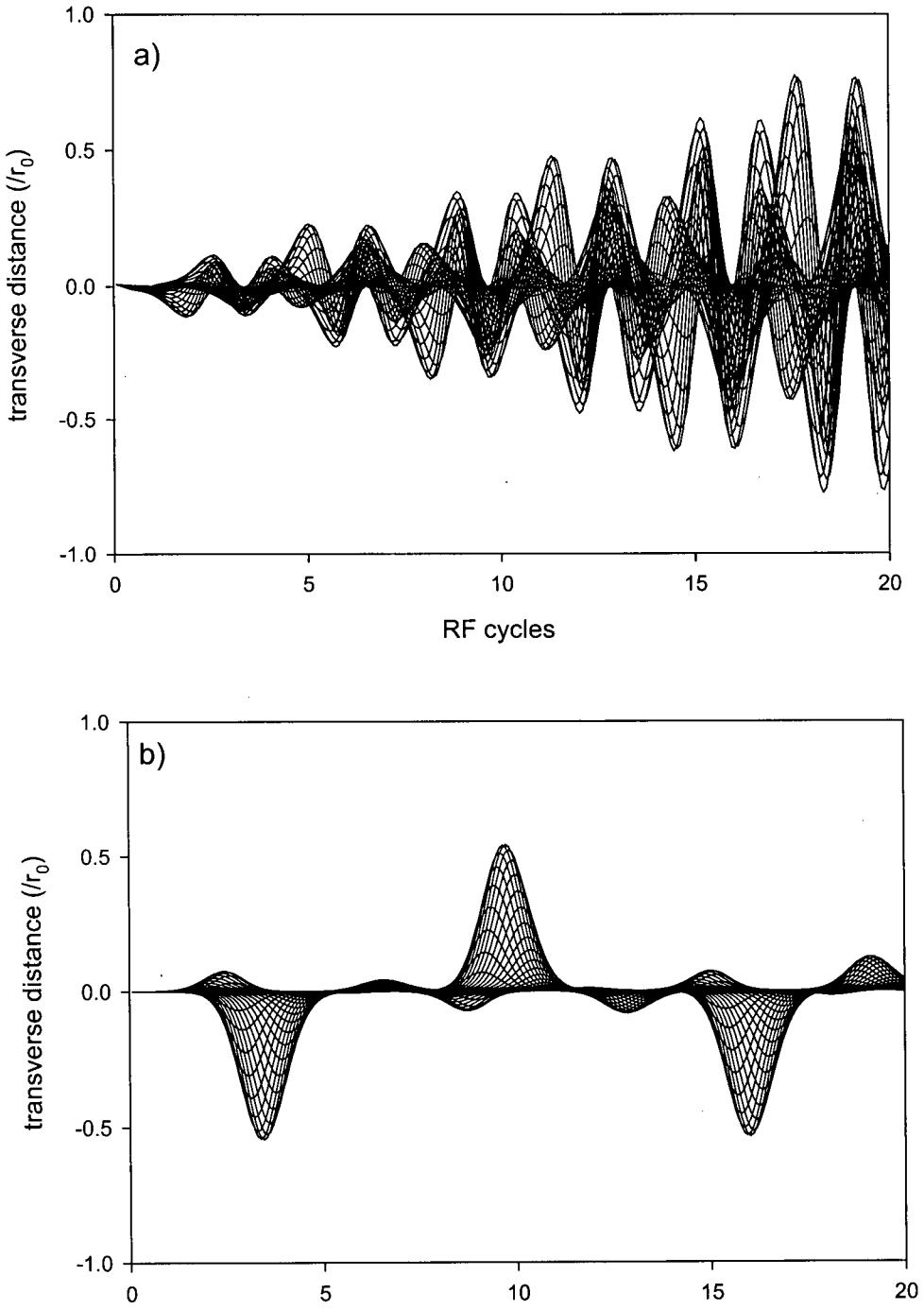

Figure 5.18 Ion trajectories for forty initial phases for the operating point E (a = 8.96991, q = 6.99845) outside the sixth stability region on a scan line that is above the upper tip of the region. (a) The trajectories in the xz plane; (b) The trajectories in the yz plane.

At the lower tip of the sixth region, the ion behavior is similar to that at the upper tip. Ion motion in the y direction determines whether an ion can pass through the quadrupole filter. On scan line 3, because the operating point G (Figure 5.19) is inside the stability region and point H (Figure 5.20) is inside the y-stability band, the ions at both points are transmitted by the quadrupole filter. At the operating point I (Figure 5.21) which is inside the x stability band, most of the ions stay in the quadrupole filter for about 9 RF cycles (59 eV $^{39}K^+$ ions). With longer residence times, the ions may hit the y rods. This means that when a scan line crosses the lower tip of the sixth region, the peak shape is not determined by the intersection of the scan line with the stability region boundaries, but is determined only by the intersection with the y-stability boundaries. When the input ion energy increases (for example, the energy of $^{39}K^+$ ions is larger than 100 eV), ions at operating points G, H and I are all transmitted by the quadrupole, thus the peak broadens. For the operating points on scan line 4, only ions at the point K (Figure 5.22) are stable. Although point J (Figure 5.23) is outside of both the x and y-stability zones, it is closer to the y-stability band than point L. The ions thus have relatively more stable trajectories in the y direction than those at point L, at least for residence times below 20 RF cycles. These ion trajectories show that it is possible to obtain a peak with operation outside of the sixth stability region, and the ion transmission is determined mostly by ion motion in the y direction. Because the ion trajectory simulations only show ion behavior at certain operating points and for one initial x_0, y_0, $\dot{x}_0$ and $\dot{y}_0$, transmission curve simulations were used to give a direct view of the ion optical properties with operation inside and near the sixth stability region.

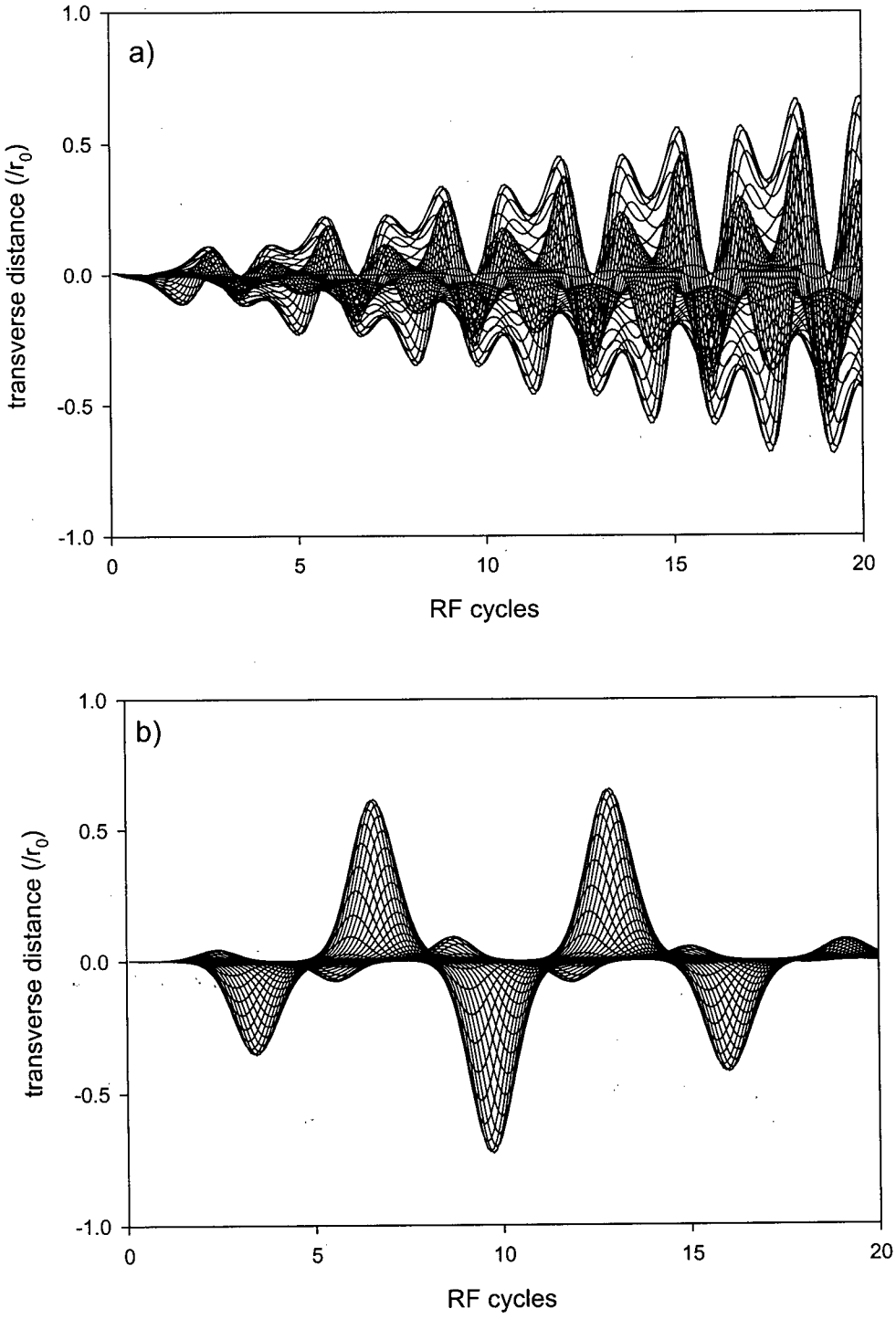

Figure 5.19 Ion trajectories for forty initial phases for the operating point G (a =7.97764, q = 6.3839) inside the sixth stability region on a scan line across the lower tip of the region. (a) The trajectories in the xz plane; (b) The trajectories in the yz plane.

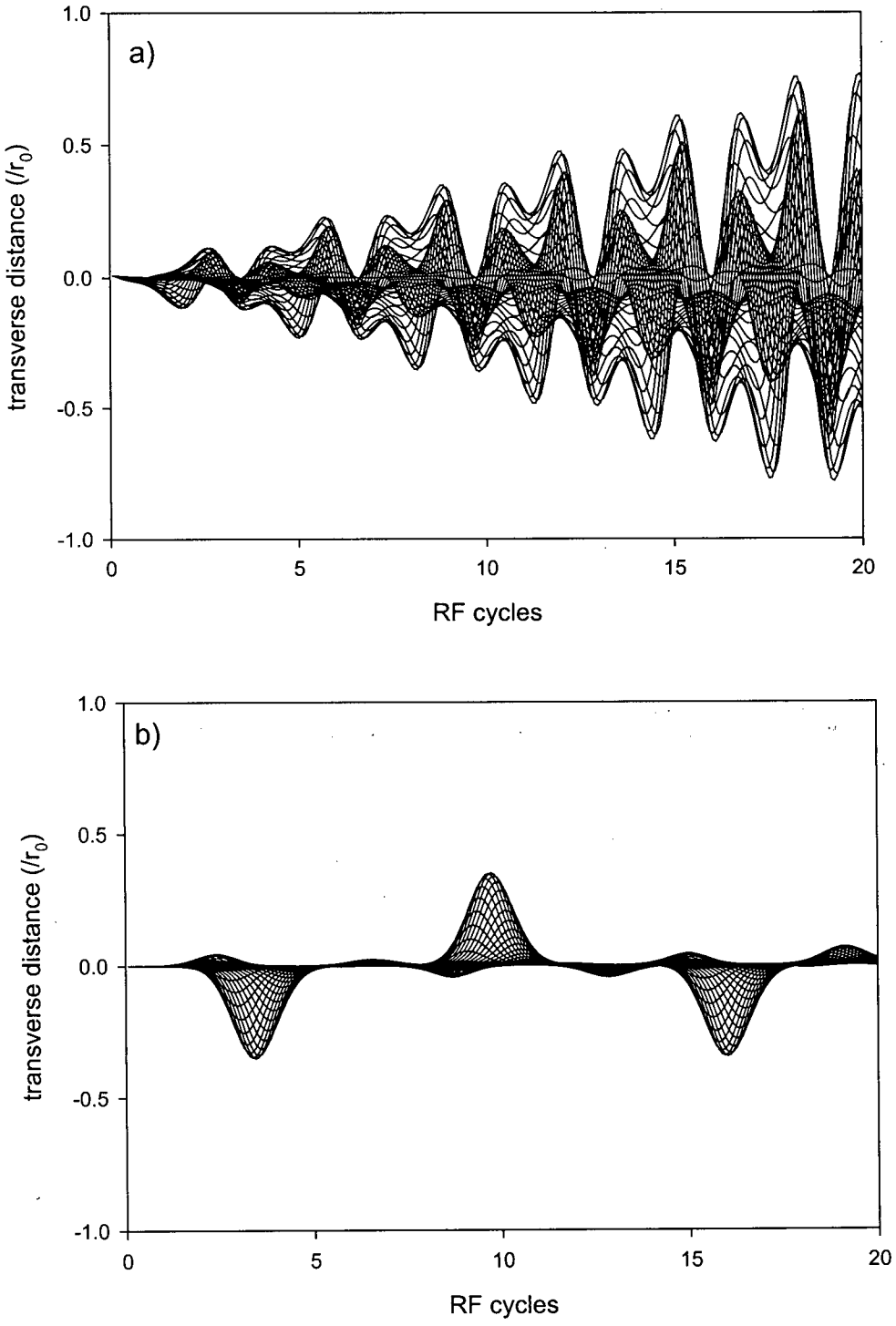

Figure 5.20 Ion trajectories for forty initial phases for the operating point H (a =7.97195, q = 6.37935) outside the sixth stability region on a scan line across the lower tip of the region. (a) The trajectories in the xz plane; (b) The trajectories in the yz plane.

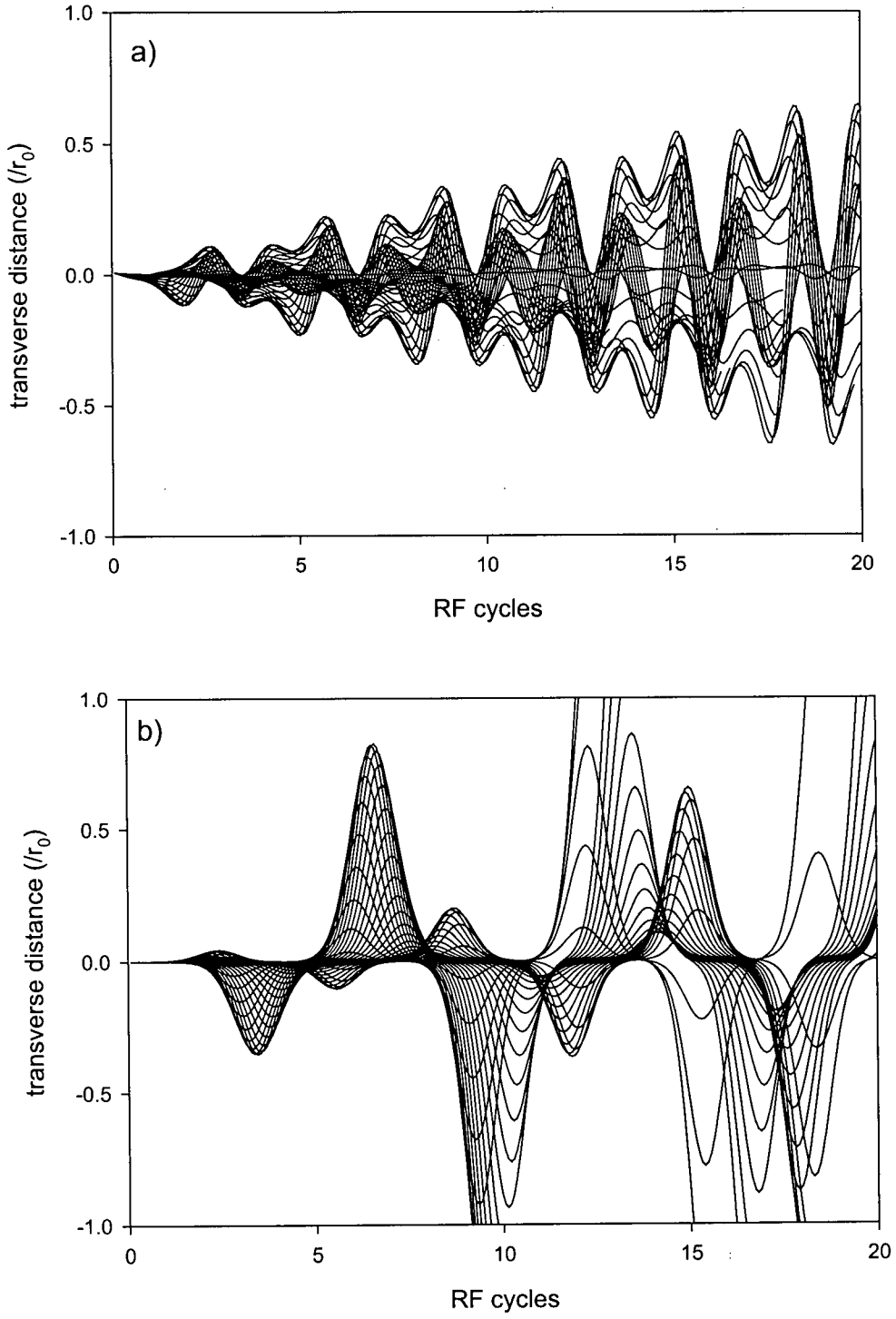

Figure 5.21 Ion trajectories for forty initial phases for the operating point I (a =7.97964, q = 6.38550) outside the sixth stability region on a scan line across the lower tip of the region. (a) The trajectories in the xz plane; (b) The trajectories in the yz plane.

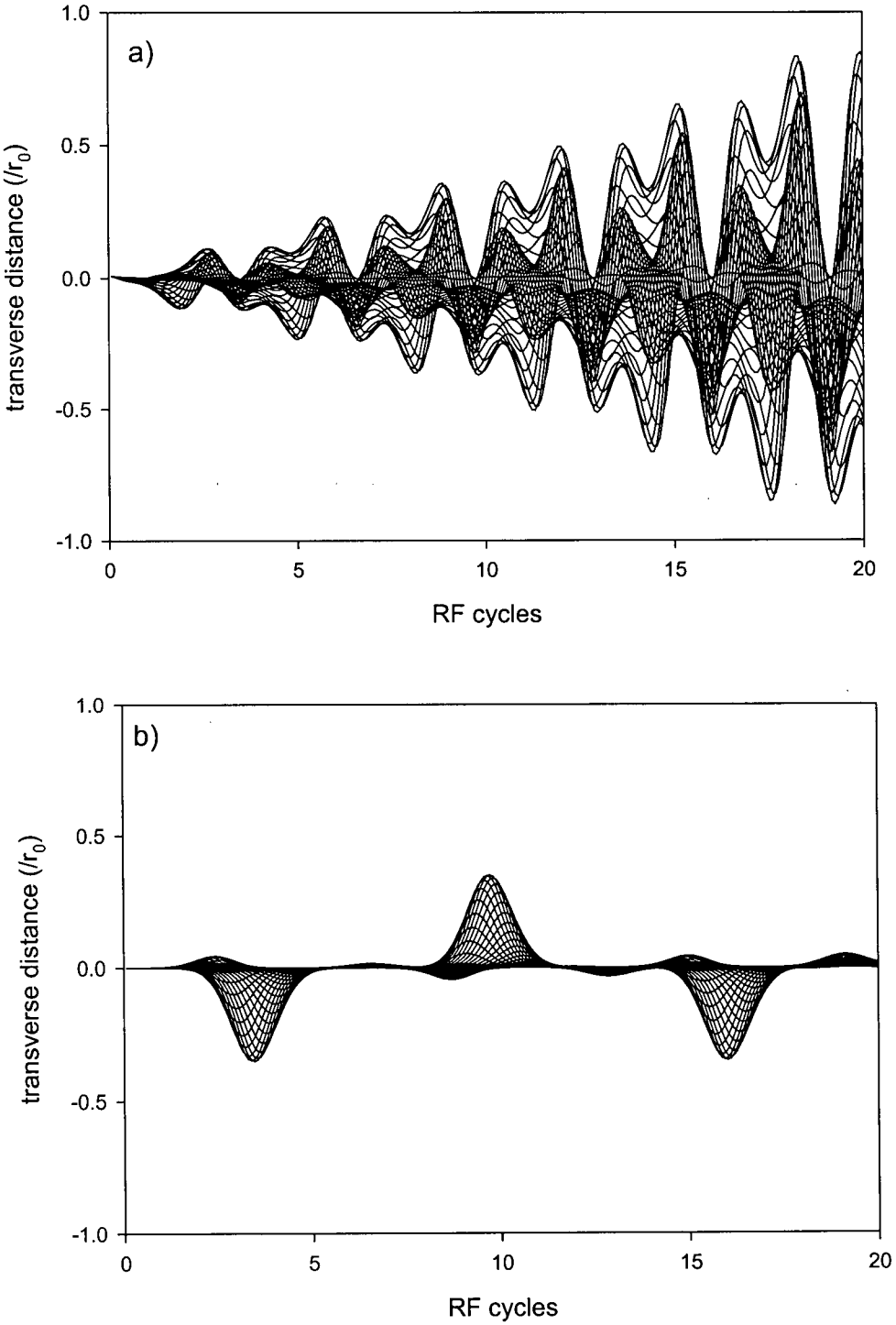

Figure 5.22 Ion trajectories for forty initial phases for the operating point K (a = 7.96756, q = 6.37660) outside the sixth stability region on a scan line that is below the lower tip of the region. (a) The trajectories in the xz plane; (b) The trajectories in the yz plane.

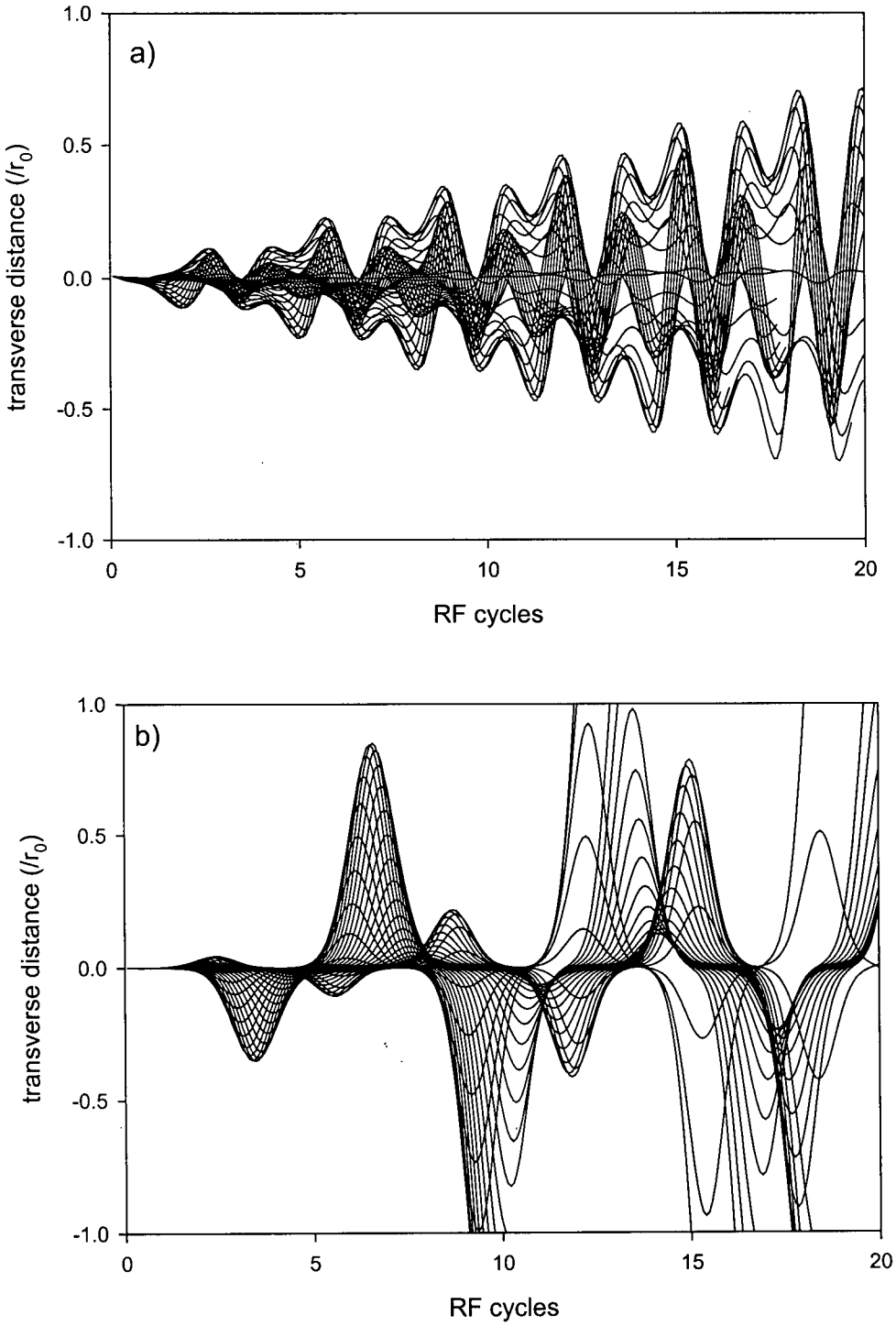

Figure 5.23 Ion trajectories for forty initial phases for the operating point J (a = 7.97556, q = 6.38300) outside the sixth stability region on a scan line across the lower tip of the region. (a) The trajectories in the xz plane; (b) The trajectories in the yz plane.

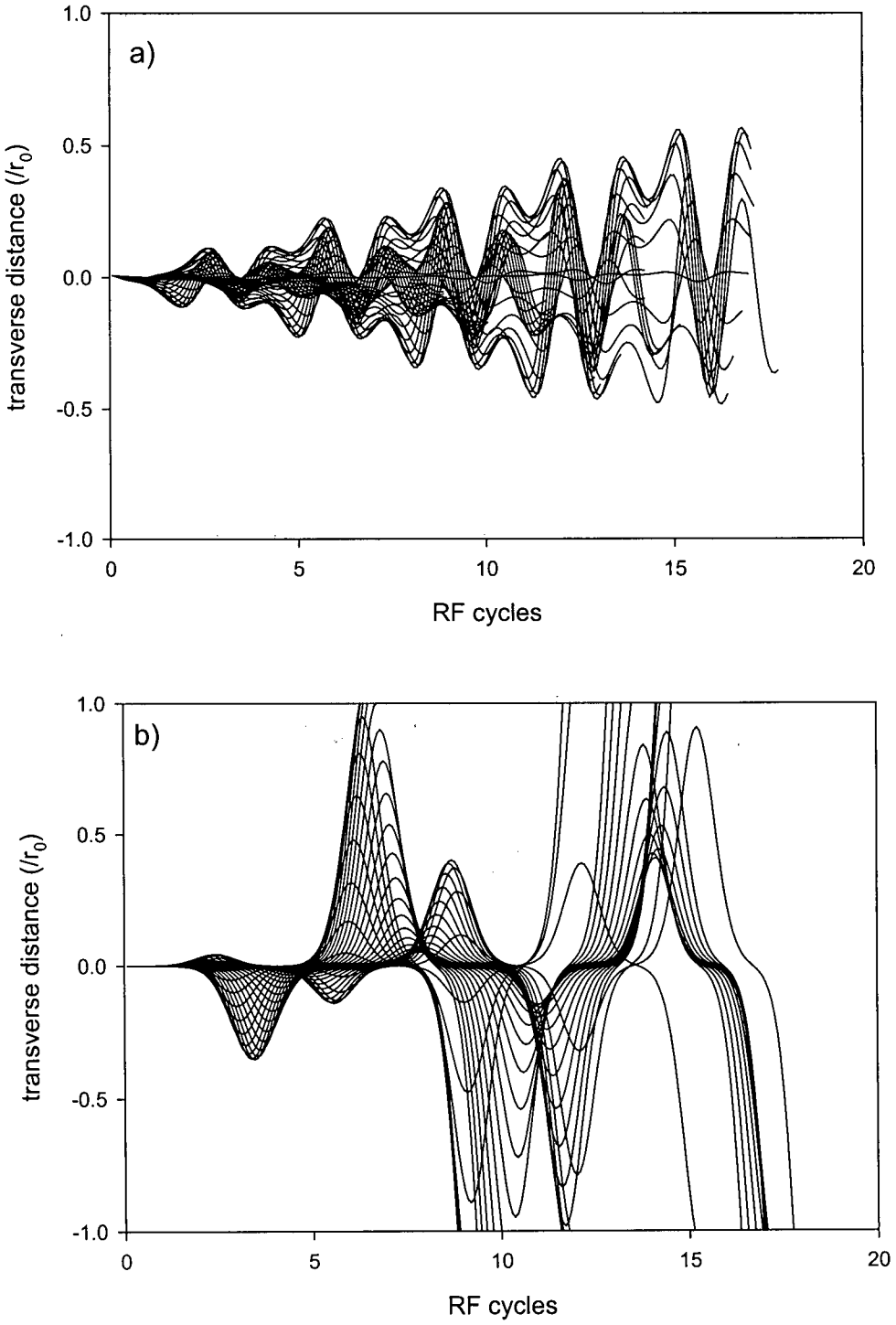

Figure 5.24 Ion trajectories for forty initial phases for the operating point L (a =7.97806, q = 6.38500) outside the sixth stability region on a scan line across the lower tip of the region. (a) The trajectories in the xz plane; (b) The trajectories in the yz plane.

b) Transmission Curve simulations

Both the ion trajectory simulations and experiments show that it is possible to obtain a peak with a scan line outside of the sixth stability region. Figure 5.25 shows four groups of peaks with different ion injection energies calculated for a series of scan lines moving through the sixth region from below the lower tip to above the upper tip. For the 20 eV ions, most of the peaks are obtained for *a, q* within the sixth region (Figure 5.25a). It is seen that the ion transmission decreases as the scan line moves towards the tips. The peak becomes narrower at the upper tip and has almost no change at the lower tip. This is probably because the ion transmission mostly depends on the stability of ion motion in the y direction, and the y-stability band becomes narrower as the *a, q* values increase. As the ion injection energy increases, the peak becomes broader for the whole region, especially at the lower tip. It is also seen that peaks can be produced with a scan line moved further away from the tips of the sixth stability region. When the ion energy is very large (i.e. 1000 eV), there is no decrease in intensity at the lower tip. This probably means that, when the ion injection energy is sufficiently high, the transverse distance for the ion motion in the x direction is always less than the field radius whether the quadrupole is operated inside or outside the stability band in the x direction. The ion transmission is totally determined by the ion motion in the y direction. With operation outside but near the y boundaries, as the ion injection energy increases, more ions are transmitted. The y boundaries become diffuse and the peaks become broader.

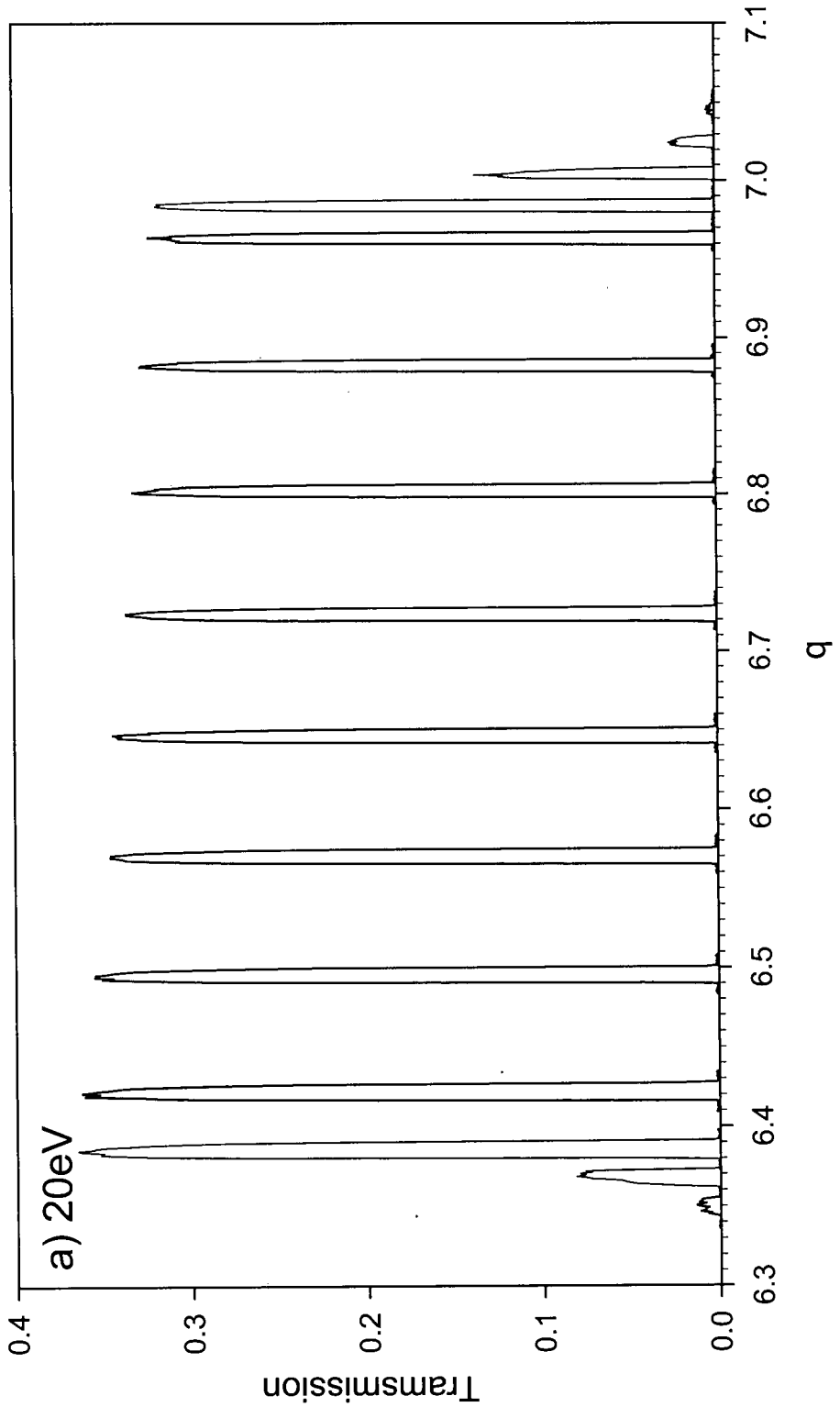
a) 20eV
Transmission
0.0
0.1
0.2
0.3
0.4
6.3
6.4
6.5
6.6
6.7
6.8
6.9
7.0
7.1
q

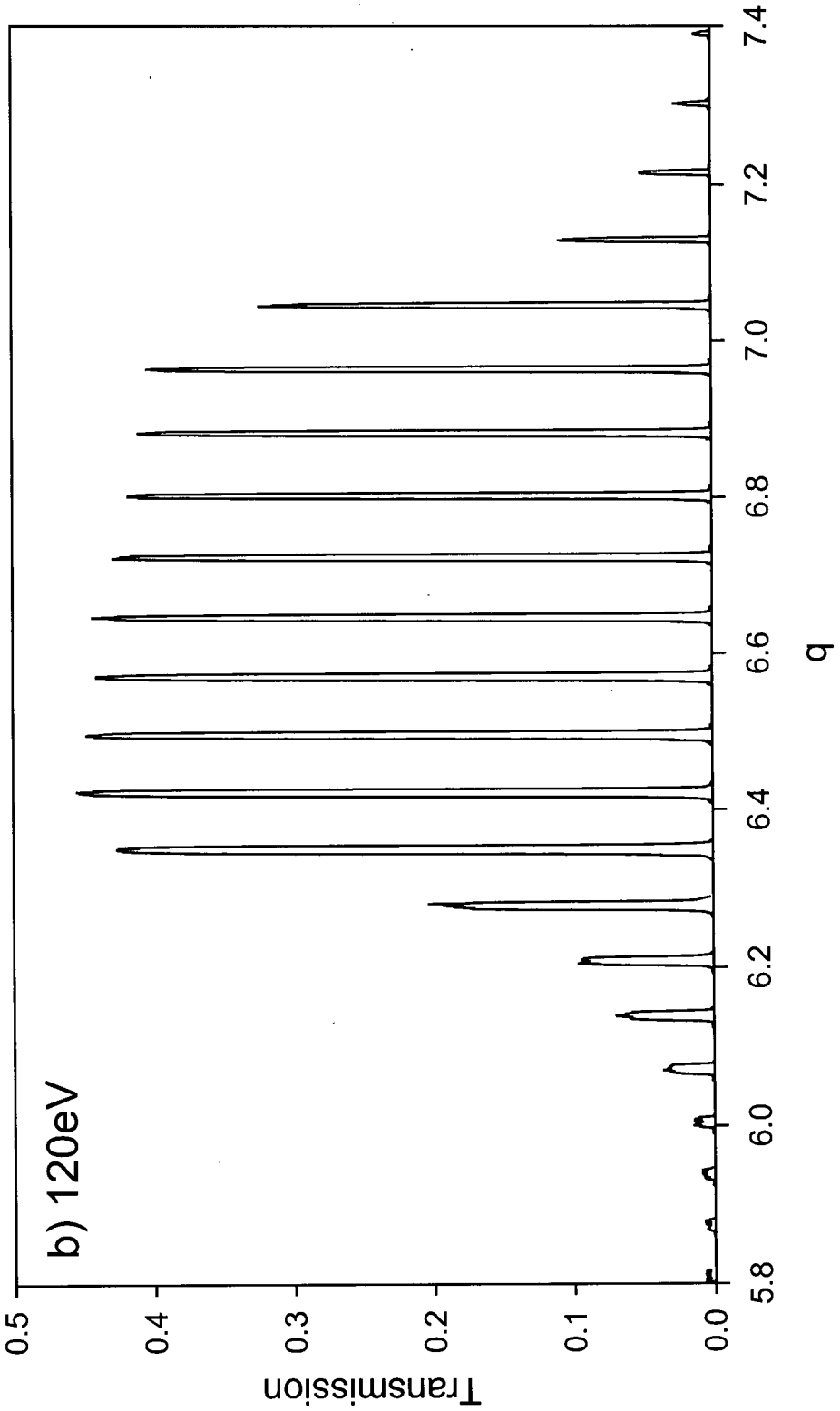
b) 120eV
Transmission
0.0
0.1
0.2
0.3
0.4
0.5
5.8
6.0
6.2
6.4
6.6
6.8
7.0
7.2
7.4
q

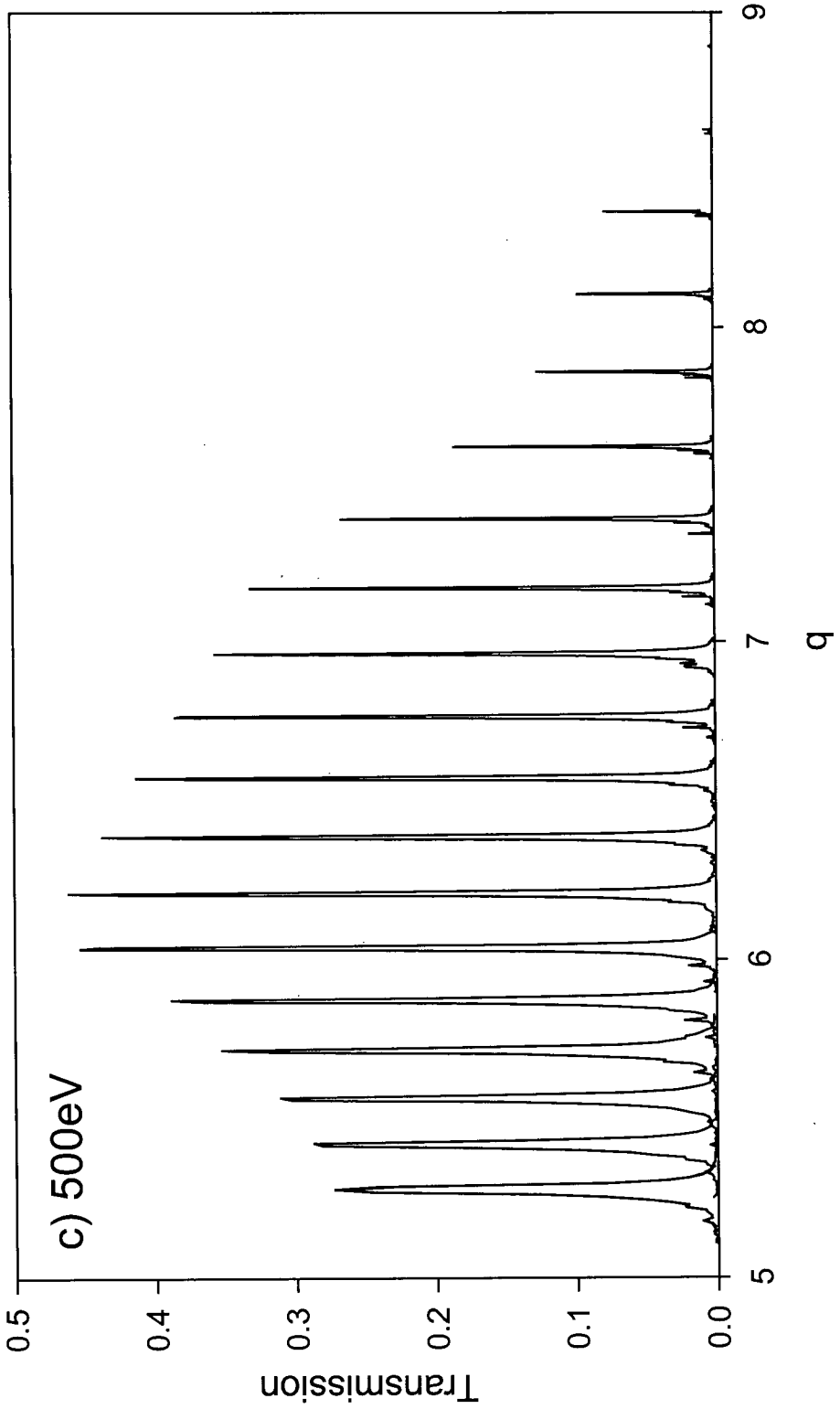
c) 500eV
Transmission
0.0
0.1
0.2
0.3
0.4
0.5
5
6
7
8
9
q

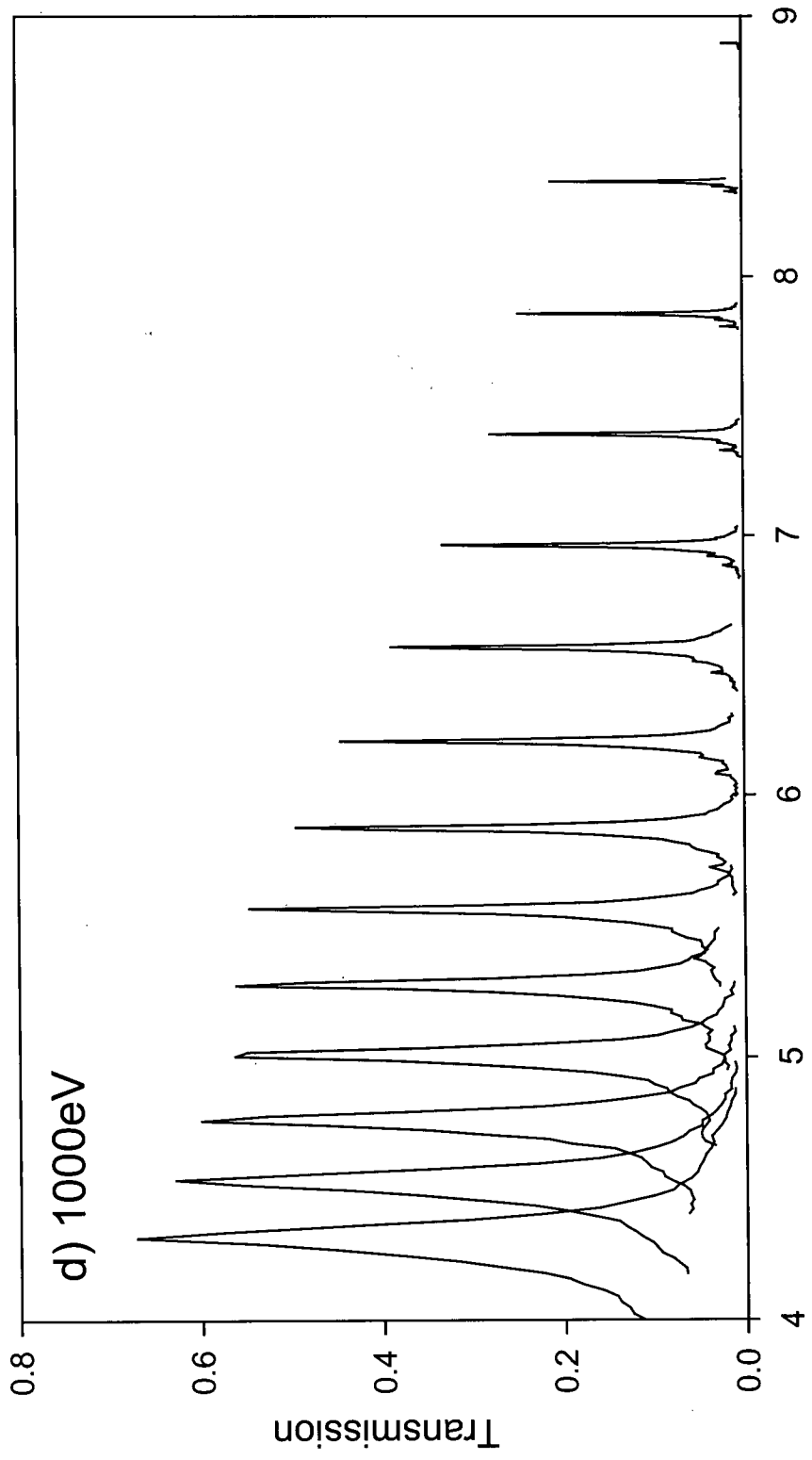

Figure 5.25 The calculated peak shapes with an operating line lying inside and outside the 6th stability region. The ion injection energies are a) 20 eV, b) 120 eV, c) 500 eV and d) 1000 eV. The upper and lower tips have q values of 6.9938 and 6.3835, respectively.

This simulation also clarifies the T-R behavior that was observed with operation at the lower tip of the region. The mass resolution is equal to $q/\Delta q$ in this simulation. When a scan line moves toward the lower tip or even further, the q value decreases. For the lower energy ions, the Δq values almost have no change, only the ion intensity decreases. This gives a sharply dropping T-R curve. For the higher energy ions, Δq increases with slight decreases in transmission. Therefore the T-R curve shows that the ion transmission decreases as the resolution decreases. Calculated T-R curves from the simulated peak shapes for 20 eV ions are shown in Figure 5.26. Because the T-R curves depend on many factors such as the emittance of the ion source, the acceptance of the quadrupole field, the overlap between the emittance and the acceptance, fringing field and the quality of the field, here we only compare the trend of the calculated T-R curves with that of the experimental curves. The T-R curve for operation at the upper tip is quite similar to the experimental curve. Although we did obtain the T-R curve experimentally at the lower tip for 20 eV ions, the calculated trend is more like that for 120 eV ions (see Figure 4.15).

The stability boundaries in the y direction can be taken as the edges of the peak defined at a small percentage of the maximum. Based on the calculated peaks in Figure 5.25, several calculated diffuse boundaries for the y direction with different ion energies are shown in Figure 5.27. For a given λ, the q values for the diffuse boundary are chosen at the sides of the calculated peak, where the ion transmission is 50 out of 5000 ions (1%). It is seen that at lower ion energies, the boundaries match the stability diagram. As the ion injection energy increases, the boundaries become diffuse and the region of stability expands.

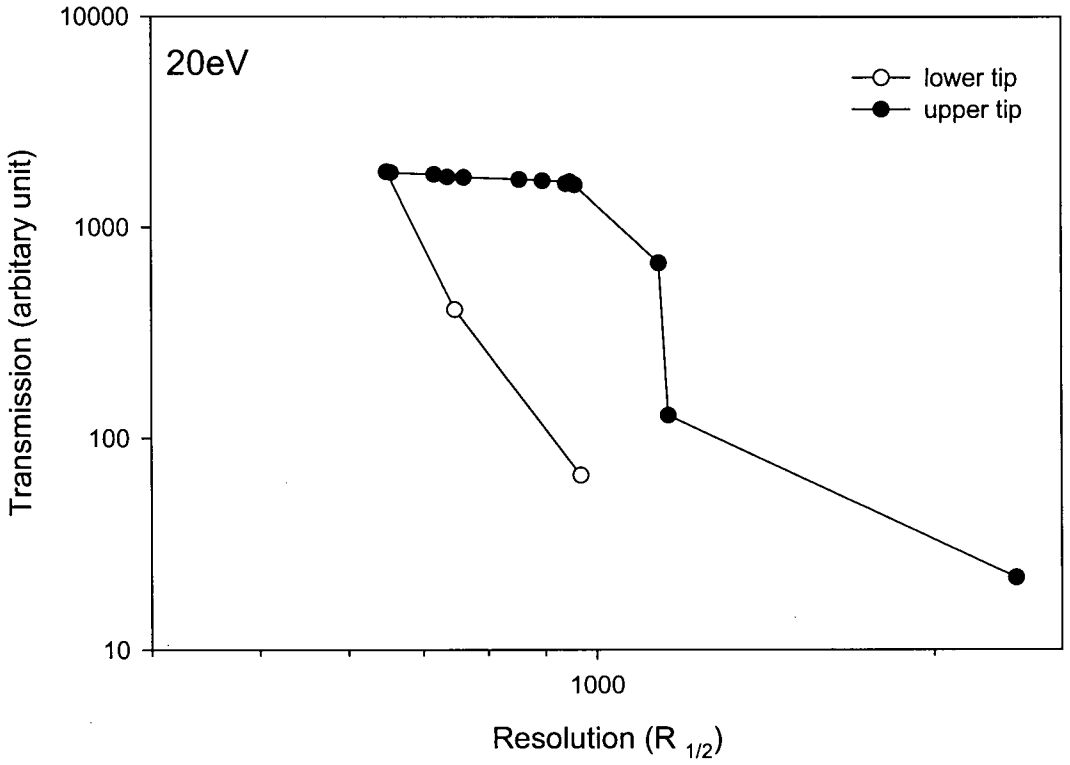

Figure 5.26 Calculated T-R curves at the upper tip and the lower tip of the sixth stability region with 20 eV $^{39}K^{+}$ ions.

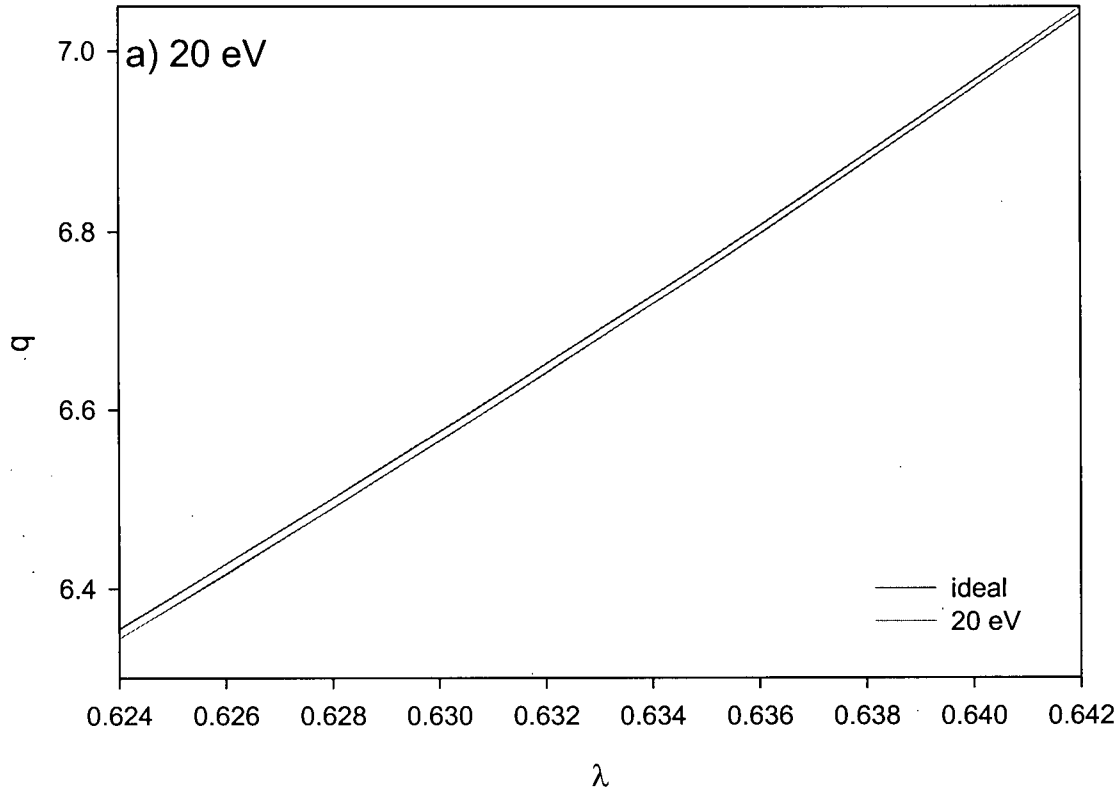
a) 20 eV
7.0
6.8
6.6
6.4
q
ideal
20 eV
0.624
0.626
0.628
0.630
0.632
0.634
0.636
0.638
0.640
0.642
λ

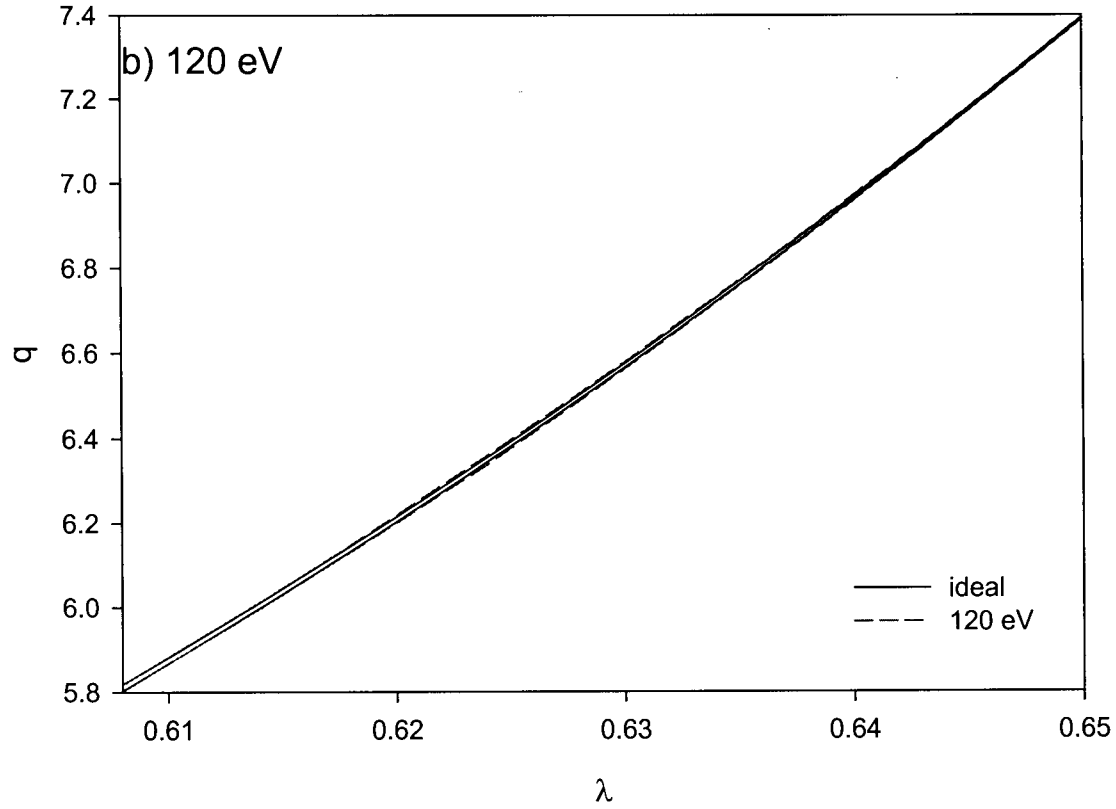
b) 120 eV
7.4
7.2
7.0
6.8
6.6
6.4
6.2
6.0
5.8
q
ideal
120 eV
0.61
0.62
0.63
0.64
0.65
λ

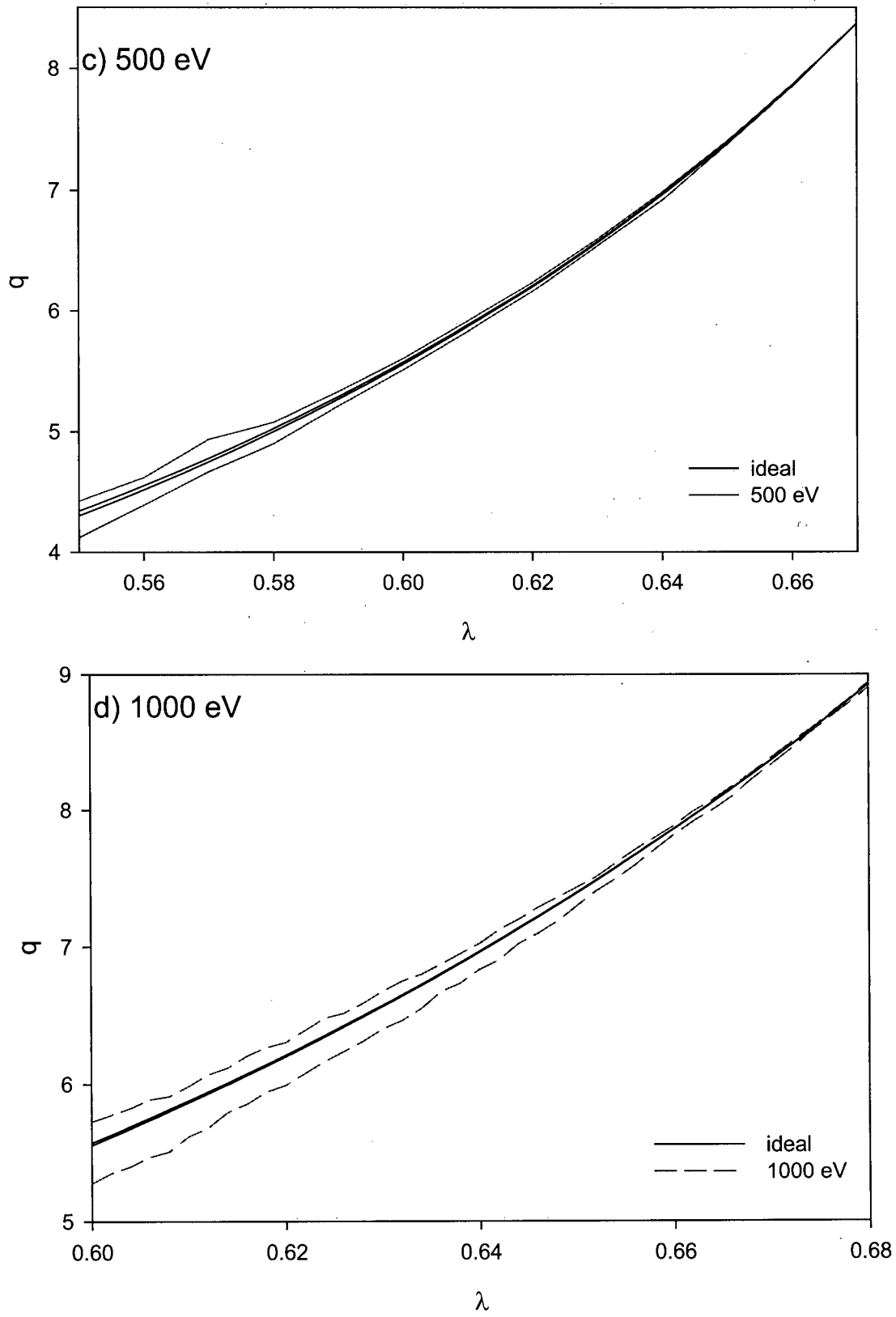

Figure 5.27 The calculated diffuse boundaries in the y direction with ion energies of a) 20 eV, b) 120 eV, c) 500 eV and d) 1000 eV.

5.4 Summary

For higher stability regions, ions need higher energy to penetrate the fringing field at the entrance of the quadrupole rods. Under these conditions, they experience fewer RF cycles inside the quadrupole field. This can result in diffuse boundaries. For the fourth stability region, a narrower peak could not be obtained with $a>0$ for ion energies larger than 500 eV. When the scan line is just above the apex, a split peak formed with a deep dip at the center. As the scan line moves to higher values, two peaks are obtained. For the sixth stability region, broader peaks are obtained with higher energy ions and the y-stability band dominates the ion transmission. When the ion injection energy is sufficiently high, ion transmission increases and resolution decreases as the scan line moves towards the lower tip.

Chapter 6

Summary and future work

This thesis describes an experimental and theoretical study of the ion optical properties of a quadrupole mass filter, operated in the fourth stability region with Mathieu parameters (a, q)≈(0.0, 21.3), and in the sixth stability region with Mathieu parameters (a, q)≈(8,6). Operation in the fourth stability region gives a resolution at half height at m/z = 39 of up to 13,900 with low energy ions and a resolution of several thousand with ions of several keV energy. The transmission is somewhat lower than that of the second stability region for a given resolution, but higher than that expected from acceptance calculations. With a quadrupole operated in the sixth region, the maximum resolution achieved was $R_{1/2}$ = 2000 with $^{39}K^{+}$ ions with an axial ion energy of 20 eV, and a resolution of several hundred was obtained with high energy ions (>1000 eV). This region could be used as an additional mass filter to eliminate alias ions when a quadrupole is operated in regions II or IV. For ions of intermediate energy, the sixth stability region also can be used as an independent mass filter.

For higher stability regions, ions generally experience fewer RF cycles inside the quadrupole field because higher energies are required to penetrate the fringing field at the entrance of the quadrupole rods. As a result, ions outside the stability regions can

pass through the quadrupole and the boundaries are diffuse. For the fourth stability region, a narrower peak could not be obtained with $a>0$ for ion energies larger than 500 eV. For the sixth stability region, broader peaks are obtained with higher energy ions and the y-stability band dominates the ion transmission.

One potential use of higher stability regions is to obtain high resolution on high energy ion beams. This can reduce the space charge problems in ICP-MS. Extracting such beams with current densities at least 100 times greater than that of commercial ICP-MS systems has been reported. Thus important future work with higher stability regions is to explore the combination of new ion extraction methods with operation of a quadrupole in higher regions to realize a simple, inexpensive, compact, fast scanning, and high resolution quadrupole ICP-MS system. Besides the stability regions that have been explored (i.e. region I, II, III, IV and VI), there is an unlimited number of stability regions that could be investigated for this purpose.

Bibliography

(1) McLuckey, S. A.; Wells, J. M. *Chemical Reviews*: United States, **2001**, *101*, 571-606.

(2) Dawson, P. H. *Mass Spectrom. Rev.*, **1986**, *5*, 1-37.

(3) Paul, W.; Reinhard, H. P.; Zahn, V. *Z. Physik*, **1958**, *152*, 143-82.

(4) *Quadrupole Mass Spectrometry and its Applications*; Dawson, P. H., Ed.; Elsevier:Amsterdam, **1976**.

(5) March, P. E.; Hughes, R. J. *Quadrupole Storage Mass Spectrometry*; John Wiley and Sons: New York, **1989**, .

(6) Douglas, D. J.; Thomson, B.; Corr, J.; Hager, J. ; U.S. Patent, 5,248,875, **1993**.

(7) Thomson, B. A.; Douglas, D. J.; Corr, J. J.; Hager, J. W.; Jolliffe, C. L. *Anal. Chem.*, **1995**, *67*, 1696-704.

(8) Thomson, B. A. *Can. J. Chem.*, **1998**, *76*, 499-505.

(9) Mansoori, B. A.; Dyer, E. W.; Lock, C. M.; Bateman, K.; Boyd, R. K. *J. Am. Soc. Mass Spectrom.*, **1998**, *9*, 775-788.

(10) Collings, B. A.; Campell, J. M.; Mao, D.; Douglas, D. J. *Rapid Commun. Mass Spectrom.* **2001**, *15*, 1777-1795.

(11) Chernushevich, I. V.; Ens, W.; Standing, K. G. *Anal. Chem.* **1999**, *71*, 452A-461A.

(12) Campbell, J. M.; Collings, B. A.; Douglas, D. J. *Rapid Commun. Mass Spectrom.*, **1998**, *12*, 1463-1474.

(13) Tanner, S. D.; Baranov, V. I. *J. Am. Soc. Mass Spectrom.*, **1999**, *10*, 1083-1094.

(14) Tanner, S. D.; Baranov, V. I. *At. Spectrosc.*, **1999**, *20*, 45-52.

(15) Tanner, S. D.; Baranov, V. I.; Vollkopf, U. *J. Anal. At. Spectrom.*, **2000**, *15*, 1261-1269.

(16) Amad, M. H.; Houk, R. S. *Anal. Chem.*, **1998**, *70*, 4885-4889.

Bibliography

(17) Amad, M. H.; Houk, R. S. *J. Am. Soc. Mass Spectrom.*, **2000**, *11*, 407-415.

(18) Miseki, K. *U.S. Patent*, **1993**, , 5,227,629.

(19) de Maack, F.; Devant, G.; Lapetit, G.; Rolando, C. *Proceedings of the 36th ASMS conf. on Mass Spectrom. Allied. Topics, San Francisco, CA* **1988**, 817.

(20) Beaugrand, C. *personal communication* **1998**.

(21) Konenkov, N. V.; Cousins, L. M.; Baranov, V. I.; Sudakov, M. Y. *Int. J. Mass Spectrom.*, **2001**, *208*, 17-27.

(22) Du, Z.; Olney, T. N.; Douglas, D. J. *J. Am. Soc. Mass Spectrom.*, **1997**, *8*, 1230-1236.

(23) Douglas, D. J.; Konenkov, N. V. *J. Am. Soc. Mass Spectrom.*, **1998**, *9*, 1074-1080.

(24) Du, Z.; Douglas, D. J.; Konenkov, N. *J. Am. Soc. Mass Spectrom.*, **1999**, *10*, 1263-1270.

(25) Du, Z.; Douglas, D. J.; Konenkov, N. *J. Anal. At. Spectrom.*, **1999**, *14*, 1111-1119.

(26) Du, Z.; Douglas, D. J. *J. Am. Soc. Mass Spectrom.*, **1999**, *10*, 1053-1066.

(27) Du, Z.; Douglas, D. J.; Glebova, T.; Konenkov, N. V. *Int. J. Mass Spectrom.*, **2000**, *197*, 113-121.

(28) Chen, W.; Collings, B. A.; Douglas, D. J. *Anal. Chem.*, **2000**, *72*, 540-545.

(29) Vanhaecke, F.; Moens, L. *Fresenius J. Anal. Chem.* **1999,** *364*, 440-451.

(30) Fairman, B.; Hinds, M. W.; Nelms, S. M.; Penny, D. M.; Goodall, P. *J. Anal. At. Spectrom.*, **1999**, *14*, 1937-1969.

(31) Sharp, B. L.; Batey, J.; Begley, I. S.; Gregson, D.; Skilling, J.; Sulaiman, A. B.; Verbogt, G. *J. Anal. At. Spectrom.*, **1999**, *14*, 99-108.

(32) Greenfield, S.; Foulkes, M. *Inductively Coupled Plasma Spectrometry and Its Applications*, **1999**, 1-34.

(33) Kikawada, Y. *Nippon Kaisui Gakkaishi*, **1999**, *53*, 115-116.

(34) Ebihara, M. *Radioisotopes*, **2001**, *50*, 113-115.

Bibliography

(35) Bacon, J. R.; Crain, J. S.; Van Vaeck, L.; Williams, J. G. *J. Anal. At. Spectrom.*, **2001**, *16*, 879-915.

(36) *Inductively Coupled Plasma Mass Spectrometry*; Montaser, A., Ed.; Wiley-VCH: New York, **1998**, .

(37) Horlik, G.; Shao, Y. *Chapter 12* in *Inductively Coupled Plasmas In Analytical Atomic Spectrometry, Second Edition*; Montaser, A., Golightly, D. W., Eds.; VCH Publishers, Inc.: New York, **1992**; , .

(38) Moens, L.; Jakubowski, N. *Anal. Chem.*, **1998**, *70*, 251A-256A.

(39) Marchante-Gayon, J.; Muniz, C.; Alonso, J.; Sanz-Medel, A. *Anal. Chim. Acta*, **1999**, *400*, 307-320.

(40) Milgram, K. E.; White, F. M.; Goodner, K. L.; Watson, C. H.; Koppenaal, D. W.; Barinaga, C. J.; Smith, B. H.; Winefordner, J. D.; Marshall, A. G.; Houk, R. S.; Eyler, J. R. *Anal. Chem.*, **1997**, *69*, 3714-3721.

(41) Douglas, D. J.; French, J. B. *J. Anal. At. Spectrom.*, **1988**, *3*, 743-7.

(42) Tanner, S. D. *Spectrochim. Acta,* **1992**, *47B*, 809-23.

(43) Tanner, S. D. *Anal. Proc. (London)*, **1992**, *29*, 281.

(44) Niu, H.; Houk, R. S. *Spectrochim. Acta, Part B*, **1996**, *51B*, 779-815.

(45) Dawson, P. H.; Yu, B. *Int. J. Mass Spectrom. Ion Processes*, **1984**, *56*, 25-39.

(46) Dawson, P. H.; Yu, B. *Int. J. Mass Spectrom. Ion Processes*, **1984**, *56*, 41-50.

(47) Konenkov, N. V.; Kratenko, V. I. *Int. J. Mass Spectrom. Ion Processes*, **1991**, *108*, 115-36.

(48) Olney, T. N.; Chen, W.; Douglas, D. J. *J. Anal. At. Spectrom.*, **1999**, *14*, 9-17.

(49) Al Moussalami, S.; Chen, W.; Collings, B. A.; Douglas, D. J. *Rev. of Sci. Instr.*, **2002**, *73*, 884-886.

(50) Dawson, P. H. *Adv. Electron. Electron Phys.*, **1980**, *53*, 153.

(51) Douglas, D. J. *Can. J. Spectrosc.*, **1989**, *34*, 38-49.

Bibliography

(52) Austin, W. E.; Holme, A. E.; Leck, J. H. *Chapter 6* in *Quadrupole Mass Spectrometry and its Applications*; Dawson, P., Ed.; Elsevier: Amsterdam, **1976**, pp 121-52.

(53) Titov, V. V. *J. Am. Soc. Mass Spectrom.*, **1998**, *9*, 50-69.

(54) Titov, V. V. presented at *The 1998 Winter Conference on Plasma Spectrochemistry*, Scottsdale, Arizona, Jan. 5-10 **1998**; ; .

(55) Titov, V. V. *J. Am. Soc. Mass Spectrom.*, **1998**, *9*, 70-87.

(56) Ying, J.F.; Douglas, D. J. *Rapid Commun. Mass Spectrom.*, **1996**, *10*, 649-52.

(57) Hennequin, J. F.; Inglebert, R. L. *Int. J. Mass Spectrom. Ion Phys.*, **1978**, *26*, 131-5.

(58) Dawson, P. H. *Int. J. Mass Spectrom. Ion Phys.*, **1976**, *21*, 317-32.

(59) Hennequin, J. F.; Inglebert, R. L. *Rev. Phys. Appl.*, **1979**, *14*, 275-87.

(60) Dawson, P. H.; Yu, B. *Int. J. Mass Spectrom. Ion Processes*, **1983**, *54*, 159-67.

(61) Dawson, P. H. *Int. J. Mass Spectrom. Ion Processes*, **1990**, *100*, 41-50.

(62) Brubaker, W. M. *Advan. Mass Spectrom.*, **1968**, *4*, 293-9.

(63) Dawson, P. H. *Int. J. Mass Spectrom. Ion Phys.*, **1971**, *6*, 33-44.

(64) Dawson, P. H. *Int. J. Mass Spectrom. Ion Phys.*, **1974**, *14*, 317-37.

(65) McIntosh, B. J.; Hunter, K. L. *Int. J. Mass Spectrom. Ion Processes*, **1989**, *87*, 157-79.

(66) Konenkov, N. V. *Int. J. Mass Spectrom. Ion Processes*, **1993**, *123*, 101-5.

(67) Dawson, P. H. *Int. J. Mass Spectrom. Ion Phys.*, **1975**, *17*, 423.

(68) Dawson, P. H. *Int. J. Mass Spectrom. Ion Phys.*, **1977**, *25*, 375-92.

(69) Ehlert, T. C. *J. Phys.* **1971**, *E3*, 237.

(70) Dawson, P. H. *Quadrupole Mass Spectrometry and its Applications.*, **1976**, , 95-119.

(71) Dawson, P. H.; Whetten, N. R. *Int. J. Mass Spectrom. Ion Phys.*, **1969**, *3*, 1-12.

Bibliography

(72) Wang, Y.; Franzen, J.; Wanczek, K. P. *Int. J. Mass Spectrom. Ion Processes*, **1993**, *124*, 125-44.

(73) *Quadrupole Mass Spectrometry and its Applications,* Dawson, P. H.; Editor , **1976**, , 349 pp.

(74) Dawson, P. H. *J. Vac. Sci. Technol., A*, **1986**, *4*, 1709-14.

(75) Post, R. F. *Univ. Calif. Radiat. Lab. Rept.*, **1953**, , 2209.

(76) Uchida, Y.; Miwa, T.; Hattory, S. *Mass Spectrosc. (Tokyo)* **1982,** *30*, 219.

(77) Shagimuratov, G. I.; Konenkov, N. V.; Moglichenko, G. A.; Silakov, S. S. *J. Tech. Phys. (Leningrad)* **1990,** *60*, 112.

(78) Hiroki, S.; Kaneko, K.; Murakami, Y. *Vacuum*, **1995**, *46*, 1445-7.

(79) Grimm, C. C.; Clawson, R.; Short, R. T. *J. Am. Soc. Mass Spectrom.*, **1997**, *8*, 539-544.

(80) Wei, J. *Proc. Electrochem. Soc.*, **1997**, , 97-9.

(81) Konenkov, N. V.; Silakov, S. S.; Mogil'chenko, G. A. *Pis'ma Zh. Tekh. Fiz.*, **1991**, *17*, 21-4.

(82) Konenkov, N. V.; Mogil'chenko, G. A.; Silakov, S. S.; Shagimuratov, G. I. *Prib. Tekh. Eksp.*, **1990**, , 179-81.

(83) Hiroki, S.; Abe, T.; Murakami, Y. *Rev. Sci. Instrum.*, **1991**, *62*, 2121-4.

(84) Hiroki, S.; Abe, T.; Murakami, Y. *Rev. Sci. Instrum.*, **1992**, *63*, 3874-6.

(85) Hiroki, S.; Abe, T.; Murakami, Y.; Yanagishita, K.; Nakamura, S. *J. Vac. Sci. Technol., A*, **1994**, *12*, 2711-15.

(86) Hiroki, S.; Abe, T.; Murakami, Y. *Rev. Sci. Instrum.*, **1994**, *65*, 1912-17.

(87) Hiroki, S.; Abe, T.; Murakami, Y. *Int. J. Mass Spectrom. Ion Processes*, **1994**, *136*, 85-9.

(88) Hiroki, S.; Sakata, K.; Sugiyama, N.; Muramoto, S.; Abe, T.; Murakami, Y. *Vacuum*, **1995**, *46*, 681-3.

(89) Hiroki, S.; Abe, T.; Murakami, Y. *Vacuum*, **1996**, *47*, 767-769.

Bibliography

(90) Pedder, R. E.; Schaeffer, R. A. *Proceedings of The 43rd ASMS Conference on Mass Spectrometry and Allied Topics*, Atlanta, Georgia, May 21-26 **1995**; 1069.

(91) Pedder, R. E.; Schaeffer, R. A. *Proceedings of The 44th ASMS Conference on Mass Spectrometry and Allied Topics*, Portland, Oregon, May 12-16 **1996**; 1153.

(92) Konenkov, N. V.; Kitaeva, T. I.; Nikol'skii, P. S.; Silakov, S. S.; Tolstoguzov, A. B. *Radiotekh. Elektron. (Moscow)*, **1992**, *37*, 1528-30.

(93) Dawson, P. H. *J. Vac. Sci. Technol.*, **1974**, *11*, 1151.

(94) Konenkov, N. V.; Dowell, J. T. *Int. J. Mass Spectrom. Ion Proc.*, **1997**, *164*, 201-206.

(95) Dormand, J. R.; Prince, P. J. *Celestial Mechanics*, **1978**, , 223-232.

(96) Dormand, J. R.; Prince, P. J. *J. Comp. Appl. Math.* **1980,** *6*, 19-26.

(97) Konenkov, N. V.; Douglas, D. J. , *Rapid Commun. Mass Spectrom.,* in press.

(98) Bronson, R. *Modern Introductory Differential Equations*; McGraw-Hill , Inc.: New York, **1973**.

(99) Szilgyi, M. *Electron and Ion Opticas*; Mir.: Moscow, **1990**.

(100) Konenkov, N. V. *Elektronic Tekh: Ser: Electrovakh. Gasocydel. Apparat.* **1991,** *3*, 14.

(101) Konenkov, N. V.; Mogil'chenko, G. A.; Silakov, S. S. *Sov. J. Tech. Phys.*, **1990**, *1*, 117.

(102) Dawson, P. H. *Adv. Electron. Electron Phys., Suppl.*, **1980**, *13B*, 173-256.

Appendix

Appendix I The ion trajectory simulation program

```
program pro;
uses crt,dos,graph;
const n=2;
    nmax=30000;uround=1.73e-15;
    alph1=0.1;alph2=0.2;alph3=3.0/8.0;alph4=0.5;
    sq21=4.58257569495584;{sqrt(21)}
    alph5=(7.0-sq21)/14.0;
    alph6=(7+sq21)/14.0;
    c0=0.05;c4=16.0/45.0;c5=49.0/180.0;
    g10=1.0/200;g20=1.0/150.0;g21=1.0/75.0;g30=171.0/8192.0;
    g31=45.0/4096.0;g32=315.0/8192.0;g40=5.0/288.0;g41=25.0/528.0;
    g42=25.0/672.0;g43=16.0/693.0;
    g50=(1003-205*sq21)/12348.0;g51=(-18775+4325*sq21)/90552.0;
    g52=(15600-3425*sq21)/43218.0;g53=(-46208+10112*sq21)/237699.0;
    g54=(3411.0-745*sq21)/24696.0;g60=(793+187*sq21)/12348.0;
    g61=(-8275-2825*sq21)/90552.0;g62=(26100+6175*sq21)/43218.0;
    g63=-(1905280+483712*sq21)/9745659.0;g64=(3327+797*sq21)/24696.0;
    g65=-(581+127*sq21)/1722.0;g70=(-157+3*sq21)/378.0;
    g71=(3575-250*sq21)/2772.0;g72=-(21900+1375*sq21)/3969.0;
    g73=(1168640+23040*sq21)/596673.0;g74=-(1353+26*sq21)/2268.0;
    g75=(12439+2639*sq21)/4428.0;g76=(35-7*sq21)/36.0;
    g80=0.05;g84=8.0/45.0;g85=(49+7*sq21)/360.0;g86=(49-7*sq21)/360.0;
    posneg=1.0;
var
    grDriver: Integer;
    grMode: Integer;
    ErrCode: Integer;

    fll :text;
    chrr,crr:string;
    hh, mm, ss, hund : Word;
    hh1, mm1, ss1, hund1 : Word;
    mx,my:integer;
    m:longint;
    u,v,k0,k1,k2,k3,k4:array[0..51] of extended;
    y1,y,yp:array[0..n+1] of extended;
    z,zz,mmx:array[0..n+1] of extended;
    reject:boolean;
    j,ii,nfcn,nstep,naccpt,nrejct:integer;
    h,eps,hp2,hnew,err,denom,den,fac,hmax,
    dd,kk,s,t,x,xend,yls,xph:extended;
    a,a2,a3,a4,a5,a6,a7,a8,a9,a10,q,x0:extended;
    b2,b3,b4,b5,b6,b7,b8,b9,b10,d2,d3,d4,fp:extended;
    st:longint;
label 21;
```

Appendix

```
function LeadingZero(w : Word) : String;
var
  s : String;
begin
  Str(w:0,s);
  if Length(s) = 1 then
    s := '0' + s;
  LeadingZero := s;
end;
procedure fcn(x:extended;y:array of extended;var f:array of extended);
var gg:extended;
    xx,x2,x4,x8:extended;
    yy,y2,y4,y8:extended;d2,d3,d4:extended;
    gx3,gx4,gx5,gx6,gx7,gx8,gx9,gx10:extended;
    gy3,gy4,gy5,gy6,gy7,gy8,gy9,gy10:extended;
    wwx,wwy,vvx,vvy:extended;
begin
gg:=(a-2*q*cos(2*(x-x0)));

xx:=y[1];x2:=sqr(xx);x4:=sqr(x2);x8:=sqr(x4);
yy:=y[2];y2:=sqr(yy);y4:=sqr(y2);y8:=sqr(y4);

gx3:=3*(x2-y2);
gy3:=-6*xx*yy;

gx4:=4*xx*(x2 -3*y2);
gy4:=-4*yy*(3*x2-y2);

gx5:=5*(x4-6*x2*y2+y4);
gy5:=-20*xx*yy*(x2-y2);

gx6:=6*xx*(x4-10*x2*y2+5*y4);
gy6:=6*yy*(-5*x4+10*x2*y2-y4);

gx7:=7*(x2*x4-15*x4*y2+15*x2*y4-y2*y4);
gy7:=xx*yy*(-42*x4+140*x2*y2-42*y4);

gx8:=8*xx*(x2*x4-21*x4*y2+35*x2*y4-7*y2*y4);
gy8:=8*yy*(-7*x2*x4+35*x4*y2-21*x2*y4+y2*y4);

  gx9:=9*(x8-28*x2*x4*y2+70*x4*y4-28*x2*y2*y4+y8);
  gy9:=72*xx*yy*(-x2*x4+7*x4*y2-7*x2*y4+y2*y4);

   gx10:=10*xx*(x8-36*x2*x4*y2+126*x4*y4-84*x2*y2*y4+9*y8);
   gy10:=10*yy*(-9*x8+84*x2*x4*y2-126*x4*y4+36*x2*y2*y4-y8);

 wwx:=a3*gx3+a4*gx4+a5*gx5+a6*gx6+a7*gx7+a8*gx8+a9*gx9+a10*gx10;
    wwy:=a3*gy3+a4*gy4+a5*gy5+a6*gy6+a7*gy7+a8*gy8+a9*gy9+a10*gy10;

    vvx:=b3*gx3+b4*gx4+b5*gx5+b6*gx6+b7*gx7+b8*gx8+b9*gx9+b10*gx10;
    vvy:=b3*gy3+b4*gy4+b5*gy5+b6*gy6+b7*gy7+b8*gy8+b9*gy9+b10*gy10;

    f[1]:=(-xx-wwx-vvy)*gg;
    f[2]:=(yy-wwy+vvx)*gg;
```

```
end;


function max(a,b:extended):extended;
begin
if a>b then max:=a else max:=b;
end;
function min(a,b:extended):extended;
begin
if a<b then min:=a else min:=b;
end;


procedure doprin;
label 1,79,999;
var i:integer;
begin
eps:=max(eps,9*uround);
reject:=false;
naccpt:=0;
nfcn:=1;
nstep:=0;
nrejct:=0;
fcn(x,y,k0);
z[1]:=y[1];z[2]:=y[2];
1:
if (nstep>nmax) or (x+0.05*h=x) then goto 79;
if (x-xend+uround>0) then goto 999;
if (x+h-xend>0) then h:=xend-x;
hp2:=h*h;
nstep:=nstep+1;
for i:=1 to n do
y1[i]:=y[i]+alph1*h*yp[i]+hp2*g10*k0[i];
fcn(x+alph1*h,y1,k1);
for i:=1 to n do
y1[i]:=y[i]+alph2*h*yp[i]+hp2*(g20*k0[i]+g21*k1[i]);
fcn(x+alph2*h,y1,k2);
for i:=1 to n do
y1[i]:=y[i]+alph3*h*yp[i]+hp2*(g30*k0[i]+g31*k1[i]+g32*k2[i]);
fcn(x+alph3*h,y1,k3);
for i:=1 to n do
y1[i]:=y[i]+alph4*h*yp[i]+hp2*(g40*k0[i]+g41*k1[i]+g42*k2[i]+g43*k3[i]);
fcn(x+alph4*h,y1,k4);
for i:=1 to n do
y1[i]:=y[i]+alph5*h*yp[i]+hp2*(g50*k0[i]+g51*k1[i]+g52*k2[i]+g53*k3[i]
+g54*k4[i]);
for i:=1 to n do
begin
yls:=g60*k0[i]+g61*k1[i]+g62*k2[i]+g63*k3[i]+g64*k4[i];
k3[i]:=g70*k0[i]+g71*k1[i]+g72*k2[i]+g73*k3[i]+g74*k4[i];
k2[i]:=yls;
end;
fcn(x+alph5*h,y1,k1);
for i:=1 to n do
y1[i]:=y[i]+alph6*h*yp[i]+hp2*(k2[i]+g65*k1[i]);
```

Appendix

```
fcn(x+alph6*h,y1,k2);
for i:=1 to n do
y1[i]:=y[i]+h*yp[i]+hp2*(k3[i]+g75*k1[i]+g76*k2[i]);
xph:=x+h;
fcn(xph,y1,k3);
for i:=1 to n do
y1[i]:=y[i]+h*yp[i]+hp2*(g80*k0[i]+g84*k4[i]+g85*k1[i]+g86*k2[i]);
for i:=1 to n do
k4[i]:=yp[i]+h*(c0*(k0[i]+k3[i])+c4*k4[i]+c5*(k1[i]+k2[i]));
fcn(xph,y1,k1);
for i:=1 to n do
k2[i]:=hp2*(k1[i]-k3[i])/20.0;
nfcn:=nfcn+8;
err:=0;

for i:=1 to n do
begin
den:=max(1.0e-06,abs(y1[i]));
denom:=max(den,abs(y[i]));
den:=max(denom,2*uround/eps);
denom:=den;
err:=err+sqr(k2[i]/denom);
end;
err:=sqrt(err/n);
if err=0 then t:=0 else
            t:=exp(ln(err/eps)/7.0);
fac:=max(0.1,min(5,t/0.9));
hnew:=h/fac;
if err<eps then
begin
   naccpt:=naccpt+1;
      x:=xph;
      for i:=1 to n do
   begin
      yp[i]:=k4[i]; k0[i]:=k1[i]; y[i]:=y1[i];
      line(round(dd*s),round(mmx[i]-kk*z[i]),
      round(dd*x),round(mmx[i]-kk*y[i]));
      z[i]:=y[i];
   end;
   st:=st+1;
   if st mod 1 =0 then
            begin
            append(fll);
            writeln(fll,x,' ',y[1],' ',y[2]);
            close(fll);
            end;
    s:=x;
   solut2;
   for i:=1 to n do
   if abs(y[i])>1 then goto 79;
   if (hnew>hmax) then
   hnew:=hmax;
   if reject then
   begin
   hnew:=min(hnew,h);
```

```
    reject:=false;
   end
   else
    reject:=true;
    if (naccpt>1) then nrejct:=nrejct+1;
   end;
h:=hnew;
goto 1;
79:writeln(' exit of doprin at x=', x);
999:
end;

begin

clrscr;
GetTime(hh,mm,ss,hund);
grDriver := Detect;
 InitGraph(grDriver, grMode,'');

 ErrCode := GraphResult;
 if ErrCode = grOk then
 begin
 mx:=getmaxx;
 my:=getmaxy;

writeln;
outtext('Input filename for output data  ');
readln(chrr);
chrr:=chrr+'.txt';
assign(fll,chrr);

rewrite(fll);
outtext('Input comments line:');
readln(crr);
writeln(fll,crr);
writeln;
close(fll);

      a2:=1.0  ;b2:=0;
      a3:=0;        b3:=0;
      a4:=0;    b4:=0;
      a5:=0;        b5:=0;
      a6:=0;     b6:=0;
      a7:=0;        b7:=0;
      a8:=-0;    b8:=0;
      a9:=0;         b9:=0;
      a10:=0;   b10:=0;

      d2:=a2*a2;d3:=a2*a2*a2;d4:=d2*d2;
      a3:=a3/sqrt(d3)*0.5;      b3:=b3/sqrt(d3)*0.5;
      a4:=a4/d2*0.5;           b4:=b4/d2*0.5;
      a5:=a5/sqrt(d2*d3)*0.5;   b5:=b5/sqrt(d2*d3)*0.5;
      a6:=a6/d3*0.5;           b6:=b6/d3*0.5;
      a7:=a7/sqrt(d3*d4)*0.5;   b7:=b7/sqrt(d3*d4)*0.5;
      a8:=a8/d4*0.5;           b8:=b8/d4*0.5;
```

Appendix

```
      a9:=a9/sqrt(a2*d4*d4)*0.5; b9:=b9/sqrt(a2*d4*d4)*0.5;
      a10:=a10/(a2*d4)*0.5;     b10:=b10/(a2*d4)*0.5;


u[1]:=1;u[2]:=20;u[3]:=1;u[4]:=1;u[5]:=1;
v[1]:=0.1;v[2]:=0.1;v[3]:=2.1;v[4]:=3.1;v[5]:=4.1;

for j:=0 to 39 do
begin
x:=0;
xend:=10*pi;
y[1]:=0.0001; y[2]:=0.0001;
fp:=-1.0;
yp[1]:=fp*y[1];
yp[2]:=fp*y[2];
eps:=0.0000001;h:=pi/40;hmax:=pi/40;
a:=0.0155497;q:=21.30095;
x0:=j*pi/40;
append(fll);
writeln(fll,'a=',a, ', q=',q, ', Ux=',y[1],', Uy=',y[2],', FP=', fp, ', h=', h, ', # of initial phase=',j);
close(fll);
mmx[1]:=round(my/4.0);
mmx[2]:=3*round(my/4.0);
kk:=mmx[1]*1;
dd:=1/((xend-x)/mx);
 setcolor(9+j);
 s:=x;
 doprin;

 readln;
 end
end
 else
 Writeln('Graphics error:', GraphErrorMsg(ErrCode));

writeln(mx,my,mmx[1],mmx[2]);
writeln(y[1],y[2],round(x*dd));

Writeln('It was    ',LeadingZero(hh),':',
      LeadingZero(mm),':',LeadingZero(ss),
      '.',LeadingZero(hund));


GetTime(hh1,mm1,ss1,hund1);
Writeln('It is now ',LeadingZero(hh1),':',
      LeadingZero(mm1),':',LeadingZero(ss1),
      '.',LeadingZero(hund1));


end
```

Appendix II The program for simulation of peak shapes or ion transmission curves.

```
program pro;
{$D+}
uses crt,dos;
const n=2;
    nmax=30000;uround=1.73e-15;
    alph1=0.1;alph2=0.2;alph3=3.0/8.0;alph4=0.5;
    sq21=4.582575694955840177 8092;
    alph5=(7.0-sq21)/14.0;
    alph6=(7+sq21)/14.0;
    c0=0.05;c4=16.0/45.0;c5=49.0/180.0;
    g10=1.0/200;g20=1.0/150.0;g21=1.0/75.0;g30=171.0/8192.0;
    g31=45.0/4096.0;g32=315.0/8192.0;g40=5.0/288.0;g41=25.0/528.0;
    g42=25.0/672.0;g43=16.0/693.0;
    g50=(1003-205*sq21)/12348.0;g51=(-18775+4325*sq21)/90552.0;
    g52=(15600-3425*sq21)/43218.0;g53=(-46208+10112*sq21)/237699.0;
    g54=(3411.0-745*sq21)/24696.0;g60=(793+187*sq21)/12348.0;
    g61=(-8275-2825*sq21)/90552.0;g62=(26100+6175*sq21)/43218.0;
    g63=-(1905280+483712*sq21)/9745659.0;g64=(3327+797*sq21)/24696.0;
    g65=-(581+127*sq21)/1722.0;g70=(-157+3*sq21)/378.0;
    g71=(3575-250*sq21)/2772.0;g72=-(21900+1375*sq21)/3969.0;
    g73=(1168640+23040*sq21)/596673.0;g74=-(1353+26*sq21)/2268.0;
    g75=(12439+2639*sq21)/4428.0;g76=(35-7*sq21)/36.0;
    g80=0.05;g84=8.0/45.0;g85=(49+7*sq21)/360.0;g86=(49-7*sq21)/360.0;
    posneg=1.0;
var
    grDriver: Integer;
    grMode: Integer;
    ErrCode: Integer;
    amp,traect, KeyPressed: boolean;
    fll:text;
    chrr,crr:string;
    ch:char;
    hh, mm, ss, hund : Word;
    hh1, mm1, ss1, hund1 : Word;
    mx,my:integer;
    m,oo:longint;
    u,v,qq,k0,k1,k2,k3,k4:array[0..51] of double;
    y1,y,yp:array[0..n+1] of double;
    z,zz,mmx:array[0..n+1] of double;
    reject:boolean;
    j,j1,j2,j3,j4,ii,sum,nfcn,nstep,naccpt,nrejct:integer;
    xz,nf,fz,h,eps,hp2,hnew,err,denom,den,fac,hmax,
    qb,qend,dd,kk,s,t,x,xend,yls,xph:double;
    a,a3,q,x0,la,rr,ff,fp,nrf,rr0:double;
    la0:integer;
    a2,a4,a6,a8,a10,a12,a14,a16,a18:double;
label 21;

function LeadingZero(w : Word) : String;
```

Appendix

```
var
 s : String;
begin
 Str(w:0,s);
 if Length(s) = 1 then
   s := '0' + s;
 LeadingZero := s;
end;

procedure fcn(x:double;y:array of double;var f:array of double);
var gg:double;
   xx,x2,x4,x8,xz,fz:double;
   yy,y2,y4,y8:double;

begin
gg:=(a-2*q*cos(2*(x-x0)));
if x>=pi*nf then
        begin
        f[1]:=-gg*y[1];f[2]:=gg*y[2];
        end
        else
        begin
        xz:=1.5*x/pi/nf;
        fz:=1-exp(-xz*(2.13+1.55*xz));
        f[1]:=-gg*y[1]*fz;f[2]:=gg*y[2]*fz;
        end;



procedure solut2;
begin
if (abs(y[1])>1) or (abs(y[2])>1) then amp:=false;

end;

function max(a,b:double):double;
begin
if a>b then max:=a else max:=b;
end;
function min(a,b:double):double;
begin
if a<b then min:=a else min:=b;
end;

procedure doprin;
label 1,79,999;
var i:integer;
begin
eps:=max(eps,9*uround);
reject:=false;
naccpt:=0;
nfcn:=1;
nstep:=0;
nrejct:=0;
fcn(x,y,k0);
```

Appendix

```
z[1]:=y[1];z[2]:=y[2];
1:
if (x-xend+uround>0) then goto 999;
if (x+h-xend>0) then h:=xend-x;
hp2:=h*h;
nstep:=nstep+1;
for i:=1 to n do
y1[i]:=y[i]+alph1*h*yp[i]+hp2*g10*k0[i];
fcn(x+alph1*h,y1,k1);
for i:=1 to n do
y1[i]:=y[i]+alph2*h*yp[i]+hp2*(g20*k0[i]+g21*k1[i]);
fcn(x+alph2*h,y1,k2);
for i:=1 to n do
y1[i]:=y[i]+alph3*h*yp[i]+hp2*(g30*k0[i]+g31*k1[i]+g32*k2[i]);
fcn(x+alph3*h,y1,k3);
for i:=1 to n do
y1[i]:=y[i]+alph4*h*yp[i]+hp2*(g40*k0[i]+g41*k1[i]+g42*k2[i]+g43*k3[i]);
fcn(x+alph4*h,y1,k4);
for i:=1 to n do
y1[i]:=y[i]+alph5*h*yp[i]+hp2*(g50*k0[i]+g51*k1[i]+g52*k2[i]+g53*k3[i]
+g54*k4[i]);
for i:=1 to n do
begin
yls:=g60*k0[i]+g61*k1[i]+g62*k2[i]+g63*k3[i]+g64*k4[i];
k3[i]:=g70*k0[i]+g71*k1[i]+g72*k2[i]+g73*k3[i]+g74*k4[i];
k2[i]:=yls;
end;
fcn(x+alph5*h,y1,k1);
for i:=1 to n do
y1[i]:=y[i]+alph6*h*yp[i]+hp2*(k2[i]+g65*k1[i]);
fcn(x+alph6*h,y1,k2);
for i:=1 to n do
y1[i]:=y[i]+h*yp[i]+hp2*(k3[i]+g75*k1[i]+g76*k2[i]);
xph:=x+h;
fcn(xph,y1,k3);
for i:=1 to n do
y1[i]:=y[i]+h*yp[i]+hp2*(g80*k0[i]+g84*k4[i]+g85*k1[i]+g86*k2[i]);
for i:=1 to n do
k4[i]:=yp[i]+h*(c0*(k0[i]+k3[i])+c4*k4[i]+c5*(k1[i]+k2[i]));
fcn(xph,y1,k1);
for i:=1 to n do
k2[i]:=hp2*(k1[i]-k3[i])/20.0;
nfcn:=nfcn+8;
err:=0;

for i:=1 to n do
begin
den:=max(1.0e-06,abs(y1[i]));
denom:=max(den,abs(y[i]));
den:=max(denom,2*uround/eps);
denom:=den;
err:=err+sqr(k2[i]/denom);
end;
err:=sqrt(err/n);
if err=0 then t:=0 else
```

Appendix

```
                t:=exp(ln(err/eps)/7.0);
fac:=max(0.1,min(5,t/0.9));
hnew:=h/fac;
if err<eps then
begin
   naccpt:=naccpt+1;
      x:=xph;
      for i:=1 to n do
   begin
      yp[i]:=k4[i]; k0[i]:=k1[i]; y[i]:=y1[i];
if (abs(y[1])>1) or (abs(y[2])>1) then amp:=false;
if not amp then goto 999;
   for i:=1 to n do
   if (hnew>hmax) then
   hnew:=hmax;
   if reject then
   begin
   hnew:=min(hnew,h);
   reject:=false;
  end
  else
   reject:=true;
   if (naccpt>1) then nrejct:=nrejct+1;
  end;
h:=hnew;
goto 1;
79:writeln(' exit of doprin at x=', x);
999:
end;

begin
writeln;
writeln('Input filename for output data');
readln(chrr);
assign(fll,chrr);{open file 'data.t'}
write('Do you want to append to (existing) file (y/any key)?');
ch:=readkey;
writeln(ch);
if ch='y' then
          begin
          append(fll);
          {writeln(fll);}
          end

       else Rewrite(fll);{clear file 'data.t'}
writeln('Input comments line:');
readln(crr);
writeln(fll,crr);
close(fll);

GetTime(hh,mm,ss,hund);

                {INITIAL DATA}

nrf:=15.4405;
```

Appendix

```
nf:=0.805994;
xend:=(nrf+nf)*pi;eps:=0.00001;
hmax:=pi/50;
for la0:=0 to 15  do
begin
la:=0.62+la0/500;
qb:=44.7040-159.1880*la+156.5714*la*la;
qend:=37.1972-135.0370*la+137.2143*la*la;
amp:=true;
randomize;
for j:=0 to 39 do
begin
sum:=0;
q:=qb+(qend-qb)/40*j;
a:=2*la*q;
for j1:=0 to 49 do
begin
x0:=pi/50.0*j1;
{for j2:=-5 to 5 do begin
for j3:=-5 to 5 do begin
if (j2<>0) and (j3<>0) then
begin}
for j2:=1 to 100 do
begin
rr0:=0.01;{aperture radius: rr:=0.1}
rr:=sqrt(random(2500)/2500)*rr0;{ radius R in polar coordinate}
ff:=random(5000)/2500.0*pi;   { angle of R in polar coordinate}
x:=0;
fp:=-2;
y[1]:= rr*cos(ff);
y[2]:= rr*sin(ff);
yp[1]:=fp*y[1]; yp[2]:=fp*y[2];
h:=pi/40;{initial step}

end;
assign(fll,chrr);{open file 'data.t'}

append(fll);

writeln(fll,q,',',sum,',',sum/5000); {5000=j1*j2, full number of ions}

close(fll);
write(j,': ',q,',',sum);
GetTime(hh1,mm1,ss1,hund1);
Writeln('  --  ',LeadingZero(hh1),':',
      LeadingZero(mm1),':',LeadingZero(ss1),
      '.',LeadingZero(hund1));
end;

append(fll);
writeln(' lamda=', la);
writeln(fll,'nrf=',nrf,' nf=', nf,' lamda=',la, ' fp=', fp, ' aperture radius= ',rr0 );
close(fll);
end;
Write('It was   ',LeadingZero(hh),':',
```

```
        LeadingZero(mm),':',LeadingZero(ss),
        '.',LeadingZero(hund),'.');


GetTime(hh1,mm1,ss1,hund1);
Writeln(' It is now ',LeadingZero(hh1),':',
        LeadingZero(mm1),':',LeadingZero(ss1),
        '.',LeadingZero(hund1));
readln;

end.
```

Appendix III The program for acceptance calculation

```
1 DEFDBL A-H, O-Z
2 REM OPEN "aclx25.dat" FOR OUTPUT AS #1
5 PI = 3.141592653589793#
10 A = 7.981841#'INPUT "A ="; A
15 Q = 6.3854754#' INPUT "Q ="; Q
16 INPUT "Transmission level ="; TL
110 DIM S(2, 200), D(2, 200), W(2, 200)
130 DIM M(100), N(100), K(100)
140 DIM A(100), B(100), G(100)
141 DIM Y(100), X(100), Z(100)
142 DIM X8(200), Y8(200), X9(100), Y9(100)
170 DIM E(2, 2), T(2, 2)
180 DIM R(2, 2), F(2, 2), I1(2, 2)
181 DATA 1,0,0,1
182 DEF FNZ (X) = 1 - EXP(-2.13 * X - 1.55 * X * X)
185 REM DEF FNZ(X)=0.53*X*X*X-1.94*X*X+2.39*X
186 REM FNZ(X)=1-EXP(-2.4*X-1.47*X*X)
200 DEF FNC (X) = (EXP(X) + EXP(-X)) / 2
210 DEF FNS (X) = (EXP(X) - EXP(-X)) / 2
220 K = 0
221 i = 0
230 M = 10
240 T = PI / 1000
250 E(1, 1) = 1
251 E(1, 2) = 0
252 E(2, 1) = 0
254 E(2, 2) = 1
260 K = K + 1
270 H = A + 2 * Q * COS(2 * T * K)
280 IF H >= 0 THEN 350
290 V = SQR(ABS(H))
300 T(1, 1) = FNC(V * T)
310 T(1, 2) = FNS(V * T) / V
320 T(2, 1) = FNS(V * T) * V
330 T(2, 2) = FNC(V * T)
340 GOTO 400
350 V = SQR(H)
360 T(1, 1) = COS(V * T)
370 T(1, 2) = SIN(V * T) / V
380 T(2, 1) = -SIN(V * T) * V
390 T(2, 2) = COS(V * T)
400 F(1, 1) = T(1, 1) * E(1, 1) + T(1, 2) * E(2, 1)
401 F(1, 2) = T(1, 1) * E(1, 2) + T(1, 2) * E(2, 2)
402 F(2, 1) = T(2, 1) * E(1, 1) + T(2, 2) * E(2, 1)
403 F(2, 2) = T(2, 1) * E(1, 2) + T(2, 2) * E(2, 2)
410 FOR I2 = 1 TO 2
411 FOR J = 1 TO 2
412 E(I2, J) = F(I2, J)
413 NEXT J
414 NEXT I2
420 IF K = M THEN 450
430 GOTO 260
```

Appendix

```
450 S(1, i + 1) = F(1, 1)
460 S(1, i + 2) = F(1, 2)
470 S(2, i + 1) = F(2, 1)
480 S(2, i + 2) = F(2, 2)
490 IF K >= 1000 THEN 540
500 E(1, 1) = 1
501 E(1, 2) = 0
502 E(2, 1) = 0
503 E(2, 2) = 1
510 M = M + 10
520 i = i + 2
530 GOTO 260
540 L = 0
560 FOR I2 = 1 TO 2
561 FOR J = 1 TO 200
562 W(I2, J) = S(I2, J)
563 NEXT J
564 NEXT I2
580 K = 1
590 T(1, 1) = W(1, 1)
600 T(1, 2) = W(1, 2)
610 T(2, 1) = W(2, 1)
620 T(2, 2) = W(2, 2)
630 R(1, 1) = W(1, K + 2)
640 R(1, 2) = W(1, K + 3)
650 R(2, 1) = W(2, K + 2)
660 R(2, 2) = W(2, K + 3)
670 F(1, 1) = R(1, 1) * T(1, 1) + R(1, 2) * T(2, 1)
671 F(1, 2) = R(1, 1) * T(1, 2) + R(1, 2) * T(2, 2)
672 F(2, 1) = R(2, 1) * T(1, 1) + R(2, 2) * T(2, 1)
673 F(2, 2) = R(2, 1) * T(1, 2) + R(2, 2) * T(2, 2)
680 FOR I2 = 1 TO 2
681 FOR J = 1 TO 2
682 T(I2, J) = F(I2, J)
683 NEXT J
684 NEXT I2
690 IF K >= 197 THEN 720
700 K = K + 2
710 GOTO 630
720 L = L + 1
750 Z = (F(1, 1) + F(2, 2)) / 2
760 IF Z > 0 THEN 790
770 X = 3 + ATN(SQR(1 - Z ^ 2) / Z) / PI
780 GOTO 800
790 X = 2 + ATN(SQR(1 - Z ^ 2) / Z) / PI
800 Y(L) = F(1, 2) / SIN(PI * X)
820 X(L) = -F(2, 1) / SIN(PI * X)
840 Z(L) = (F(1, 1) - F(2, 2)) / 2 / SIN(PI * X)
841 COLOR 5
860 PRINT "BETA="; X
890 FOR I2 = 1 TO 2
891 FOR J = 1 TO 200
892 D(I2, J) = W(I2, J)
893 NEXT J
894 NEXT I2
```

Appendix

```
900 FOR I2 = 1 TO 2
910 FOR J = 1 TO 198
920 W(I2, J) = D(I2, J + 2)
930 NEXT J
940 NEXT I2
950 W(1, 199) = D(1, 1)
960 W(1, 200) = D(1, 2)
970 W(2, 199) = D(2, 1)
980 W(2, 200) = D(2, 2)
990 IF L <= 99 THEN 580
1000 COLOR 11
1010 PRINT "A="; A, "Q="; Q, "Beta="; X
1030 REM LPRINT "A="; A, "Q="; Q, "Beta="; X
1040 D = 0
1050 FOR i = 1 TO 100
1060 IF D > Y(i) THEN 1080
1070 D = Y(i)
1080 NEXT i
1081 M8 = 0
1855 REM ************************************************************************
1856 INPUT "Number of cycles from"; N1S
1857 INPUT "to"; N1F
1858 INPUT "step"; N1ST
1860 FOR N1 = N1S TO N1F STEP N1ST
1870 K1 = 1.5
1880 FOR i = 1 TO 100
1890 A(i) = Z(i)
1900 B(i) = Y(i)
1910 G(i) = X(i)
1920 NEXT i
1995 N0 = 1000
2000 H = PI / N0
2001 D1 = PI / 100
2002 N7 = N1 * PI
2010 Z0 = K1 / N1 / PI
2020 FOR i = 1 TO 100
2030 T0 = -(i - 1) * D1 + N7
2040 X1 = 1
2050 Y1 = 0
2060 X2 = 0
2070 Y2 = 1
2080 K = 0
2100 T = H * K
2110 Z1 = Z0 * T
2120 R1 = X1
2130 W1 = Y1
2140 R2 = X2
2150 W2 = Y2
2160 F2 = FNZ(Z1)
2170 A0 = A + 2 * Q * COS(2 * (T - T0))
2180 E0 = -A0 * F2 * H
2190 E1 = E0 * R1
2200 E2 = E0 * R2
2210 T1 = T + H / 2
2220 V1 = R1 + W1 * H / 2 + E1 * H / 8
```

```
2230 V2 = R2 + W2 * H / 2 + E2 * H / 8
2240 Z2 = T1 * Z0
2250 F3 = FNZ(Z2)
2260 A1 = A + 2 * Q * COS(2 * (T1 - T0))
2270 G0 = -A1 * F3 * H
2280 G1 = G0 * V1
2290 G2 = G0 * V2
2300 T2 = T + H
2310 Z3 = Z0 * T2
2320 F4 = FNZ(Z3)
2330 V3 = R1 + W1 * H + G1 * H / 2
2340 V4 = R2 + W2 * H + G2 * H / 2
2350 A2 = A + 2 * Q * COS(2 * (T2 - T0))
2360 S0 = -A2 * F4 * H
2370 S1 = S0 * V3
2380 S2 = S0 * V4
2390 X1 = R1 + (W1 + (E1 + 2 * G1) / 6) * H
2400 X2 = R2 + (W2 + (E2 + 2 * G2) / 6) * H
2410 Y1 = W1 + E1 / 6 + 2 * G1 / 3 + S1 / 6
2420 Y2 = W2 + E2 / 6 + 2 * G2 / 3 + S2 / 6
2450 K = K + 1
2460 T = K * H
2470 Z1 = Z0 * T
2480 A5 = (A + 2 * Q * COS(2 * (T - 2 * H - T0))) * FNZ(Z0 * (T - 2 * H))
2490 A6 = (A + 2 * Q * COS(2 * (T - H - T0))) * FNZ(Z0 * (T - H))
2500 A7 = (A + 2 * Q * COS(2 * (T - T0))) * FNZ(Z0 * T)
2510 E4 = (1 + H * H * A5 / 12)
2520 E5 = E4 * R1
2530 E6 = E4 * R2
2540 G4 = -2 * (1 - 5 * H * H * A6 / 12)
2550 G5 = G4 * X1
2560 G6 = G4 * X2
2570 F5 = 1 + H * H * A7 / 12
2580 M1 = -(E5 + G5) / F5
2590 M2 = -(E6 + G6) / F5
2600 IF A7 > 0 THEN 2660
2610 U = SQR(ABS(A7))
2620 B = H * U
2630 A3 = FNS(B) * U
2640 A4 = FNC(B)
2650 GOTO 2820
2660 U = SQR(A7)
2670 B = H * U
2680 A3 = -SIN(B) * U
2690 A4 = COS(B)
2820 Y3 = X1 * A3 + Y1 * A4
2830 Y4 = X2 * A3 + Y2 * A4
2840 R1 = X1
2850 R2 = X2
2860 X1 = M1
2870 X2 = M2
2880 Y1 = Y3
2890 Y2 = Y4
2900 IF K >= N1 * N0 THEN 2920
2910 GOTO 2450
```

Appendix

```
2920 C = X1
2930 C1 = Y1
2940 S = X2
2950 S1 = Y2
2960 REM PRINT " I= "; I, " DELTA= "; C * S1 - S * C1
2970 M(i) = S1 * S1 * B(i) + 2 * S * S1 * A(i) + S * S * G(i)
2980 N(i) = C1 * S1 * B(i) + (C1 * S + C * S1) * A(i) + C * S * G(i)
2990 K(i) = C1 * C1 * B(i) + 2 * C * C1 * A(i) + C * C * G(i)
3000 NEXT i
3010 FOR i = 1 TO 100
3020 B(i) = M(i)
3030 G(i) = K(i)
3040 A(i) = N(i)
3050 NEXT i


3060 REM ------------------------------ ------------ -----------------
3070 E1 = 1 / D
3080 i = 1
3090 X = 0
3100 Y = 0
3110 R1 = 1
3120 F2 = PI / 200
3130 FOR LI = 0 TO 200
3132 X1 = X
3134 Y1 = Y
3140 F3 = PI / 2 - LI * F2
3150 A1 = 0
3160 B1 = 2
3170 K = 0
3180 R1 = (A1 + B1) / 2
3190 FOR J = 1 TO 100
3200 R2 = R1 * R1
3210 E5 = G(J) * COS(F3) * COS(F3) + A(J) * SIN(2 * F3) + B(J) * SIN(F3) * SIN(F3)
3220 IF E5 * R2 > E1 THEN 3240
3230 K = K + 1
3240 NEXT J
3250 IF ABS(K - TL) < 1 THEN 3300
3260 IF K <= TL - 1 THEN 3285
3270 A1 = R1
3280 GOTO 3170
3285 B1 = R1
3286 REM PRINT USING "##.#"; K
3290 GOTO 3170
3300 X = R1 * COS(F3)
3310 Y = R1 * SIN(F3)
3320 X8(LI) = X
3330 Y8(LI) = Y
3340 GOTO 3740
3345 NEXT LI
3350 REM------------------------------------------------------------
3360 FOR i = 1 TO 100
3370 X9(i) = X8(201 - i)
3380 Y9(i) = -Y8(201 - i)
3390 NEXT i
```

Appendix

```
3392 FOR i = 1 TO 200
3394 REM PRINT #1, X8(i), Y8(i)
3396 NEXT i

3400 S = 0
3410 S8 = 0
3420 S9 = 0
3430 FOR i = 1 TO 99
3440 S8 = S8 + (Y8(i + 1) + Y8(i)) * (X8(i + 1) - X8(i)) / 2
3450 S9 = S9 + (Y9(i + 1) + Y9(i)) * (X9(i + 1) - X9(i)) / 2
3460 NEXT i
3465 SA = 2 * (S8 + S9)
3480  PRINT USING "#.##############"; 2 * (S8 + S9)
3486  PRINT USING "#.##"; N1
3500 REM LPRINT USING "###.######";2*(S8+S9),N1
3505 REM PRINT #1, N1, A, Q, SA
3510 NEXT N1
3515 CLOSE #1

3520 GOTO 4130


3740 SCREEN 9
3780 IF M8 > 0 THEN 3920
3790 INPUT "X,Y max"; X8
3791 INPUT "Velocity max"; Y8
3795 REM Xc=320
3796 REM Yc=240
3797 Xc = 100
3798 Yc = 140
3800 LINE (Xc, Yc)-(Xc + 320, Yc)
3810 LINE (Xc, Yc - 140)-(Xc, Yc + 140)
3830 REM MARK ON LINE X
3840 FOR i = Xc TO Xc + 320 STEP 32
3850 LINE (i, Yc - 5)-(i, Yc + 5)
3860 NEXT i
3870 REM ON LINE Y
3880 FOR i = (Yc - 140) TO (Yc + 140) STEP 28
3890 LINE (Xc - 5, i)-(Xc + 5, i)
3900 NEXT i
3910 M8 = 1
3920 X4 = ABS(X / X8) * 320
3930 Y4 = ABS(Y / Y8) * 140
3936 X3 = ABS(X1 / X8) * 320
3937 Y3 = ABS(Y1 / Y8) * 140
3940 IF X >= 0 THEN 3970
3950 Xkoor = Xc - X4
3960 GOTO 3980
3970 Xkoor = Xc + X4
3980 IF Y >= 0 THEN 4010
3990 Ykoor = Yc + Y4
4000 GOTO 4020
4010 Ykoor = Yc - Y4
4020 IF X1 >= 0 THEN 4060
```

Appendix

```
4040 Xn = Xc - X3
4050 GOTO 4070
4060 Xn = Xc + X3
4070 IF Y1 >= 0 THEN 4100
4080 Yn = Yc + Y3
4090 GOTO 4110
4100 Yn = Yc - Y3
4110 LINE (Xn, Yn)-(Xkoor, Ykoor)
4120 GOTO 3345
4130 END
4140 END
```